

**Synthesis and characterisation of metal dichalcogenide based nano
materials**

Submitted by Yan Wen to the University of Exeter
as a thesis for the degree of
Doctor of Philosophy in Engineering
In September 2014

This thesis is available for Library use on the understanding that it is
copyright material and that no quotation from the thesis may be
published without proper acknowledgement.

I certify that all material in this thesis which is not my own work has been
identified and that no material has previously been submitted and
approved for the award of a degree by this or any other University.

Signature:*Yan Wen*.....

Abstract

WS₂, MoS₂ and ZrS₂ nanomaterials in various forms, such as nanoflakes, inorganic fullerene-like nanoparticles and nanorattles, were synthesised using two modified conventional techniques: solid-gas reaction and chemical vapour deposition. Both of these techniques are essentially based on reactions between metal oxides/chlorides and sulphur at a relatively low temperature in the range of 350-950°C in H₂/Ar. Compared with other common techniques, these techniques are cost effective and environmentally friendly and produce well-crystallised WS₂, MoS₂ and ZrS₂ nanomaterials with controllable sizes and morphologies, arising from the involvement of simple equipment and a H₂S-free process.

With the solid-gas reaction technique, the formation of WS₂ and MoS₂ inorganic fullerene like (IF) particles follows a so-called "template growth" mechanism, which implies that the sizes of the final products resemble their metal oxide raw materials. Therefore, because of the usage of WO₃ nanoparticles and MoO₃ submicron particles as precursors, nanosized WS₂ (<100 nm) and submicron-sized MoS₂ (approximately 500 nm) particles were generated, respectively. Further investigation of the reaction mechanism reveals that H₂ is a vital factor in the formation of WS₂ IF nanoparticles. Without H₂, WS₂ nanoflakes are instead produced, which is attributed to that the formation of WS₂ IF nanoparticles based on the synergy between H₂ reduction and S sulphidation.

Using the CVD technique, WS₂ IF nanoparticles with sizes below 100 nm were readily produced. However, the initially formed WS₂ IF nanoparticles were poorly crystallised with numerous defects and disconnections, which is consistent with the results of other researchers. In this project, an additional annealing process was introduced to eliminate these defects and disconnections. After this process, well-crystallised WS₂ IF nanoparticles were formed, which should exhibit improved mechanical properties and stability. In addition to the WS₂ IF nanoparticles, ZrS₂ was also prepared using the same route from the reaction of ZrCl₄ with S. Unlike the WS₂, the generated ZrS₂ was in the form of nanoflakes with sizes below 30 nm. Consequently, these

nanoflakes exhibited a strong quantum confinement effect and good photocatalytic performance for the decomposition of 4-NP.

Based on the investigation of the WO_3 sulphidation mechanism, novel $W@WS_2$ and $WS_2@WS_2$ nanorattles were designed and first synthesised using a simple gas-solid reaction. The as-synthesised nanorattles were composed of tiny, moveable W/WS_2 cores and continuous WS_2 shells with much larger sizes. By simply tailoring the processing parameters, several types of nanostructures, including WS_2 nanoflakes, IF nanoparticles and nanorattles (with desirable core size and shell thickness) were selectively prepared. Moreover, it was observed for the first time that the as-prepared nanorattles exhibited excellent catalytic activities, which were close to or even better than their much more expensive Au- and Pt-based counterparts.

Publication list

1. J. T. Huang, S. W. Zhang, Z. H. Huang, Y. Wen, M. H. Fang, and Y. A. Liu, "Catalyst-assisted synthesis and growth mechanism of ultra-long single crystal α - Si_3N_4 nanobelts with strong violet-blue luminescent properties," *Crystrngcomm*, vol. 14, pp. 7301-7305, 2012.
2. S. W. Zhang, Y. Wen, and H. A. Yeprem, "Low temperature synthesis of high quality zirconium carbide powder", *Applied Mechanics and Materials*, vol. 319, ed, 2013, pp. 219-223.
3. S. W. Zhang and Y. Wen, "Low Temperature Preparation of Tungsten Nanoparticles from Molten Salt", *Powder Technology*, vol. 253, pp. 464-466.
4. Y. Wen, H. J. Zhang and S. W. Zhang, "One-Step Synthesis of W@WS_2 Nanorattles via Gas-Solid Reaction and Their Catalytic Performance" *Nanoscale*, 2014,6, 13090-13096.
5. Y. Wen and S. W. Zhang, "Synthesis and characterisation of WS_2 IF nanoparticles via decomposition of $(\text{NH}_4)_2\text{WS}_4$, Euromat 2013 conference

Contents

Chapter One	Introduction	1
	Thesis outline	2
Chapter Two	Literature Review	3
	2.1 Structures and properties of metal dichalcogenides	3
	2.2 Introduction to nanorattles.....	6
	2.3 Synthesis routes of metal dichalcogenides	8
	2.3.1 Physical ablation.....	8
	2.1.2 Hydrothermal/solvothermal reaction	12
	2.1.2 Solid-assisted reaction.	18
	2.1.2 Chemical vapour deposition.....	32
	2.4 Properties of metal dichalcogenide nanoflakes, IF nanoparticles and nanotubes	39
	2.5 Synthesis techniques and properties of core-in-hollow-shell spheres	44
Chapter Three	Experimental Techniques	55
	3.1 Characterisation techniques	55
	3.1.1 X-ray diffraction (XRD).....	55
	3.1.2 Transmission electron microscopy (TEM)	57
	3.1.3 Scanning electron microscopy (SEM) and energy dispersive X-ray spectroscopy (EDS)	59
	3.1.3 Raman spectroscopy	61
	3.1.4 Atomic force microscopy (AFM).....	62
	3.1.5 Thermogravimetric analysis (TGA), differential heat flow (DTA) and mass spectroscopy (MS).....	63
	3.1.6 Ultraviolet-visible (UV-vis) spectroscopy	64
	3.1.7 Electrochemical measurements.....	65
	References.....	66
Chapter Four	82
	Synthesis and characterisation of WS ₂ nanoparticles <i>via</i> solid-gas reaction between WO ₃ and S	82
	Introduction	82
	Experimental	83
	Results and discussion.....	83
	4.1 Fabrication of WS ₂ nanoflakes <i>via</i> template reaction route	83
	4.2 Fabrication of WS ₂ IF nanoparticles <i>via</i> template reaction route	94
	Conclusions	118
	References.....	118

Chapter Five	122
Synthesis and characterisation of MoS ₂ nanoparticles <i>via</i> solid-gas reaction between MoO ₃ and S.....	122
Introduction	122
Experimental	124
Results and discussion.....	124
Conclusions	135
References.....	136
Chapter Six	138
Synthesis of metal dichalcogenide nanoflakes and IF nanoparticles <i>via</i> CVD technique	138
Introduction	138
Experimental	140
Results and discussion.....	141
Synthesis and characterisation of WS ₂ nanoflakes and IF nanoparticles.....	141
6.1 Effect of reaction temperature	141
6.2 Effect of gas flow rate	147
6.3 Effect of holding time.....	148
6.4 Annealing of WS ₂ products.....	151
6.5 Comprehensive analysis on the synthesis of WS ₂ IF nanoparticles	156
Conclusions	157
Synthesis and characterisation of ZrS ₂ nanoflakes	157
6.6 Composition and morphology of products	157
6.7 Effect of temperature.....	160
Conclusions	164
References.....	165
Chapter Seven	168
One-Step Synthesis and Characterisation of WS ₂ based Nanorattles via Gas-Solid Reaction ..	168
7.1 Synthesis of W@WS ₂ nanorattles and their catalytic performance	168
7.1.1 Introduction.....	168
7.1.2 Experimental	170
Preparation of W@WS ₂ nanorattles	170
Characterisation	170
Catalytic reduction of 2-nitroaniline	170
7.1.3 Results and Discussion	171
1. Effect of heating temperature on synthesis and phase morphology.....	171
2. Effect of H ₂ flow rate on synthesis and phase morphology	177

3. Formation mechanism of W@WS ₂ nanorattles	180
4. Thermal stability of as-prepared W@WS ₂ nanorattles	182
7.5 Catalytic activity of as-prepared nanorattles	186
7.1.4 Conclusions.....	189
7.2 Synthesis of WS ₂ @WS ₂ nanorattles and their catalytic activity in the hydrogen evolution reaction	190
7.2.1 Introduction.....	190
7.2.2 Experimental	192
7.2.3 Results and discussion.....	193
1. Composition and morphology analysis of WS ₂ @WS ₂ nanorattles.....	193
2. Properties of WS ₂ @WS ₂ nanorattles.....	197
7.2.4 Conclusions.....	202
Chapter Eight.....	208
Conclusions and Suggestions for Future Work	208
Conclusions	208
Further Work.....	209

Chapter One Introduction

Metal dichalcogenides such as MoS₂ and WS₂ are currently under extensive investigation because of the successful fabrication of monolayer WS₂ and MoS₂ nanoflakes, which have excellent catalytic properties [1-3]. In addition to this latest graphene-like structure, metal dichalcogenides have many other forms such as nanoflakes, inorganic fullerene-like (IF) nanoparticles and nanotubes, which exhibit good mechanical properties [4-6], tribological performance [7-11] and biocompatibility [12]. These properties make metal dichalcogenides attractive as composite reinforcements, lubricants and drug carriers [11-13]. Therefore, it is necessary to develop efficient routes to produce metal dichalcogenides on a large scale and at low cost.

Many approaches have previously been, or are still being, investigated worldwide to synthesise metal dichalcogenides with various morphologies, including gas-solid reaction, physical ablation, and hydrothermal synthesis processes. Among these techniques, the most efficient route is the so-called “falling bed synthesis”, which has already been used for the commercial production of MoS₂ and WS₂ IF nanoparticles and nanotubes. Using this technique, a solid-metal-containing precursor (e.g., MoO₃ and WO₃) reacts with H₂S vapour, forming corresponding metal dichalcogenides with designed structures [14]. However, this technique has two main drawbacks: the usage of special equipment and toxic H₂S gas, which largely increases the production cost and causes safety/environmental concern. Therefore, it is necessary to develop a simple, cost-effective, and high-efficiency technique to prepare the carbide materials for large-scale productions.

In the present thesis, two simple scalable routes that do not require special equipment or toxic H₂S are proposed to produce well-crystallised WS₂ and MoS₂ IF nanoparticles and nanoflakes. Using these techniques, metal oxides or chlorides were reacted with S and H₂ in a conventional tube furnace to produce corresponding metal dichalcogenides with controllable nanostructures on a large scale. In addition to MoS₂ and WS₂ based nanomaterials, ZrS₂ nanoflakes with sizes below 30 nm were produced from the reaction between ZrCl₄ and S;

these materials exhibited good photocatalytic performance. Based on the investigation of the sulphidation mechanism of the oxides, novel $W@WS_2$ and $WS_2@WS_2$ nanorattles were designed and synthesised. Because these materials were first prepared by the author, future investigations of the properties of the synthesised nanorattles would be valuable. For example, the as-synthesised nanorattles were observed to exhibit excellent catalytic properties. Because of this unique nanorattle structure, the WS_2 shell can prevent W and WS_2 nanocores from agglomeration, while a sufficient volume remains for the later catalytic reaction (e.g., hydrogenation and the hydrogen evolution reaction (HER)). Therefore, the catalysts enclosed in the nanorattles exposed much more active surface, leading to better catalytic performance than their naked counterparts. Because these nanorattles were produced *via* a simple, environmentally friendly and scalable technique with relatively inexpensive raw materials (WO_3 and S) and exhibited excellent chemical and electrochemical catalytic performance, they have good potential to replace many commonly used expensive catalysts such as Au and Pt.

Thesis outline

This thesis contains eight chapters. Chapter one provides an overall introduction to the thesis, including the inspiration and innovation of this project and project objectives. Chapter two is a comprehensive literature review on various synthesis techniques and properties of metal dichalcogenides nanoflakes, IF nanoparticles, nanotubes and nanorattles. In Chapter three, the experimental techniques for the characterisation and property measurements used in this thesis are introduced. Chapters four and five present the reaction parameters and mechanisms for the formation of the WS_2 , MoS_2 IF nanoparticles and nanoflakes *via* solid-gas reaction. Chapters six discuss the effects of the reaction parameters and mechanisms for the formation of the WS_2 IF nanoparticles and ZrS_2 nanoflakes *via* the chemical vapour deposition technique. The synthesis procedures, mechanism and properties of novel $W@WS_2$ and $WS_2@WS_2$ nanorattles are presented and discussed in Chapters seven. Chapter eight ends with final conclusions and suggestions for future work.

Chapter Two Literature Review

2.1 Structures and properties of metal dichalcogenides

Many metal dichalcogenides (MX_2 , M = Mo, W, Zr and Ti. and X = S or Se) have a similar hexagonal graphite-like layered structure (Table 1.1). Graphite is composed of mono-atomic carbon sheets containing hexagonal honeycomb unit cells, which have strong in-layer covalent bonds and weak van der Waals forces between adjacent layers (Figure 1.1). Unlike graphite, the layer of MX_2 is made of “sandwich-like” unit cells with three atomic planes. For example, WS_2 has a typical “sandwich-like” layered structure. Each “sandwich” is composed of two planes of S atoms and an intermediate plane of W atoms, which are all arranged in a hexagonal shape (Figure 1.1). Depending on the stacking sequences, metal dichalcogenides have two different crystal structures: 2H hexagonal polymorph and 3R rhombohedral polymorph. Compared with the 3R structure, the 2H hexagonal structure packing with AbA BaB sequence is the most stable phase under ambient conditions [15].

Table 1.1 Basic physical properties of some common MX_2 [15]

Materials	Melting point (°C)	Density (g/cm^3)	Appearance	Crystal structure
WS_2	1250 decompose	7.5	blue-grey powder	hexagonal polymorph
MoS_2	1185 decompose	5.06	black/lead-grey solid	hexagonal polymorph
ZrS_2	1480	3.82	red-brown crystals	rhombohedral polymorph
TiS_2	N/A	3.22	yellow powder	hexagonal polymorph
WSe_2	N/A	9.32	grey powder	hexagonal polymorph
MoSe_2	N/A	6.98	crystalline solid	hexagonal polymorph

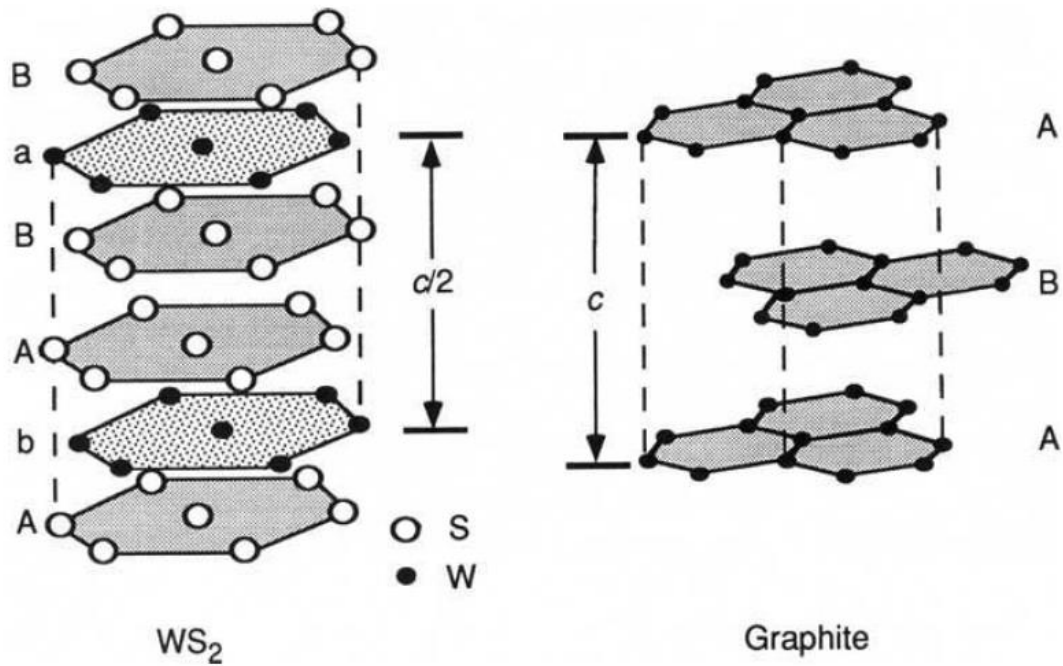


Figure 1.1 Layered structures of WS_2 and graphite [16].

Because of the layered structure, most MX_2 materials can exist in many forms such as multilayer flakes, fullerene-like nanoparticles, nanotubes and graphene-like flakes.

Multilayer flakes: Among all forms of MX_2 , multilayer flakes are the most stable phase [17]. By adjusting the synthesis conditions, the sizes of produced MX_2 flakes can be controlled from several nanometres to tens of micrometres. Because the adjacent layers of MX_2 are connected by weak van der Waals bonds, the layers can easily slide away under a shear force. Therefore, MX_2 flakes exhibit excellent tribological performance and have been used to replace graphite as dry lubricants [7-10]. When the sizes of MX_2 particles are reduced to the nanoscale, their specific surface areas are increased dramatically, which makes them attractive as catalysts [18, 19].

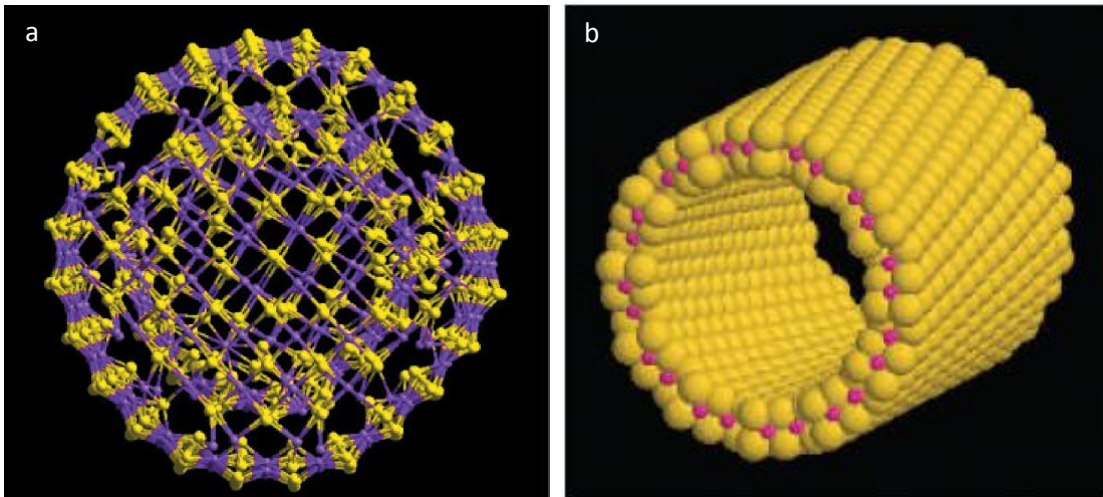


Figure 1.2 Computer simulation of (a) IF nanoparticles and (b) nanotubes [20].

IF nanoparticles and nanotubes: Similar to carbon, which can exist as carbon fullerenes or carbon nanotubes [21], MX_2 can also form seamless nanotubular and spherical structures with all the M and X atoms being fully bonded (Figure 1.2). In most cases, the sizes of the synthesised MX_2 fullerenes and nanotubes are below 200 nm, above which MX_2 platelets become the main phase because this structure is thermodynamically favourable [17]. The synthesis of MX_2 nanotubes and fullerenes with single wall structure is also possible but much more difficult than that of multiwalled structures [22]. Hence, multiwalled MX_2 nanotubes and fullerenes are most commonly selected for both laboratory and industry uses.

MX_2 fullerenes and nanotubes exhibit outstanding lubricating performance compared with MX_2 flakes because of their rolling friction mechanism [11]; thus, these structures are considered alternative ideal lubricants. In addition to this common application, MX_2 fullerenes and nanotubes can be used as hydrogen storage components [23, 24] and drug carriers [12] because of their high specific surface area and good biocompatibility.

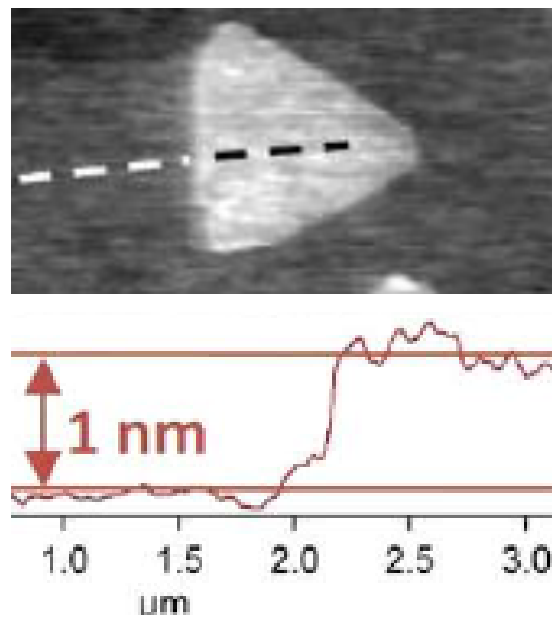


Figure 1.3 AFM image of a WS_2 island and the corresponding height profile along the dashed line [25].

Graphene-like flakes: The successful synthesis of single-layer graphene by Geim and Novoselov [26] showed that a single-layer carbon molecular could be produced and could exist under ambient conditions. Because MX_2 has a similar layer structure as graphite, it is possible to produce stable MX_2 analogues of graphene with less than five layers. According to Ramakrishna Matte's research [27], graphene-like WS_2 and MoS_2 with only 1-3 layers could be prepared using the intercalation and exfoliation method (Figure 1.3). Recently, the graphene-like MX_2 nanoflakes were confirmed to exhibit excellent HER catalytic performance [1-3]. Although many other properties of such graphene-like MX_2 structures are not clear, these materials have good potential to be used as lubricants or reinforcements of composites. For the latter, the thermal and electrical conductivities of the composites could be improved dramatically.

2.2 Introduction to nanorattles

With the development of modern synthetic technologies and analytical instruments, various types and forms of nanoparticles have been synthesised and widely used in many areas. For example, transition metals are good catalysts for many reaction systems because these materials can easily donate or receive electrons from reactants by changing their metal oxidation states

over a wide range (normally from 0 to +6). Upon reducing their sizes to the nanoscale, their catalytic performance can be improved dramatically. This improvement is attributed to the increased specific surface areas of the catalysts, which increases the chances of collision between catalysts and reactants [28, 29]. However, due to their high specific area, nanoparticles are also extremely unstable and tend to aggregate easily, which will sharply decrease their surface area and the activity. To overcome this issue, many countermeasures have been taken. In general, two routes are widely used: ligand protection and core–shell configuration. The former is an efficient route to stabilise nanoparticles against agglomeration by modifying their surface with a layer of organic groups [30-32]. However, because of the poor high temperature stability of most coated organic materials, the ligand protection layer will decompose at high temperatures. Therefore, such coated materials are not suitable for high-temperature applications. Alternatively, organic ligand layers are replaced by some more stable inorganic materials, such as silicon oxide and carbon, forming core-shell-structured particles [33]. Such core-shell nanoparticles can be easily dispersed and remain stable in harsh environments (e.g., high temperature and corrosion). However, this route is still not suitable for the dispersion of nano catalysts because the active surface of nano catalysts is covered by a dense shell of inorganic material. Hence, the reactants must diffuse through the shell to reach the surface of the catalyst, which will result in a dramatic decrease in the catalytic activity of the core materials.

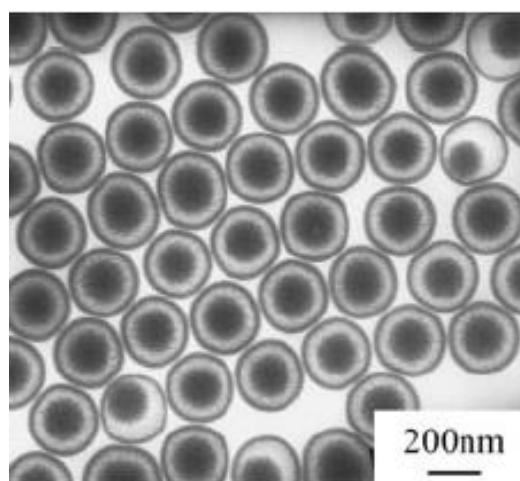


Figure 1.4 TEM image of typical silica nanorattles [34]

To address these problems, materials with novel core-hollow structures (“nanorattles”) were synthesised [34]. These materials had similar shells as the normal core-shell particles; however, the enclosed core was much smaller than the hollow chamber, leaving a sufficient volume for catalytic reactions (Figure 1.4). This novel structure not only effectively isolates nanoparticle cores and prevents their agglomeration but also enables more active surface to be exposed. Consequently, the nanorattles perform much better as catalysts compared with their naked nanoparticle and conventionally coated nanoparticle counterparts. Because MX_2 IF nanoparticles exhibit good high temperature stability and corrosion resistance [35], these materials are suitable for use as nanorattle shells that can survive under harsh conditions [36]. Thus, WS_2 -based nanorattles may also exhibit good properties.

2.3 Synthesis routes of metal dichalcogenides

Since the first preparation of WS_2 IF nanoparticles by Tenne et al.[16], MX_2 materials have received considerable attention because these materials can form unique, stable and controllable structures that could be potentially used in many areas. The commonly used synthesis methods for MX_2 include the following four routes: (1) physical ablation, (2) hydrothermal reaction, (3) solid assisted reaction and (4) chemical vapour deposition (CVD).

2.3.1 Physical ablation

Laser ablation is an effective route to produce nanoparticles. Compared with other techniques, such as solid-phase and gas-solid phase reactions, laser ablation has been observed to be feasible in the preparation of nanocrystals with specific shapes and sizes [37]. Using this technique, a pellet that is composed of the same material as the target product is exposed to a pulsed laser. Because of the high incidence energy, numerous tiny particles are ablated from the pellet, forming a hot plume, which is then condensed and collected in a cold gas or solvent. The entire process can be divided into four steps: light-absorption, photoionisation, heat diffusion and the evaporation of

the plume consisting of atoms, clusters and ions. Because of the high energy of the laser, the duration of the ablation process is very short, a few nanoseconds at most. The subsequent fast quenching process prevents atoms from diffusing and growing, leading to the formation of small atom clusters composed of only a few thousands atoms [37].

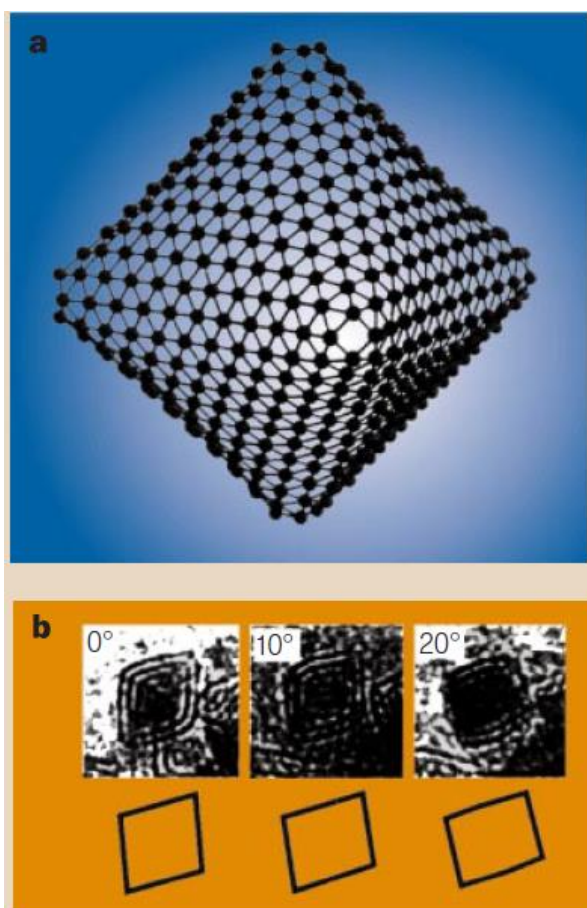


Figure 2.1 (a) Computer simulation and (b) TEM images of synthesised MoS₂ IF nanoparticles *via* ablation [37].

Although the detailed formation mechanism of carbon fullerenes remains unclear, this technique has already been applied to the synthesis of C₆₀ by Kroto et al. [38]. Considering the structural similarity between C and MX₂, it is reasonable to extend this technique to fabricate MX₂ nanoparticles such as IFs, nanoflakes and nanotubes. In 1999, the laser ablation technique was first applied to the preparation of MoS₂ IF nanoparticles (Figure 2.1) [37]. MoS₂ powder was initially pressed to form MoS₂ pellets, followed by laser ablation with various levels of power. Then, the ablated tiny particles were quenched in He or Ar. Finally, MoS₂ IF nanoparticles were synthesised with sizes of

approximately 3-5 nm. According to this research, the target temperature controlled by the laser power was vital for the formation of IF nanoparticles. If the temperature was above 550 °C, only crystalline folded sheets of MoS₂ were produced. In addition to MoS₂, many other metal dichalcogenides with IF structures, such as WS₂, MoSe₂, Hf₂S, TaS₂ and SnS₂/SnS [39-43], were prepared using the same technique. Because of the fast condensation process, the sizes of these produced IF particles were below 20 nm.

The formation of the IF structure is driven by energy minimisation, which is achieved through the connection of dangling bonds on layer edges [37]. During ablation, small MX₂ particles (<15 nm) made of some parallel basal planes are formed instantaneously. Then, these planes grow and connect with each other to minimise their thermodynamic energy, leading to the formation of closed caged particles. The sizes and morphologies of the final products can generally be controlled by adjusting the non-equilibrium plasma conditions, i.e., the laser power and quench rates [44].

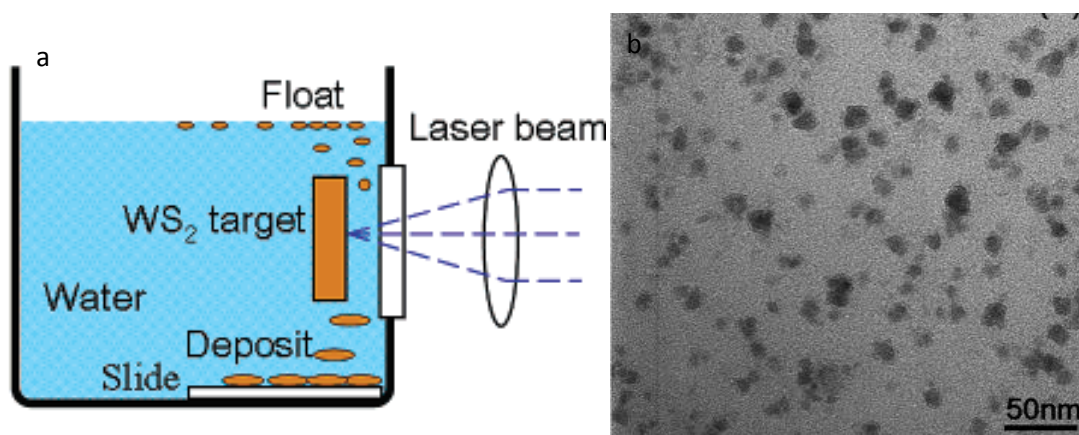


Figure 2.2 (a) Schematic diagram of laser ablation in water. (b) TEM image of deposited nanoparticles [45].

In addition to IF nanoparticles, WS₂ nanoflakes with an average size of 10 nm were fabricated using a similar laser ablation method. Because of the usage of a high energy laser and water quenching, the initially formed tiny particles could not fold to form a closed cage structure, leading to the formation WS₂ nanoflakes smaller than 10 nm (Figure 2.2) [45].

Arc discharge synthesis is an alternative physical ablation route for the synthesis of MX_2 nanoparticles. In this technique, the energy source is changed from the high-cost pulsed laser to the low-cost arc discharge, and MoS_2 IF nanoparticles can still be produced [46]. Moreover, the resultant particles are condensed in water rather than in an inert gas. This water-condensing device is much more flexible and cost effective. During the ablation process, large particles mostly fall on the bottom of the water tank, while small nanoparticles float on the surface of water, leading to easy collection and high purity of the products. Similar to the laser and arc discharge, electron irradiation, as another high-energy source, has also been used to produce MoS_2 IF nanoparticles [47].

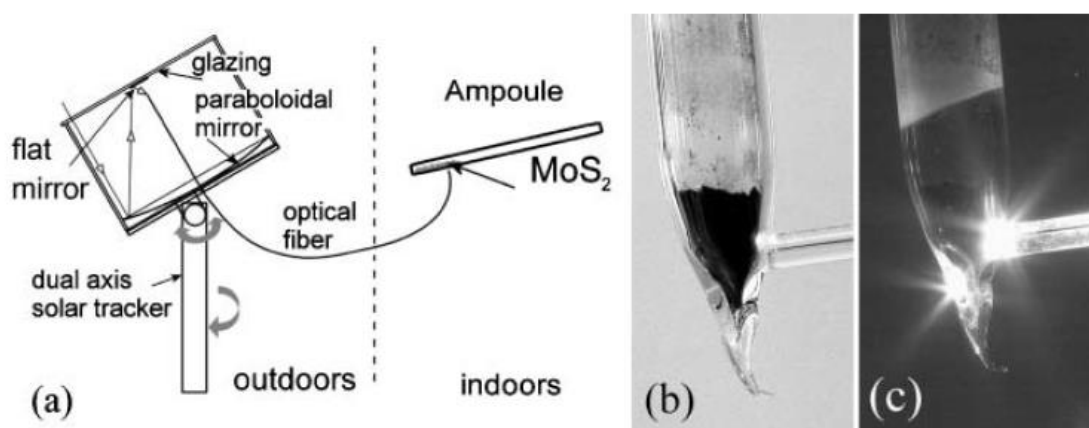


Figure 2.3 (a) Schematic illustration of solar ablation device. Images of sample (b) before irradiation and (c) during irradiation [48].

In addition to these artificial high-energy sources, solar energy, as a natural, green energy source, has recently drawn much attention. Tenne et al. [48] first fabricated MoS_2 IF nanoparticles *via* solar ablation. The solar radiation was concentrated and transmitted from outdoors to an indoor device using optical fibres (Figure 2.3). The incident light was controlled by the numerical aperture and aimed on MoS_2 precursors in a sealed ampoule for 300-900 s. Both IF nanoparticles and single-walled nanotubes were produced with an average size of 50 nm. This technique was modified using Pb as a catalyst during solar ablation [49]. MX_2 precursors were mixed with PbO-coated Pb powder and sealed in quartz ampoules under a vacuum of 3×10^{-5} Torr. The ampoules were then irradiated with highly concentrated solar beam radiation to produce MX_2 nanotubes. Depending on the precursors, well-crystallised WS_2 , WSe_2 and

MoS₂ nanotubes with approximately 50-nm diameters and 100-nm-10- μ m lengths were generated. Because of the presence of Pb, MX₂ first reacted with water–air residues in the ampoule to form M(Pb)O_{3-x} nanowhiskers, which were gradually transformed into MX₂ nanotubes by reacting with the X vapour generated from the decomposition of nearby MX₂. Although the physical ablation technique is an effective route to prepare high-purity MX₂ nanoflakes, IF nanoparticles and nanotubes, this technique suffers from several drawbacks, including complexity in operation and low yield, which makes it unsuitable for large-scale production.

2.1.2 Hydrothermal/solvothermal reaction

Hydrothermal/solvothermal synthesis is a common route that exploits the high-temperature properties of solvents to produce nanoparticles. Depending on the types of solvents, this technique can be classified into two types: hydrothermal synthesis (water solvent) and solvothermal synthesis (non-water solvent). Using this technique, reactant solutions are sealed in a vessel and heated to temperatures well above the boiling points of the solvents. Because the entire system is sealed, the evaporated solvents are trapped in the vessel, leading to the generation of high-pressure vapour. Combined with the relatively high temperatures, this process greatly changes the structures of the solvent materials. For example, when water is used as the solvent, there is a critical point at 374 °C and 218 atm, above which supercritical water is formed that exhibits characteristics of both liquid and gas states, such as low surface tensions between solids and supercritical water, high viscosities and obvious solubility improvements of insoluble materials. When a reaction is conducted under this critical condition, the properties of the dissolved reactants are also changed. These changes make this route applicable to the fabrication of certain materials that are difficult to produce under normal conditions. In addition, even if the reaction temperature and pressure are below the critical point, the increased solubility and reactivity of reactants can also promote the reaction. Because of these advantages, this technique has already been applied to the synthesis of several types of nanomaterials, including TiO₂[50], ZrO₂[51], CrN[52] and GaN[53].

2.1.2.1 Hydrothermal synthesis of metal chalcogenide nanoparticles

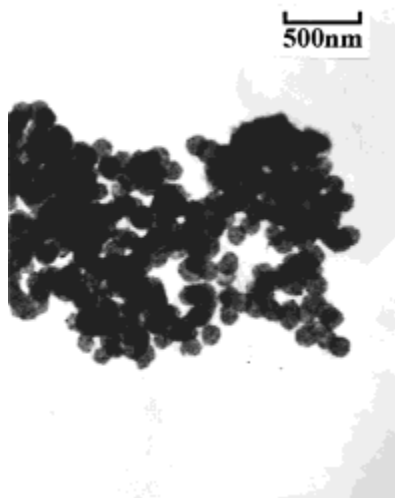


Figure 2.4 TEM image of prepared nanocrystalline ZnSe [54].

Nanocrystalline ZnSe was successfully synthesised *via* a hydrothermal route by the straightforward reaction between elemental Zn and Se [55]. With the help of pyridine, these elements easily reacted with each other at only 180°C for 8 h. Nanocrystalline ZnSe that was approximately 10 nm in size was generated. Upon replacement of the toxic solvent pyridine with water, ZnSe could still be synthesised from the reaction between Zn and Se at 180°C for 24 h but with much larger sizes (70-100 nm) (Figure 2.4). [54].

Apart from metal precursors, metal chlorides are alternative precursors for the hydrothermal synthesis of MX_2 . For example, MSe_2 (M=Ni, Co, Fe) was produced by reacting the corresponding metal chlorides with Se powder [56]. All the reactants were added to a solution composed of 6 solvents (distilled water, N,N-dimethyl formamide, pyridine, acetyl acetone, hydrazine and ethylenediamine) and sealed in a vessel. These reactions were performed at 80-200°C for 12-48 h. The final products were filtered and washed with distilled water to remove any residual impurities. Depending on the reaction time, the resultant products had a large size distribution from 25 nm to 1.5 μm . Similar to MSe_2 (M=Ni, Co, Fe), MS_2 (M=Ni, Co, Fe) was also generated by the reaction between MCl_2 (M=Ni, Co, Fe) and $\text{Na}_2\text{S}_2\text{O}_3$ *via* hydrothermal synthesis when water was used as the only solvent [57]. In this case, all the products had large specific areas due to their extremely tiny sizes (average 5 nm).

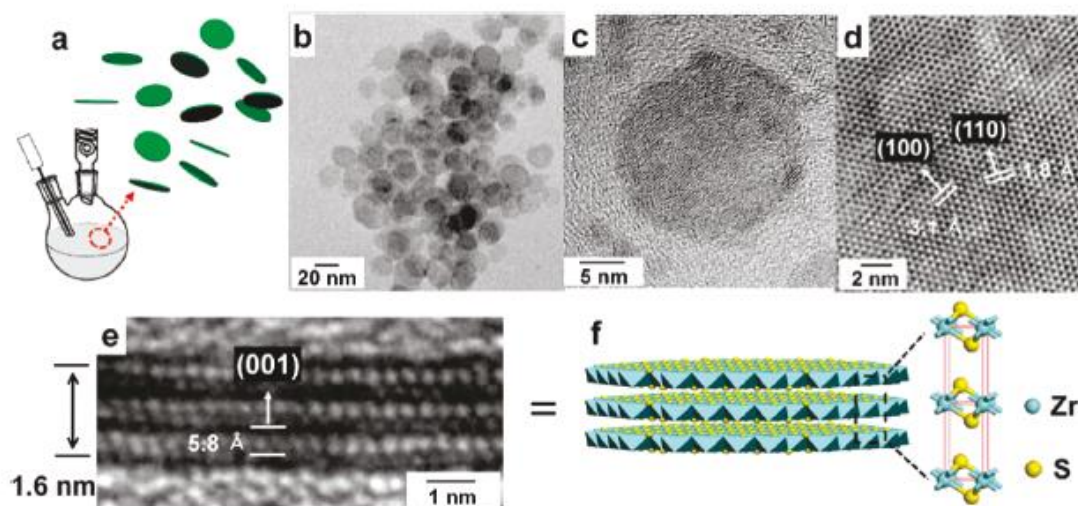


Figure 2.5 (a) Schematic illustration and (b-e) TEM images and (f) ball-and-stick model of as-synthesised ZrS_2 nanodiscs [58].

Recently, ultrathin ZrS_2 nanodiscs were synthesised at 300°C in Ar using ZrCl_4 , CS_2 and oleylamine as the reactants [58]. The produced ZrS_2 nanodiscs were well dispersed with an almost uniform size distribution (30 nm in diameter and 1.6 nm in thickness) (Figure 2.5). When testing with Li^+ intercalation, these nanodiscs exhibited excellent nanoscale size effects, enhancing the discharge capacity by 230% and greatly improving their stability compared with bulk ZrS_2 . By adjusting the diameters of the nanodiscs, the nanoscale size effects could be controlled, and smaller nanodiscs exhibited higher discharge capacity.

For the hydrothermal synthesis of MX_2 , $(\text{NH}_4)_2\text{MO}_4$ materials are also efficient precursors because of their high water solubilities. To produce MoS_2 , $(\text{NH}_4)_2\text{MoO}_4$ was first mixed with $\text{Na}_2\text{S}_2\text{O}_4$ in the presence of ammonia solution and thioacetamide [59]. Then, this mixture was sealed in a Teflon-lined autoclave and fired at 180°C for 1 h. The resulting product had a unique flower structure with a size distribution from approximately 200 nm to 1 μm . These flowers were made up of tens to hundreds of self-assembled petals growing in all directions. Each petal was a thin flake with a size of approximately 100-200 nm and thickness of approximately 5-10 nm. Similar WS_2 nanoflakes with thicknesses of 10-15 nm were also fabricated by changing the starting materials to $(\text{NH}_4)_2\text{WS}_4$, NaBH_4 , pyridine and trioctylamine [60]. After the hydrothermal

synthesis, the products were annealed at 850°C to form discrete nanoflakes instead of nanoflowers.

2.1.2.1 Hydrothermal synthesis of metal chalcogenide nanowires and nanorods

In addition to common nanoflakes, metal chalcogenide nanowires were prepared *via* hydrothermal synthesis. According to Li et al., MoO₃ can react with Na₂S in HCl solution at 260°C [61]. After a 12-h reaction in a sealed stainless steel autoclave, MoS₂ nanowires with an average diameter of approximately 4 nm and length of 50 nm were successfully synthesised. By adjusting the reaction temperature and concentration of the precursors, the sizes and morphologies of the MoS₂ products could be controlled. In addition, the use of additive agents such as CH₃COONa and NH₄Cl increased the sizes of the nanowires, which might be due to the shielding effect of these additives at the interfaces of the initial MoS₂ nuclei [61].

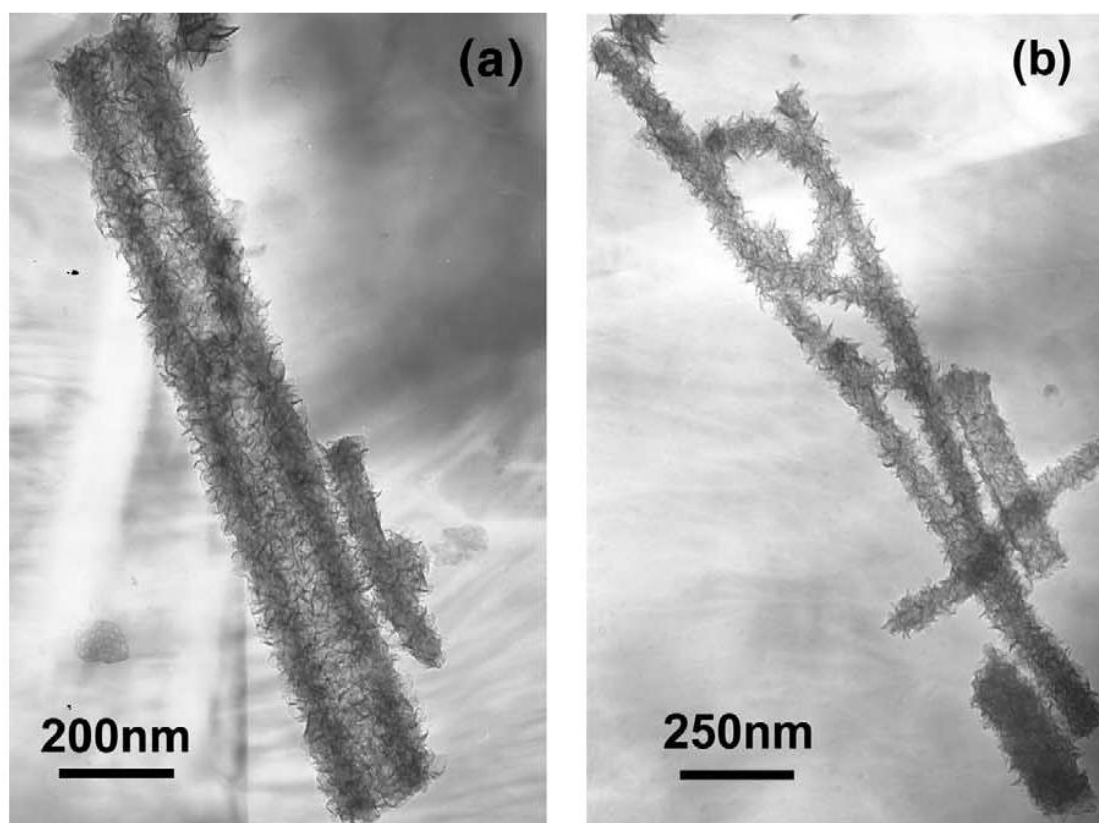


Figure 2.6 TEM images of resulting MoS₂ (a) nanotubes and (b) nanorods [62].

MoS₂ clusters with “rag”-like morphology were first synthesised by the hydrothermal reaction of (NH₄)₆Mo₇O₂₄ with S in a hydrazine solution at 170-200°C [63]. The reaction time was extended to 30 days to promote the crystallisation of MoS₂. Because of this long holding time, the generated nanowires intertwined with each other to reduce their surface energy, forming a “rag” structure. Upon adjustment of the reaction parameters, the generated MoS₂ nanowires could also stack to form relatively large nanotubes and nanorods. This unique stacking mode was also investigated by Tian et al. [62]. MoO₃ reacted with potassium thiocyanate in water at 160-220°C for 24 h. Crystalline MoS₂ nanorods and nanotubes were readily generated (Figure 2.6). The synthesised nanotubes were approximately 200 nm in diameter and several microns in length, while the nanorods had similar lengths but smaller diameters (60-100 nm). Because these nanotubes and nanorods were composed of numerous stacked MoS₂ nanowires, their edges were neither regular nor trimmed.

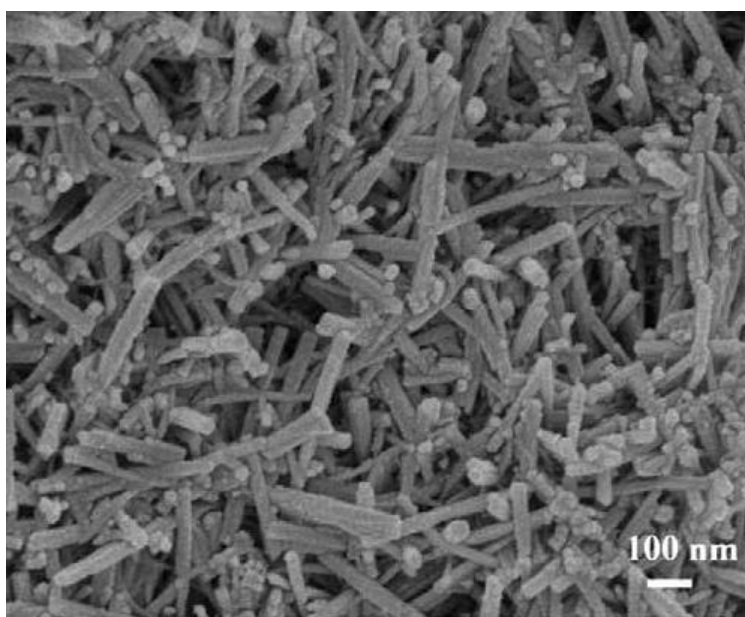


Figure 2.7 SEM image of MoS₂ nanorods obtained using sillicontungstic acid as the additive [64].

When sillicontungstic acid, Na₂MoO₄, CH₃CSNH₂ and water were used as the reactants, MoS₂ nanorods with diameters of approximately 20-50 nm and lengths of 400-500 nm were fabricated *via* hydrothermal synthesis (Figure 2.7) [64]. Unlike the morphology of the assembled nanorods (Figure 2.6b), the as-synthesised nanorods were discrete with smooth edges. When sillicontungstic

acid was absent, MoS₂ could still be produced using the same route. However, agglomerated nanoparticles were produced instead, which implied that the sillicontungstic acid was crucial in the formation of MoS₂ nanorods.

2.1.2.2 Hydrothermal synthesis of metal chalcogenide IF nanoparticles and nanotubes

Although the hydrothermal route has already been widely used to synthesise metal chalcogenides, there are few reports on the synthesis of metal chalcogenide IF nanoparticles and nanotubes because the formation of these structures is based on the folding and recrystallisation of the formed MX₂ layers, which requires more energy than flake formation. During hydrothermal synthesis, the supplied energy is not sufficient to complete this process. Therefore, annealing is an essential step to supply additional energy for the post-hydrothermal-reaction process.

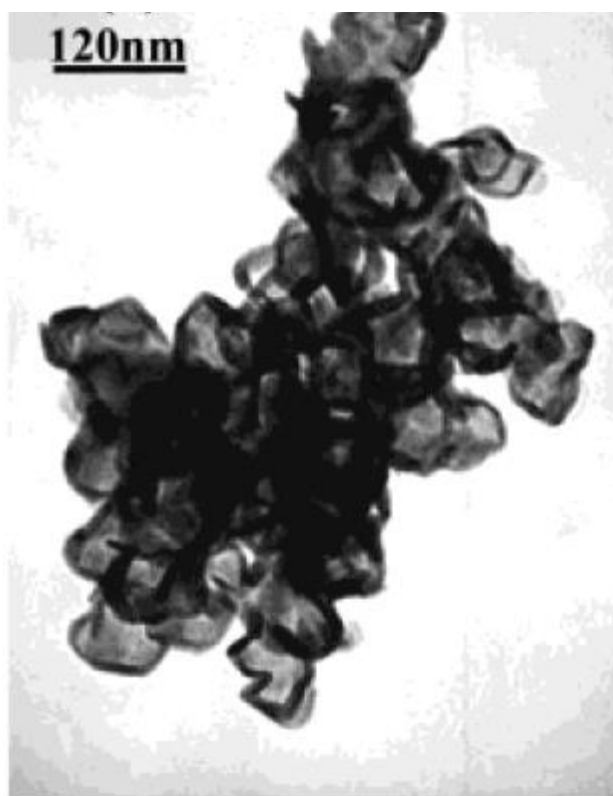


Figure 2.8 TEM image of MoS₂ nanoparticles prepared by annealing the solution product of Na₂MoO₄ and CH₃CSNH₂ at 700°C[65].

MoS₂ IF nanoparticles were successfully produced by the reaction of Na₂MoO₄ with CH₃CSNH₂ *via* a two-step synthesis route: hydrothermal synthesis and annealing. Similar to the above mentioned hydrothermal synthesis, a sealed vessel containing the well-mixed Na₂MoO₄, CH₃CSNH₂ and HCl mixture was heated at 180°C for 24 h [65]. The resulting precipitates were then washed with distilled water and dried in vacuum at 80°C. The following annealing step at 700°C was vital to obtain IF nanoparticles. When this step was absent, poorly crystallised MoS₂ thin layers were formed instead of MoS₂ IF nanoparticles. The generated MoS₂ IF nanoparticles after annealing exhibited a typical closed hollow cage structure with an average size of approximately 60 nm (Figure 2.8). This two-step method has been extended to fabricate MoS₂ IF nanoparticles using various starting materials, such as (NH₄)₆Mo₇O₂₄, CS₂, CCl₄ and S [66]; (NH₄)₆Mo₇O₂₄, Na₂S·9H₂O and NH₂OH·HCl [67]; and (NH₄)₆Mo₇O₂₄·4H₂O, monoethanolamine and S [68]. After annealing, MoS₂ IF nanoparticles with sizes below 50 nm were generated using all three routes.

Hydrothermal synthesis is a powerful technique for the production of various MX₂ nanoparticles. However, the high pressure in a sealed vessel during synthesis is always considered a potential danger. Moreover, the yield of this method is usually not high even under well-controlled conditions. All these reasons make this technique unpopular for large-quantity production.

2.1.2 Solid-assisted reaction.

2.1.2.1 Synthesis of metal dichalcogenides from metal oxides/metals

Some metal oxides and metals, such as MoO₃, WO₃, ReO₃, W and Mo, can react with chalcogen elements and/or hydrogen chalcogenides to form corresponding metal dichalcogenides. Depending on the morphologies of the solid precursors and heat-treatment parameters, nanoflakes, IF nanoparticles and nanotubes can be generated.

1). Synthesis of metal dichalcogenide nanoflakes from various precursors

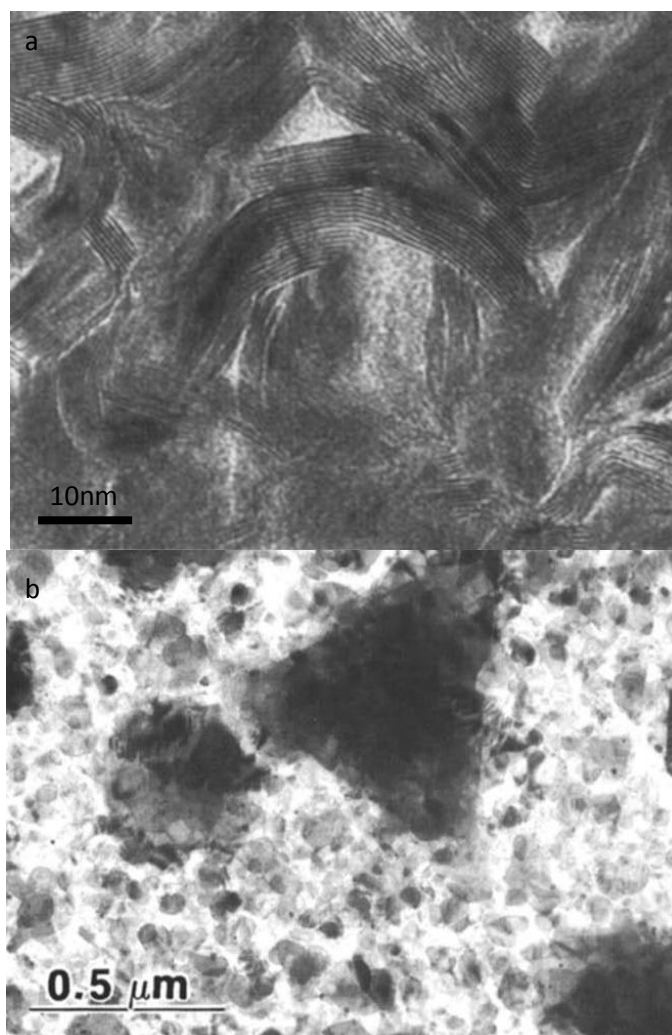


Figure 2.9 TEM image of (a) type I and (b) type II WS_2 films synthesised in the presence of low sulphur concentration [69].

WS_2 thin films were first produced by the direct reaction of W thin films (approximately 50-nm thick) with H_2S in the temperature range from $500^\circ C$ to $1000^\circ C$ [69]. Because the sizes of the W thin films were very small, the complete reaction temperature was decreased to as low as $650^\circ C$. Different WS_2 films were obtained by varying the reaction temperatures. Low temperatures (less than $950^\circ C$) resulted in the common type I texture (van der Waals (vdW) planes vertical to the substrate), while high temperatures ($950^\circ C$ or above) generated type II texture (vdW planes parallel to the substrate) (Figure 2.9). When W thin films and H_2S were replaced by WO_3 thin films and S vapour, respectively, WS_2 films were also fabricated at as low as $400^\circ C$ in a sealed ampoule [70]. Unlike the WS_2 films synthesised from W and H_2S , the

effect of temperature on the orientation of WS_2 in this case was not apparent. The products were composed of both type I (thin films with 50-nm thicknesses) and type II (films with larger thickness) films at all temperatures. This route was also applied to the synthesis of ZrS_2 via the solid-gas reaction of Zr foil with S powder [71]. Depending on the reaction temperature, ZrS_3 or ZrS_2 nanobelts grew from the surface of the Zr foils with approximately 200-2000-nm widths and 5-70- μm lengths. The turn-on field (the electric field to get an emission current density of $0.1\mu\text{A}/\text{cm}^2$) and threshold field (the electric field to get an emission current density of $1\text{mA}/\text{cm}^2$) of the as-synthesised ZrS_2 nanobelts were $0.95\text{ V}/\mu\text{m}$ and $3.6\text{ V}/\mu\text{m}$, respectively, indicating that these materials were decent field emitters [58, 72].

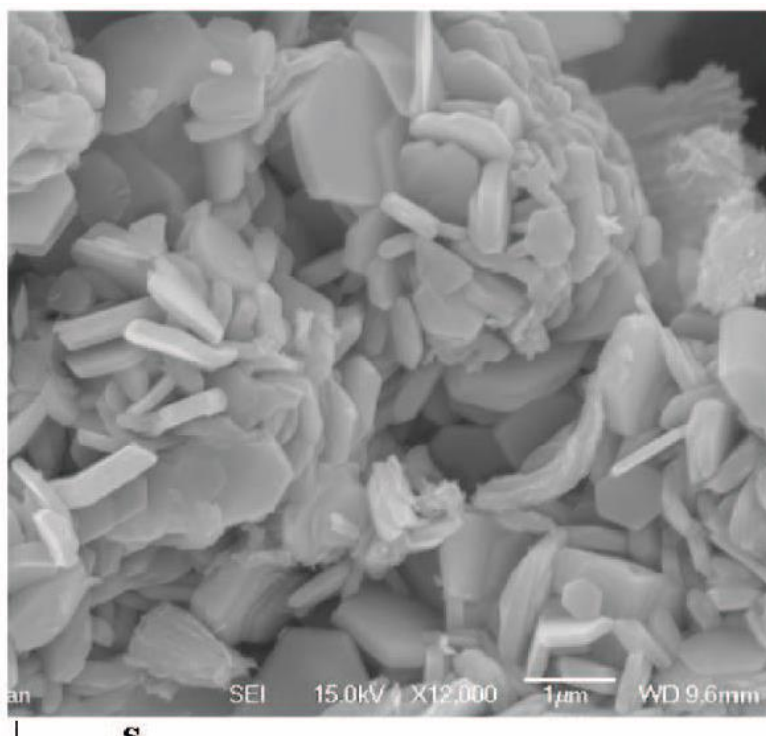


Figure 2.10 SEM images of synthesised WS_2 nanoflakes

When the film precursors were replaced by powder, metal dichalcogenides flakes could also be produced. For example, tungsten and molybdenum nanopowders with an average particle size of 100-120 nm were mixed with sulphur and sodium chloride diluent and then pressed into cylindrical pellets [73]. The self-combustion reaction was triggered by the electric current applied to the metal coil in Ar at $P=30\text{ atm}$. Depending on the amount of NaCl diluent, the maximum temperature could reach 2000°C . Because of this high temperature,

the generated WS_2 materials were well crystallised and had a regular hexagonal shape and lamellar structure that was approximately 100 nm in thickness and several microns in size. According to Pol et al. [74], micron-sized Mo and W powders reacted with S at 750°C in a stainless steel reactor in N_2 . Although the sizes of the starting materials were quite large, the synthesised WS_2 and MoS_2 particles had much smaller sizes (the sizes were in the range of a hundred to a few hundred nm, while the thicknesses were between 5 and 80 nm) (Figure 2.10). This conversion was due to the direct diffusion and reaction between the metal and S vapour, resulting in the generation and exfoliation of layered MS_2 plates.

MX_2 flakes could also be produced from corresponding metal oxide powder. For instance, both WS_2 and MoS_2 flakes were readily synthesised from micron-sized WO_3 , MoO_3 and S reactants [19, 75, 76]. Complete conversion was achieved at as low as 600°C. Ball milling of the starting materials and the usage of extra S vapour during the reaction had a clear effect on the decrease of the reaction temperature. Unlike the raw materials, which had micron sizes, tiny WS_2 and MoS_2 nanoflakes were produced with average widths and sizes of approximately 50 nm and 10 nm, respectively. This size change was attributed to the mechanical activation process of ball milling. After ball milling, the sizes of the raw materials were decreased, and the materials were mixed uniformly with close contact. Therefore, the reaction was much faster than the reaction without ball milling. MX_2 thin flakes were generated immediately, leaving no time for the growth of oxide precursors and thus restricting the sizes of the products.

Li et al. prepared WS_2 from WO_3 precursors with two sizes: WO_3 microparticles (average size of approximately 2 μm) and nanoparticles (average size of approximately 100 nm) [77]. WO_3 and S powders were mixed without ball milling and sealed in an evacuated ampoule, followed by heating to 850°C-900°C for 4 h. The sizes of the tungsten oxide precursors were observed to be closely related to the formation and morphologies of the final product. At 900°C, WS_2 irregular microparticles with an average size of approximately 2 μm and WS_2 hexagonal nanoflakes with an average size of approximately 700 nm were produced from micron-sized and nanosized WO_3 precursors, respectively. Based on their analysis, the appearance of these two different morphologies

was due to the different S diffusion rates on WO_3 microparticles and nanoparticles.

Similarly, ZrS_2 was produced by the sulphidation of ZrO_2 . Unlike WO_3 and MoO_3 , ZrO_2 could not react with H_2S at as high as 1300°C [78]. Therefore, C was used as a reducing agent to activate this reaction at lower temperature. During reaction, ZrOS appeared as an intermediate phase and finally converted into ZrS_2 after a 2-h heat treatment at 1300°C . This temperature could be reduced to 1000°C when CS_2 was used as the reactant and the holding time was extended to 24 h [79].

Very recently, MoS_2 monolayer flakes with thicknesses of approximately 0.72 nm were synthesised from the reaction of MoO_3 with S on SiO_2/Si substrates [80]. To generate the MoS_2 monolayer flakes, some ultra-large, monolayer reduced graphite oxide (rGO) nanosheets were spun on substrates. The sizes and thicknesses of the final MoS_2 products could be controlled by varying the morphologies of the rGO flakes.

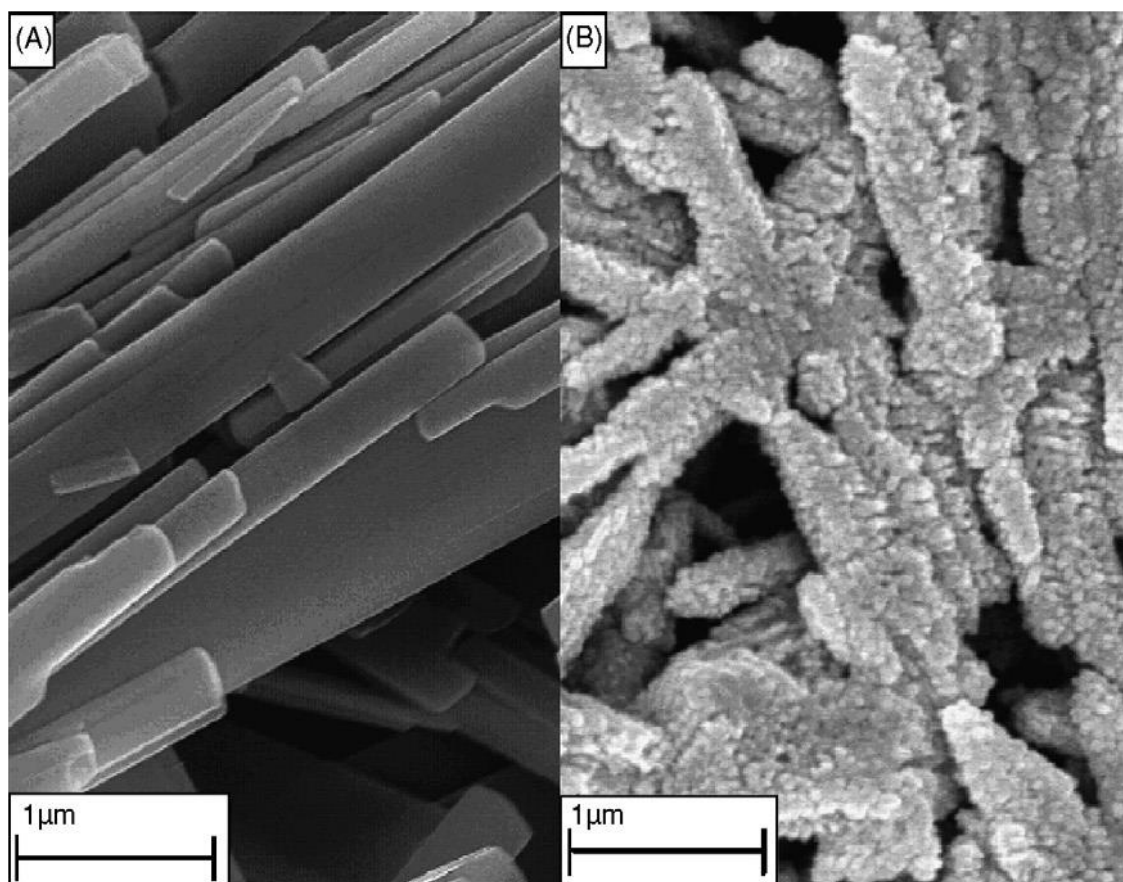


Figure 2.11 SEM image of (A) MoO₃ nanoribbons and (B) resulting MoS₂ nanoflakes [18].

Apart from the common metal oxide microparticles with irregular shapes, many metal oxide nanoparticles with various morphologies have been used to produce MX₂. WO₃ nanorods [77], W₁₈O₄₉ nanobundles [81], MoO₃ nanoribbons [18] and MoO₃ nanobelts [82] and all reacted with H₂S or S in the temperature range of 500°C-1000°C. Although these precursors have different morphologies, the final products were similar hexagonal MX₂ nanoflakes with various sizes and thicknesses. Moreover, these generated nanoflakes stacked together and retained the morphologies of the precursors (Figure 2.11).

2). Synthesis of metal dichalcogenide IF nanoparticles and nanotubes from various precursors

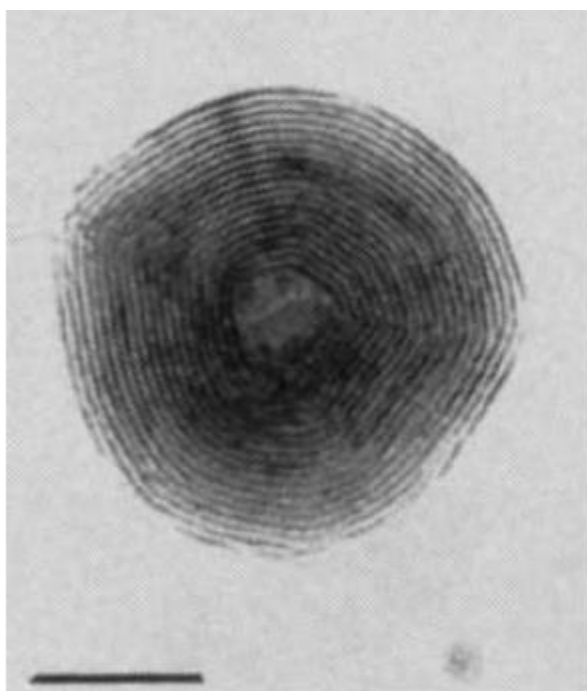


Figure 2.12 HRTEM of synthesised WS₂ IF nanoparticles[16]

In 1992, WS₂ IF nanoparticles were first synthesised from the straightforward reaction of thin W films with H₂S [16]. The synthesised WS₂ IF nanoparticles had a typical onion-like hollow structure with sizes of approximately 20 nm (Figure 2.12). Then, MoS₂ IF nanoparticles with sizes in the range of 20 nm-100 nm were generated by heating MoO₃ powder in a H₂S/H₂ atmosphere at

approximately 840°C [22]. Because MoO₃ was very volatile and would sublime above 650°C, the formation of MoS₂ was essentially via the gas-gas reaction between the sublimed MoO₃ and H₂S vapour. Therefore, the morphologies and sizes of the MoS₂ products would be irrelative to those of the raw material MoO₃. To improve the yield of IF MoS₂, two opposite nozzles flowing with H₂S and MoO₃ vapour were placed in the hot zone of the furnace. During the reaction, a turbulent flow containing both H₂S and MoO₃ vapour was formed to improve the contact of the reactants. Consequently, more MoS₂ IF nanoparticles were generated.

Similarly to MoO₃, WO₃ also reacts with H₂S to form WS₂. However, because of its high boiling point (1700°C), the gas-solid reaction between H₂S and WO₃ was instead involved to produce WS₂ IF nanoparticles. Therefore, the sizes and morphologies of the WO₃ precursor had a clear effect on the formation of IF WS₂. To obtain WS₂ IF nanoparticles, the maximum size of the WO₃ precursor should be 200 nm; above this size, 2H-WS₂ platelets were predominantly obtained under the same conditions (820°C, 2 h) [83]. Further investigations to improve the quality and quantity of WS₂ and MoS₂ IF nanoparticles by optimising the heat-treatment parameters and designing new reactors were performed by Tenne's group [14, 84]. The so-called "falling bed synthesis" technique was proposed and has been applied for commercial production.

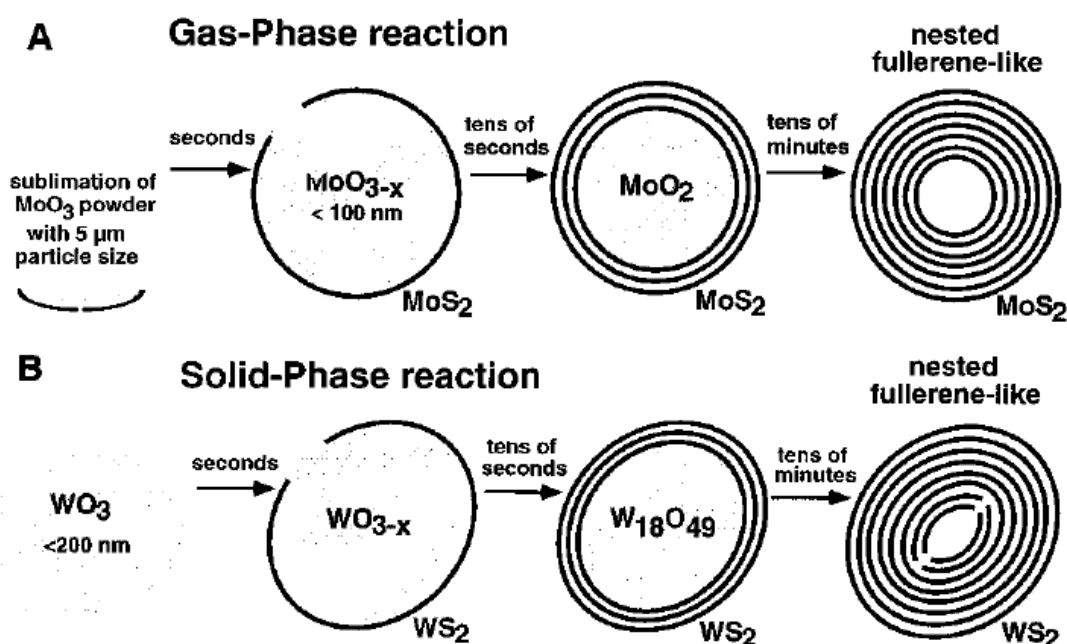


Figure 2.13 Schematic representation of growth mechanism for (A) MoS₂ and (B) WS₂ from corresponding oxides [83].

After many years of investigation, the formation mechanism of WS₂/MoS₂ IF nanoparticles from the reaction between the corresponding oxides and H₂S has been understood. Figure 2.13 illustrates the step-by-step conversion from oxides to IF nanoparticles. First, the metal oxides are rapidly reduced to the corresponding metal suboxides. Then, these suboxides are sulfurised to the metal sulphides layer by layer from the surface to the core. With the proceeding of the reaction, metal sulphide IF nanoparticles are generated. Based on this mechanism, ReS₂ IF nanoparticles are also produced from the reaction of ReO₂ with H₂S [85].

When H₂S was replaced by CS₂, WS₂ could still be generated at 900°C [86]. However, because the raw WO₃ powder was quite large (approximately 620 nm), WS₂ flakes with an average size approximately 2 µm were produced rather than the IF nanoparticles. To form IF nanoparticles, the above route was modified by simply reducing the sizes of the raw material WO₃ to <100 nm. WS₂ IF nanoparticles with sizes of 50-70 nm were fabricated at 800°C *via* the same route after this modification [87]. In addition to WS₂ IF nanoparticles, some nanotubes (approximately 10%) were formed.

When the starting materials were changed from WO₃ nanoparticles to nanowires and nanowhiskers, WS₂ nanotubes were produced that resembled the oxide precursors [88-91]. However, for the synthesis of MoS₂ nanotubes, direct reaction between MoO₃ nanowires with H₂S is not feasible due to the low sublimation point of MoO₃. Because of MoO₃ sublimation, the sizes and morphologies of the MoO₃ precursor did not resemble those of the synthesised MoS₂ [92].

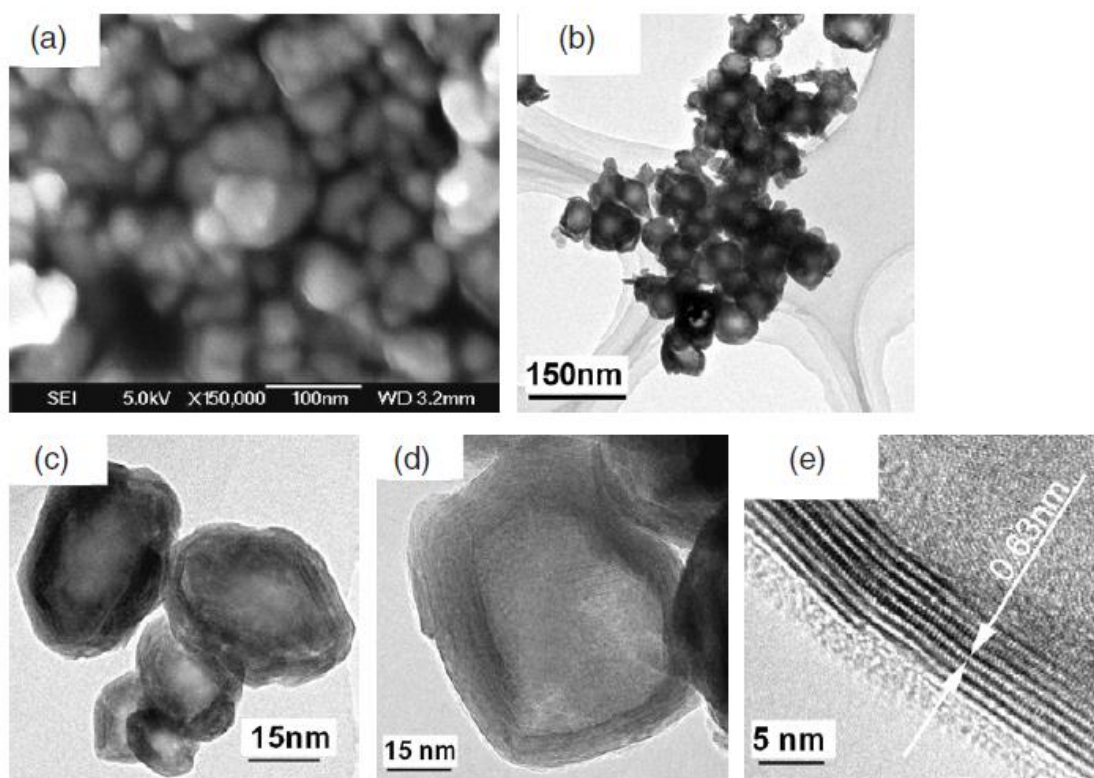


Figure 2.14 (a) SEM and (b) TEM images of synthesised WS_2 IF nanoparticles from the reaction between WO_3 and S under H_2 atmosphere [11].

It is apparent that the involvement of toxic H_2S and CS_2 in the above cases was harmful and largely increased production costs. Yang et al. [11] overcame this drawback by replacing H_2S with S powder in a simple tube furnace under H_2 atmosphere. To produce pure WS_2 IF nanoparticles, the temperatures and holding times were limited below $630^\circ C$ and 10 min, respectively. If either the temperature or holding time exceeded these values, $2H-WS_2$ platelets were generated. Compared with WS_2 IF nanoparticles fabricated from “falling bed synthesis”, the sizes of the resulting products were quite similar (approximately 45 nm). However, most of the products had large hollow cores with very thin walls (approximately 5 nm in thickness), leading to poor high-temperature stability and mechanical properties (Figure 2.14). Another alternation was performed by replacing all these reactive gas phases (H_2 and H_2S) with solid precursors ($NaBH_4$ and S) [93]. WS_2 and MoS_2 IF nanoparticles were readily formed after 15-min heating of the $NaBH_4$, S and WO_3/MoO_3 mixture at $800^\circ C$. The reaction time could be reduced to less than 1 min when photothermal solar was used as the heating source. However, few WS_2 and MoS_2 IF nanoparticles

were generated because the extreme high temperature generated by solar radiation during synthesis resulted in the collapse of the IF structure.

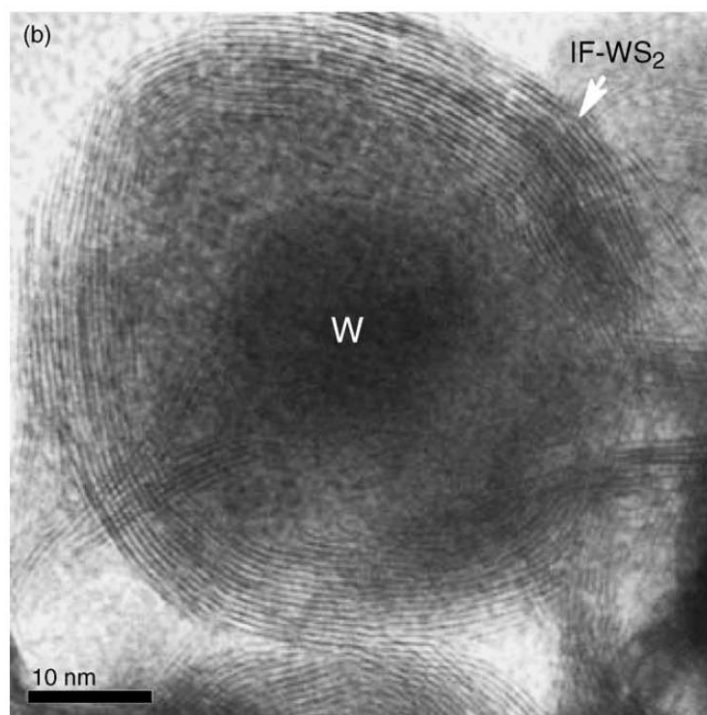


Figure 2.15 HRTEM images of W/IF-WS₂ synthesised at 500°C[94].

Unlike the metal-oxide-based reactions, Chang et al. managed to fabricate WS₂ and MoS₂ using nano Mo and W powders as the raw materials. These metal nanoparticles could react with S and H₂ to form corresponding WS₂ and MoS₂. Unlike MoO₃ and WO₃, which were easily sulfurised to phase-pure sulphides at relatively low temperatures, Mo and W could not completely react with S and H₂S even after a 2-h heat treatment at 900°C [94, 95]. Notably, when the temperature was below 600°C, residual W and Mo particles were not isolated from the formed sulphides but coated by them, leading to the formation of a core-shell structure with metal cores and continuous metal sulphide shells (Figure 2.15). GaS was also produced from the reaction between Ga and S powder at 900°C *via* a similar route [96]. Because Ga has a very low melting point (30°C) but an extremely high boiling point (2204°C), this synthesis process was essentially based on a liquid-gas reaction mechanism. Therefore, GaS-Ga core-shell nanoparticles could not be formed. After the reaction, GaS nanoflakes were generated, which was followed by annealing at 650°C for 2 h in Ar. The annealing process provided extra energy, which caused self-rolling of these nanoflakes; therefore, numerous GaS nanotubes were produced.

2.1.2.2 Synthesis of metal dichalcogenides from the decomposition of metal chalcogenide precursors

Apart from the sulphidation of metals and metal oxides, WS_2 and MoS_2 could be produced by decomposing $(\text{NH}_4)_2\text{WS}_4$ and $(\text{NH}_4)_2\text{MoS}_4$, respectively. According to DSC analysis, both $(\text{NH}_4)_2\text{MoS}_4$ (decomposition temperature of 155°C) and $(\text{NH}_4)_2\text{WS}_4$ (decomposition temperature of 180°C) exhibited poor high-temperature stability [97, 98]. The decomposition products at these temperatures were NH_3 , H_2S and corresponding MoS_3 or WS_3 . Upon increasing the temperature to approximately 350°C , the initially formed metal trisulphides would then decompose into metal disulphides and sulphur. Using this technique, the sizes of the synthesised MoS_2 and WS_2 particles were quite large. For example, MoS_2 particles with sizes up to 50 microns were produced from the decomposition of $(\text{NH}_4)_2\text{MoS}_4$ in Ar [99, 100].

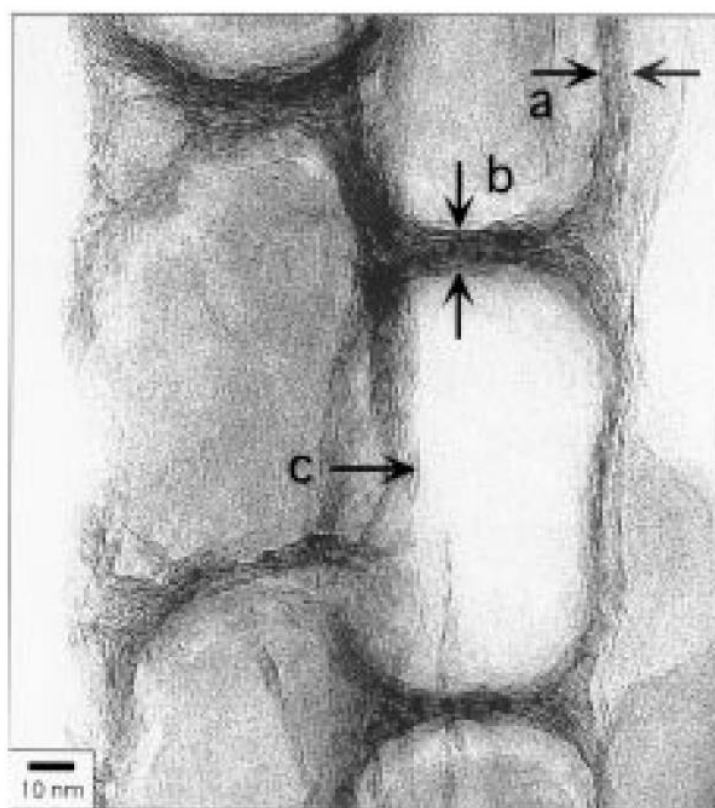


Figure 2.16 TEM image of MoS_2 nanotubes prepared from template synthesis route [101].

When the decomposition process of $(\text{NH}_4)_2\text{WS}_4$ occurred in a porous Al_2O_3 template, WS_2 nanotubes were produced rather than large bulk materials [101].

To obtain WS_2 nanotubes, $(NH_4)_2WS_4$ powder was dissolved in pyridine solvent to form a homogeneous solution. Then, the precursor solution was dropped on a porous Al_2O_3 template (pore diameters of approximately 50 nm), followed by low-temperature heating to evaporate the pyridine. Finally, the loaded template was heated at $450^\circ C$ for 1 h in H_2/N_2 . The synthesised products were composed of MoS_2 “bamboo-like” nanotubes with diameters of 50 nm and lengths of 30 μm (Figure 2.16). Because these nanotubes were evenly coated on the entire inner surface of the Al_2O_3 template, the nanotubes had uniform diameters, which were the same as the Al_2O_3 pore size.

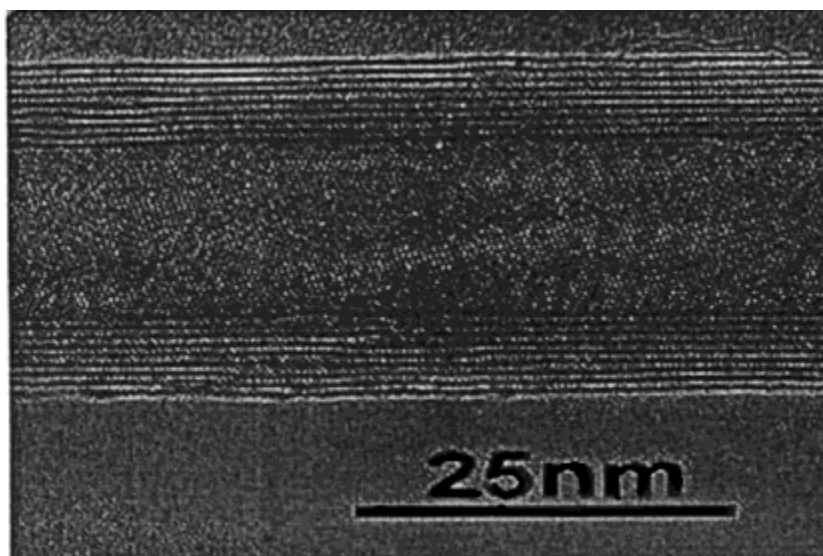


Figure 2.17 TEM image of a WS_2 nanotube [102].

Without the help of a porous template, Nath et al. were able to fabricate MoS_2 and WS_2 nanotubes by directly heating $(NH_4)_2WS_4$ and $(NH_4)_2MoS_4$ powder at $1200^\circ C$ - $1300^\circ C$ in a H_2/Ar atmosphere [103]. The outer diameters of the synthesised nanotubes ranged from 15-35 nm, with a wall thickness of approximately 15 nm. The synthesis temperature was decreased dramatically to $360^\circ C$ - $450^\circ C$ when thiophene vapour was used as the catalyst in H_2 [102, 104]. Before heat treatment, the $(NH_4)_2WS_4$ precursor was ball-milled at 800 rpm for 1 h in H_2 . After this process, amorphous $(NH_4)_2WS_4$ nanoparticles were generated. This “activation” process was an essential step to decrease the synthesis temperature to as low as $360^\circ C$; otherwise, nanotubes could not be observed even at $600^\circ C$. The average length and outer diameter of the synthesised nanotubes were approximately 5 μm and 25-50 nm, respectively (Figure 2.17).

When $(\text{NH}_4)_2\text{WS}_4$ -ethanol solution was used as a precursor, unique WS_2 nanoboxes were formed *via* spray pyrolysis [105]. First, uniform micrometre-sized $(\text{NH}_4)_2\text{WS}_4$ droplets were generated from the pneumatic spray generator. The subsequent pyrolysis of these droplets lasted for only 1 s at 900°C in Ar, leading to the formation of WS_2 nanoboxes. The produced WS_2 nanoboxes had closed parallelepiped shapes with all the dimensions below 300 nm. By varying the pyrolysis temperatures, amorphous and crystallised WS_2 nanoboxes were generated at 300°C and 900°C , respectively. Yin et al. [106] extended this route to synthesise MoS_2 IF nanoparticles at 220°C . MoS_3 hollow microspheres were initially formed by the spray pyrolysis of $(\text{NH}_4)_2\text{MoS}_4$ water solution. Further decomposition of these MoS_3 microspheres was performed at 850°C for 5 h in H_2/Ar to produce MoS_2 , which retained a similar hollow spherical morphology as the MoS_3 precursor. According to the HRTEM images, these microspheres were composed of numerous MoS_2 IF nanoparticles with diameters ranging from tens to hundreds of nanometres.

Because MS_3 is an intermediate associated with the decomposition of $(\text{NH}_4)_2\text{MS}_4$, it can be directly used as a precursor for the synthesis of MS_2 . For example, NbS_3 and TaS_3 were heated at 1000°C for 30-60 min in H_2 , forming NbS_2 nanotubes and TaS_2 nanotubes, respectively [107]. The diameters of these nanotubes ranged from 4-15 nm with closed ends. Inspired by this result, MoS_3 obtained from the reaction between $(\text{NH}_4)_2\text{MoS}_4$ solution and $\text{H}_2\text{C}_2\text{O}_4 \cdot 2\text{H}_2\text{O}$ was also heated at 800°C for 1 h in N_2 [108]. However, MoS_2 nanolamellas that were approximately 80 nm in size and 20-30 nm in thickness were formed rather than nanotubes. This finding was consistent with a previous investigation by Afanasiev et al. [109]. The MoS_3 precursor was synthesised from the reaction between $(\text{NH}_4)_2\text{MoS}_4$ and N_2H_4 or $\text{NH}_2\text{OH} \cdot \text{H}_2\text{SO}_4$. After the heat treatment of the generated MoS_3 at 400°C in N_2 , the resulting MoS_2 consisted of amorphous nanoparticles with high specific surface areas (as high as $210 \text{ m}^2/\text{g}$).

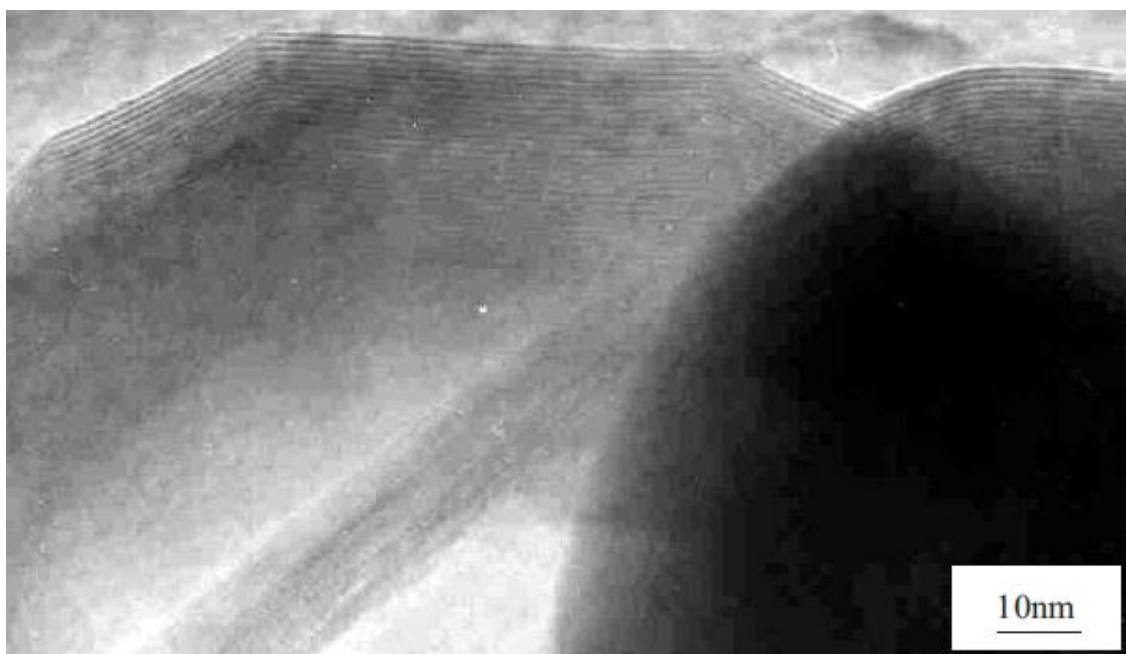


Figure 2.18 TEM image of MoS₂ IF nanoparticles [110].

To obtain IF nanoparticles, polyethylene glycol (PEG) was added into the reactant solutions to stabilise the initially formed MS₃. This method was first used for the formation of MoS₂ IF nanoparticles [110]. In this case, (NH₄)₂MoO₄ solution was mixed with the (NH₄)₂S solution and PEG. The pH value of the solution was adjusted using HCl. MoS₃ precipitates were collected and then fired at 900°C for 6 h in a H₂ atmosphere. MoS₂ IF nanoparticles with sizes ranging from 60 nm to 200 nm were generated (Figure 2.18). Due to the usage of PEG, the initially formed metal trisulphide was coated and separated by the PEG, preventing their further agglomeration. Consequently, during the subsequent firing process, the resulting MoS₂ nanoparticles would not sinter with surrounding particles to form large flakes. [110]. If the S source was changed from (NH₄)₂S to Na₂S·9H₂O, MoS₂ could still be produced *via* the same route after firing at 800°C for 30 min in a H₂ atmosphere. Differently, however, numerous MoS₂ nanospheres with an average diameter of 300 nm were produced [111]. HRTEM revealed that these nanospheres were composed of numerous IF nanoparticles with an average size of approximately 30 nm. This route was extended to fabricate WS₂ IF nanoparticles with sizes of 50-78 nm using (NH₄)₂WS₄ as a precursor [112].

2.1.2 Chemical vapour deposition

Chemical vapour deposition (CVD) is another traditional technique to produce nanoparticles. Using this technique, gaseous reactants react with each other to form tiny product nuclei, followed by crystallisation and deposition processes. For the synthesis of metal dichalcogenides, two types of metal precursors were used: metal halides and metal carbonyls. All these compounds have high vapour pressures at temperatures below 300°C and are active enough to react with chalcogenide vapour instantaneously at high temperatures.

2.1.2.1 Synthesis of metal dichalcogenides from metal halides

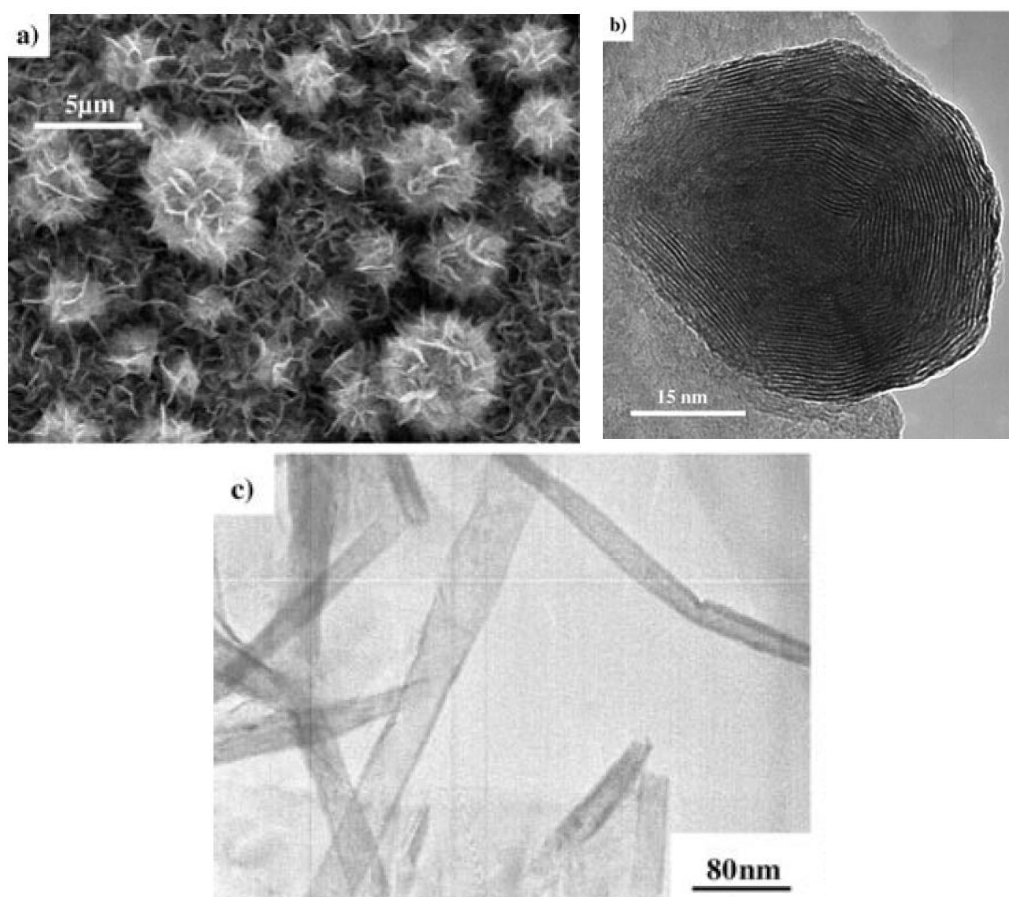


Figure 2.19 (a) SEM image of MoS₂ nanoflowers and TEM images of (b) MoS₂ IF nanoparticles and (c) nanotubes [113].

WS₂ and MoS₂ IF nanoparticles and nanotubes were successfully produced *via* CVD using WCl₆, MoCl₅ and S as the reactants [113]. WCl₆/MoCl₅ and S were loaded into two separate quartz boats. A tube furnace was preheated to 850°C

and flushed with Ar to exhaust the residual air. When the furnace was fully filled with Ar, two quartz boats were rapidly pushed into its hot zone. S powder was placed in the upstream gas flow, while $WCl_6/MoCl_5$ was placed in the downstream gas flow. A silicon substrate was used to collect the products. The entire reaction lasted for 1 h in an Ar atmosphere. Pure MoS_2 was synthesised at as low as $550^\circ C$. When the temperature was increased to $650^\circ C$, MoS_2/WS_2 nanoflowers were produced (Figure 2.19a). These nanoflowers were made of many petals that were approximately 100–300 nm in size and 40 nm in thickness. When the temperature was further increased to $750^\circ C$, the morphology of the MoS_2 product was changed dramatically to open-ended nanotubes with diameters ranging from 30 to 100 nm (Figure 2.19c). MoS_2 IF nanoparticles with average diameters of approximately 40 nm were generated only when the temperature reached $850^\circ C$ (Figure 2.19b), indicating that the generation of this morphology required high thermodynamic energy. The formation of these IF nanoparticles was attributed to the fast nucleation associated with the very rapid reaction at $850^\circ C$. Consequently, numerous WS_2 nuclei were created, followed by crystal growth. When the crystals reached a critical size, the clusters tended to bend to form IF structures and deposited on the silicon substrate.

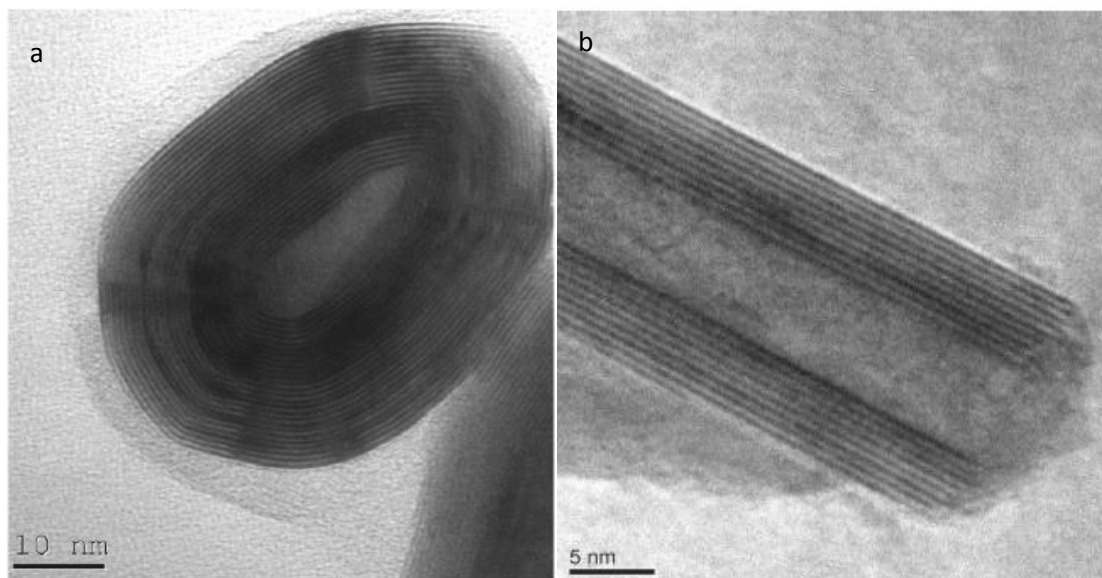


Figure 2.20 TEM images of (a) WS_2 IF nanoparticles and (b) nanotubes synthesised from the reaction between WCl_6 and H_2S [114].

Upon replacement of S with H₂S, WS₂/MoS₂ IF nanoparticles and nanotubes could also be synthesised *via* CVD [114, 115]. A specially designed facility composed of two connected furnaces (an auxiliary furnace and a vertical furnace) was designed to facilitate the formation of IF structures. First, metal chloride precursors were heated to temperatures close to their boiling points (approximately 300°C) to generate corresponding gas phases. Then, the metal chloride vapour was carried by flowing N₂ and/or H₂ to the top of the preheated vertical furnace. Simultaneously, H₂S was blown to the same location from the opposite direction and mixed with the metal chloride vapour. The typical reaction period was 30 min. After reaction, the products were deposited on a filter that was placed in the middle of the furnace. The sizes of the resultant IF MoS₂ nanoparticles were in the range of 20-80 nm, while the sizes of the IF WS₂ nanoparticles were approximately 50 nm. When the reaction temperatures were restricted to 800°C-900°C, all the produced IF nanoparticles contained large voids. If the reaction temperatures were below 800°C, these voids were filled with amorphous materials. When the temperature was increased to above 900°C, some open-ended WS₂ and MoS₂ nanotubes were formed instead. The diameters of the WS₂ and MoS₂ nanotubes were in the range of 20-30 nm and 30-35 nm, respectively (Figure 2.20). The formation mechanism of this route was similar to that of the above method. The sulphidation process of metal chlorides could be indicated by the following reaction:



The formation of the IF structure was also attributed to the self-folding of the initially formed WS₂/MoS₂ nuclei.

In addition to MoS₂ and WS₂, many other metal sulphides, such as TiS₂, TaS₂, and NbS₂ [41, 58, 116, 117], have been synthesised *via* CVD. TiS₂, TaS₂ and NbS₂ IF nanoparticles with sizes below 100 nm were readily produced via high-temperature treatment. The formed TiS₂ IF nanoparticles were not hollow, which is quite different from others, due to their low boiling point (136°C). Some Nb-doped MoS₂ IF nanoparticles were also synthesised *via* CVD using a NbCl₅-MoCl₅-H₂S mixture gas as the starting material [118]. The mixture was heated to 800, 850 and 900°C in the same special furnace mentioned in ref. [114].

Depending on the temperature, the synthesised $\text{Mo}_{1-x}\text{Nb}_x\text{S}_2$ were either 50-nm spherical IF nanoparticles (below 850°C) or 40-nm faceted IF nanoparticles (above 850°C).

2.1.2.1 Synthesis of metal dichalcogenides using metal organic chemical vapour deposition (MOCVD)

MOCVD is an alternative route to fabricate metal dichalcogenides by reacting metal hexacarbonyls with chalcogenides in an inert atmosphere. Similar to metal halides, metal hexacarbonyls have relatively low melting points and boiling points. Therefore, these materials can be easily evaporated and then reacted with chalcogenide vapour to form metal dichalcogenides. According to Chung et al., this route can be used to fabricate WS_2 thin films [119]. In this case, $\text{W}(\text{CO})_6$ powder was initially evaporated in a bubbler. The generated $\text{W}(\text{CO})_6$ vapour was carried by flowing N_2 and mixed with H_2S in a fused quartz reactor. A silicon substrate was placed in the reactor and heated to 900 K by a small halogen lamp on its back. After the reaction between $\text{W}(\text{CO})_6$ and H_2S , well-crystallised WS_2 films were generated on the substrate. The formed WS_2 films had two different orientations: basal planes parallel or nonparallel to the substrate. Upon increasing the deposition time, the thicknesses of the products increased from 65 nm (5 min) to 350 nm (15 min). Some other MoS_2 and MoSe_2 films could also be produced *via* this route with no substrate [120]. For example, $\text{Mo}(\text{CO})_6$ and S/Se were mixed and sealed in a stainless container in a nitrogen-filled glove box. This container was heated to 750°C for 1-3 h to complete the reaction. Because C generated from the decomposition of $\text{Mo}(\text{CO})_6$ was also sealed in the container, the formed products were composed of $\text{MoS}_2/\text{MoSe}_2$ and C. The average length and thickness of the produced films were approximately 100 nm and 20 nm, respectively. The products also assembled to form bulk particles with sizes of approximately 800 nm.

In addition to films, MOCVD is suitable to produce metal dichalcogenides IF nanoparticles. WS_2 and MoS_2 IF nanoparticles were synthesised by the reaction of $\text{M}(\text{CO})_6$ (M=W and Mo) with H_2S in Ar [121]. The reactants were heated by a microwave plasma generator with controllable frequency from 0.915 to 2.45 GHz. The reaction temperatures were controlled in the range of 260-580°C by

adjusting the generator frequency, and the reaction time was limited to below 8 ms. When the frequency was set to 2.45 GHz, both the resulting WS₂ and MoS₂ were irregular nanoparticles with average 5-nm sizes. Some slightly bent lattice fringes with larger lattice spacing (0.65 nm) than those of the bulk materials (0.62 nm) could be observed from these nanoparticles. Decreasing the frequency to 0.915 GHz did not significantly change the sizes of the nanoparticles. However, WS₂ and MoS₂ IF nanoparticles with irregular, open-cage structures were generated. This route has already been extended to fabricate other metal dichalcogenides (MoSe₂, WSe₂, SnS₂, ZrSe₂) under the same condition (0.915 GHz and 2.45 GHz) [122]. All these products were irregular flakes except for ZrSe₂, which were IF nanoparticles with a closed cage structure.

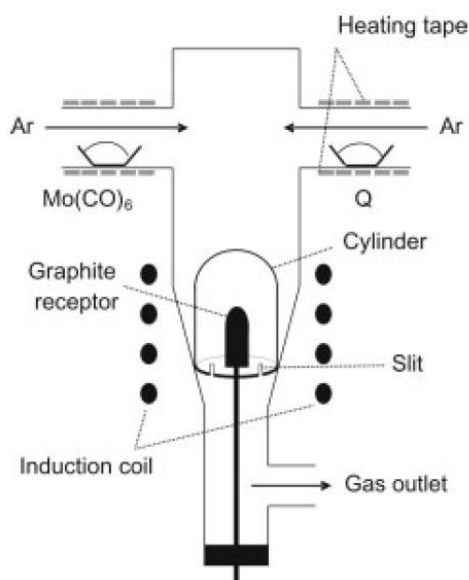


Figure 2.21 Schematic representation of the equipment for the synthesis of MoS₂ and MoSe₂ IF nanoparticles [123].

To improve the yield of metal dichalcogenide IF nanoparticles synthesised *via* MOCVD, a special instrument was designed (Figure 2.21) [123]. Similar to other MOCVD routes, gaseous reactants (Mo(CO)₆ and S/Se) were initially generated by heating corresponding powders. These evaporated reactants were delivered by constant Ar flow into a quartz cylinder that was placed in the heating zone of the furnace. A graphite receptor, situated in the quartz cylinder, was used to control the reaction temperature at 450°C for MoS₂ and 500°C for MoSe₂. After a few minutes of reaction, a fine black powder was collected from the inner wall of quartz cylinder, followed by a 1-h annealing process at 700°C or 800°C in Ar.

According to their research, both MoS_2 and MoSe_2 samples before annealing were composed of sintered nanoparticles with sizes ranging from 5-20 nm. Each particle consisted of amorphous components and some slightly curved layers. After 1-h annealing at 700-800°C, these nanoparticles were converted into hollow, closed spherical particles that were 30-60 nm in size. A further increase of the temperature led to the generation of MoS_2 and MoSe_2 nanotubes and nanorods.

The detailed mechanism of MOCVD in the formation of metal dichalcogenide IF nanoparticles was investigated using in situ heating TEM examination using $\text{W(CO)}_6/\text{Mo(CO)}_6$ and S as the starting materials [124, 125]. In the absence of the annealing process, the products generated from MOCVD were composed of two types of nanoparticles: whisker-like particles with sizes of approximately 10 nm (called S-type particles) and sphere-like particles with diameters ranging from 25 to 200 nm (called R-type particles). The formation of these two different types of particles was due to different retention times in the hot zone. During the reaction, some reactants were trapped on the inner wall of the quartz cylinder and were only heated for a short time, resulting in the formation of an irregular whisker shape. However, the fully heated particles exhibited agglomerated spherical morphology because this phase was the most energetically preferred phase. The amount of R-style particles increased with increasing temperature and reaction time. After annealing at high temperature, these S-style particles and R-style particles crystallised to form nanowhiskers (10–15 nm in size and 1.9-6.0 in aspect ratios) and IF nanoparticles (hollow cages with sizes ranging from 15-100 nm), respectively.

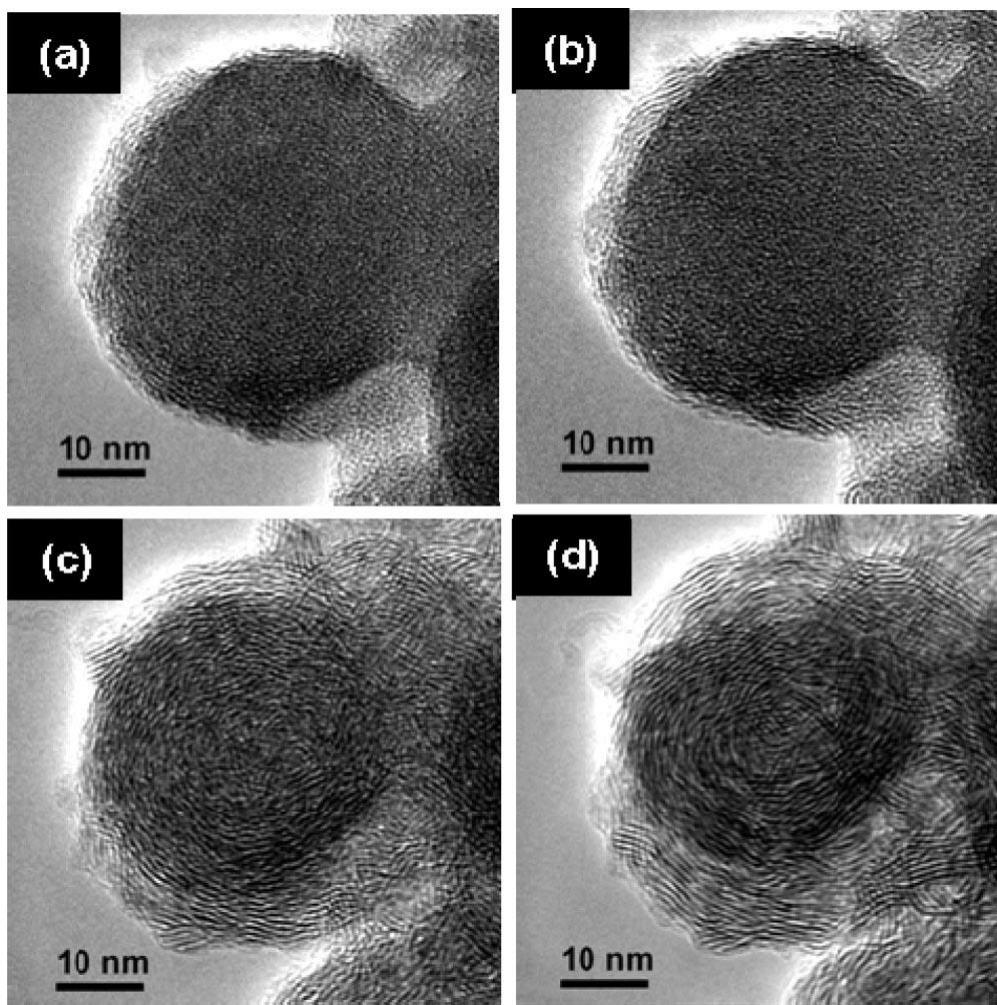


Figure 2.22 TEM image of an R-type particle in a MoS₂ sample at (a) 24°C, (b) 100°C, (c) 300°C, and (d) 500°C.

The step-by-step changes in the R-style particles with increasing temperature were also investigated (Figure 2.22). For MoS₂, the reaction was completed at a relatively low temperature (<300°C), and crystallisation occurred simultaneously throughout the entire particle. A higher temperature promoted the healing of defects, leading to better crystallisation. Compared with MoS₂, the complete reaction temperature for WS₂ was higher (400-500°C), and the crystallisation process started at the outer particle boundaries. This difference in reaction temperature and crystallisation between WS₂ and MoS₂ might be attributed to the stronger W-W bond compared with the Mo-Mo bond, which suppressed the reaction with S. The entire reaction for synthesising WS₂ could be described as the following: at high temperature, W(CO)₆ vapour initially decomposed into W and reacted with S to form amorphous WS₂. Crystallised WS₂ was initially formed on the outer surface of the amorphous WS₂ particles, leading to the generation of WS₂ core-shell nanoparticles with crystallised WS₂ shells and

amorphous WS_2 cores. Because the density of the WS_2 crystal was higher than its amorphous phase, mass transport driven by the concentration gradient from the interior of the particle to the outer surface occurred. This process caused the depletion of particle cores, resulting in the formation of the hollow structure. The same MOCVD route was modified by adding I_2 during the synthesis of MoS_2 [126]. Nanoparticles with similar morphology as the original route were generated before annealing. However, after annealing, MoS_2 IF nanoparticles with “giant” voids were formed rather than common IF nanoparticles. These synthesised IF nanoparticles were composed of MoS_2 and $Mo_2S_5I_3$, with shell thicknesses of approximately 5 nm and void sizes of approximately 120 nm. This finding was attributed to the generation of I_2 vapour during the annealing process, which led to high vapour pressure within the IF cage. Upon increasing the pressure, the IF cage was enlarged and sometimes crushed if the pressure was higher than a critical value.

2.4 Properties of metal dichalcogenide nanoflakes, IF nanoparticles and nanotubes

The theoretical stability of the IF structure was investigated by Seifert et al. on MoS_2 IF nanotubes and flat molecular sheets using a combination of a semi-empirical model and the density-functional tight-binding (DFTB) method [127]. Because of the strain energy generated by bending layers in IF nanoparticles, this bending structure is less energetically favoured than the flake structure. However, when the sizes of the nanoparticles are above a critical value, the strain energy stored in the bending layers is compensated by the elimination of dangling bonds on the edges of the layers due to the reconnection to the closed structure.

For MoS_2 nanotubes, the critical outer diameter is 12 nm and 7 layers. When initial nanotube nuclei are formed, they tend to grow in two directions: radially or longitudinally depending on the balance between the energy obtained by Van der Waals interaction among layers and the stored strain energy. If the former is higher, then longitudinal growth is predominant, and if the latter is higher, then radial growth is predominant [127]. For the spherical IF nanoparticles, the

stored energy in the folded layers is higher than the energy in the nanotubes due to the involvement of two directions bending in IF nanoparticles rather than one direction in nanotubes. Therefore, defects are generated to stabilise this spherical structure by reducing the strain energy. Furthermore, the stability of IF nanoparticles is affected by the number of their layers. Thin-layer nanoparticles can maintain spherical shapes, while thick-layer nanoparticles always exhibit facet shapes with some defects. The reason for this difference is related to the stored strain energy, which is higher in thick-layer nanoparticles than in thin-layer ones. The appearance of facet shapes and defects is necessary to relieve this energy and maintain the structure [128]. For WS_2 IF nanoparticles, when their sizes are above a critical value (usually 200 nm), the strain energy will become too high to maintain balance with the energy loss from elimination of dangling bonds and the introduction of defects. The IF nanoparticles and nanotubes will unfold and crush, forming flakes to eventually relieve the extra energy.

The thermal stability of NbS_2 , WS_2 and MoS_2 IF nanoparticles and nanoflakes were examined by TG-DTA in oxidising and inert atmospheres [35]. The results revealed that metal dichalcogenide nanoflakes had higher thermal stability than the corresponding IF nanoparticles. The decomposition temperatures for all these particles were similar, approximately 1350°C in N_2 atmosphere and 350-400°C in the oxidising atmosphere. In addition, the sizes of the particles had little effect on the decomposition temperatures. After the decomposition in N_2 atmosphere, WS_2 IF nanoparticles were converted into a mixture of WS_2 , W and $W_{18}O_{49}$. All the IF nanoparticles were transformed into nanoflakes, indicating that the IF structure was not as stable as the flake structure at this temperature.

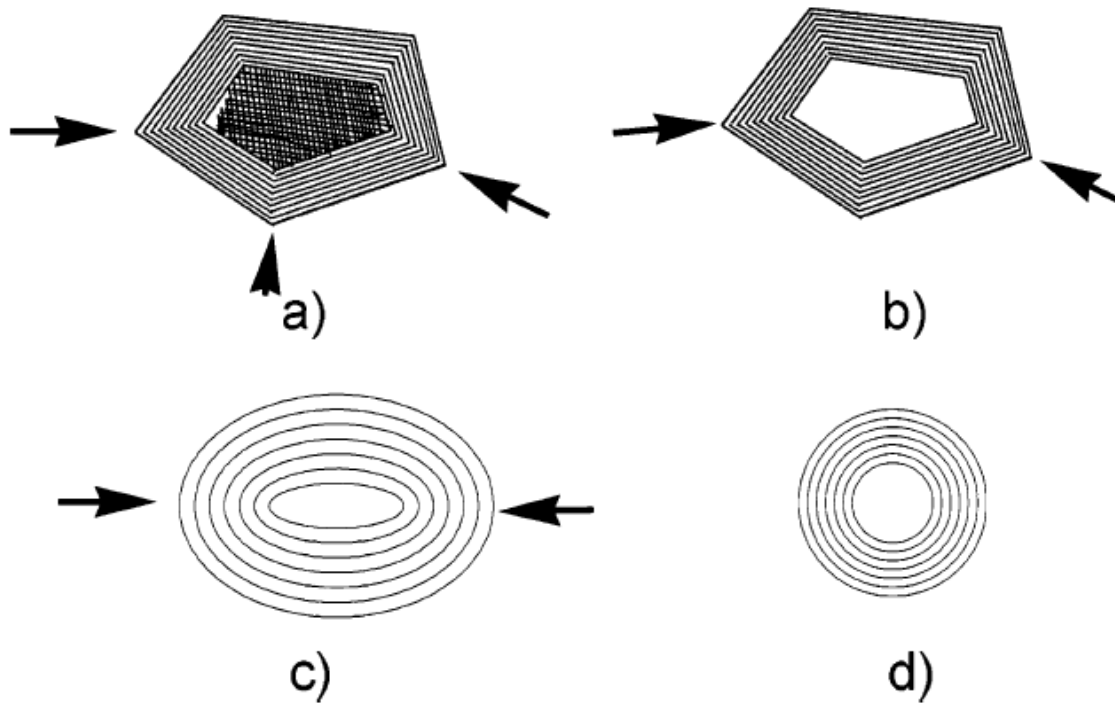


Figure 2.23 Schematic illustration of the likelihood of damage of IFs under shock wave pressure. All the damage may occur at the ends (arrow). Perfectly shaped spherical WS_2 IF nanoparticles may exhibit the best shock wave resistance because these particles do not have obvious ends [129].

The mechanical properties of IF nanoparticles and nanotubes can be measured under AFM and HRSEM. AFM was used to measure the force applied on the samples while their movement was controlled by HRSEM. The Young's modulus, tensile strength, fracture strain and shear modulus of the synthesised WS_2 nanotubes were measured to be approximately 150-170 GPa, 16 GPa, 14% and 2 GPa, respectively [4]. Because the yield strength/Young's modulus ratio of the WS_2 nanotubes (calculated to be 0.11) was very high, the cracking of the nanotubes was due to the rupture of an individual chemical bond rather than other macroscopic mechanisms, i.e., dislocation and intergranular fracture [5]. Because the WS_2 IF nanoparticles were much smaller than WS_2 nanotubes, only the stiffness and compression failure strength were measured. Both the stiffness and compression failure strength varied with the sizes and shapes of the IF nanoparticles, ranging from 55-480 N/m and 1-3.5 GPa, respectively [6]. In addition to these properties, the shock wave resistance of WS_2 and MoS_2 IF nanoparticles and nanotubes were measured to be approximately 25 GPa and 21 GPa, respectively [129-131]. Their crushing might follow two mechanisms:

direct stress-induced breakage failure and diffusion-controlled oxidation (Figure 2.23). This superbly high shockwave resistance makes these structures potentially applicable to a high-pressure environment, i.e., bullet-proof armour.

Because many metal dichalcogenides (WS_2 , NbS_2 , MoS_2 etc.) have graphite-like layer structures, they could be ideally used as solid lubricants. For the corresponding IF nanoparticles, their lubricating performance is also superb, arising from two reasons: (1) the closed cage structure makes IF nanoparticles chemically inert. This property retards the reaction with other materials and the formation of oil sludge. (2) The spherical shape changes the friction mechanism from sliding friction to rolling friction, leading to a low friction coefficient. To measure the friction coefficient, 0.1-2 wt% IF nanoparticles were mixed into the base oil and pressed under 0.66-1.5 GPa pressure. The friction coefficients of IF WS_2 [11], NbS_2 [41], TiS_2 [116] and TaS_2 [41] were measured to be 0.08, 0.07, 0.03 and 0.09, respectively. The friction coefficients were observed to be closely related to the sizes and shapes of the sample.

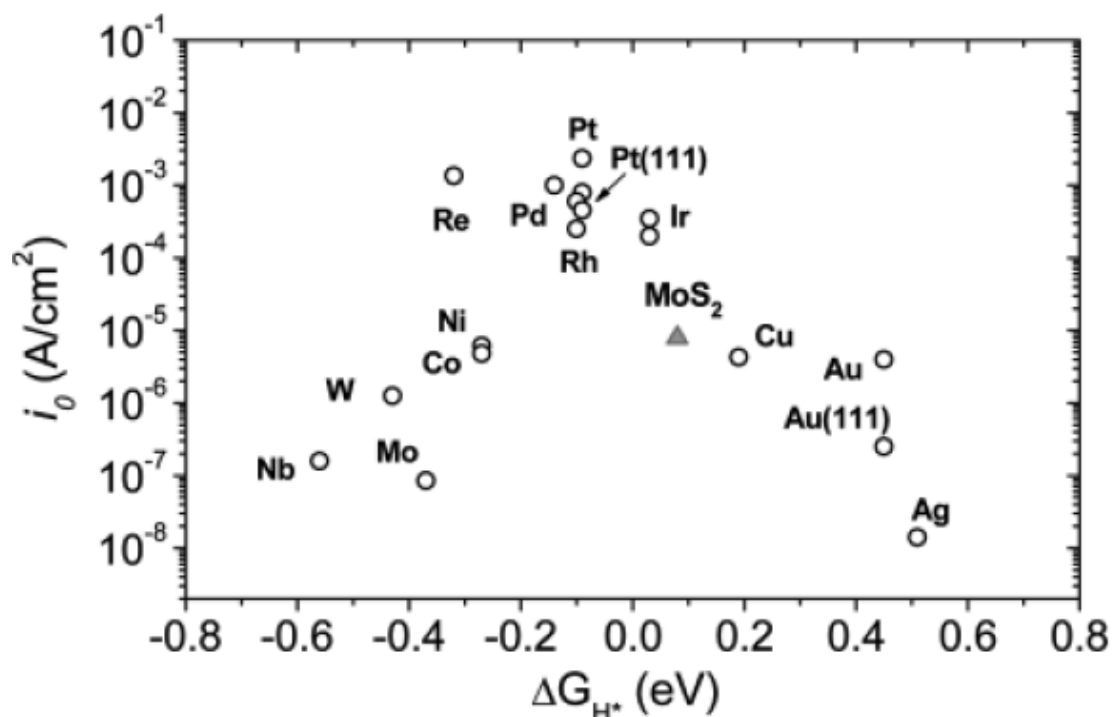
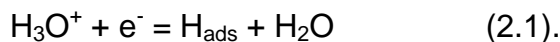
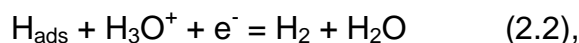


Figure 2.24 Volcano plot of the exchange current density as a function of the DFT-calculated Gibbs free energy of adsorbed atomic hydrogen for MoS_2 and pure metals [132].

Recently, the excellent hydrogen evolution reaction (HER) performance of WS₂ and MoS₂ has drawn significant attention as H₂ becomes increasingly important in the fuel area. In general, the HER process can be divided into three possible reaction steps [133]. The first step is the primary discharge step (Volmer reaction):



This step is followed by either an electrochemical desorption step (Heyrovsky reaction),



or a recombination step (Tafel reaction),



Because of the extremely high H_{ads} coverage (Θ_{h} is approximately 1), Pt exhibits the best HER performance [133] and follows the Volmer-Tafel mechanism. For MoS₂, the Gibbs free energy of adsorbed atomic hydrogen is similar to that of Pt (Figure 2.24), indicating that these materials might also exhibit decent HER performance. However, the HER performance results of the MoS₂ bulk materials were quite poor (the overpotentials were above 200 mV, and the Tafel slopes were approximately 100 mV/dec). These results were attributed to two reasons: (1) the poor electrical conductivity of MoS₂ and (2) for normal 2H MoS₂, active sites are only limited to the edges of the flakes, which are not a large part of a bulk material [134]. To improve the HER performance, many measures have been attempted, including adding highly conductive reduced graphene oxide [135], introducing more defects to increase the number of active sites [136] and preparing single-layer 1T MoS₂ which has high conductivity and contains many more active sites [3]. All these techniques efficiently lower the overpotentials and Tafel slopes to approximately 100 mV and 60 mV/dec, respectively. Compared with MoS₂, WS₂ also exhibits similar but slightly inferior HER performance, which might due to its poor electrical conductivity [2, 137, 138].

Although many techniques for the fabrication of MX_2 have been developed in the past 20 years, most of these techniques are complicated or require the involvement of toxic reactants such as H_2S , hydrazine hydrate, which largely increase the production cost and cause safety/environmental concern. Therefore, it is necessary to develop a new route to overcome these drawbacks.

2.5 Synthesis techniques and properties of core-in-hollow-shell spheres

Because the core-in-hollow-shell structure has only been developed recently, this structure does not have a specific name and is called the rattle-type structure [139-142] or yolk-shell structure [143-145]. Nanoparticles that have this structure are denoted as A@B , where A and B mean the materials of the core and shell, respectively. To synthesise nanorattle materials, a few techniques have been proposed, among which the template synthesis technique is the most commonly used because of its good reliability and controllability. In this technique, a core-shell structured precursor is used. This precursor is initially coated with another material, forming a three-layered egg-like composite particle (analogous to 'yolk, egg white, and eggshell'). This composite particle is further subjected to chemical etching or calcination, after which, the 'egg white' part can be removed, and a nanorattle, with a core inherited from the precursor and a shell from the coating, is generated.

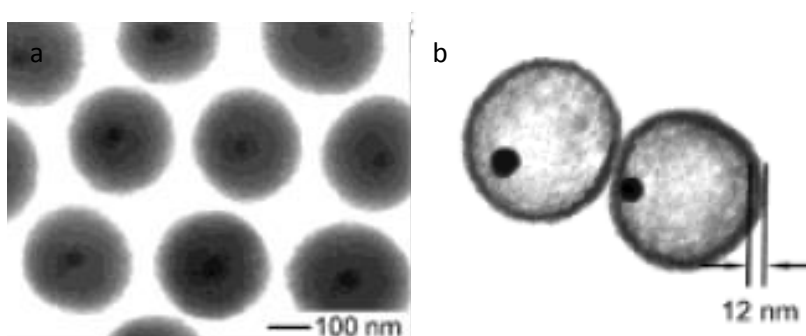


Figure 2.25 TEM images of Au-SiO₂-PbzMA composite (a) before and (b) after HF solution etching [146].

Based on the above theory, Xia and co-workers synthesised Au-poly(benzyl methacrylate) (PbzMA) nanorattles [146]. The produced egg-like composite was

composed of Au-SiO₂-PbzMA, which was then etched with HF solution to remove the SiO₂ “egg white”. Moveable Au nanoparticles with an average diameter of approximately 10 nm were enclosed in a 12-nm-thick PbzMA shell (Figure 2.25). Based on this route, many nanoparticles with the rattle-type structure have been synthesised, including Au@ZrO₂ nanorattles from a Au-SiO₂-ZrO₂ composite precursor [147], Au-Pt hybrid cores in a α-Fe₂O₃ shell from a Au-Pt- polyelectrolyte multilayer (PEM)-α-FeOOH precursor [148], Pt@ hollow porous carbon (hmC) nanorattles from a Pt-SiO₂- phenol-formaldehyde resin (PF) precursor [149] or a Pt-TiO₂-phenol precursor [150], and SiO₂@TiO₂ from SiO₂-polystyrene-sulfonated polystyrene-TiO₂ composites [151]. For the synthesis of Au@SiO₂ nanorattles, it is difficult to directly apply the above procedure because SiO₂ easily reacts with the etching agent (e.g., HF solution). Therefore, several modified routes were developed to overcome this problem. Song and co-workers first coated porous SiO₂ on the surface of Au nanoparticles. Then, the coated sample was selectively etched with KCN solution. Because the porous SiO₂ coating is permeable, KCN can easily diffuse through the coating to react with the Au cores, leading to the formation of smaller Au nanoparticles and Au(CN)₂ enclosed in the original SiO₂ shell. The gold core sizes were controllable by adjusting the amount of KCN solution [143, 152]. Alternatively, Au@SiO₂ nanorattles were also produced *via* NaOH solution etching of Au-SiO₂ core-shell nanospheres. Because NaOH can react with SiO₂, poly(vinyl pyrrolidone) (PVP) layers were first coated on the surface of the Au-SiO₂ composites as a protecting ligand. Therefore, OH⁻ could not rapidly react with SiO₂ on the surface. Instead, these ions diffused into and reacted the interior of the SiO₂ coatings, leading to a relatively rapid reaction rate compared with that on the surface. Finally, with continuous etching, Au@SiO₂ nanorattles were produced [153].

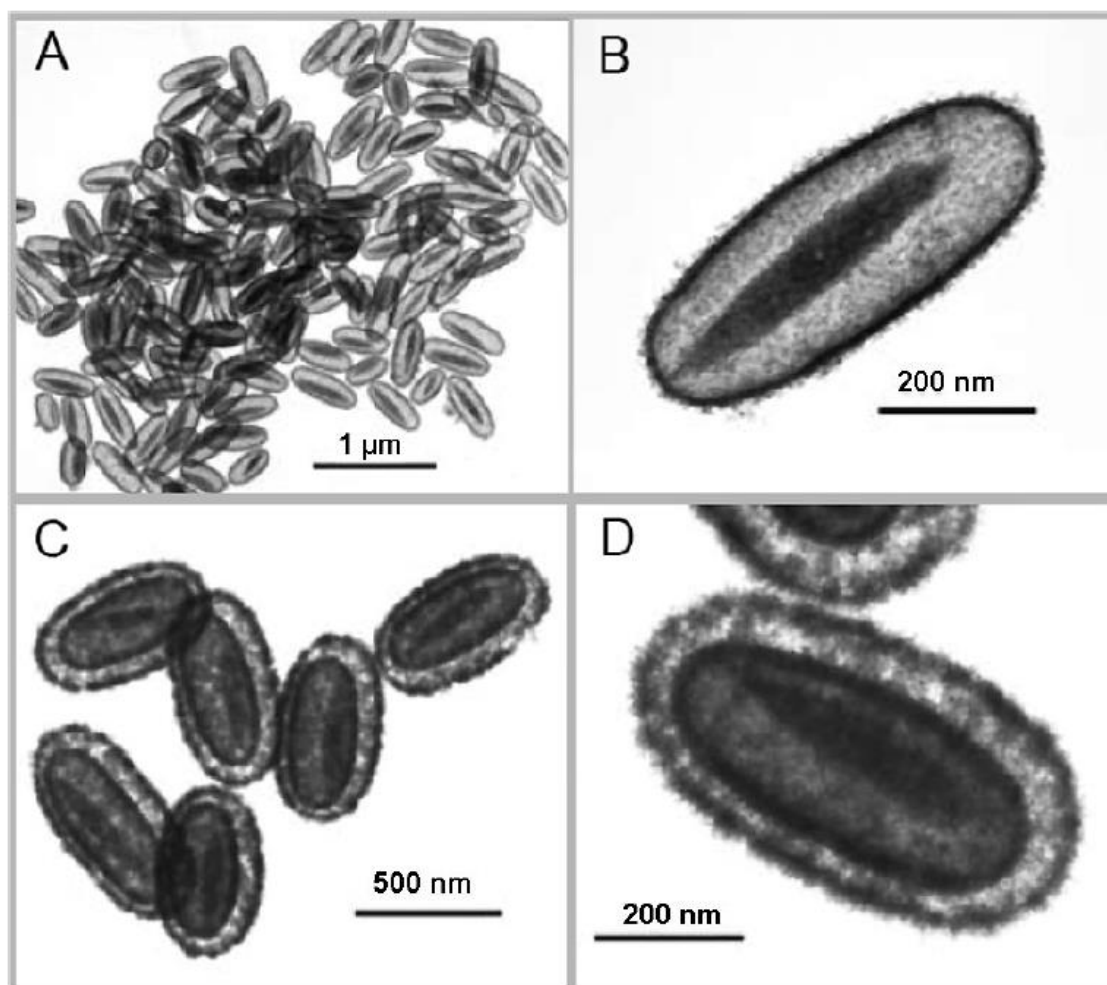


Figure 2.26 TEM images of (A, B) single-walled $\alpha\text{-Fe}_2\text{O}_3\text{@SnO}_2$ nanococoons and (C, D) double-shelled SnO_2 nanococoons [154].

Because of the usage of spherical templates, all the synthesised nanorattles mentioned above had a spherical shape. Therefore, it is possible to produce nanorattles with different shapes by varying the shapes of the templates [154-156]. Archer et al. successfully synthesised $\alpha\text{-Fe}_2\text{O}_3\text{@SnO}_2$ nanorattles with a cocoon-like shape [154]. The key operation to generate nanococoons rather than nanospheres was to select $\alpha\text{-Fe}_2\text{O}_3$ nanospindles as templates. After coating with SiO_2 and SnO_2 , the formed $\alpha\text{-Fe}_2\text{O}_3\text{-SiO}_2\text{-SnO}_2$ composites were etched by NaOH solution to remove SiO_2 , resulting in the generation of $\alpha\text{-Fe}_2\text{O}_3\text{@SnO}_2$ nanorattles (Figure 2.26). By reducing the amount of $\alpha\text{-Fe}_2\text{O}_3\text{-SiO}_2$ in the SnO_2 coating process, some porous double-shelled SnO_2 nanococoons were produced. This result was attributed to the Ostwald ripening of extra SnO_2 deposition on the surface of the $\text{Fe}_2\text{O}_3\text{@SnO}_2$ nanorattles.

In general, the main advantage of this template synthesis method is its controllability. By tuning the experimental parameters, the core sizes, shell sizes, shell thicknesses and shapes can be precisely controlled. Unfortunately, this technique suffers from several drawbacks, including the requirement of a core-shell structured precursor, which is not readily available, relying on a complex multi-step process and the usage of hazard etching agents.

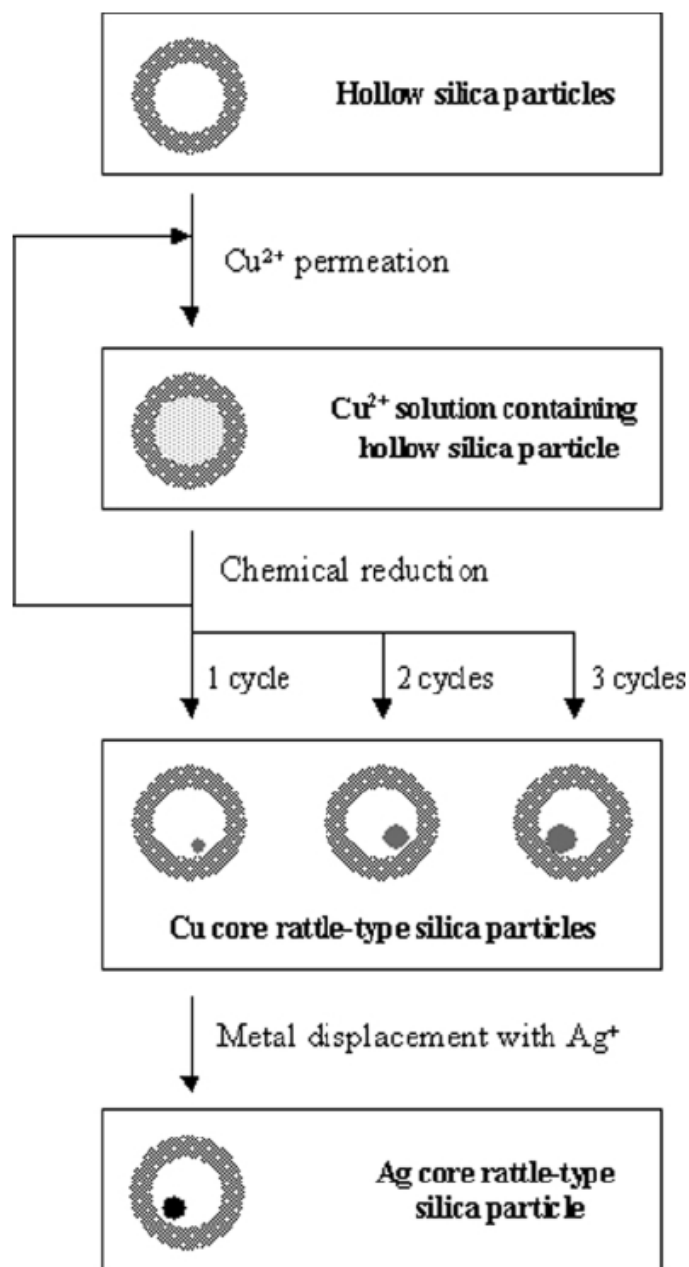


Figure 2.27 Schematic for the preparation of rattle-type silica particles with metal cores by pre-shell/post-core method [140].

An alternative strategy for the synthesis of nanorattles is the preshell/postcore method [157]. The key procedure of this method is the application of hollow

nanospheres as nanoreactors. The reactants can diffuse and react with each other in the hollow chamber of these nanoreactors [140, 158-160]. For instance, Koo and co-workers successfully synthesised Cu@SiO₂ nanorattles *via* this route [140]. Hollow SiO₂ nanoreactors were prepared in advance. Then, ethanolic solution containing copper nitrate hydrate (Cu(NO₃)₂ · 2H₂O) was mixed with the SiO₂ precursor. After sonication for 1 h in an ultrasonic bath, the mixture was added to hydrazine monohydrate (N₂H₄ · H₂O) and stirred for 3 h. Finally, Cu nanoparticles were generated within the SiO₂ nanoreactors from the reaction between the copper nitrate and hydrazine, leading to the formation of Cu@SiO₂ nanorattles. The detailed schematic procedure for this route is presented in Figure 2.27. It is apparent that the main drawback of this route is the difficulty of ensuring that the Cu production reaction occurs in the nanoreactors. Therefore, the produced nanorattles were always accompanied with numerous impurities. As a response, Chan and co-workers improved this method to produce Ag@polypyrrole-chitosan (Ppy-CS) nanorattles [160]. Similar to the above synthesis, Ppy-CS hollow nanospheres were used as nanoreactors and mixed with AgNO₃ solution. Then, the pH of the solution was lowered to 2.2. Because Ppy-CS had the least permeability at this pH, Ag⁺ ions were sealed in the nanospheres. Then, the Ag⁺ ions outside the nanospheres were removed by dialysis using a membrane bag. Finally, Ag nanoparticles were generated by the further reaction between AgNO₃ and hydroxymethyl radicals under ultraviolet irradiation using a low-pressure mercury lamp. Although this modified route can improve the purity of the product, the complex reactions and involvement of ultraviolet irradiation make it difficult to scale up.

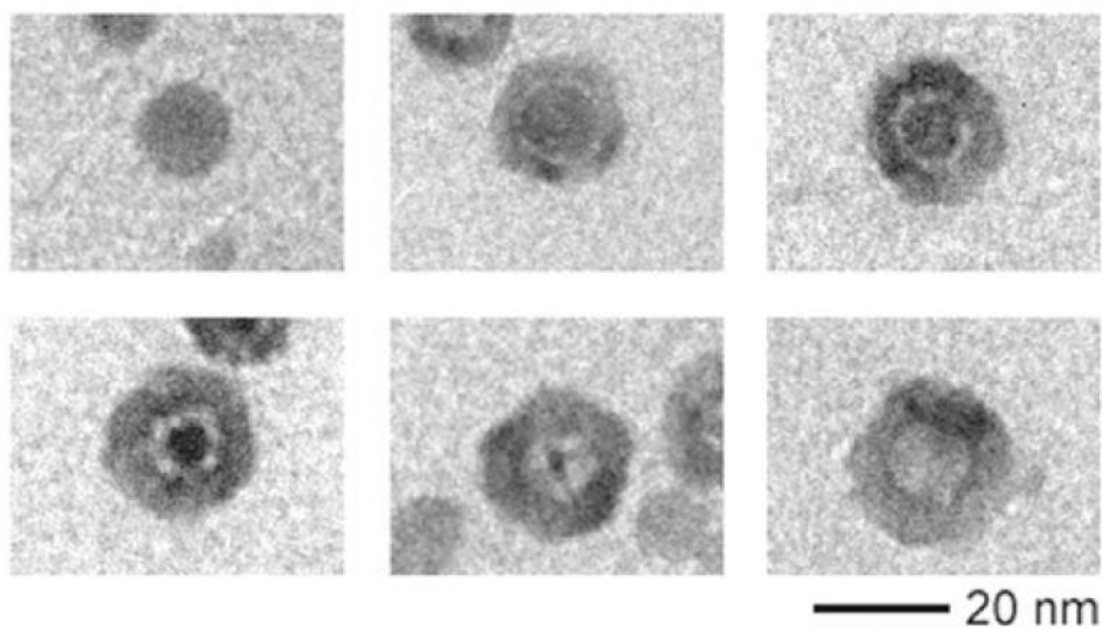


Figure 2.28 HRTEM images of reaction between Co and Se at 455 K; from top-left to bottom-right: 0 s, 10 s, 20 s, 1 min, 2 min and 30 min [161].

In addition to the template-based synthesis routes described above, nanorattles can be produced by controlling the interdiffusion process between different components based on the Kirkendall effect and Ostwald ripening mechanism. The Kirkendall effect refers to different material interdiffusion rates in a bulk diffusion couple [162]. During the diffusion, the net flow of mass is compensated by a flux of vacancies, resulting in the generation of voids near the interface. Although this phenomenon becomes more complicated when applied on the nanoscale because of the effects of curvature and surface energetics cannot be neglected, it has been applied to the synthesis of nanoparticles and nanotubes [161, 163, 164]. By controlling the diffusion rate, this effect can also be applied to the nanorattle synthesis. Yin and co-workers first produced Co@CoSe nanorattles using this technique [161]. A Co solution and a Se solution were mixed by stirring at 455 K. Initially, the Co nanocrystals were covered with a very thin layer of CoSe. Because of the different diffusion rates between Co and CoSe, further reaction required the outward diffusion of Co from the interior through the formed CoSe layer. Therefore, the Co cores were consumed gradually and reacted with the outside Se to form a CoSe shell, leading to the final production of CoSe hollow nanospheres (Figure 2.30). During the reaction process, Co@CoSe nanorattles were formed as an intermediate of the Kirkendall diffusion.

The Ostwald ripening mechanism is a crystal growth process in solution from small crystals to large crystals, which is a thermodynamically driven spontaneous process and occurs because larger particles are more energetically favoured than smaller particles. Because molecules on the surface of a particle are energetically less stable than those in the interior, small particles tend to stick on large particles to reduce the surface energies. Therefore, large particles grow larger, while small particles are consumed. Based on this mechanism, many hollow particles were produced [165, 166]. Recently, nanorattles have also been fabricated *via* this approach [167-170]. For instance, Zeng and co-workers synthesised ZnS nanorattles using this self-assembly process [171]. The ZnS nanoparticles first aggregated with each other to form large spheres. The surface of the large spheres was composed of loosely packed, tiny crystals. During the crystallisation process, crystals below the initially crystallised surface were consumed, and voids were generated between the shell and core, resulting in the formation of ZnS nanorattles.

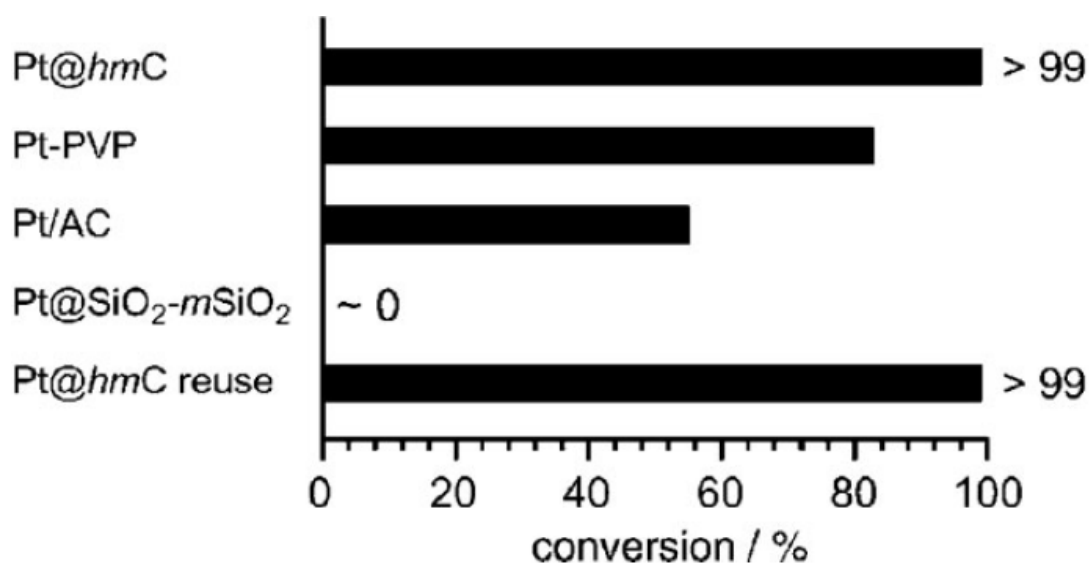


Figure 2.29 Liquid-phase hydrogenation of nitrobenzene into aniline by various Pt catalysts at 303 K [149].

As mentioned earlier (section 2.2), this novel nanorattle structure can improve the catalytic performance of enclosed nanoparticles. For example, to improve the catalytic performance of Pt on the hydrogenation of nitrobenzene, Ikeda and co-workers prepared Pt@hollow porous carbon (hmC) nanorattles *via* the template synthesis route [149]. Pt nanoparticles were first coated with double-

layer SiO_2 (a SiO_2 layer and a mesoporous SiO_2 layer). Then, a layer of carbon was added on the surface of the outer mesoporous SiO_2 layer, leading to the formation of Pt- SiO_2 -C composites. After etching with HF solution, Pt@hmC nanorattles were produced. To investigate the catalytic performance of the Pt@hmC nanorattles, several other Pt-based composites were used for comparison, such as Pt-poly(N-vinyl-2-pyrrolidone)(Pt-PVP), Pt-activated carbon (Pt-AC), Pt- SiO_2 and reused Pt@hmC nanorattles. Figure 2.29 shows the conversion rates of nitrobenzene using various catalysts. Compared with other catalysts, Pt@hmC nanorattles had the best conversion rate, which was almost 100%. Moreover, these nanorattles also exhibited good reused efficiency. After being washed and centrifuged, the catalytic performance of the reused Pt@hmC nanorattles was the same as that of the original nanorattles. The high-temperature catalytic performance of Au@ ZrO_2 nanorattles was investigated by Arnal and co-workers [147]. The performance was measured by the catalytic oxidation of CO in air. The as-synthesised Au@ ZrO_2 nanorattles exhibited much better catalytic performance than the Au nanoparticles, with values of almost 100% and 50% at 320°C, respectively. In addition, nanorattles calcined at 800°C exhibited very similar catalytic performance as the original nanorattles, indicating that the Au@ ZrO_2 nanorattles exhibited good high temperature stability.

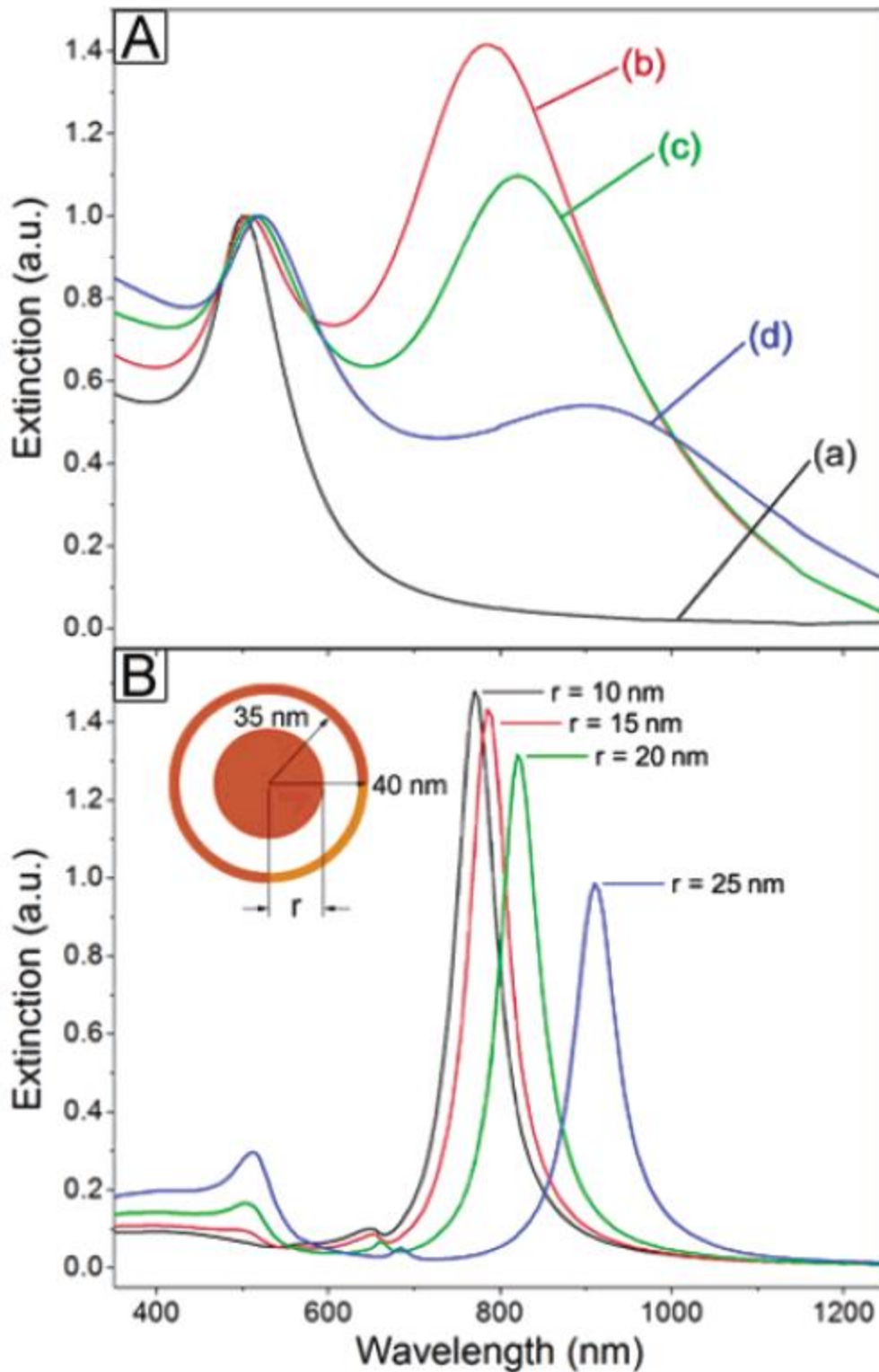


Figure 2.30 (A) UV-visible-NIR extinction spectra of nanorattles produced by mixing Au/Ag alloy-Ag core-shell nanoparticles with different volumes of 1 mM HauCl_4 solution: (a) 0, (b) 0.4, (c) 0.5 and (d) 0.6 ml. (B) Extinction spectra of nanorattles with fixed inner and outer shell diameters of 70 nm and 80 nm, respectively, and various core sizes [172].

In addition to the improved catalytic performance, the nanorattles exhibited some unique optical properties. Xia et al. investigated the optical properties of Au/Ag@Au/Ag nanorattles [172]. Au/Ag alloy-Ag core-shell nanoparticles were first produced and used as a precursor. These nanoparticles were added to HauCl_4 solution to generate Au/Ag alloy- Au/Ag alloy core-shell nanoparticles. Because of the different diffusion rates between Au and Ag, materials on the interface between the core and shell were consumed, and Au/Ag@Au/Ag nanorattles were generated based on the Kirkendall effect. According to the UV-visible-NIR extinction spectra, the synthesised nanorattles exhibited different surface plasmon resonance (SPR) properties from those of the original Au/Ag alloys. Figure 2.30A demonstrates that only one obvious peak was observed in the spectrum of the original Au/Ag alloy centred at approximately 502 nm, while all the extinction spectra acquired from the synthesised nanorattles exhibited an additional peak in the range of 350-1250 nm. Therefore, the formed nanorattles could be called dual-colour nanoparticles, which means that their extinction peaks were located in two different regions, such as the green and red regions. The appearance of this new peak was attributed to the formation of the Au/Ag shell, which would emit SPR scatter signals. In addition, the volume of added HauCl_4 solution was also observed to be related to the red shift of all the extinction peaks, which could be attributed to the decrease in the wall thickness for the outer shells as well as the generation of pinholes in the walls arising from selective removal of Ag. Moreover, the sizes of the cores also affected the extinction spectra. The intensity of the peak originating from the Au/Ag cores decreased with decreasing core sizes. When the core size was below 15 nm, no peak was observed because the core was screened by the shell, and no SPR would be excited in the core.

Recently, several types of nanorattles have been used as drug-delivery vehicles because of their good biocompatibility, large specific surface areas and mesoporous structure. More importantly, modification of the cores and shells (i.e., magnetic-material-based nanorattles) can make the targeted delivery possible, which will dramatically improve the pharmaceutical effect [173-176]. For instance, Stucky and co-workers successfully delivered drug molecules to a target area. During their experiments, $\text{Fe}_3\text{O}_4@\text{SiO}_2@\alpha\text{-NaYF}_4/\text{Yb, Er}$ magnetic upconversion fluoride nanorattles (MUC-F-NR) were synthesised as delivery

vehicles. The small-molecule drug doxorubicin (DOX) was loaded into the free volume of these nanorattles. By applying an external magnetic field, MUC-F-NRs loaded with DOX were transferred to xenograft tumours. This transfer was confirmed by the high luminescence intensity in the tumour, indicating that an external magnetic field had accumulated MUC-F-NRs with DOX at the target.

Although nanorattles have numerous beneficial properties, these structures have still not been used on a large scale, which is most likely due to the complex operation process, high cost and low yield in all the current synthesis routes mentioned above. To address these issues, in this work, a novel one-step route has been developed to produce $W@WS_2$ nanorattles *via* the reduction and sulphidation of WO_3 nanoparticles. Because this reaction is based on a simple gas-solid reaction among WO_3 , S and H_2 , the batch size could be easily increase to tens of grams, which makes the process suitable for large-scale production. In addition, the usage of non-toxic raw materials ensures that this process is environmentally friendly. As mentioned before, WS_2 has good high temperature stability and corrosion resistance. Therefore, the WS_2 -coated nanorattles could survive under harsh conditions, which could extend their applications. By further reacting these produced $W@WS_2$ nanorattles with S or CH_4 for example, new nanorattles could also be prepared, such as $WS_2@WS_2$ and $WC@WS_2$ nanorattles, which should exhibit good HER catalytic properties. In addition to WS_2 -based nanorattles, this technique could be potentially used to produce a range of different types of nanorattles, such as MoS_2 and TiS_2 on a large scale.

Chapter Three Experimental Techniques

3.1 Characterisation techniques

3.1.1 X-ray diffraction (XRD)

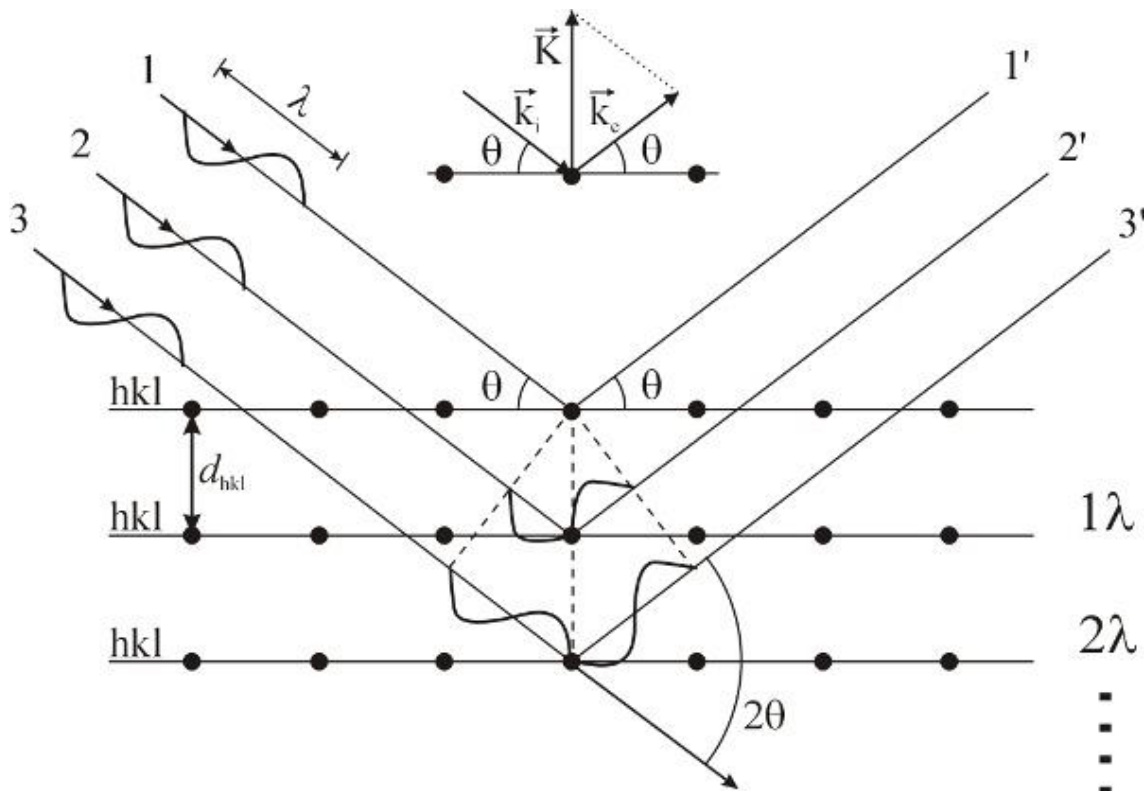


Figure 3.1 Schematic representation of Bragg's law

XRD is a non-destructive technique based upon the Bragg-Brentano para-focusing geometry and is used to identify the crystal structure and chemical composition of a phase. X-rays incident on a crystal will be diffracted by the atoms in the crystal in many specific directions. The positions and intensities of these diffracted X-rays can be measured by a sensor film. The calculation of the spacing between diffracting planes of crystal is based on Bragg's law:

$$2d\sin\theta = n\lambda, \quad (3.1)$$

where d , θ , λ and n are the spacing between diffracting planes, incident angle, wavelength of the beam and any positive integer, respectively (Figure 3.1).

In this project, phase analysis on the reacted powders was performed using an X-ray diffractometer (D500 Siemens) at 30 mA and 40 kV with Ni-filtered Cu K α radiation ($\lambda=0.154$ nm). The scan rate (2θ) was $2^\circ/\text{min}$, and a step size of 0.02° was used within a scan range of $10-80^\circ$. Because all of the samples were in the powder form, they were pressed on a glass substrate to ensure that the height of the entire sample was uniform. ICDD cards used for phase identifications included WS_2 (No. 84-1398), WO_3 (No. 32-1395), $\text{W}_{18}\text{O}_{49}$ (No. 36-101), WO_2 (No. 32-1393), $\alpha\text{-W}$ (No. 47-1319), MoS_2 (No. 37-1492), MoO_3 (No. 5-508), MoO_2 (No. 32-671), $(\text{NH}_4)_2\text{WS}_4$ (No. 48-1663), ZrS_3 (No. 15-790) and ZrS_2 (11-679).

3.1.2 Transmission electron microscopy (TEM)

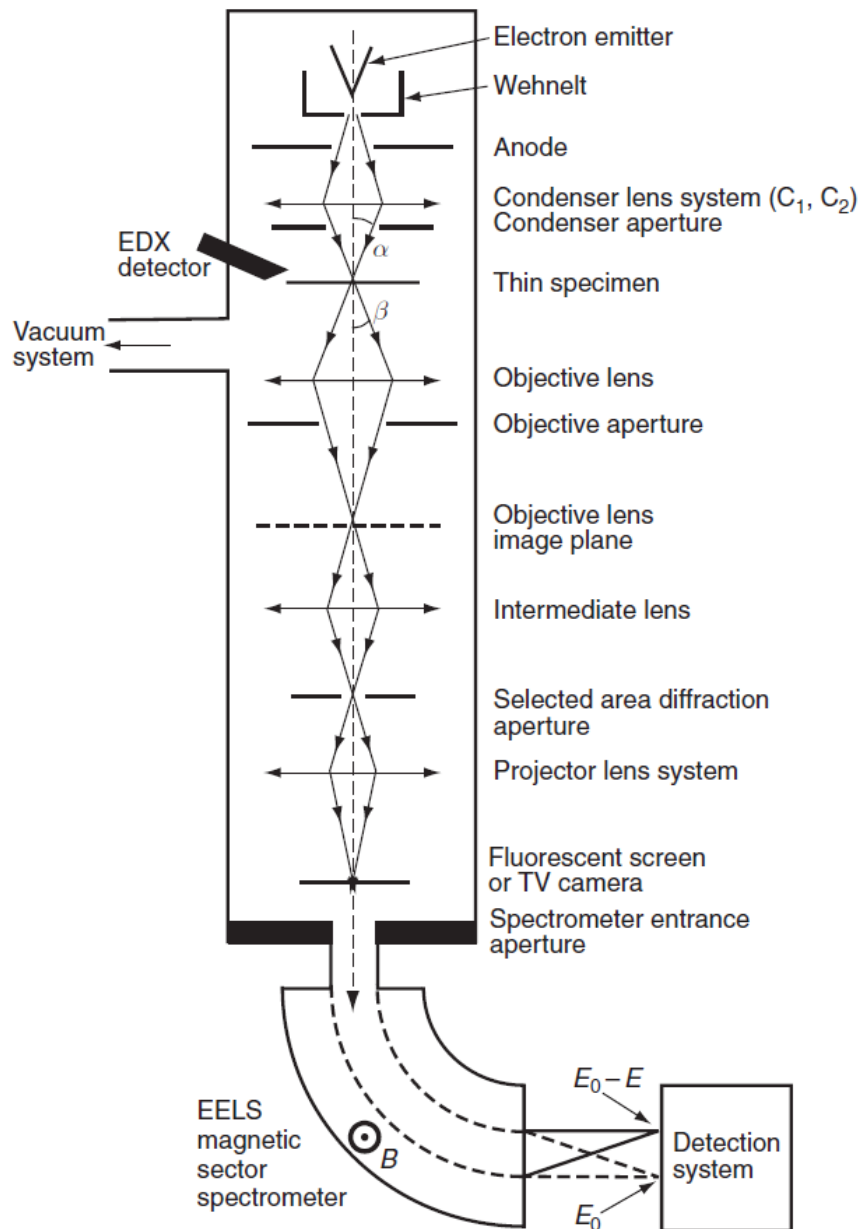


Figure 3.2 Schematic of the layout of an analytical transmission electron microscope [177].

TEM is an efficient technique to obtain images with ultra-high resolution. Therefore, this technique is indispensable in the nanomaterial analysis area. Figure 3.2 presents a schematic illustration of the basic components and layout of a TEM. On top of this equipment, electrons are generated and accelerated by a high voltage (100-400 kV). Because of this high voltage, the electron wavelength is decreased dramatically, leading to the capture of high-resolution images. Moreover, the high accelerated voltage allows electrons to easily

penetrate a relatively thick specimen. During the imaging process, the electron beam will pass through two apertures: the condenser aperture and objective aperture. The former controls the fraction of the beam that is allowed to hit the specimen and thus controls the intensity of illumination. The latter can select electrons that will contribute to the image and also control the contrast of the final image. Depending on the position of the objective aperture, a bright field image (image of the specimen structure, with the objective aperture centred on the optical axis) or a dark field image (diffraction pattern, without or with displaced objective aperture) can be obtained.

A JEOL 2100 TEM at an accelerating voltage of 200 kV was selected to characterise the detailed morphology of the samples. To investigate the morphology of individual nanoparticles, a small number of samples were first dispersed in ethanol for 1 h in an ultrasonic bath and then dropped on a carbon film grid. The grid was then dried at room temperature in air to ensure that all of the ethanol was evaporated. Finally, this grid was loaded on the sample holder for characterisation.

3.1.3 Scanning electron microscopy (SEM) and energy dispersive X-ray spectroscopy (EDS)

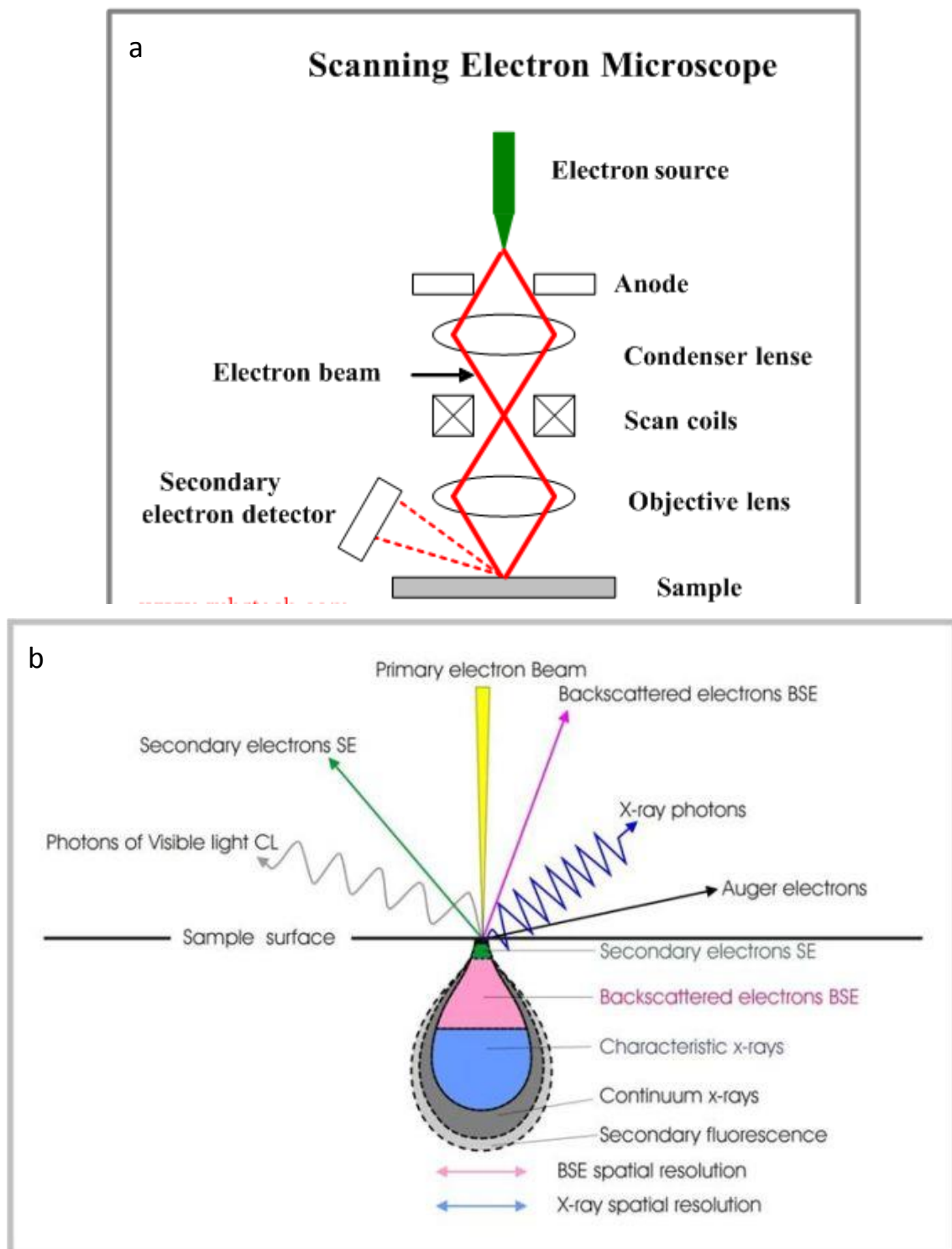


Figure 3.3 (a) Schematic of the layout of an SEM and (b) interaction between electron beam and sample [178].

SEM is a powerful tool to examine the surface and composition of a sample. In a vacuum atmosphere, an electron beam is accelerated and focused by an anode, condenser lens and objective lens and finally hits the surface of the sample (Figure 3.3a). Because of the interaction between the sample and electron beam, many beams such as secondary electrons (SEs), backscattered electrons (BSEs), photons of visible light (CL), X-ray photons and Auger electrons are immediately emitted (Figure 3.3b). By analysing the SE signal, which is generated as ionisation products, the detailed surface morphology of the sample can be determined. BSEs are beam electrons that are reflected from the sample by elastic scattering. Because the scattering intensity is closely related to the atomic numbers of the elements (heavy atoms give a strong signal), the BSE spectrum is useful in identifying the composition of a sample. To further verify the composition of a product, it is always necessary to obtain the EDS spectrum of the sample. The EDS spectrum is obtained by analysing the characteristic X-ray photons that are generated from the electronic transition of the sample. In this project, a field-emission scanning electron microscope (FESEM Inspect F, FEI at an accelerating voltage of 20 kV) was used to determine the morphology of the samples on large areas. The samples were dropped directly on carbon films, which were attached on a metal supporter. To obtain clear images, the samples were covered with a gold coating to increase their conductivity. For the EDS analysis, three scan modes (spot scan, linear scan and elemental mapping) were used for different purposes. An Oxford INCA EDX (equipped on an Inspect F at 20 kV) was employed with SEM to investigate the chemical composition of the synthesised samples.

3.1.3 Raman spectroscopy

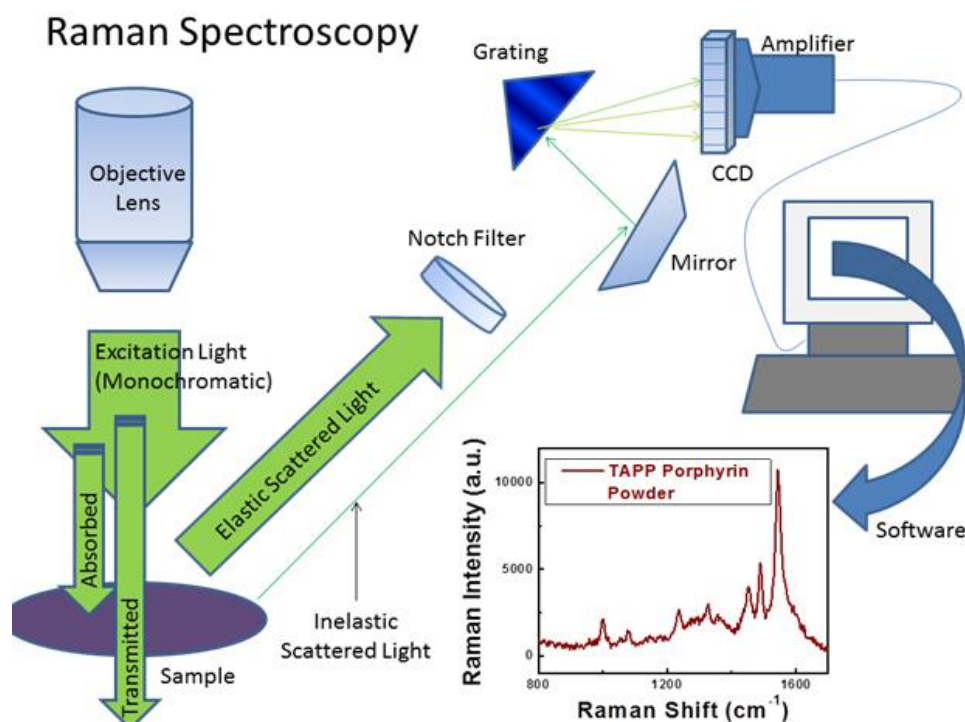


Figure 3.4 Schematic of the layout of Raman spectroscopy [179].

Raman spectroscopy is a spectroscopic technique used to analyse the chemical composition of a sample. Lasers with different ranges (visible, near infrared, or near ultraviolet) are emitted to interact with molecular vibrations, leading to the generation of up or down shifts of the energy of laser phonons (Figure 3.4). By analysing these shifts, the vibration modes of sample can be measured. A Renishaw InVia micro-Raman spectrometer with the 514.5 nm line of an Ar laser was employed to perform the Raman test. A laser power of ~20 mW was focused on a ~2- μm spot. The samples were placed on a glass plate and then interacted with the laser beam at room temperature.

3.1.4 Atomic force microscopy (AFM)

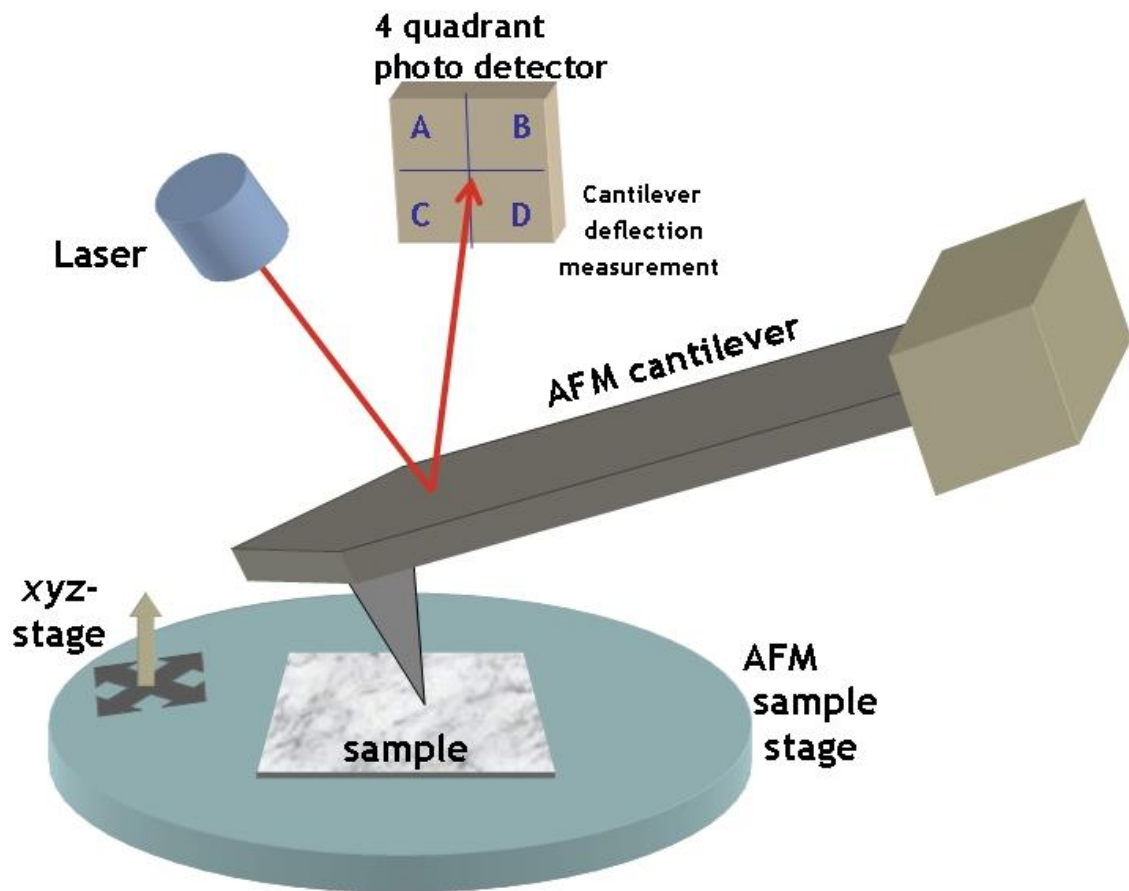


Figure 3.5 Schematic of the layout of an AFM [179].

AFM is useful in imaging the surface of a specimen using a cantilever for morphological studies (Figure 3.5). Depending on the distance between the cantilever and sample surface, two modes (contact mode and tapping mode) can be used. For contact-mode AFM, the cantilever is very close to the sample surface, and thus, a repulsive force is formed between the sample and cantilever. By measuring this force, the thickness of the sample can be calculated. For tapping-mode AFM, the cantilever is further away from the sample surface. Signals are collected from the oscillation of the cantilever at a resonant frequency to measure the sample thickness. In this project, an Agilent 5500 AFM was used to test all the samples using tapping mode.

3.1.5 Thermogravimetric analysis (TGA), differential heat flow (DTA) and mass spectroscopy (MS)

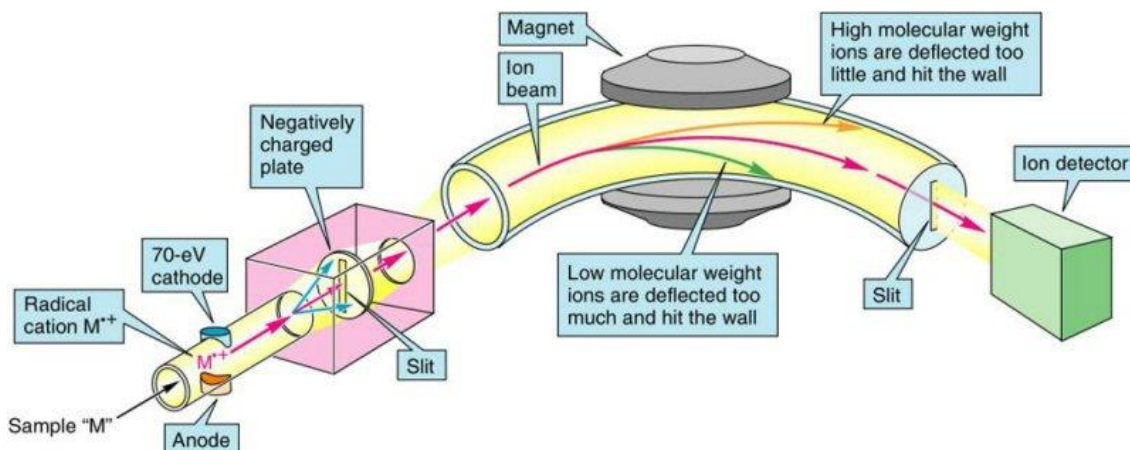


Figure 3.6 Schematic of the layout of a mass spectrometer [180].

TGA is used to investigate the phase change and reaction of a sample during heating by measuring the weight change and heat flow of the sample. During the analysis, some gases may be generated from the decomposition of the sample and/or its reaction with the atmosphere. MS is used to detect the molecular weights of the emitted gases and thus can determine their compositions (Figure 3.6). A SDT Q600 meter equipped with a Hiden HAL 201 RC mass spectrometer was used to analyse the entire reaction. For each test, approximately 20 mg samples were loaded into an alumina crucible and heated to 1000°C with a 10°C/min rate under an air or N₂ atmosphere.

3.1.6 Ultraviolet-visible (UV-vis) spectroscopy

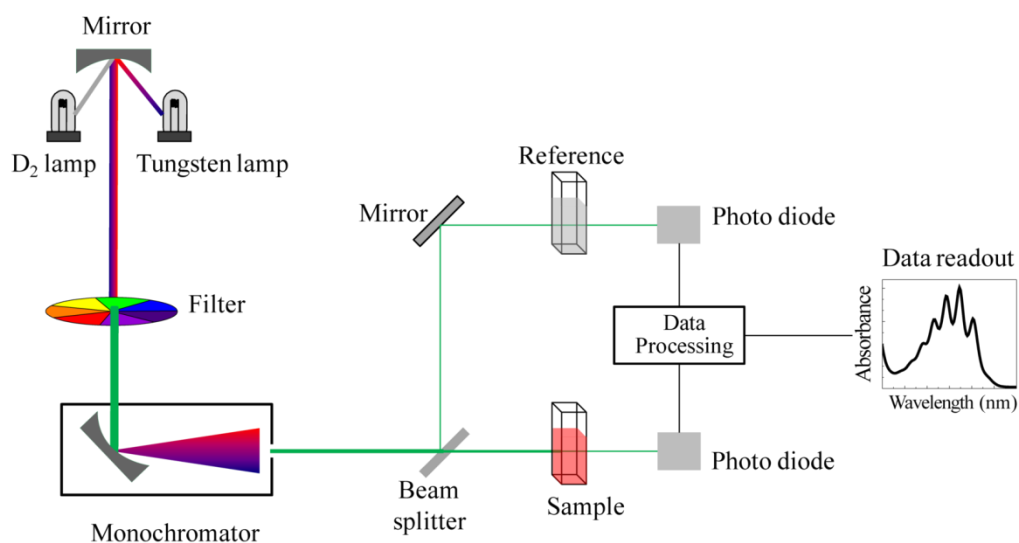


Figure 3.7 Schematic of the layout of a UV-vis spectrometer [181].

UV-vis spectroscopy is a spectroscopic technique used to analyse the chemical composition of sample using an ultraviolet-visible beam. During the measurement, the UV-visible beam is absorbed as the electronic transition energy of molecules from the ground state to the excited state (Figure 3.7). By analysing the positions of these absorption peaks, the composition can be determined. In this work, a Jenway 6715 UV/visible spectrophotometer was used to examine the UV spectra of the samples. To obtain accurate results, very small amounts of samples were dispersed by ultra-sonication in ethanol for 30 min before the test.

3.1.7 Electrochemical measurements

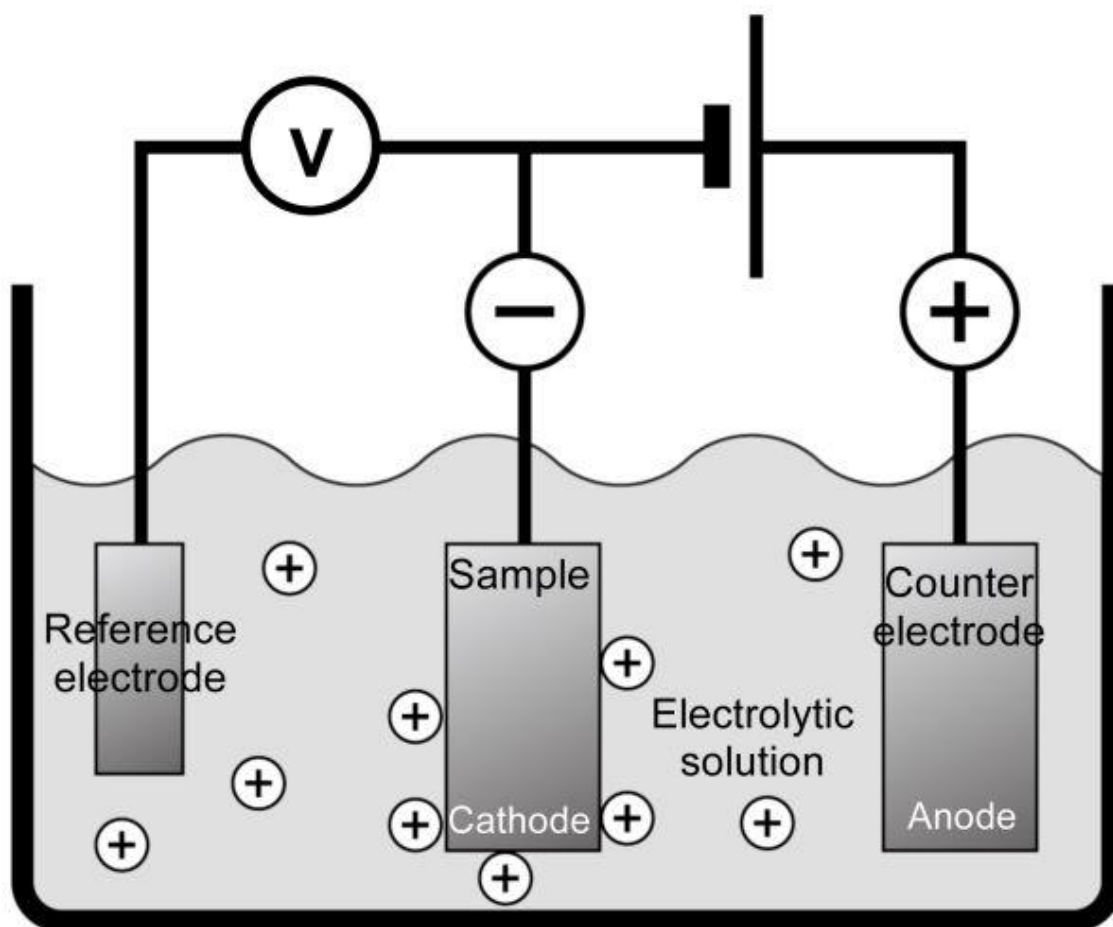


Figure 3.8 Schematic illustration of the layout of an electrochemical workstation.

An electrochemical workstation is efficient equipment to monitor and control the change of current and potential in an electrolytic cell. For HER performance analysis, a three-electrode workstation is used to test the electrochemical performance of a sample. As its name implies, the three-electrode workstation is composed of three electrodes: a working electrode (e.g., glassy carbon, Pt or Au electrode), a counter electrode (e.g., Pt or graphite electrode) and a reference electrode (Ag/AgCl, standard hydrogen electrode or saturated calomel electrode). In the three-electrode system, samples are normally placed on the surface of the working electrode, which is connected with the counter electrode to form a circuit. Because the reference electrode has a fixed potential, the potential of the working electrode can be easily tested from the voltmeter. Based on this principle, many techniques can be applied, such as cyclic voltammetry (CV), linear sweep voltammetry (LSV) and Tafel tests. In this project, LSV was used to evaluate the electrochemical performance of a sample.

Linear sweep voltammetry is a voltammetric method in which the current at a working electrode is measured while the potential between the working electrode and a reference electrode is swept linearly with time. By plotting the current-potential curves, the oxidation or reduction reactions occurring on the working electrodes can be observed as peaks, which clearly indicate the onset overpotential and current density. In this project, a CHI 602D potentiostat from CHI instruments Inc. was used to perform all the electrochemical analysis.

References

- [1] J. N. Coleman, M. Lotya, A. O'Neill, S. D. Bergin, P. J. King, U. Khan, K. Young, A. Gaucher, S. De, R. J. Smith, I. V. Shvets, S. K. Arora, G. Stanton, H. Y. Kim, K. Lee, G. T. Kim, G. S. Duesberg, T. Hallam, J. J. Boland, J. J. Wang, J. F. Donegan, J. C. Grunlan, G. Moriarty, A. Shmeliov, R. J. Nicholls, J. M. Perkins, E. M. Grievson, K. Theuwissen, D. W. McComb, P. D. Nellist, and V. Nicolosi, "Two-Dimensional Nanosheets Produced by Liquid Exfoliation of Layered Materials," *Science*, vol. 331, pp. 568-571, Feb 4 2011.
- [2] D. Voiry, H. Yamaguchi, J. W. Li, R. Silva, D. C. B. Alves, T. Fujita, M. W. Chen, T. Asefa, V. B. Shenoy, G. Eda, and M. Chhowalla, "Enhanced catalytic activity in strained chemically exfoliated WS₂ nanosheets for hydrogen evolution," *Nature materials*, vol. 12, pp. 850-855, Sep 2013.
- [3] M. A. Lukowski, A. S. Daniel, F. Meng, A. Forticaux, L. S. Li, and S. Jin, "Enhanced Hydrogen Evolution Catalysis from Chemically Exfoliated Metallic MoS₂ Nanosheets," *Journal of the American Chemical Society*, vol. 135, pp. 10274-10277, Jul 17 2013.
- [4] I. Kaplan-Ashiri and R. Tenne, "Mechanical properties of WS₂ nanotubes," *Journal of Cluster Science*, vol. 18, pp. 549-563, Sep 2007.
- [5] I. Kaplan-Ashiri, S. R. Cohen, K. Gartsman, V. Ivanovskaya, T. Heine, G. Seifert, I. Wiesel, H. D. Wagner, and R. Tenne, "On the mechanical behavior of WS₂ nanotubes under axial tension and compression," *Proceedings of the National Academy of Sciences of the United States of America*, vol. 103, pp. 523-528, Jan 17 2006.
- [6] O. Tevet, O. Goldbart, S. R. Cohen, R. Rosentsveig, R. Popovitz-Biro, H. D. Wagner, and R. Tenne, "Nanocompression of individual multilayered polyhedral nanoparticles," *Nanotechnology*, vol. 21, Sep 10 2010.
- [7] T. W. Scharf, S. V. Prasad, M. T. Dugger, P. G. Kotula, R. S. Goeke, and R. K. Grubbs, "Growth, structure, and tribological behavior of atomic layer-deposited tungsten

- disulphide solid lubricant coatings with applications to MEMS," *Acta Materialia*, vol. 54, pp. 4731-4743, Oct 2006.
- [8] V. R. Johnson and G. W. Vaughn, "Investigation of the Mechanism of MoS₂ Lubrication in Vacuum," *Journal of Applied Physics*, vol. 27, pp. 1173-1179, 1956.
- [9] M. T. Lavik, T. B. Daniel, and A. N. Abbott, "Friction of Molybdenum Diselenide," *Journal of Applied Physics*, vol. 32, p. 1795, 1961.
- [10] V. R. Johnson, M. T. Lavik, and G. W. Vaughn, "Mechanism of WS₂ Lubrication in Vacuum," *Journal of Applied Physics*, vol. 28, p. 821, 1957.
- [11] H. B. Yang, S. K. Liu, J. X. Lil, M. H. Li, G. Peng, and G. T. Zou, "Synthesis of inorganic fullerene-like WS₂ nanoparticles and their lubricating performance," *Nanotechnology*, vol. 17, pp. 1512-1519, Mar 14 2006.
- [12] H. Wu, R. Yang, B. Song, Q. Han, J. Li, Y. Zhang, Y. Fang, R. Tenne, and C. Wang, "Biocompatible inorganic fullerene-like molybdenum disulfide nanoparticles produced by pulsed laser ablation in water," *Acs Nano*, vol. 5, pp. 1276-81, Feb 22 2011.
- [13] L. Rapoport, O. Nepomnyashchy, I. Lapsker, A. Verdyan, A. Moshkovich, Y. Feldman, and R. Tenne, "Behavior of fullerene-like WS₂ nanoparticles under severe contact conditions," *Wear*, vol. 259, pp. 703-707, Jul-Aug 2005.
- [14] Y. Feldman, A. Zak, R. Popovitz-Biro, and R. Tenne, "New reactor for production of tungsten disulfide hollow onion-like (inorganic fullerene-like) nanoparticles," *Solid State Sciences*, vol. 2, pp. 663-672, Oct 2000.
- [15] M. Remskar and A. Mrzel, "High-temperature fibres composed of transition metal inorganic nanotubes," *Current Opinion in Solid State & Materials Science*, vol. 8, pp. 121-125, Mar 2004.
- [16] R. Tenne, L. Margulis, M. Genut, and G. Hodes, "Polyhedral and Cylindrical Structures of Tungsten Disulfide," *Nature*, vol. 360, pp. 444-446, Dec 3 1992.
- [17] R. Tenne, M. Homyonfer, and Y. Feldman, "Nanoparticles of layered compounds with hollow cage structures (inorganic fullerene-like structures)," *Chemistry of Materials*, vol. 10, pp. 3225-3238, Nov 1998.
- [18] A. Carnacho and M. J. Yacaman, "Structure and catalytic properties of molybdenum sulfide nanoplatelets," *Applied Catalysis a-General*, vol. 328, pp. 88-97, Aug 31 2007.
- [19] C. F. Castro-Guerrero, F. L. Deepak, A. Ponce, J. Cruz-Reyes, M. Del Valle-Granados, S. Fuentes-Moyado, D. H. Galvan, and M. Jose-Yacaman, "Structure and catalytic properties of hexagonal molybdenum disulfide nanoplates," *Catalysis Science & Technology*, vol. 1, pp. 1024-1031, 2011.
- [20] R. Tenne, "Inorganic nanotubes and fullerene-like nanoparticles," *Journal of Materials Research*, vol. 21, pp. 2726-2743, Nov 2006.

- [21] S. Iijima, "Helical Microtubules of Graphitic Carbon," *Nature*, vol. 354, pp. 56-58, Nov 7 1991.
- [22] Y. Feldman, E. Wasserman, D. J. Srolovitz, and R. Tenne, "High-Rate, Gas-Phase Growth of MoS₂ Nested Inorganic Fullerenes and Nanotubes," *Science*, vol. 267, pp. 222-225, Jan 13 1995.
- [23] J. Chen, N. Kuriyama, H. Yuan, H. T. Takeshita, and T. Sakai, "Electrochemical hydrogen storage in MoS₂ nanotubes," *Journal of the American Chemical Society*, vol. 123, pp. 11813-4, Nov 28 2001.
- [24] J. Chen, S. L. Li, and Z. L. Tao, "Novel hydrogen storage properties of MoS₂ nanotubes," *Journal of Alloys and Compounds*, vol. 356, pp. 413-417, Aug 11 2003.
- [25] A. Berkdemir, H. R. Gutierrez, A. R. Botello-Mendez, N. Perea-Lopez, A. L. Elias, C. I. Chia, B. Wang, V. H. Crespi, F. Lopez-Urias, J. C. Charlier, H. Terrones, and M. Terrones, "Identification of individual and few layers of WS₂ using Raman Spectroscopy," *Scientific Reports*, vol. 3, Apr 30 2013.
- [26] A. K. Geim and K. S. Novoselov, "The rise of graphene," *Nature materials*, vol. 6, pp. 183-91, Mar 2007.
- [27] H. S. S. R. Matte, A. Gomathi, A. K. Manna, D. J. Late, R. Datta, S. K. Pati, and C. N. R. Rao, "MoS₂ and WS₂ Analogues of Graphene," *Angewandte Chemie-International Edition*, vol. 49, pp. 4059-4062, 2010.
- [28] C. Burda, X. B. Chen, R. Narayanan, and M. A. El-Sayed, "Chemistry and properties of nanocrystals of different shapes," *Chemical Reviews*, vol. 105, pp. 1025-1102, Apr 2005.
- [29] E. C. Scher, L. Manna, and A. P. Alivisatos, "Shape control and applications of nanocrystals," *Philosophical Transactions of the Royal Society of London Series a-Mathematical Physical and Engineering Sciences*, vol. 361, pp. 241-255, Feb 15 2003.
- [30] G. Kickelbick and U. Schubert, "Organic functionalization of metal oxide nanoparticles," *ChemInform*, vol. 35, 2004.
- [31] B. Pukánszky and E. Fekete, "Adhesion and Surface Modification," in *Mineral Fillers in Thermoplastics I*. vol. 139, J. Jancar, E. Fekete, P. R. Hornsby, J. Jancar, B. Pukánszky, and R. N. Rethon, Eds., ed: Springer Berlin Heidelberg, 1999, pp. 109-153.
- [32] S. G. Grancharov, H. Zeng, S. H. Sun, S. X. Wang, S. O'Brien, C. B. Murray, J. R. Kirtley, and G. A. Held, "Bio-functionalization of monodisperse magnetic nanoparticles and their use as biomolecular labels in a magnetic tunnel junction based sensor," *Journal of Physical Chemistry B*, vol. 109, pp. 13030-13035, Jul 7 2005.
- [33] V. Salgueirino-Maceira and M. A. Correa-Duarte, "Increasing the complexity of magnetic core/shell structured nanocomposites for biological applications," *Advanced Materials*, vol. 19, pp. 4131-4144, Dec 3 2007.

- [34] D. Chen, L. L. Li, F. Q. Tang, and S. O. Qi, "Facile and Scalable Synthesis of Tailored Silica "Nanorattle" Structures," *Advanced Materials*, vol. 21, pp. 3804-3807, Oct 5 2009.
- [35] C. Schuffenhauer, G. Wildermuth, J. Felsche, and R. Tenne, "How stable are inorganic fullerene-like particles? Thermal analysis (STA) of inorganic fullerene-like NbS₂, MoS₂, and WS₂ in oxidizing and inert atmospheres in comparison with the bulk material," *Physical Chemistry Chemical Physics*, vol. 6, pp. 3991-4002, 2004.
- [36] V. Stolojan, S. R. P. Silva, M. J. Goringe, R. L. D. Whitby, W. K. Hsu, D. R. M. Walton, and H. W. Kroto, "Dielectric properties of WS₂-coated multiwalled carbon nanotubes studied by energy-loss spectroscopic profiling," *Applied Physics Letters*, vol. 86, Feb 7 2005.
- [37] P. A. Parilla, A. C. Dillon, K. M. Jones, G. Riker, D. L. Schulz, D. S. Ginley, and M. J. Heben, "The first true inorganic fullerenes?," *Nature*, vol. 397, pp. 114-114, 1999.
- [38] H. W. Kroto, J. R. Heath, S. C. O'Brien, R. F. Curl, and R. E. Smalley, "C-60 - Buckminsterfullerene," *Nature*, vol. 318, pp. 162-163, 1985.
- [39] P. A. Parilla, A. C. Dillon, B. A. Parkinson, K. M. Jones, J. Alleman, G. Riker, D. S. Ginley, and M. J. Heben, "Formation of nanooctahedra in molybdenum disulfide and molybdenum diselenide using pulsed laser vaporization," *Journal of Physical Chemistry B*, vol. 108, pp. 6197-6207, May 20 2004.
- [40] S. Y. Hong, R. Popovitz-Biro, Y. Prior, and R. Tenne, "Synthesis of SnS₂/SnS fullerene-like nanoparticles: A superlattice with polyhedral shape," *Journal of the American Chemical Society*, vol. 125, pp. 10470-10474, Aug 27 2003.
- [41] C. Schuffenhauer, B. A. Parkinson, N. Y. Jin-Phillipp, L. Joly-Pottuz, J. M. Martin, R. Popovitz-Biro, and R. Tenne, "Synthesis of fullerene-like tantalum disulfide nanoparticles by a gas-phase reaction and laser ablation," *Small*, vol. 1, pp. 1100-1109, Nov 2005.
- [42] R. Sen, A. Govindaraj, K. Suenaga, S. Suzuki, H. Kataura, S. Iijima, and Y. Achiba, "Encapsulated and hollow closed-cage structures of WS₂ and MoS₂ prepared by laser ablation at 450-1050 degrees C," *Chemical Physics Letters*, vol. 340, pp. 242-248, Jun 1 2001.
- [43] M. Nath, C. N. R. Rao, R. Popovitz-Biro, A. Albu-Yaron, and R. Tenne, "Nanoparticles produced by laser ablation of HfS₃ in liquid medium: Inorganic fullerene-like structures of Hf₂S," *Chemistry of Materials*, vol. 16, pp. 2238-2243, Jun 1 2004.
- [44] N. Sano, H. L. Wang, M. Chhowalla, I. Alexandrou, G. A. J. Amaratunga, M. Naito, and T. Kanki, "Fabrication of inorganic molybdenum disulfide fullerenes by arc in water," *Chemical Physics Letters*, vol. 368, pp. 331-337, Jan 17 2003.

- [45] J. J. Hu, J. S. Zabinski, J. H. Sanders, J. E. Bultman, and A. A. Voevodin, "Pulsed laser syntheses of layer-structured WS₂ nanomaterials in water," *Journal of Physical Chemistry B*, vol. 110, pp. 8914-8916, May 11 2006.
- [46] J. J. Hu, J. E. Bultman, and J. S. Zabinski, "Inorganic fullerene-like nanoparticles produced by arc discharge in water with potential lubricating ability," *Tribology Letters*, vol. 17, pp. 543-546, Oct 2004.
- [47] M. JoseYacaman, H. Lopez, P. Santiago, D. H. Galvan, I. L. Garzon, and A. Reyes, "Studies of MoS₂ structures produced by electron irradiation," *Applied Physics Letters*, vol. 69, pp. 1065-1067, Aug 19 1996.
- [48] J. M. Gordon, E. A. Katz, D. Feuermann, A. Albu-Yaron, M. Levy, and R. Tenne, "Singular MoS₂, SiO₂ and Si nanostructures-synthesis by solar ablation," *Journal of Materials Chemistry*, vol. 18, pp. 458-462, 2008.
- [49] O. Brontvein, D. G. Stroppa, R. Popovitz-Biro, A. Albu-Yaron, M. Levy, D. Feuerman, L. Houben, R. Tenne, and J. M. Gordon, "New High-Temperature Pb-Catalyzed Synthesis of Inorganic Nanotubes," *Journal of the American Chemical Society*, vol. 134, pp. 16379-16386, Oct 3 2012.
- [50] Y. Oguri, R. E. Riman, and H. K. Bowen, "Processing of Anatase Prepared from Hydrothermally Treated Alkoxy-Derived Hydrous Titania," *Journal of Materials Science*, vol. 23, pp. 2897-2904, Aug 1988.
- [51] A. A. Burukhin, B. R. Churagulov, and N. N. Oleynikov, "Characterization of ultrafine zirconia and iron oxide powders prepared under hydrothermal conditions," *High Pressure Research*, vol. 20, pp. 255-264, 2001.
- [52] X. F. Qian, X. M. Zhang, C. Wang, K. B. Tang, Y. Xie, and Y. T. Qian, "Benzene-thermal preparation of nanocrystalline chromium nitride," *Materials Research Bulletin*, vol. 34, pp. 433-436, Feb 1999.
- [53] Y. Xie, Y. T. Qian, W. Z. Wang, S. Y. Zhang, and Y. H. Zhang, "A benzene-thermal synthetic route to nanocrystalline GaN," *Science*, vol. 272, pp. 1926-1927, Jun 28 1996.
- [54] Q. Peng, Y. J. Dong, Z. X. Deng, X. M. Sun, and Y. D. Li, "Low-temperature elemental-direct-reaction route to II-VI semiconductor nanocrystalline ZnSe and CdSe," *Inorganic Chemistry*, vol. 40, pp. 3840-+, Jul 30 2001.
- [55] Y. D. Li, Y. Ding, Y. T. Qian, Y. Zhang, and L. Yang, "A solvothermal elemental reaction to produce nanocrystalline ZnSe," *Inorganic Chemistry*, vol. 37, pp. 2844-2845, Jun 15 1998.
- [56] J. Yang, G. H. Cheng, J. H. Zeng, S. H. Yu, X. M. Liu, and Y. T. Qian, "Shape control and characterization of transition metal diselenides MSe₂ (M = Ni, Co, Fe) prepared by a

- solvothermal-reduction process," *Chemistry of Materials*, vol. 13, pp. 848-853, Mar 2001.
- [57] X. H. Chen and R. Fan, "Low-temperature hydrothermal synthesis of transition metal dichalcogenides," *Chemistry of Materials*, vol. 13, pp. 802-805, Mar 2001.
- [58] J. T. Jang, S. Jeong, J. W. Seo, M. C. Kim, E. Sim, Y. Oh, S. Nam, B. Park, and J. Cheon, "Ultrathin Zirconium Disulfide Nanodiscs," *Journal of the American Chemical Society*, vol. 133, pp. 7636-7639, May 25 2011.
- [59] R. H. Wei, H. B. Yang, K. Du, W. Y. Fu, Y. M. Tian, Q. J. Yu, S. Liu, M. H. Li, and G. I. Zou, "A facile method to prepare MoS₂ with nanoflower-like morphology," *Materials Chemistry and Physics*, vol. 108, pp. 188-191, Apr 15 2008.
- [60] X. D. Shan, L. P. You, J. M. Zhang, X. Z. Zhang, J. F. Wu, X. Fu, D. P. Yu, and H. Q. Ye, "A New Type of 2H-WS₂ Particle with Discrete-Formed Plate-Texture Structure," *Crystal Growth & Design*, vol. 8, pp. 4420-4423, Dec 2008.
- [61] W. J. Li, E. W. Shi, J. M. Ko, Z. Z. Chen, H. Ogino, and T. Fukuda, "Hydrothermal synthesis of MoS₂ nanowires," *Journal of Crystal Growth*, vol. 250, pp. 418-422, Apr 2003.
- [62] Y. Tian, Y. He, and Y. F. Zhu, "Low temperature synthesis and characterization of molybdenum disulfide nanotubes and nanorods," *Materials Chemistry and Physics*, vol. 87, pp. 87-90, Sep 15 2004.
- [63] Y. Y. Peng, Z. Y. Meng, C. Zhong, J. Lu, W. C. Yu, Z. P. Yang, and Y. T. Qian, "Hydrothermal synthesis of MoS₂ and its pressure-related crystallization," *Journal of Solid State Chemistry*, vol. 159, pp. 170-173, Jun 2001.
- [64] H. T. Lin, X. Y. Chen, H. L. Li, M. Yang, and Y. X. Qi, "Hydrothermal synthesis and characterization of MoS₂ nanorods," *Materials Letters*, vol. 64, pp. 1748-1750, Aug 15 2010.
- [65] X. L. Li and Y. D. Li, "MoS₂ nanostructures: Synthesis and electrochemical Mg²⁺ intercalation," *Journal of Physical Chemistry B*, vol. 108, pp. 13893-13900, Sep 16 2004.
- [66] K. Du, W. Y. Fu, R. H. Wei, H. B. Yang, S. K. Liu, S. D. Yu, and G. T. Zou, "Synthesis of inorganic fullerene-like MoS₂ nanoparticles by a facile method," *Materials Letters*, vol. 61, pp. 4887-4889, Nov 2007.
- [67] L. X. Chang, H. B. Yang, W. Y. Fu, J. Z. Zhang, Q. J. Yu, H. Y. Zhu, J. J. Chen, R. H. Wei, Y. M. Sui, X. F. Pang, and G. T. Zou, "Simple synthesis of MoS₂ inorganic fullerene-like nanomaterials from MoS₂ amorphous nanoparticles," *Materials Research Bulletin*, vol. 43, pp. 2427-2433, Aug-Sep 2008.

- [68] P. K. Panigrahi and A. Pathak, "A novel route for the synthesis of nanotubes and fullerene-like nanostructures of molybdenum disulfide," *Materials Research Bulletin*, vol. 46, pp. 2240-2246, Dec 2011.
- [69] M. Genut, L. Margulis, G. Hodes, and R. Tenne, "Preparation and Microstructure of WS₂ Thin-Films," *Thin Solid Films*, vol. 217, pp. 91-97, Sep 30 1992.
- [70] S. B. Sadale and P. S. Patil, "Synthesis of type-I textured tungsten disulfide thin films on quartz substrate," *Journal of Crystal Growth*, vol. 286, pp. 481-486, Jan 15 2006.
- [71] Y. L. Zhang, X. C. Wu, Y. R. Tao, C. J. Mao, and J. J. Zhu, "Fabrication and field-emission performance of zirconium disulfide nanobelt arrays," *Chemical Communications*, pp. 2683-2685, 2008.
- [72] L. Li, X. S. Fang, T. Y. Zhai, M. Y. Liao, U. K. Gautam, X. C. Wu, Y. Koide, Y. Bando, and D. Golberg, "Electrical Transport and High-Performance Photoconductivity in Individual ZrS₂ Nanobelts," *Advanced Materials*, vol. 22, pp. 4151-+, Oct 1 2010.
- [73] V. An, F. Bozheyev, F. Richecoeur, and Y. Irtegov, "Synthesis and characterization of nanolamellar tungsten and molybdenum disulfides," *Materials Letters*, vol. 65, pp. 2381-2383, Aug 2011.
- [74] V. G. Pol, S. V. Pol, and A. Gedanken, "Micro to nano conversion: A One-Step, environmentally friendly, solid state, bulk fabrication of WS₂ and MoS₂ nanoplates," *Crystal Growth & Design*, vol. 8, pp. 1126-1132, Apr 2008.
- [75] Z. Z. Wu, D. Z. Wang, X. Q. Zan, and A. K. Sun, "Synthesis of WS₂ nanosheets by a novel mechanical activation method," *Materials Letters*, vol. 64, pp. 856-858, Apr 15 2010.
- [76] Z. Z. Wu, D. Z. Wang, and A. K. Sun, "Preparation of MoS₂ nanoflakes by a novel mechanical activation method," *Journal of Crystal Growth*, vol. 312, pp. 340-343, Jan 1 2010.
- [77] P. G. Li, M. Lei, X. F. Wang, H. L. Tang, and W. H. Tang, "Thermal conversion of tungsten oxide nanorods to tungsten disulfide nanoflakes," *Journal of Alloys and Compounds*, vol. 474, pp. 463-467, Apr 17 2009.
- [78] B. T. Kaminskii, G. N. Prokof'eva, A. S. Plygunov, and P. A. Galitskii, "Manufacture of zirconium and hafnium sulfide powders," *Soviet Powder Metallurgy and Metal Ceramics*, vol. 12, pp. 521-524, 1973/07/01 1973.
- [79] A. Clearfield, "The Synthesis and Properties of Zirconium Disulfide," *Journal of the American Chemical Society*, vol. 80, pp. 6511-6513, 1958.
- [80] Y. H. Lee, X. Q. Zhang, W. J. Zhang, M. T. Chang, C. T. Lin, K. D. Chang, Y. C. Yu, J. T. W. Wang, C. S. Chang, L. J. Li, and T. W. Lin, "Synthesis of Large-Area MoS₂ Atomic Layers with Chemical Vapor Deposition," *Advanced Materials*, vol. 24, pp. 2320-2325, May 2 2012.

- [81] S. B. Sun, Z. J. Li, and X. T. Chang, "Synthesis and structural characterization of tungsten disulfide nanomaterials," *Materials Letters*, vol. 65, pp. 3164-3166, Oct 2011.
- [82] G. M. Cai, J. K. Jian, X. L. Chen, M. Lei, and W. Y. Wang, "Regular hexagonal MoS₂ microflakes grown from MoO₃ precursor," *Applied Physics a-Materials Science & Processing*, vol. 89, pp. 783-788, Nov 2007.
- [83] Y. Feldman, G. L. Frey, M. Homyonfer, V. Lyakhovitskaya, L. Margulis, H. Cohen, G. Hodes, J. L. Hutchison, and R. Tenne, "Bulk synthesis of inorganic fullerene-like MS(2) (M=Mo, W) from the respective trioxides and the reaction mechanism," *Journal of the American Chemical Society*, vol. 118, pp. 5362-5367, Jun 12 1996.
- [84] R. Rosentsveig, A. Margolin, A. Gorodnev, R. Popovitz-Biro, Y. Feldman, L. Rapoport, Y. Novema, G. Naveh, and R. Tenne, "Synthesis of fullerene-like MoS₂ nanoparticles and their tribological behavior," *Journal of Materials Chemistry*, vol. 19, pp. 4368-4374, 2009.
- [85] K. S. Coleman, J. Sloan, N. A. Hanson, G. Brown, G. P. Clancy, M. Terrones, H. Terrones, and M. L. H. Green, "The formation of ReS₂ inorganic fullerene-like structures containing Re-4 parallelogram units and metal-metal bonds," *Journal of the American Chemical Society*, vol. 124, pp. 11580-11581, Oct 2 2002.
- [86] D. W. Shin, D. H. Yoon, and S. J. Kim, "Synthesis of tungsten disulfide solid lubricant by solid-gas reactions," *Journal of Materials Science Letters*, vol. 17, pp. 1731-1734, Oct 15 1998.
- [87] M. Tehrani, C. C. Luhrs, M. S. Al-Haik, J. Trevino, and H. Zea, "Synthesis of WS₂ nanostructures from the reaction of WO₃ with CS₂ and mechanical characterization of WS₂ nanotube composites," *Nanotechnology*, vol. 22, Jul 15 2011.
- [88] S. B. Sun, Z. D. Zou, and G. H. Min, "Synthesis of tungsten disulfide nanotubes from different precursor," *Materials Chemistry and Physics*, vol. 114, pp. 884-888, Apr 15 2009.
- [89] A. Margolin, R. Rosentsveig, A. Albu-Yaron, R. Popovitz-Biro, and R. Tenne, "Study of the growth mechanism of WS₂ nanotubes produced by a fluidized bed reactor," *Journal of Materials Chemistry*, vol. 14, pp. 617-624, Feb 21 2004.
- [90] A. Rothschild, J. Sloan, and R. Tenne, "Growth of WS₂ nanotubes phases," *Journal of the American Chemical Society*, vol. 122, pp. 5169-5179, May 31 2000.
- [91] H. A. Therese, J. X. Li, U. Kolb, and W. Tremel, "Facile large scale synthesis of WS₂ nanotubes from WO₃ nanorods prepared by a hydrothermal route," *Solid State Sciences*, vol. 7, pp. 67-72, Jan 2005.
- [92] X. L. Li and Y. D. Li, "Formation MoS₂ inorganic fullerenes (IFs) by the reaction of MoO₃ nanobelts and S," *Chemistry-a European Journal*, vol. 9, pp. 2726-2731, Jun 16 2003.

- [93] I. Wiesel, H. Arbel, A. Albu-Yaron, R. Popovitz-Biro, J. M. Gordon, D. Feuermann, and R. Tenne, "Synthesis of WS₂ and MoS₂ Fullerene-Like Nanoparticles from Solid Precursors," *Nano Research*, vol. 2, pp. 416-424, May 2009.
- [94] L. X. Chang, H. B. Yang, W. Y. Fu, N. Yang, J. J. Chen, M. H. Li, G. T. Zou, and J. X. Li, "Synthesis and thermal stability of W/WS₂ inorganic fullerene-like nanoparticles with core-shell structure," *Materials Research Bulletin*, vol. 41, pp. 1242-1248, Jul 13 2006.
- [95] L. X. Chang, H. B. Yang, J. X. Li, W. Y. Fu, Y. H. Du, K. Du, Q. J. Yu, J. Xu, and M. H. Li, "Simple synthesis and characteristics of Mo/MoS₂ inorganic fullerene-like and actinomorphic nanospheres with core-shell structure," *Nanotechnology*, vol. 17, pp. 3827-3831, Aug 14 2006.
- [96] P. A. Hu, Y. Q. Liu, L. Fu, L. C. Cao, and D. B. Zhu, "GaS multi-walled nanotubes from the lamellar precursor," *Applied Physics a-Materials Science & Processing*, vol. 80, pp. 1413-1417, Apr 2005.
- [97] A. Muller, R. Menge, and T. P. Prasad, "Thermal-Decomposition of (Nh₄)₂mos₄ and (Nh₄)₂ws₄ Heat of Formation of (Nh₄)₂mos₄," *Zeitschrift Fur Anorganische Und Allgemeine Chemie*, vol. 391, pp. 107-&, 1972.
- [98] J. L. Brito, M. Ilija, and P. Hernandez, "Thermal and Reductive Decomposition of Ammonium Thiomolybdates," *Thermochimica Acta*, vol. 256, pp. 325-338, Jun 1 1995.
- [99] H. W. Wang, P. Skeldon, G. E. Thompson, and G. C. Wood, "Synthesis and characterization of molybdenum disulphide formed from ammonium tetrathiomolybdate," *Journal of Materials Science*, vol. 32, pp. 497-502, Jan 15 1997.
- [100] A. Leist, S. Stauf, S. Loken, E. W. Finckh, S. Ludtke, K. K. Unger, W. Assenmacher, W. Mader, and W. Tremel, "Semiporous MoS₂ obtained by the decomposition of thiomolybdate precursors," *Journal of Materials Chemistry*, vol. 8, pp. 241-244, Jan 1998.
- [101] C. M. Zelenski and P. K. Dorhout, "Template synthesis of near-monodisperse microscale nanofibers and nanotubules of MoS₂," *Journal of the American Chemical Society*, vol. 120, pp. 734-742, Feb 4 1998.
- [102] J. Chen, S. L. Li, F. Gao, and Z. L. Tao, "Synthesis and characterization of WS₂ nanotubes," *Chemistry of Materials*, vol. 15, pp. 1012-1019, Feb 25 2003.
- [103] M. Nath, A. Govindaraj, and C. N. R. Rao, "Simple synthesis of MoS₂ and WS₂ nanotubes," *Advanced Materials*, vol. 13, pp. 283-+, Feb 19 2001.
- [104] J. Chen, S. L. Li, F. Gao, Q. Xu, and K. Tanaka, "Low-temperature catalytic preparation of multi-wall MoS₂ nanotubes," *Science in China Series B-Chemistry*, vol. 46, pp. 191-195, Apr 2003.

- [105] S. Bastide, D. Duphil, J. P. Borra, and C. Levy-Clement, "WS₂ closed nanoboxes synthesized by spray pyrolysis," *Advanced Materials*, vol. 18, pp. 106-109, Jan 5 2006.
- [106] G. L. Yin, P. H. Huang, Z. Yu, D. N. He, Z. Z. Xia, L. L. Zhang, and J. P. Tu, "Spray drying process to synthesize multiple fullerene-like MoS₂ particles," *Materials Letters*, vol. 61, pp. 1303-1306, Mar 2007.
- [107] M. Nath and C. N. R. Rao, "New metal disulfide nanotubes," *Journal of the American Chemical Society*, vol. 123, pp. 4841-4842, May 23 2001.
- [108] T. T. Yang, X. Feng, Q. L. Tang, W. W. Yang, J. H. Fang, G. L. Wang, W. Shi, L. Y. Shi, and P. Ding, "A facile method to prepare MoS₂ with nanolamellar-like morphology," *Journal of Alloys and Compounds*, vol. 509, pp. L236-L238, Jun 16 2011.
- [109] P. Afanasiev, G. F. Xia, G. Berhault, B. Jouguet, and M. Lacroix, "Surfactant-assisted synthesis of highly dispersed molybdenum sulfide," *Chemistry of Materials*, vol. 11, pp. 3216-3219, Nov 1999.
- [110] X. C. Song, Y. Zhao, Y. F. Zheng, and E. Yang, "Large-scale synthesis of MoS₂ bucky onions," *Advanced Engineering Materials*, vol. 9, pp. 96-98, Jan 2007.
- [111] Z. Z. Wu, D. Z. Wang, and A. K. Sun, "Surfactant-assisted fabrication of MoS(2) nanospheres," *Journal of Materials Science*, vol. 45, pp. 182-187, Jan 2010.
- [112] S. M. Ghoreishi, S. S. Meshkat, and A. A. Dadkhah, "IF-WS₂ nanoparticles size design and synthesis via chemical reduction," *Materials Research Bulletin*, vol. 45, pp. 584-588, May 2010.
- [113] X. L. Li, J. P. Ge, and Y. D. Li, "Atmospheric pressure chemical vapor deposition: An alternative route to large-scale MoS₂ and WS₂ inorganic fullerene-like nanostructures and nanoflowers," *Chemistry-a European Journal*, vol. 10, pp. 6163-6171, Dec 3 2004.
- [114] A. Margolin, F. L. Deepak, R. Popovitz-Biro, M. Bar-Sadan, Y. Feldman, and R. Tenne, "Fullerene-like WS(2) nanoparticles and nanotubes by the vapor-phase synthesis of WCl(n) and H(2)S," *Nanotechnology*, vol. 19, Mar 5 2008.
- [115] F. L. DEEPAK, A. MARGOLIN, I. WIESEL, M. BAR-SADAN, R. POPOVITZ-BIRO, and R. TENNE, "MoS₂ FULLERENE-LIKE NANOPARTICLES AND NANOTUBES USING GAS-PHASE REACTION WITH MoCl₅," *Nano*, vol. 01, pp. 167-180, 2006.
- [116] A. Margolin, R. Popovitz-Biro, A. Albu-Yaron, L. Rapoport, and R. Tenne, "Inorganic fullerene-like nanoparticles of TiS₂," *Chemical Physics Letters*, vol. 411, pp. 162-166, Aug 5 2005.
- [117] C. Schuffenhauer, R. Popovitz-Biro, and R. Tenne, "Synthesis of NbS₂ nanoparticles with (nested) fullerene-like structure (IF)," *Journal of Materials Chemistry*, vol. 12, pp. 1587-1591, 2002.

- [118] F. L. Deepak, H. Cohen, S. Cohen, Y. Feldman, R. Popovitz-Biro, D. Azulay, O. Millo, and R. Tenne, "Fullerene-like (IF) Nb_xMo_{1-x}S₂ nanoparticles," *Journal of the American Chemical Society*, vol. 129, pp. 12549-12562, Oct 17 2007.
- [119] J. W. Chung, Z. R. Dai, and F. S. Ohuchi, "WS₂ thin films by metal organic chemical vapor deposition," *Journal of Crystal Growth*, vol. 186, pp. 137-150, Mar 1998.
- [120] V. G. Pol, S. V. Pol, P. P. George, and A. Gedanken, "Combining MoS₂ or MoSe₂ nanoflakes with carbon by reacting Mo(CO)₆ with S or Se under their autogenic pressure at elevated temperature," *Journal of Materials Science*, vol. 43, pp. 1966-1973, Mar 2008.
- [121] D. Vollath and D. V. Szabo, "Synthesis of nanocrystalline MoS₂ and WS₂ in a microwave plasma," *Materials Letters*, vol. 35, pp. 236-244, May 1998.
- [122] D. Vollath and D. V. Szabo, "Nanoparticles from compounds with layered structures," *Acta Materialia*, vol. 48, pp. 953-967, Feb 25 2000.
- [123] J. Etzkorn, H. A. Therese, F. Rocker, N. Zink, U. Kolb, and W. Tremel, "Metal-organic chemical vapor deposition synthesis of hollow inorganic-fullerene-type MoS₂ and MoSe₂ nanoparticles," *Advanced Materials*, vol. 17, pp. 2372-+, Oct 4 2005.
- [124] N. Zink, H. A. Therese, J. Pansiot, A. Yella, F. Banhart, and W. Tremel, "In situ heating TEM study of onion-like WS₂ and MoS₂ nanostructures obtained via MOCVD," *Chemistry of Materials*, vol. 20, pp. 65-71, Jan 8 2008.
- [125] N. Zink, J. Pansiot, J. Kieffer, H. A. Therese, M. Panthofer, F. Rocker, U. Kolb, and W. Tremel, "Selective synthesis of hollow and filled fullerene-like (IF) WS₂ nanoparticles via metal-organic chemical vapor deposition," *Chemistry of Materials*, vol. 19, pp. 6391-6400, Dec 25 2007.
- [126] A. Yella, M. Panthofer, M. Kappl, and W. Tremel, "Snapshots of the Formation of Inorganic MoS₂ Onion-Type Fullerenes: A "Shrinking Giant Bubble" Pathway," *Angewandte Chemie-International Edition*, vol. 49, pp. 2575-2580, 2010.
- [127] G. Seifert, T. Kohler, and R. Tenne, "Stability of metal chalcogenide nanotubes," *Journal of Physical Chemistry B*, vol. 106, pp. 2497-2501, Mar 14 2002.
- [128] D. J. Srolovitz, S. A. Safran, M. Homyonfer, and R. Tenne, "Morphology of Nested Fullerenes," *Physical review letters*, vol. 74, pp. 1779-1782, Mar 6 1995.
- [129] Y. Q. Zhu, T. Sekine, Y. H. Li, M. W. Fay, Y. M. Zhao, C. H. P. Poa, W. X. Wang, M. J. Roe, P. D. Brown, N. Fleischer, and R. Tenne, "Shock-absorbing and failure mechanisms of WS₂ and MoS₂ nanoparticles with fullerene-like structures under shock wave pressure," *Journal of the American Chemical Society*, vol. 127, pp. 16263-16272, Nov 23 2005.

- [130] Y. Q. Zhu, T. Sekine, Y. H. Li, W. X. Wang, M. W. Fay, H. Edwards, P. D. Brown, N. Fleischer, and R. Tenne, "WS₂ and MoS₂ inorganic fullerenes - Super shock absorbers at very high pressures," *Advanced Materials*, vol. 17, pp. 1500-1503, Jun 17 2005.
- [131] Y. Q. Zhu, T. Sekine, K. S. Brigatti, S. Firth, R. Tenne, R. Rosentsveig, H. W. Kroto, and D. R. M. Walton, "Shock-wave resistance of WS₂ nanotubes," *Journal of the American Chemical Society*, vol. 125, pp. 1329-1333, Feb 5 2003.
- [132] J. K. Norskov, T. Bligaard, A. Logadottir, J. R. Kitchin, J. G. Chen, S. Pandelov, and J. K. Norskov, "Trends in the exchange current for hydrogen evolution," *Journal of the Electrochemical Society*, vol. 152, pp. J23-J26, 2005.
- [133] B. E. Conway and B. V. Tilak, "Interfacial processes involving electrocatalytic evolution and oxidation of H₂, and the role of chemisorbed H," *Electrochimica Acta*, vol. 47, pp. 3571-3594, Aug 30 2002.
- [134] T. F. Jaramillo, K. P. Jorgensen, J. Bonde, J. H. Nielsen, S. Horch, and I. Chorkendorff, "Identification of active edge sites for electrochemical H₂ evolution from MoS₂ nanocatalysts," *Science*, vol. 317, pp. 100-102, Jul 6 2007.
- [135] Y. G. Li, H. L. Wang, L. M. Xie, Y. Y. Liang, G. S. Hong, and H. J. Dai, "MoS₂ Nanoparticles Grown on Graphene: An Advanced Catalyst for the Hydrogen Evolution Reaction," *Journal of the American Chemical Society*, vol. 133, pp. 7296-7299, May 18 2011.
- [136] J. F. Xie, H. Zhang, S. Li, R. X. Wang, X. Sun, M. Zhou, J. F. Zhou, X. W. Lou, and Y. Xie, "Defect-Rich MoS₂ Ultrathin Nanosheets with Additional Active Edge Sites for Enhanced Electrocatalytic Hydrogen Evolution," *Advanced Materials*, vol. 25, pp. 5807-+, Oct 2013.
- [137] J. Yang, D. Voiry, S. J. Ahn, D. Kang, A. Y. Kim, M. Chhowalla, and H. S. Shin, "Two-dimensional hybrid nanosheets of tungsten disulfide and reduced graphene oxide as catalysts for enhanced hydrogen evolution," *Angewandte Chemie*, vol. 52, pp. 13751-4, Dec 16 2013.
- [138] L. Cheng, W. Huang, Q. Gong, C. Liu, Z. Liu, Y. Li, and H. Dai, "Ultrathin WS₂ Nanoflakes as a High-Performance Electrocatalyst for the Hydrogen Evolution Reaction," *Angewandte Chemie International Edition*, pp. n/a-n/a, 2014.
- [139] W. R. Zhao, H. R. Chen, Y. S. Li, L. Li, M. D. Lang, and J. L. Shi, "Uniform Rattle-type Hollow Magnetic Mesoporous Spheres as Drug Delivery Carriers and their Sustained-Release Property," *Advanced Functional Materials*, vol. 18, pp. 2780-2788, Sep 23 2008.
- [140] H. J. Hah, J. I. Um, S. H. Han, and S. M. Koo, "New synthetic route for preparing rattle-type silica particles with metal cores," *Chemical Communications*, pp. 1012-1013, Apr 21 2004.

- [141] M. Kim, K. Sohn, H. Bin Na, and T. Hyeon, "Synthesis of nanorattles composed of gold nanoparticles encapsulated in mesoporous carbon and polymer shells," *Nano Letters*, vol. 2, pp. 1383-1387, Dec 2002.
- [142] J. H. Yang, L. H. Lu, H. S. Wang, and H. J. Zhang, "Synthesis of Pt/Ag bimetallic nanorattle with Au core," *Scripta Materialia*, vol. 54, pp. 159-162, Jan 2006.
- [143] J. Lee, J. C. Park, and H. Song, "A nanoreactor framework of a Au@SiO₂ yolk/shell structure for catalytic reduction of p-nitrophenol," *Advanced Materials*, vol. 20, pp. 1523-+, Apr 21 2008.
- [144] M. Chen, Y. N. Kim, H. M. Lee, C. Li, and S. O. Cho, "Multifunctional magnetic silver nanoshells with sandwichlike nanostructures," *Journal of Physical Chemistry C*, vol. 112, pp. 8870-8874, Jun 19 2008.
- [145] J. H. Gao, G. L. Liang, J. S. Cheung, Y. Pan, Y. Kuang, F. Zhao, B. Zhang, X. X. Zhang, E. X. Wu, and B. Xu, "Multifunctional yolk-shell nanoparticles: A potential MRI contrast and anticancer agent," *Journal of the American Chemical Society*, vol. 130, pp. 11828-11833, Sep 3 2008.
- [146] K. Kamata, Y. Lu, and Y. N. Xia, "Synthesis and characterization of monodispersed core-shell spherical colloids with movable cores," *Journal of the American Chemical Society*, vol. 125, pp. 2384-2385, Mar 5 2003.
- [147] P. M. Arnal, M. Comotti, and F. Schuth, "High-temperature-stable catalysts by hollow sphere encapsulation," *Angewandte Chemie-International Edition*, vol. 45, pp. 8224-8227, 2006.
- [148] W. S. Choi, H. Y. Koo, and D. Y. Kim, "Scalable synthesis of chestnut-bur-like magnetic capsules loaded with size-controlled mono- or bimetallic cores," *Advanced Materials*, vol. 19, pp. 451-+, Feb 5 2007.
- [149] S. Ikeda, S. Ishino, T. Harada, N. Okamoto, T. Sakata, H. Mori, S. Kuwabata, T. Torimoto, and M. Matsumura, "Ligand-free platinum nanoparticles encapsulated in a hollow porous carbon shell as a highly active heterogeneous hydrogenation catalyst," *Angewandte Chemie-International Edition*, vol. 45, pp. 7063-7066, 2006.
- [150] Y. H. Ng, S. Ikeda, T. Harada, S. Higashida, T. Sakata, H. Mori, and M. Matsumura, "Fabrication of hollow carbon nanospheres encapsulating platinum nanoparticles using a photocatalytic reaction," *Advanced Materials*, vol. 19, pp. 597-+, Feb 19 2007.
- [151] Z. Kai, X. H. Zhang, H. T. Chen, C. Xin, L. L. Zheng, J. H. Zhang, and Y. Bai, "Hollow titania spheres with movable silica spheres inside," *Langmuir*, vol. 20, pp. 11312-11314, Dec 21 2004.

- [152] J. Lee, J. C. Park, J. U. Bang, and H. Song, "Precise tuning of porosity and surface functionality in Au@SiO₂ nanoreactors for high catalytic efficiency," *Chemistry of Materials*, vol. 20, pp. 5839-5844, Sep 23 2008.
- [153] Q. Zhang, T. R. Zhang, J. P. Ge, and Y. D. Yin, "Permeable silica shell through surface-protected etching," *Nano Letters*, vol. 8, pp. 2867-2871, Sep 2008.
- [154] X. W. Lou, C. L. Yuan, and L. A. Archer, "Double-walled SnO₂ nano-cocoons with movable magnetic cores," *Advanced Materials*, vol. 19, pp. 3328-+, Oct 19 2007.
- [155] X. W. Lou and L. A. Archer, "A general route to nonspherical anatase TiO₂ hollow colloids and magnetic multifunctional particles," *Advanced Materials*, vol. 20, pp. 1853-+, May 19 2008.
- [156] X. W. Lou, C. Yuan, Q. Zhang, and L. A. Archer, "Platinum-functionalized octahedral silica nanocages: Synthesis and characterization," *Angewandte Chemie-International Edition*, vol. 45, pp. 3825-3829, 2006.
- [157] X. W. Lou, L. A. Archer, and Z. C. Yang, "Hollow Micro-/Nanostructures: Synthesis and Applications," *Advanced Materials*, vol. 20, pp. 3987-4019, Nov 3 2008.
- [158] S. Cavaliere-Jaricot, M. Darbandi, and T. Nann, "Au-silica nanoparticles by "reverse" synthesis of cores in hollow silica shells," *Chemical Communications*, pp. 2031-2033, 2007.
- [159] A. B. Fuertes, M. Sevilla, T. Valdes-Solis, and P. Tartaj, "Synthetic route to nanocomposites made up of inorganic nanoparticles confined within a hollow mesoporous carbon shell," *Chemistry of Materials*, vol. 19, pp. 5418-5423, Oct 30 2007.
- [160] D. M. Cheng, X. D. Zhou, H. B. Xia, and H. S. O. Chan, "Novel method for the preparation of polymeric hollow nanospheres containing silver cores with different sizes," *Chemistry of Materials*, vol. 17, pp. 3578-3581, Jul 12 2005.
- [161] Y. D. Yin, R. M. Rioux, C. K. Erdonmez, S. Hughes, G. A. Somorjai, and A. P. Alivisatos, "Formation of hollow nanocrystals through the nanoscale Kirkendall Effect," *Science*, vol. 304, pp. 711-714, Apr 30 2004.
- [162] A. D. Smigelskas and E. O. Kirkendall, "Zinc Diffusion in Alpha-Brass," *Transactions of the American Institute of Mining and Metallurgical Engineers*, vol. 171, pp. 130-142, 1947.
- [163] H. J. Fan, U. Gosele, and M. Zacharias, "Formation of nanotubes and hollow nanoparticles based on Kirkendall and diffusion processes: A review," *Small*, vol. 3, pp. 1660-1671, Oct 2007.
- [164] H. J. Fan, M. Knez, R. Scholz, K. Nielsch, E. Pippel, D. Hesse, M. Zacharias, and U. Gosele, "Monocrystalline spinel nanotube fabrication based on the Kirkendall effect," *Nature materials*, vol. 5, pp. 627-631, Aug 2006.

- [165] H. C. Zeng, "Synthetic architecture of interior space for inorganic nanostructures," *Journal of Materials Chemistry*, vol. 16, pp. 649-662, Feb 21 2006.
- [166] H. C. Zeng, "Ostwald ripening: A synthetic approach for hollow nanomaterials," *Current Nanoscience*, vol. 3, pp. 177-181, May 2007.
- [167] X. W. Lou, Y. Wang, C. L. Yuan, J. Y. Lee, and L. A. Archer, "Template-free synthesis of SnO₂ hollow nanostructures with high lithium storage capacity," *Advanced Materials*, vol. 18, pp. 2325-+, Sep 5 2006.
- [168] C. W. Guo, Y. Cao, S. H. Xie, W. L. Dai, and K. N. Fan, "Fabrication of mesoporous core-shell structured titania microspheres with hollow interiors," *Chemical Communications*, pp. 700-701, 2003.
- [169] H. X. Li, Z. F. Bian, J. Zhu, D. Q. Zhang, G. S. Li, Y. N. Huo, H. Li, and Y. F. Lu, "Mesoporous titania spheres with tunable chamber structure and enhanced photocatalytic activity," *Journal of the American Chemical Society*, vol. 129, pp. 8406-+, Jul 11 2007.
- [170] Y. F. Zhu, D. H. Fan, and W. Z. Shen, "Template-free synthesis of zinc oxide hollow microspheres in aqueous solution at low temperature," *Journal of Physical Chemistry C*, vol. 111, pp. 18629-18635, Dec 20 2007.
- [171] B. Liu and H. C. Zeng, "Symmetric and asymmetric Ostwald ripening in the fabrication of homogeneous core-shell semiconductors," *Small*, vol. 1, pp. 566-571, May 2005.
- [172] Y. G. Sun, B. Wiley, Z. Y. Li, and Y. N. Xia, "Synthesis and optical properties of nanorattles and multiple-walled nanoshells/nanotubes made of metal alloys," *Journal of the American Chemical Society*, vol. 126, pp. 9399-9406, Aug 4 2004.
- [173] Y. Hu, X. T. Zheng, J. S. Chen, M. J. Zhou, C. M. Li, and X. W. Lou, "Silica-based complex nanorattles as multifunctional carrier for anticancer drug," *Journal of Materials Chemistry*, vol. 21, pp. 8052-8056, 2011.
- [174] F. Gao, L. Li, C. Fu, L. Nie, D. Chen, and F. Tang, "LHRH-PE40 Fusion Protein Tethered Silica Nanorattles for Imaging-Guided Tumor-Specific Drug Delivery and Bimodal Therapy," *Advanced Materials*, pp. n/a-n/a, 2013.
- [175] F. Zhang, G. B. Braun, A. Pallaoro, Y. Zhang, Y. Shi, D. Cui, M. Moskovits, D. Zhao, and G. D. Stucky, "Mesoporous Multifunctional Upconversion Luminescent and Magnetic "Nanorattle" Materials for Targeted Chemotherapy," *Nano Letters*, vol. 12, pp. 61-67, 2012/01/11 2011.
- [176] F. G. Gao, L. L. Li, T. L. Liu, N. J. Hao, H. Y. Liu, L. F. Tan, H. B. Li, X. L. Huang, B. Peng, C. M. Yan, L. Q. Yang, X. L. Wu, D. Chen, and F. Q. Tang, "Doxorubicin loaded silica nanorattles actively seek tumors with improved anti-tumor effects," *Nanoscale*, vol. 4, pp. 3365-3372, 2012.

- [177] I. H. R. Kelsall, M. Geoghegan, "Nanoscale Science and Technology," *John Wiley & Sons Ltd*, pp. 76-77, 2005.
- [178] U. o. Glasgow. Available:
<http://www.gla.ac.uk/schools/ges/research/researchfacilities/isaac/services/scanningelectronmicroscopy/>
- [179] U. o. Maryland. Available:
<http://www.chem.umd.edu/sharedinstrumentation/surface-analysis-center/>
- [180] Available: <http://chemistry.umeche.maine.edu/CHY251/Ch13-Overhead4.html>
- [181] wiki. Available:
http://en.wikipedia.org/wiki/Ultraviolet%E2%80%93visible_spectroscopy#mediaviewer/File:Schematic_of_UV-visible_spectrophotometer.png

Chapter Four

Synthesis and characterisation of WS₂ nanoparticles

via solid-gas reaction between WO₃ and S

Introduction

Many metal oxides, including MoO₃, WO₃ and ReO₃ can directly react with chalcogen elements and/or hydrogen chalcogenides, forming corresponding metal dichalcogenides that are usually in flake form [1-3]. In general, the formation of these metal dichalcogenides follows a “template reaction mechanism”, indicating that the sizes and morphologies of the products are similar to those of the oxide raw materials [4]. For example, WS₂ thin films [5], nanoflakes, and microparticles [2] were produced from the reaction of S with WO₃ thin films, nanoparticles and microparticles, respectively. In 1992, WS₂ IF nanoparticles were synthesised for the first time via the straightforward reaction between thin W films and H₂S [6], which indicated that metal sulphide IF nanoparticles were stable in ambient atmosphere. Then, numerous WS₂ and MoS₂ IF nanoparticles and nanotubes were synthesised *via* various techniques [3, 7-13]. Among these techniques, the “falling bed synthesis”, as the best approach, has already been applied for commercial production [8]. However, the usage of special equipment and the toxic H₂S reactant largely increased the production cost and caused safety/environmental concern. Yang et al. [14] overcame these drawbacks by replacing H₂S with S powder in a simple tube furnace under H₂ atmosphere. Although WS₂ IF nanoparticles were readily produced at as low as 620°C, most of these nanoparticles had a large hollow core with very thin walls (approximately 5 nm in thickness), leading to poor high-temperature stability and mechanical properties.

In the work presented in this chapter, WS₂ nanoflakes and IF nanoparticles were produced *via* a modified gas-solid reaction route without using H₂S. Unlike Yang’s route, the usage of excessive S and flowing H₂ resulted in well-

crystallised WS₂ IF nanoparticles with thick shells. Based on the results, the relevant reaction mechanism was also discussed.

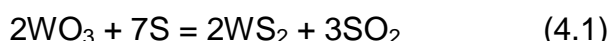
Experimental

0.232g WO₃ nanopowder (>99%, <100 nm) and micropowder (~2 μm, Sigma-Aldrich) were initially dispersed in 100 ml ethanol (>99% Sigma-Aldrich) by ultrasonication for 2 h followed by 3 h of drying in an oven at 80°C. Then, the dried powder was mixed with various amounts of S (>99.5% Sigma-Aldrich) (excessive amounts of S were used to compensate for its loss due to evaporation during the heating/reaction processes, see below) by ball milling at 400 rpm for 2 h. A quartz tube in a tube furnace was flushed with Ar at 80 ml/min for 30 min to remove any residual air. Then, the furnace was heated to a given temperature between 350-950°C. Subsequently, the ball-milled mixture was put on a ceramic boat and placed into the hot zone of a furnace preheated to a given target temperature and held for different periods. Ar, Ar/H₂S or Ar/H₂ gas flowed through the quartz furnace at 60 ml/min. For the combined gas, the volume ratio (Ar:H₂ and Ar:H₂S) was set to 2:1. Finally, the ceramic boat was removed from the hot zone and cooled down to room temperature under Ar flow. The colour of the sample changed from yellow (WO₃) to black (WS₂). The reacted mass was collected from the ceramic boat for further characterisation.

Results and discussion

4.1 Fabrication of WS₂ nanoflakes *via* template reaction route

In this section, WS₂ was produced *via* the reaction between WO₃ and S (Reaction (4.1)) in an Ar atmosphere:



Processing parameters such as the temperature, holding time and raw material size were investigated in detail. In addition, a possible formation mechanism of WS₂ was also proposed.

4.1.1 Effect of sulphur amount

Because the boiling point of S powder is 444°C, reaction (4.1) can be considered as a solid-gas reaction between solid WO_3 and gaseous S when the temperature is above this value. In this open reaction system, some S vapour would be carried away by the flowing Ar and would thus not be able to participate in the sulphidation. Therefore, if stoichiometric amounts of WO_3 and S were used, reaction (4.1) would not be complete, and some unreacted WO_3 would be left as an impurity. Therefore, to obtain pure WS_2 , it is necessary to use appropriately excessive amounts of S powder to compensate for the S loss.

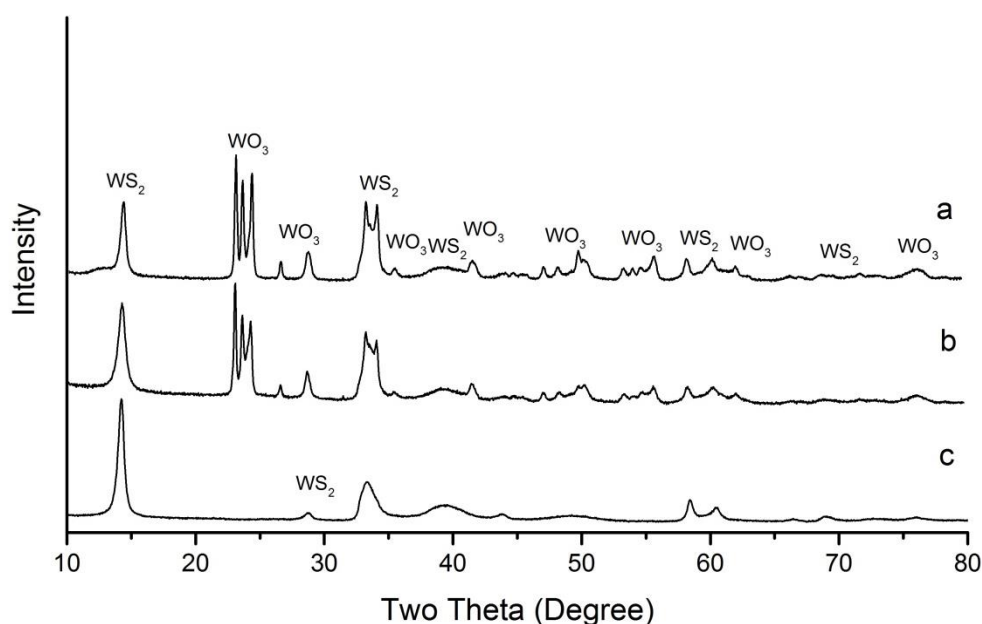


Figure 4.1 XRD patterns of samples produced from: 1-h firing at 750°C in Ar using (a) 9 times and (c) 29 times excessive S and (b) 2-h firing at 750°C in Ar using 9 times excessive S.

Figure 4.1 presents XRD patterns of the samples resulting from firing at 750°C for 1 h in Ar atmosphere using 9 and 29 times excessive S (in weight). Because of the usage of excessive S, some unreacted S vapour condensed on the inner surface of the quartz tube end and could be recycled after the reaction. As observed in Figure 4.1, strong characteristic peaks of WS_2 were observed in all the XRD patterns, indicating the high reaction extents under the conditions. However, large amounts of WO_3 were left unreacted when 9 times excessive S powder was used, whereas no S peaks appeared in Figure 4.1a. Upon

increasing the holding time to 2 h, no obvious change is observed in Figure 4.1b, indicating that the extended soaking time had little effect on the formation of WS_2 under this condition, which is different from the results reported by other researchers [4]. According to Tenne et al., the holding time is a key factor in the sulphidation of WO_3 . At $850^\circ C$, WO_3 will be gradually converted to WS_2 with the increasing of holding time from 2 min to 15 min [4]. Based on the above analysis, it could be concluded that 9 times excessive S was not sufficient to achieve a complete reaction and would be depleted after 1-h heat treatment. To compensate for the S loss and make the reaction complete, the use of additional S was required. As observed in Figure 4.1c, upon using 29 times excessive S powder, the peaks of WO_3 disappeared, and phase pure WS_2 was obtained. Therefore, the use of ≥ 29 times excessive S was necessary to complete the sulphidation in the present case.

4.1.2 Effect of temperature

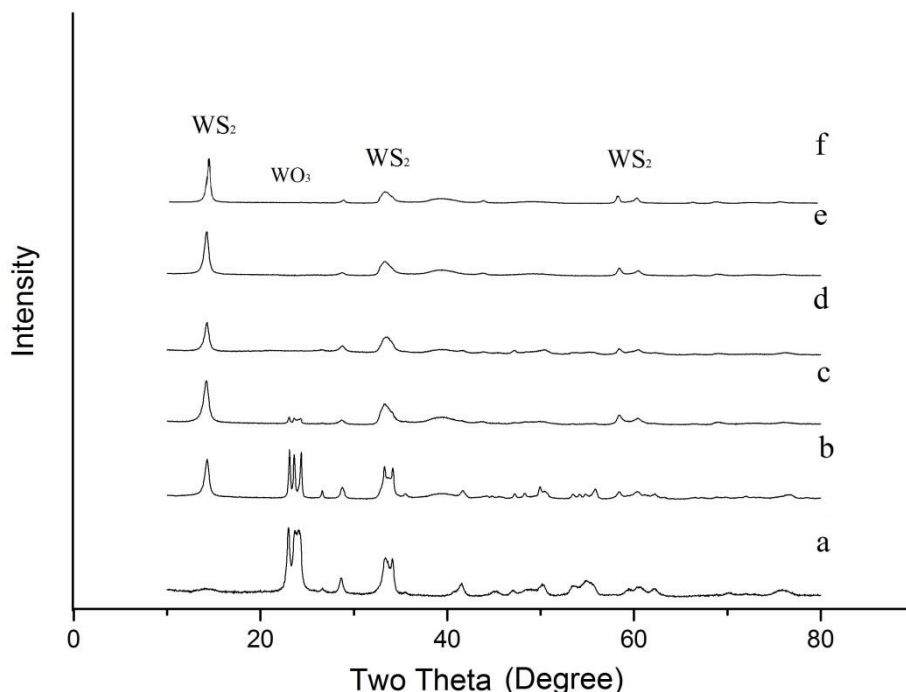


Figure 4.2 presents XRD patterns of the samples obtained from 1-h firing in Ar at (a) $400^\circ C$, (b) $450^\circ C$, (c) $500^\circ C$, (d) $600^\circ C$, (e) $750^\circ C$ and (f) $850^\circ C$ using 29 times excessive S.

In Figure 4.2, the XRD patterns of the samples resulting from 1-h firing at 400, 450, 500, 600, 750 and 850°C using 29 times excessive S in an Ar atmosphere are presented. In Figure 4.2a, WS₂ was detected at as low as 400°C in the Ar atmosphere. This finding was due to the negative Gibbs free energy of Reaction (4.1) at 400°C and the large contact area between nanosized WO₃ and S [4, 15]. However, the intensities of all the WS₂ peaks were quite low, while the characteristic peaks of WO₃ were strong and sharp, indicating that 400°C was sufficiently high to activate this reaction but still too low to make the reaction complete. Therefore, the main phase of this sample was still unreacted WO₃. Moreover, the low temperature used would also suppress the crystallisation process of WS₂, leading to the appearance of WS₂ broad peaks. Upon increasing the temperature to 450°C, the intensities of WS₂ peaks greatly increased, whereas the intensities of the WO₃ peaks decreased (Figure 4.2b). This finding was attributed to the generation of large amounts of S vapour at 450°C, which was above the boiling point of S (444°C), and thus, the solid-liquid reaction observed at 400°C was transformed to a solid-gas reaction. Because S vapour had a higher reaction activity and larger contact area with WO₃, their reaction occurred much more rapidly at 450°C. Upon further increasing the temperature to 500°C, WS₂ became the primary phase, and only small amounts of WO₃ remained (Figure 4.2c). When the reaction temperature increased to 600°C, WO₃ disappeared, and pure WS₂ was obtained (Figure 4.2d). Further temperature increases to 750°C and 850°C did not affect the compositions of the products. However, the WS₂ peaks became higher and sharper, indicating improved crystallisation (Figures 4.2e and f). Based on the above analysis, high temperatures could dramatically accelerate the reaction, and pure WS₂ was produced when the temperature was $\geq 600^\circ\text{C}$.

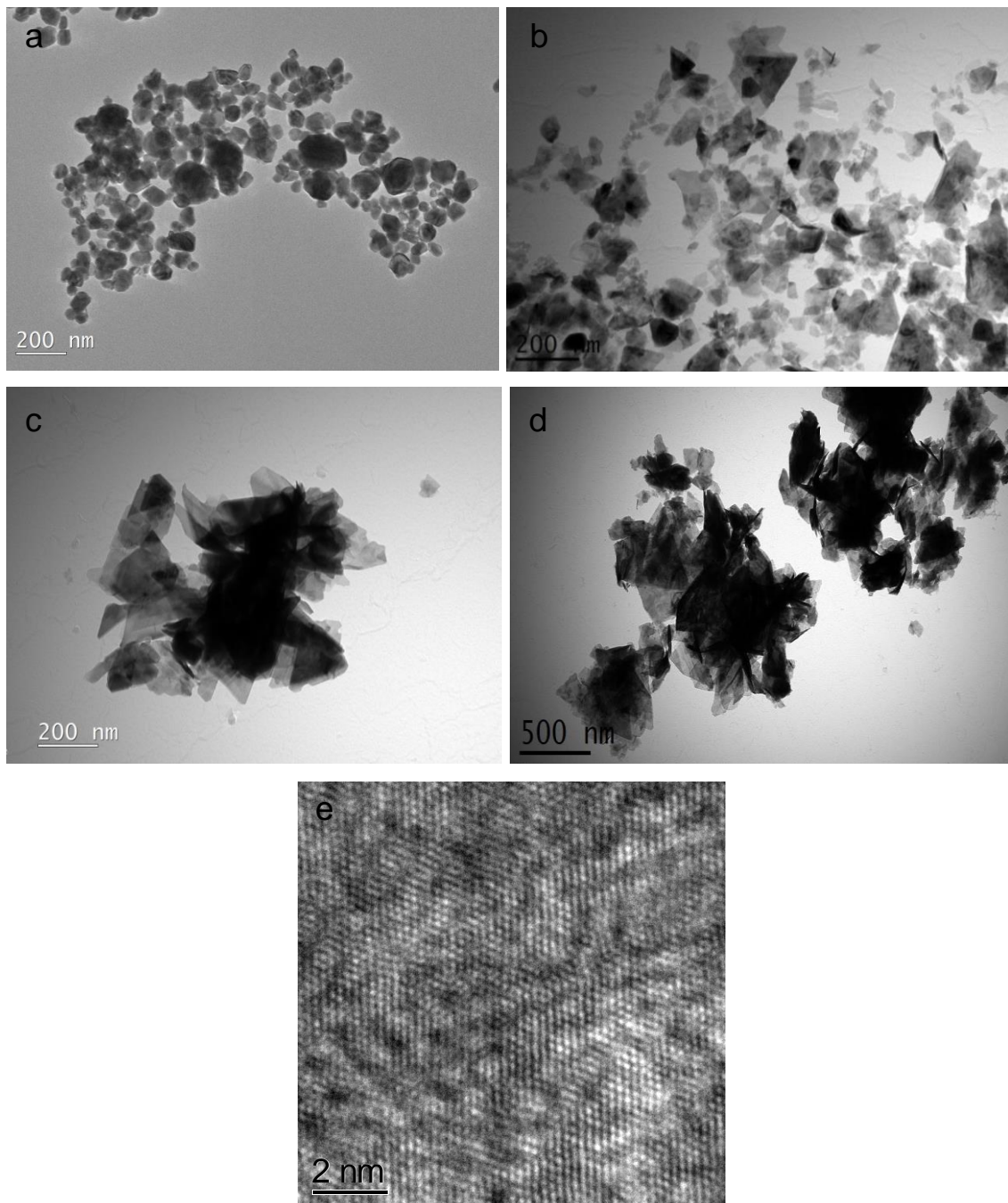


Figure 4.3 TEM images of (a) WO₃ raw material and WS₂ produced by 1-h firing in Ar at (b) 600°C (c) 750°C and (d) 850°C. (e) HRTEM image of the sample in (d).

Figure 4.3 presents TEM images of the samples whose XRD patterns are presented in Figure 4.2. According to Figure 4.3, the WS₂ products obtained under different firing conditions all exhibited a plate-like structure with obvious agglomeration. At 600°C, WS₂ nanosheets with irregular shapes and sizes < 200 nm were formed (Figure 4.3b). Upon increasing the synthesis temperatures to 750°C and 850°C, the sizes of WS₂ increased to approximately 300 nm

(Figure 4.3c) and 500 nm (Figure 4.3d), respectively. The HRTEM image shows the top view of the WS₂ flakes synthesised at 850°C. The lattice distance was approximately 0.27 nm, which is consistent with the interplanar spacing of the WS₂ (100) lattice plane. The sizes of all the WS₂ products were observed to be larger than those of the raw WO₃ nanoparticles, which were smaller than 100 nm (Figure 4.3a). Although the morphologies of these products remained similar, as irregular nanosheets, higher temperatures led to increased particle sizes because of two reasons, which will be discussed in more detail later: (1) the sintering of raw WO₃ powder before reacting with S vapour and (2) the crystal growth of the produced WS₂ particles at high temperatures.

The agglomeration of the as-synthesised WS₂ nanoflakes was attributed to the presence of dangling, unsaturated bonds on the edge of the nanosheets. These bonds tended to connect with other bonds on different nanosheets to reduce the thermodynamic energy, and this process could be accelerated by the increase of temperature arising from severe thermal vibration, leading to the formation of severe agglomeration [16, 17].

4.1.3 Effect of raw material size

Because the reaction between WO₃ and S was essentially a vapour-solid reaction, the sizes of final products should be largely determined by those of the WO₃ “template”. Therefore, it was expected that WS₂ microflakes would be generated from WO₃ microparticles.

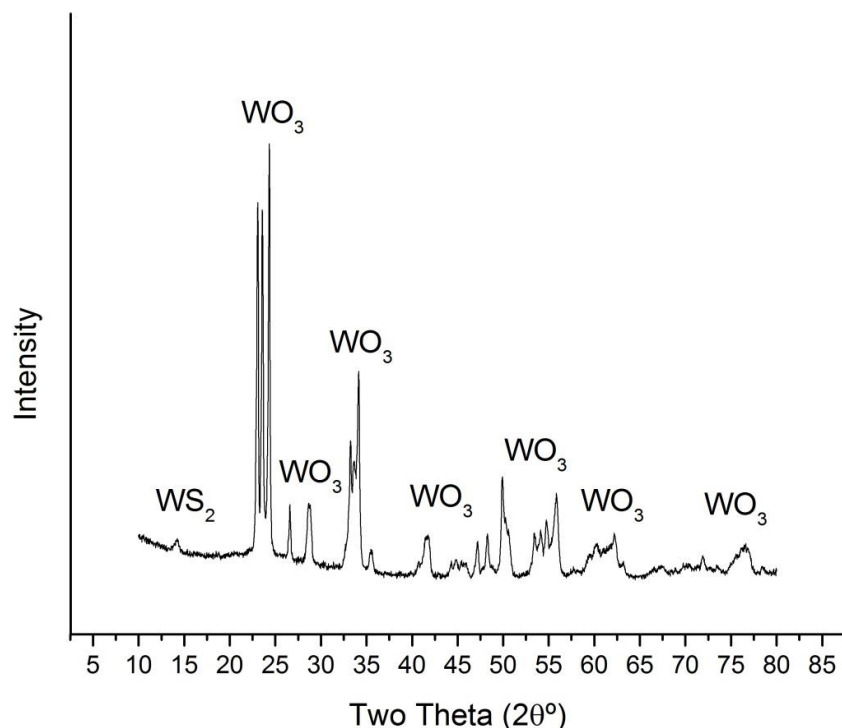


Figure 4.4 XRD pattern of the sample resulting from 1 h firing at 750°C in an Ar atmosphere using micron-sized WO₃ as the raw material.

Figure 4.4 presents the XRD pattern of the sample synthesised from micron-sized WO₃ powder at 750°C for 1 h in an Ar atmosphere. Unlike the WS₂ product fabricated from WO₃ nanopowder under the same firing conditions (Figure 4.2e), the WO₃ in this sample remained as the primary phase, and the peaks of WS₂ were much lower, indicating much lower reaction extents (Figure 4.4). Therefore, it could be concluded that the size of WO₃ affected the reaction extent. Because nanosized WO₃ has a much larger surface area than micron-sized WO₃, the nanosized structure exhibited a higher chemical activity to activate the reaction. In addition, because of the much smaller sizes of nanosized WO₃, S atoms could diffuse easily into the core of the former to convert the entire particle into WS₂. This easy diffusion was not the case with micron-sized WO₃, as S diffusion might stop on the WO₃ particle surface[18].

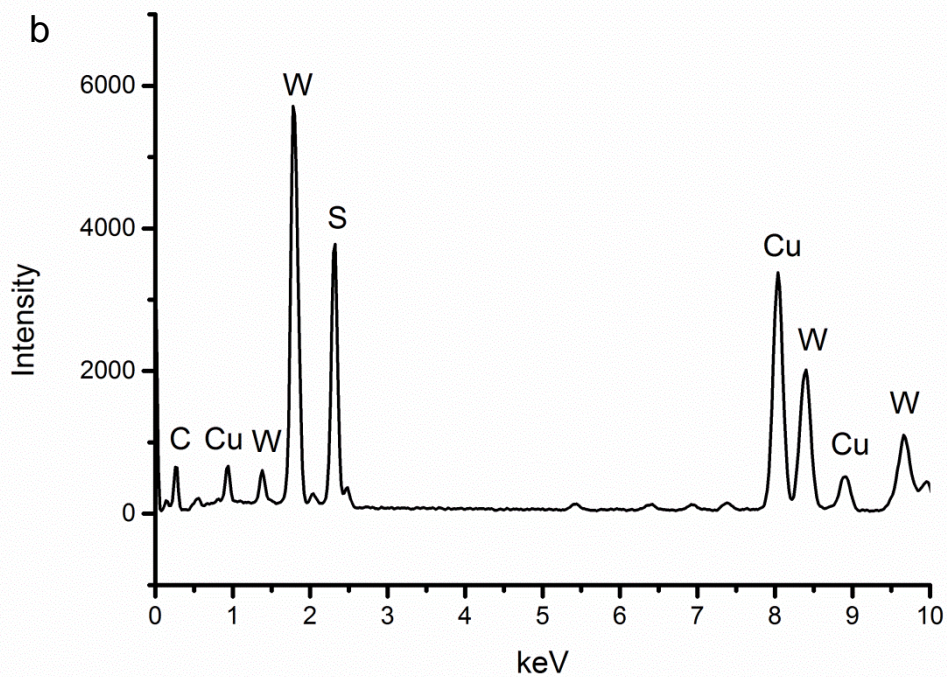
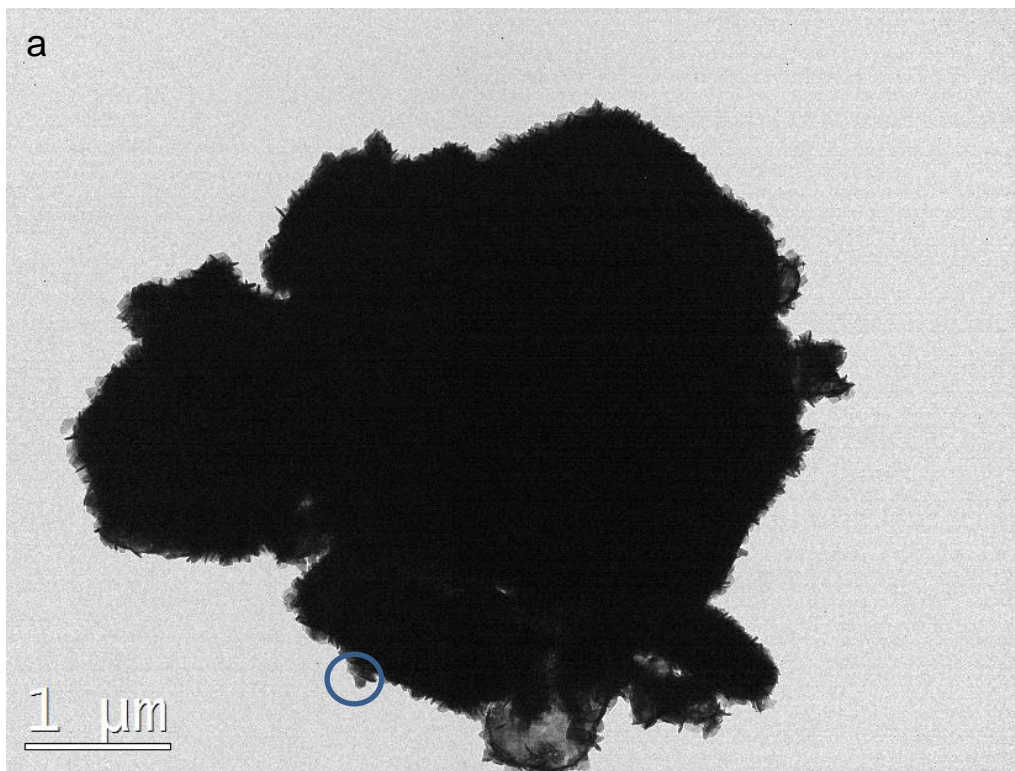


Figure 4.5 (a) TEM image of sample resulting from firing micron-sized WO_3 and S at 750°C for 1 h in an Ar atmosphere and (b) EDS spectrum of selected area in (a).

Figure 4.5 presents TEM images of the samples whose XRD patterns are shown in Figure 4.4. As observed in Figure 4.5a, some large micron-sized particles with sizes of approximately 2 μm on average were produced. Unlike the WO_3 raw material, the surfaces of these WO_3 particles were composed of large amounts of nanoflakes. According to the EDS spectrum obtained from some of these nanoflakes (Figure 4.5b), these nanoflakes were confirmed to be WS_2 . Combined with the XRD results, this result verifies the formation of WS_2 - WO_3 composites. This “micro to nano” conversion from large raw materials to tiny products has also been observed and explained by other researchers [18]. At 750°C, the reaction between S and the WO_3 surface was very fast. However, the diffusion rate of S into the WO_3 core was relatively slow, leading to the formation of partially reacted WS_2 - WO_3 composites. The generated WS_2 particles on the large WO_3 core could not form continuous layers because of the absence of H_2 , and thus, some tiny nanoflakes were formed instead [18].

4.1.4 Effect of holding time

In general, the holding time is one of the most important parameters in the heat-treatment procedure. Different holding times might result in different compositions, crystal structures and morphologies. To investigate the possible effect of holding time on the WS_2 synthesis, raw material batches were fired at 750°C for 5 min, 1 h and 2 h.

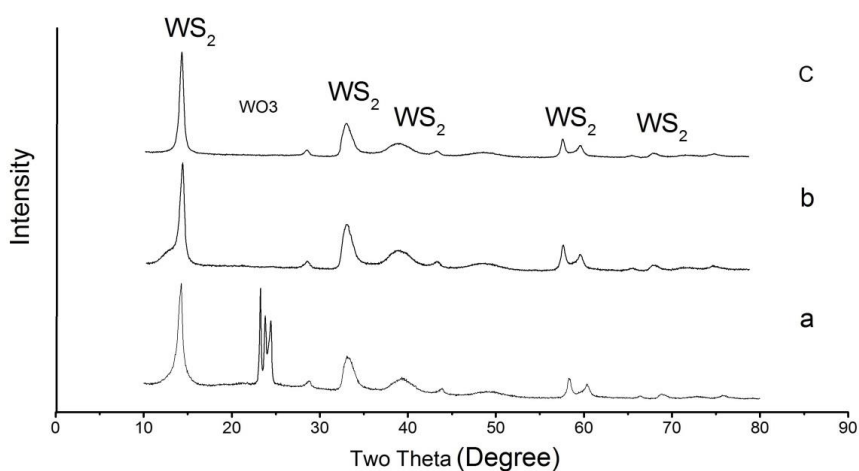


Figure 4.6 XRD patterns of samples fired at 750°C in Ar for (a) 5 min, (b) 1 h and (c) 2 h.

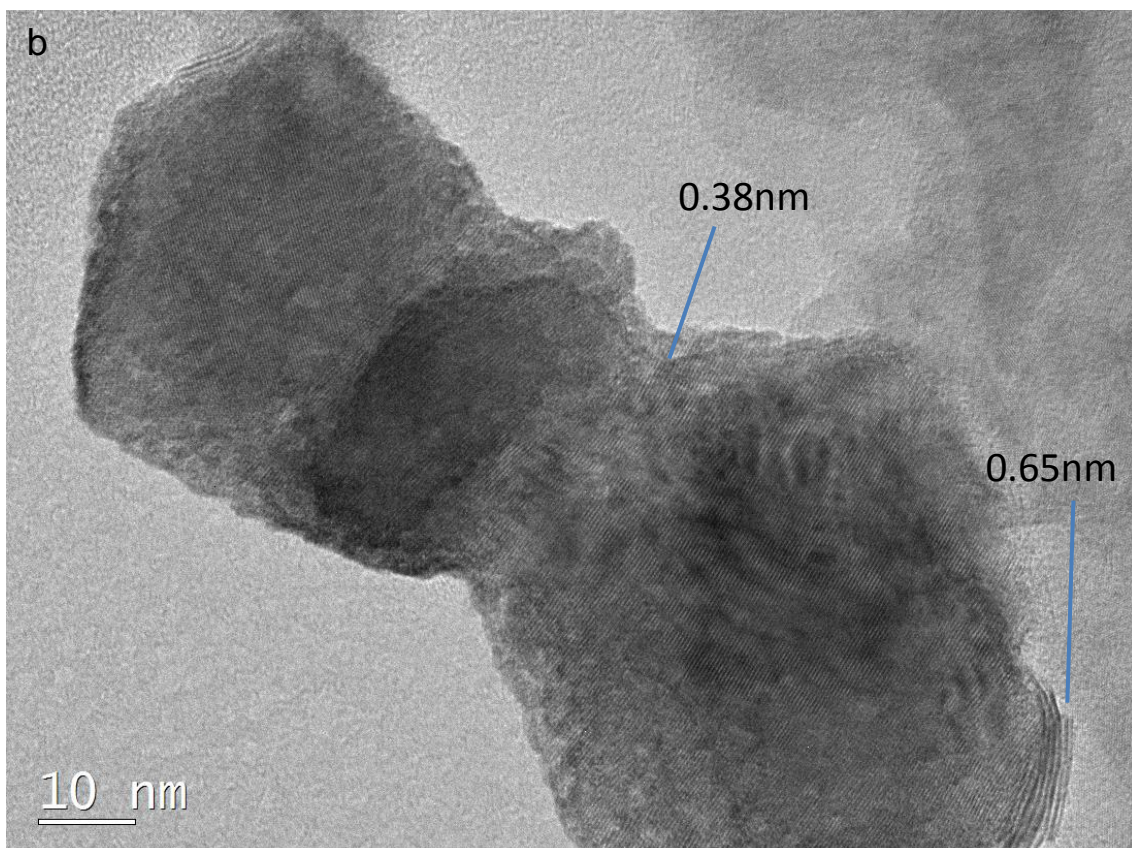
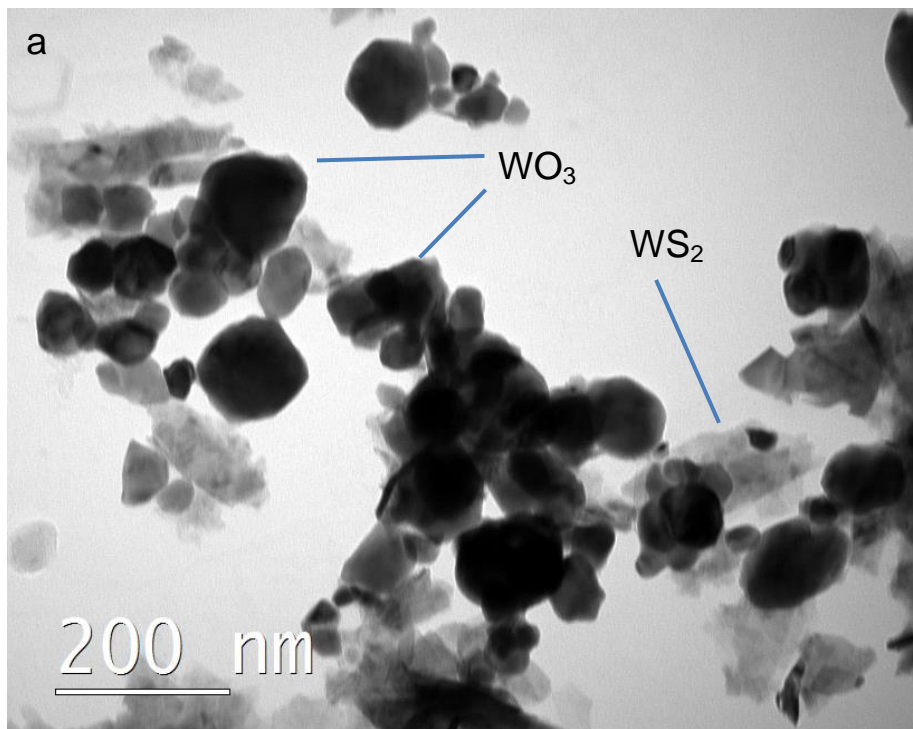


Figure 4.7 (a, b) HRTEM image of sample resulting from firing at 750°C for 5 min in an Ar atmosphere.

As observed in Figure 4.6a, large amounts of WS_2 were formed after the reaction of WO_3 with 29 times excessive S for only 5 min at 750°C, indicating the very rapid reaction at this temperature. As mentioned above, when 9 times

excessive S was used, increasing the holding time did not promote the reaction further. However, in the present case, with the use of 29 times excessive S, the extension of the holding time from 5 min to 1 h had obvious effects. The WO_3 peaks disappeared, and single phase WS_2 was obtained (Figure 4.7b). When the holding time was further increased to 2 h, no obvious change was observed (Figure 4.6c), indicating that the product formed earlier was stable under this condition. Based on the above analysis, it could be concluded that the holding time was an essential factor affecting the fabrication of WS_2 particles when sufficient S was used.

Figure 4.7 illustrates the morphologies of the samples whose XRD patterns are presented in Figure 4.6a. After the 5-min reaction, WS_2 nanoflakes with an average size of approximately 200 nm were formed (Figure 4.7a). Along with WS_2 , some unreacted WO_3 particles were also observed. Compared with the WO_3 raw material with a narrow size distribution from 30 to 80 nm (Figure 4.3a), residual WO_3 nanoparticles due to particle sintering had sizes above 100 nm, whereas a few isolated particles had sizes below 50 nm. Because of the short holding time, this reaction was not complete (Figure 4.6c). Consequently, the majority of the tiny WO_3 nanoparticles were sintered together before being sulfurised completely. Moreover, the short reaction time hindered the further crystal growth of the formed WS_2 flakes, leading to the generation of tiny WS_2 nanoflakes. In addition to these WS_2 nanoflakes and isolated WO_3 nanoparticles, some reaction intermediates were observed in the same sample. The high-magnification image of a typical intermediate particle (Figure 4.7b) reveals that two WO_3 nanoparticles were sintered together with a lattice distance of approximately 0.38 nm, which is consistent with the interlayer spacing of the WO_3 (100) lattice plane. Unlike raw WO_3 nanoparticles, some layered fragments were also observed on the edges of these nanoparticles. The lattice distances of these fragments were measured to be 0.65 nm, which is similar to the lattice distance of the WS_2 (002) lattice plane, indicating that part of the WO_3 surface was converted into WS_2 .

When WO_3 reacts with H_2S , a continuous WS_2 coating will be initially formed on the surface of WO_3 , and then, this reaction will be completed *via* interdiffusion between residual WO_3 and H_2S [4]. The continuous WS_2 coating is vital for the

formation of WS₂ IF nanoparticles because the coating can suppress the sintering of WO₃, which could lead to the formation of a more stable flake structure [4]. When H₂ was absent, the formation of WS₂ still started from the surface of WO₃ and was controlled by the interdiffusion of S and O. However, due to the lack of H₂, WO_{3-x} could not be formed as well as oxygen vacancies, and thus, S had to diffuse through dense WO₃ layers, leading to a slow diffusion rate [4]. Therefore, a continuous WS₂ coating could not be formed before the sintering of WO₃. Because the number of WS₂ layers is normally proportional to the sizes of the WO₃ particles, if the sintered WO₃ nanoparticles, which have much larger sizes, are converted into IF-WS₂ particles, the particles will contain many curved layers. Therefore, large amounts of strain energy are stored in these formed particles and will be released *via* the crushing of the IF structure into flakes beyond a critical value [19]. It has been demonstrated that 200 nm is the maximum size for the formation of the WS₂ IF hollow structure, above which a platelet structure becomes the most stable structure [19]. Because the sizes of sintered WO₃ nanoparticles were normally beyond 200 nm, WS₂ flakes were generated rather than IF nanoparticles.

4.2 Fabrication of WS₂ IF nanoparticles *via* template reaction route

The synthesis procedure of WS₂ IF nanoparticles was similar to that used for WS₂ nanoflakes. However, instead of Ar, a H₂/Ar mixture gas was used to create a reducing atmosphere. In this section, the relationship between the processing parameters and morphologies of the final WS₂ products was investigated. In addition, the effects of H₂ and the relevant reaction mechanism were examined in detail.

4.2.1 Effect of sulphur amount

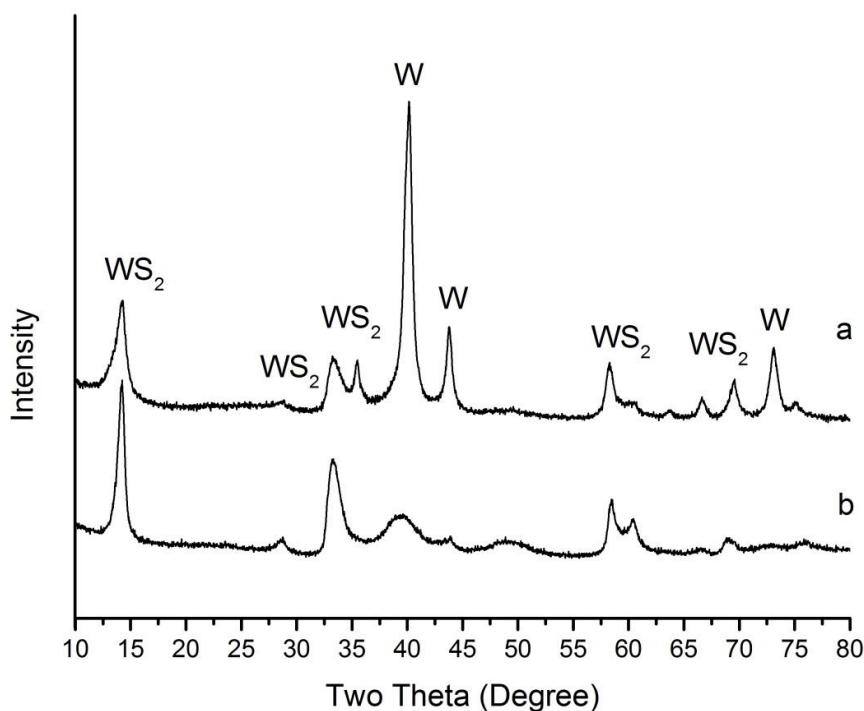
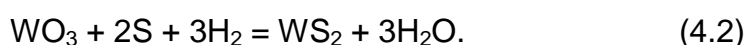


Figure 4.8 XRD patterns of samples resulting from 1-h firing at 750°C in H₂/Ar atmosphere using (a) 9 times excessive S and (b) 29 times excessive S.

Figure 4.8 presents the XRD patterns of the samples resulting from 1-h firing at 750°C in a H₂/Ar atmosphere using different amounts of S. In Figure 4.8a, some high W peaks are observed along with relatively low WS₂ peaks. Similar to the case in the Ar atmosphere, the reaction was far from completion when 9 times excessive S was used, indicating that H₂ did not accelerate the reaction. The generation of W in the sample followed a two-step reaction. First, because most of the S vapour was blown away rapidly by the flowing gas and did not participate in the sulphidation, some WO₃ was left unreacted after all the sulphur was consumed. Then, because of the long holding time, the time was still sufficient to complete the reaction of WO₃ with H₂ when no sulphur remained, leading to the formation of W. This procedure was confirmed by the XRD pattern of the sample synthesised using 29 times excessive S. When the amount of S was sufficient, a pure WS₂ sample was produced because of the following reaction (Figure 4.8b):



4.2.2 Effect of temperature

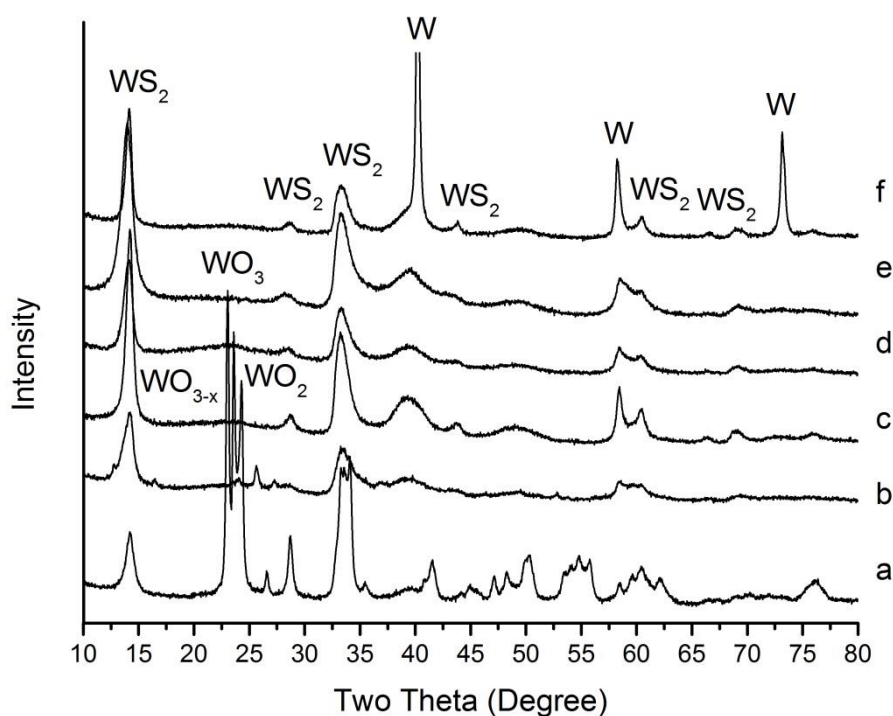


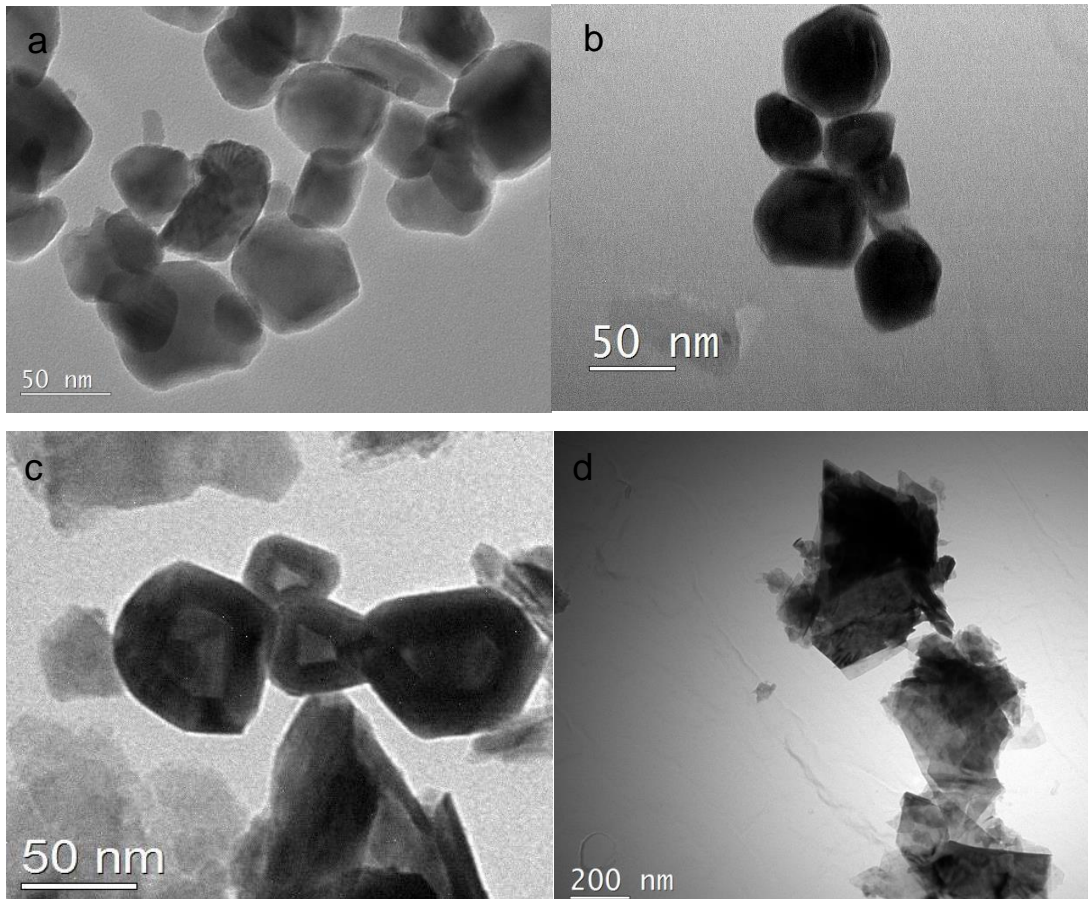
Figure 4.9 XRD patterns of samples resulting from 1-h firing in H_2/Ar atmosphere at (a) 450°C, (b) 600°C, (c) 700°C, (d) 800°C, (e) 850°C and (f) 950°C.

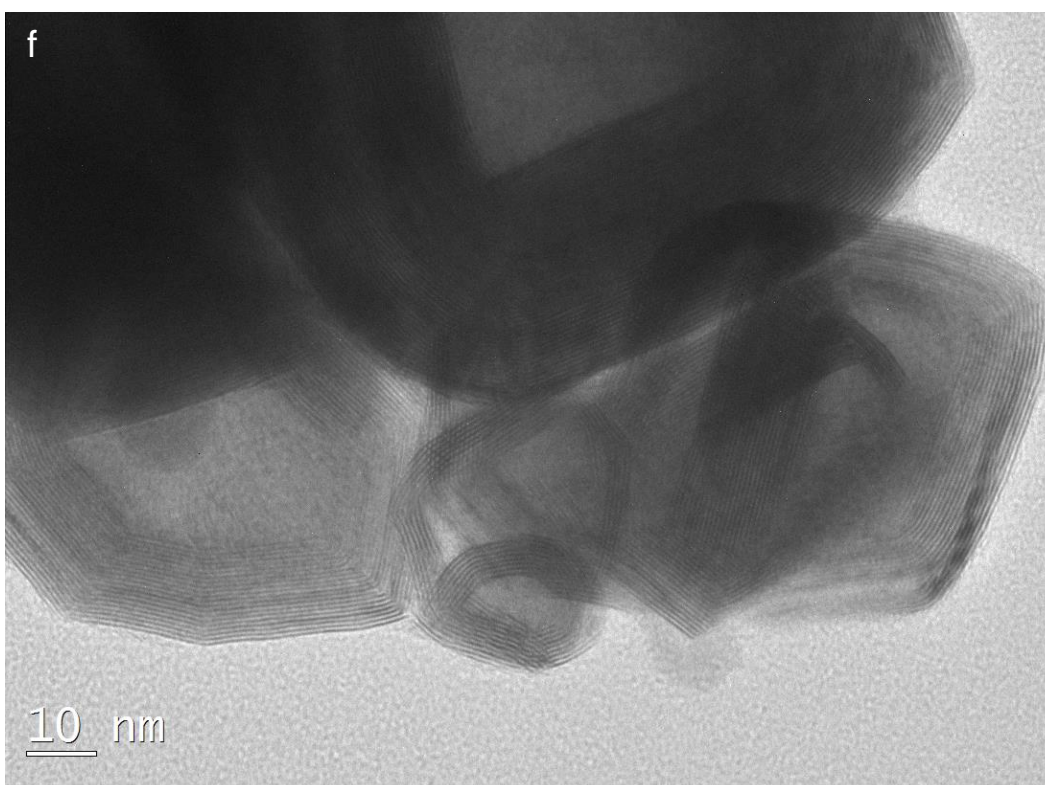
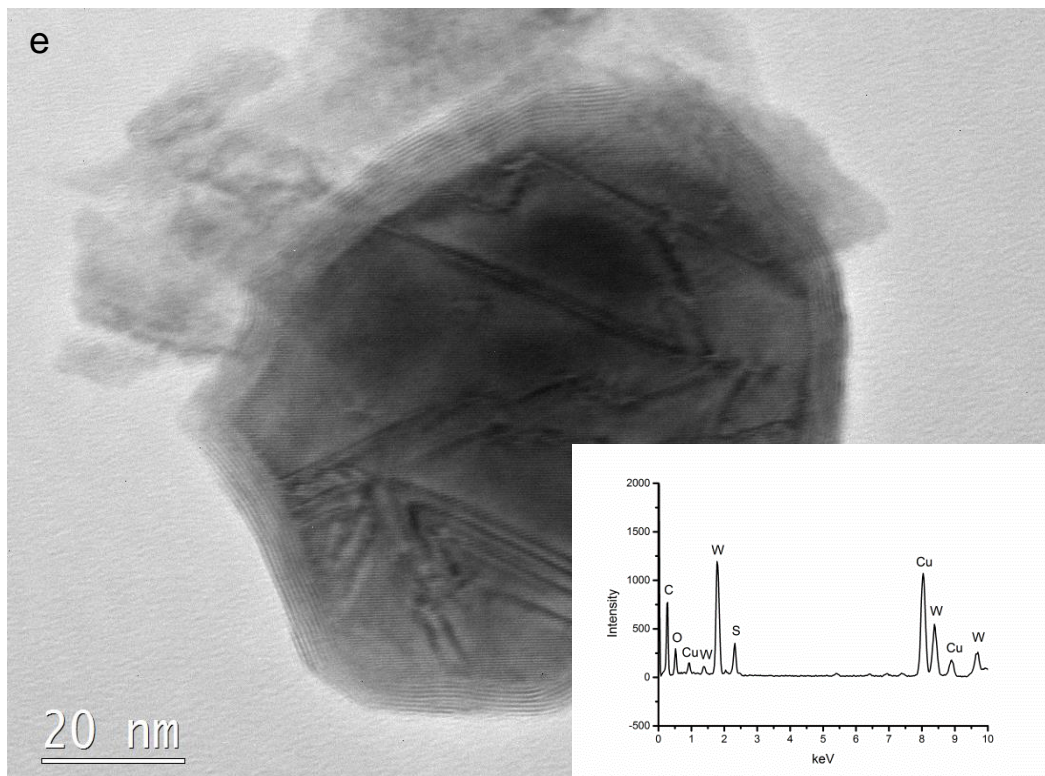
Figure 4.9 presents the XRD patterns of the samples resulting from 1-h firing at 450, 600, 700, 800, 850 and 950°C in an Ar/H_2 atmosphere. At 450°C, WS_2 was formed, while WO_3 remained as the primary phase, indicating that 450°C was sufficiently high for the formation of WS_2 in Ar/H_2 under this condition (Figure 4.9a). In addition, no S was detected, indicating its depletion. The remaining unreacted WO_3 was attributed to the slow reaction rate between WO_3 and S at this temperature and the rapid evaporation rate of S. Therefore, this reaction could not be completed before the depletion of S. When the temperature was increased to 600°C, WS_2 became the primary phase, while minor WO_2 and WO_{3-x} instead of WO_3 were detected (Figure 4.9b), which was due to the reduction by H_2 . Upon further increasing the temperature to 700°C, little WO_{3-x} was detected with strong WS_2 peaks, indicating that this reaction was close to completion (Figure 4.9c). WO_3 disappeared, and WS_2 was observed to be the only phase in the sample heated at 800 and 850°C (Figure 4.9d and e),

indicating that the reaction rate was sufficiently high at these temperatures to complete the reaction before all the S powers were depleted. By weighting the products (0.225g and 0.236g for 800°C and 850°C samples respectively), the yield of this reaction was estimated to be 92.95%. Upon further increasing the temperature to 950°C, characteristic peaks of W appeared (Figure. 4.9f). At this high temperature, the rate of reduction by H₂ was higher than that of the sulphidation [4]; therefore, WO₃ tended to be reduced to W directly rather than through sulphidation. Although the W formed from H₂ reduction could also further react with S to form WS₂, the reaction rate was much lower than that between WO₃ and S [20], leading to the formation of large amounts of W. Based on Scherrer equation:

$$d_c = \frac{k\lambda}{\beta \cos \theta}$$

the grain sizes of sample generated after 850°C is 6.62nm.





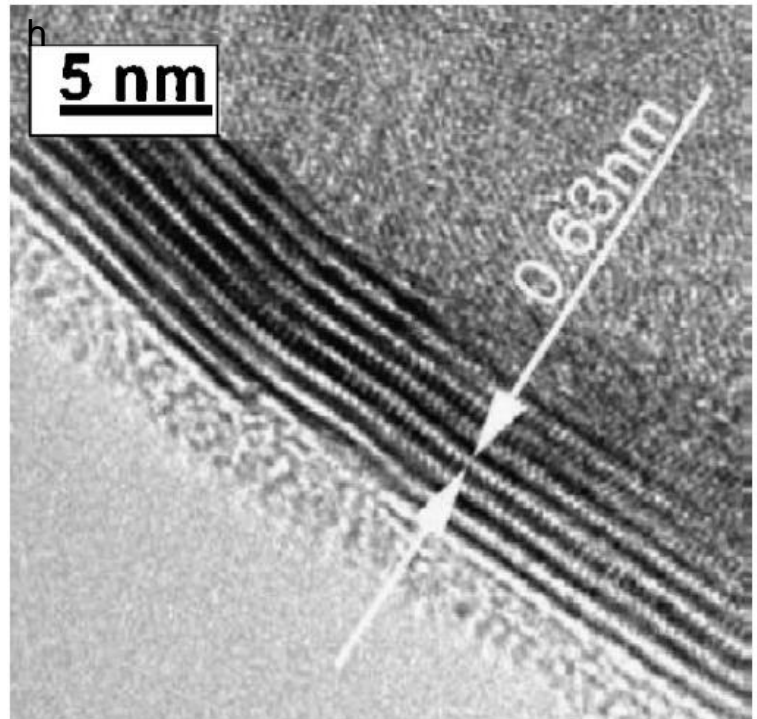
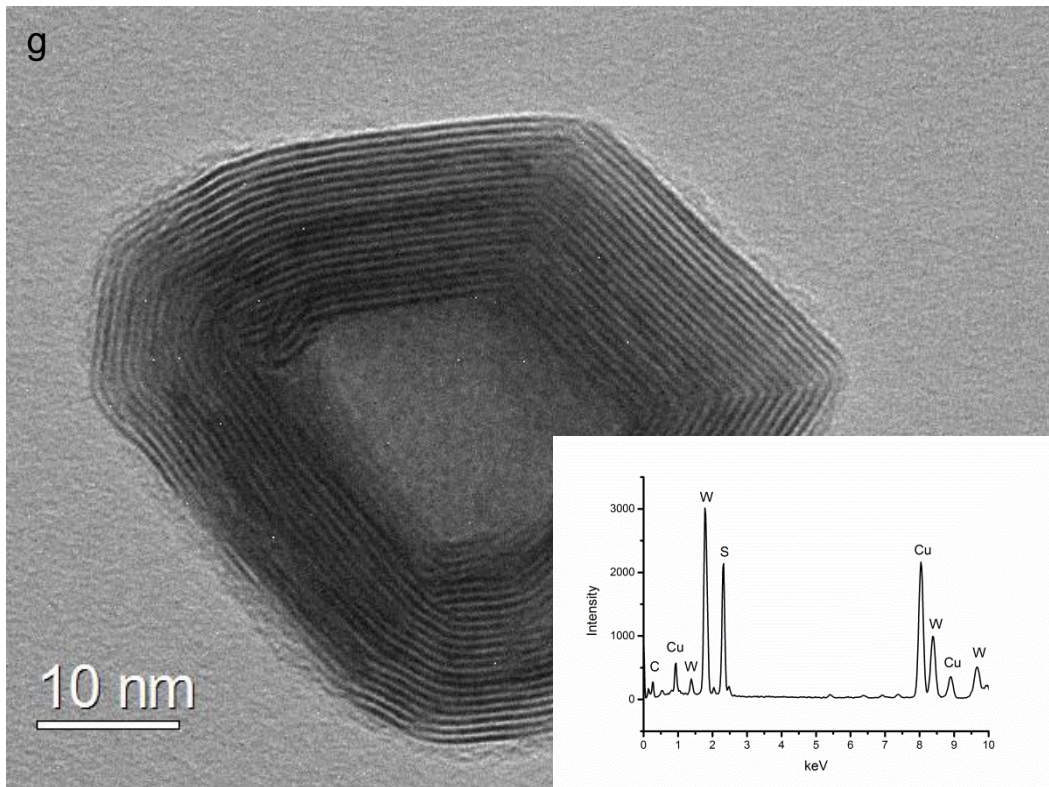


Figure 4.10 HRTEM images of (a) WO₃ raw material and samples resulting from 1-h firing in H₂/Ar atmosphere at (b, e) 700°C, (c, f and g) 850°C, and (d) 950°C. The insets in (e, g) are EDS spectra of the corresponding particles. (h) Typical morphology of synthesised WS₂ IF nanoparticle by Yang et al. [14]

In Figure 4.10, HRTEM images of the WO₃ raw material and samples resulting from 1-h firing at 700°C, 850°C and 950°C under H₂/Ar atmosphere are

presented. In Figure 4.10b, some nanoparticles with sizes of approximately 50 nm on average are observed. A high-magnification image reveals that these nanoparticles actually exhibit a core-shell structure (Figure. 4.10e). A layered shell with a thickness of approximately 10 nm was formed on the surface of each nanoparticle. The lattice distance of this shell was measured to be 0.63 nm, which was close to the interplanar spacing of the WS_2 (002) plane. In addition, the corresponding EDS spectrum reveals that this nanoparticle was composed of W, S and O. Combined with the XRD result (Figure 4.9c), this result verified that WS_2 - WO_{3-x} core-shell nanoparticles were generated at 700°C. Upon increasing the temperature to 850°C, some nanoparticles with hollow cores were formed (Figure 4.10c). The average size of the nanoparticles in both samples was approximately 50 nm, which is close to that of the WO_3 raw material (60 nm on average) (Figure 4.10a), indicating that the reaction might follow the template growth mechanism. The inner diameters of these hollow nanoparticles were close to half of the outer diameters, suggesting that these nanoparticles had relatively thick walls. In addition, these nanoparticles were faceted crystals rather than common spherical crystals. A higher magnification image clearly shows their hollow structure with diameters ranging from 20 to 60 nm (Figure 4.10f). Typical continuous WS_2 (002) layers were observed. In addition, the number of layers (6 to 40 layers) was almost proportional to the diameter of the nanoparticles. In Figure 4.10 g, an exploded view of an individual nanoparticle is shown. The nature of the closed nanoparticle is clearly manifested in this image. The size of this nanoparticle is 45 nm with 19 layers, and the interlayer spacing is 0.63 nm, which is slightly larger than that (~0.62 nm) of the bulk 2H- WS_2 . This expansion was attributed to the generation of strain because of the curvature of the layers. Based on the EDS analysis, the elemental composition was confirmed to be W and S (the C and Cu signals detected were from the C films and Cu carrier grids used). In addition, few dislocations and disconnections could be observed on the shell, indicating good crystallisation. This nanoparticle had a highly faceted structure with a distinct angle at approximately 90°. Therefore, the strain energy in this structure was higher than that in a spherical structure [8]. When the temperature was sufficiently high, the stored energy tended to be relieved by unfolding the structure, leading to the generation of WS_2 flakes. When the temperature was increased to 950°C, the morphology of the produced WS_2 was transformed to

nanoflakes with an average size of approximately 300 nm (Figure 4.10d). As mentioned above, WO_3 was first reduced to W and then reacted with S to form WS_2 at this temperature. According to Li et al., flake-shaped WS_2 would form from the W-S reaction at $>600^\circ\text{C}$. This formation might be attributed to the poor high temperature stability of the initially formed WS_2 coating on the W cores [20]. Therefore, WS_2 nanoflakes were generated at this temperature rather than IF nanoparticles.

WS_2 IF nanoparticles were produced previously by Yang et al. *via* a similar route [14]. Compared with their products (IF nanoparticles with approximately 5-6 layers) (Figure 10 h), most of the synthesised WS_2 IF nanoparticles in this work had many more layers (~19 layers). The increase of layers led to better mechanical properties [21] and thus could extend their potential applications. Although these two routes were based on the same reaction, different processing parameters resulted in different morphologies. In the present work, much more excessive S was used, along with various amounts of flowing H_2 . However, in the work of Yang et al., much smaller amounts of excessive S (molar ratio of WO_3 and S was 1:3) were used, and a fixed amount of H_2 was sealed in the reaction tube. In addition, the raw material mixture was heated gradually at $10^\circ\text{C}/\text{min}$ to the target temperatures rather than instant heating at the target temperature in this route. Yang et al. did not explain the reason for the formation of thin walls. However, based on our results, this formation should be closely related to the slow heating rate and usage of a small amount of reactants, which might hinder further sulphurisation.

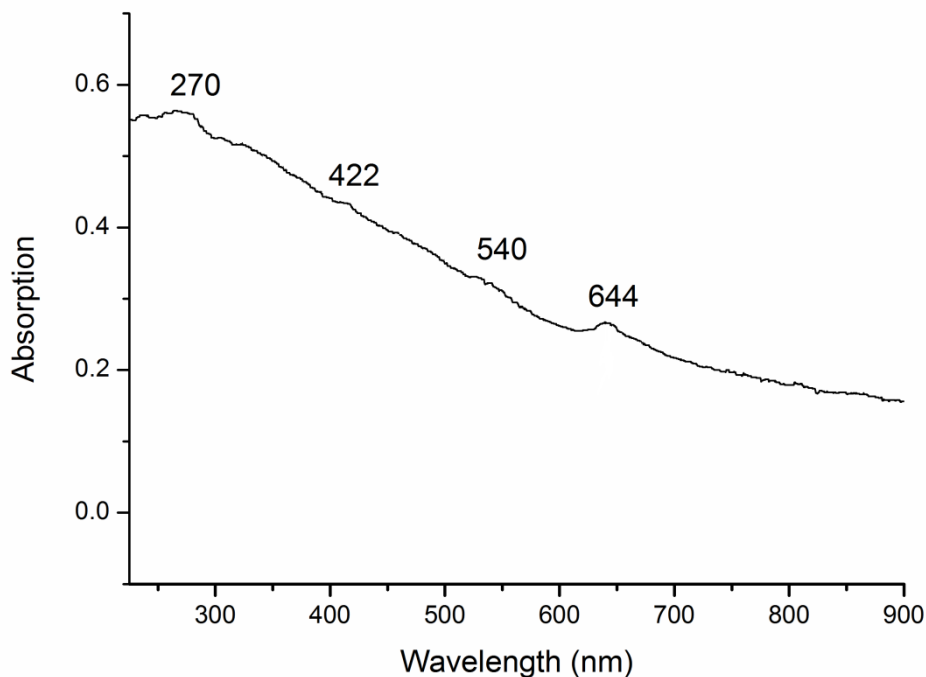


Figure 4.11 UV-vis spectrum of sample resulting from 1-h firing in H_2/Ar at $850^\circ C$.

The optical absorption spectrum was measured for the phase pure WS_2 sample resulting from 1-h firing at $850^\circ C$. According to Figure 4.11, the absorption of the UV beam was gradually increased with decreasing wavelength. This shoulder-form spectrum is usually related to two properties: (1) a wide band gap and (2) a tiny particle size [22]. According to Chen et al. [23], bulk WS_2 material has two characteristic peaks assigned to A and B excitons at 636 and 525 nm, respectively. These two excitons can also be observed in Figure 4.11 as a weak absorption edge and obvious absorption peak, indicating that this sample was composed of the WS_2 phase, which is consistent with the XRD observation. Nevertheless, the positions of these two excitons were shifted towards higher wavelengths to 644 nm and 540 nm for A and B excitons, respectively. A similar red shift of A and B excitons of WS_2 IF nanoparticles was also observed by Tenne et al. when the number of layers was larger than 10 [24]. This shift was attributed to the curvature of the layers in WS_2 IF nanoparticles, which resulted in the lattice expansion of two adjacent layers along the c axis. It has been demonstrated that the lattice expansion could cause a decrease of the band gap and thus the red shift of excitons [25]. In addition to these two peaks, two

additional peaks centred at 270 and 422 nm are observed, which correspond, respectively, to the blue shifts of A and B excitons of WS_2 peaks caused by the quantum confinement effect of the WS_2 IF nanoparticles. This effect was also observed by Tenne and co-workers [25]. Based on their research, the red or blue shift of UV peaks is only related to the number of WS_2 layers regardless of their diameters. For example, when the number of layers was less than 8, a blue shift occurs; otherwise, a red shift occurs. Therefore, the occurrence of both blue and red shifts in the present case indicated that the numbers of WS_2 layers in the as-synthesised WS_2 IF nanoparticles were variable.

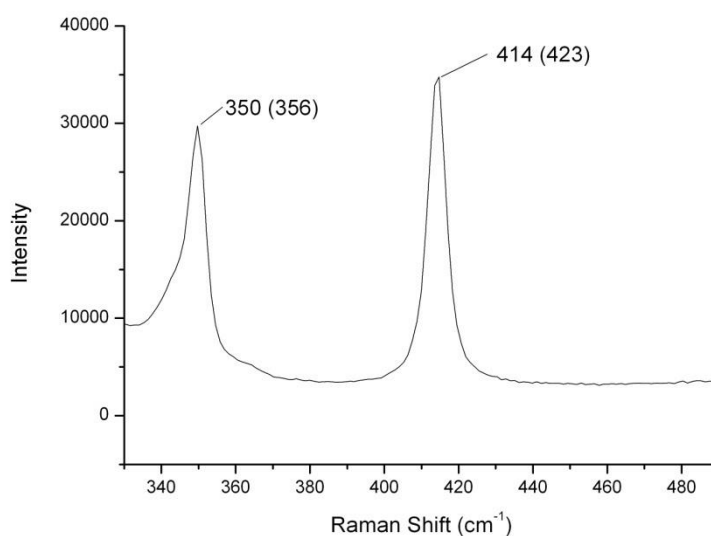


Figure 4.12 Raman spectrum of as-synthesised WS_2 IF nanoparticles from 1-h firing in a H_2/Ar atmosphere at $850^\circ C$

In Figure 4.12, the Raman spectrum of the WS_2 IF nanoparticles is presented. Two strong peaks are observed, which match with those reported for single-crystal WS_2 [26], verifying the presence of pure WS_2 in the sample. The two peaks centred at 350 cm^{-1} (E_{2g}) and 414 cm^{-1} (A_{1g}), respectively, are slightly lower than those (shown in the bracket) for bulk WS_2 . Such a low shift was also observed for MoS_2 IF nanoparticles and was attributed to the curved WS_2 layers [27, 28]. This result additionally verified the formation of WS_2 IF nanoparticles in the sample.

4.2.3 Effect of H₂ atmosphere

As presented and discussed above (sections 4.1), WS₂ nanoflakes were generated instead of IF nanoparticles when H₂ was absent from the reaction. In other words, H₂ played an important role in the synthesis of WS₂ IF nanoparticles. To further investigate this role, additional tests were performed under different atmospheres.

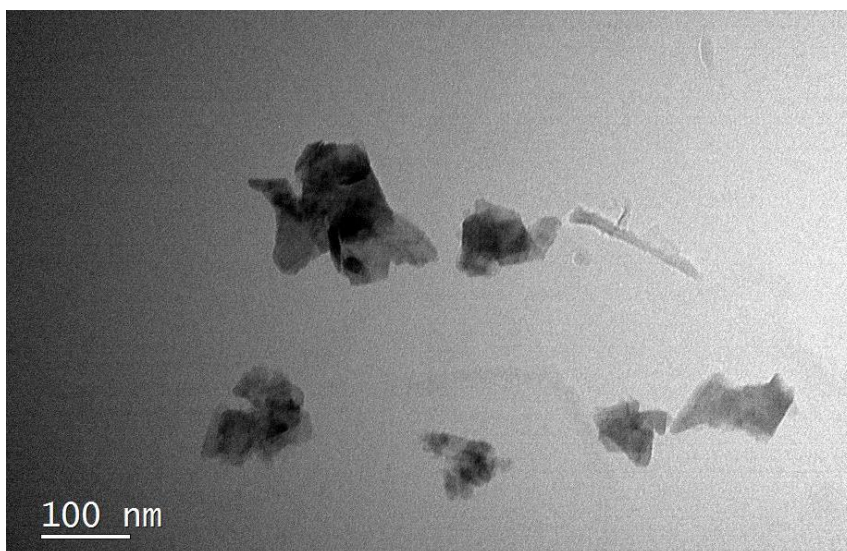


Figure 4.13 TEM image of sample resulting from 1-h firing at 600°C in H₂/Ar atmosphere.

As illustrated in Figure 4.9b, WS₂ was formed at 600°C in a H₂/Ar atmosphere. However, WS₂ nanoflakes with an average size of 100 nm were generated rather than the expected IF nanoparticles (Figure 4.13). In this case, although H₂ was used as a reducing agent, the low reaction temperature caused a slow reduction rate, which might cause the sintering of WO₃ before sulphidation and thus the formation of WS₂ nanoflakes.

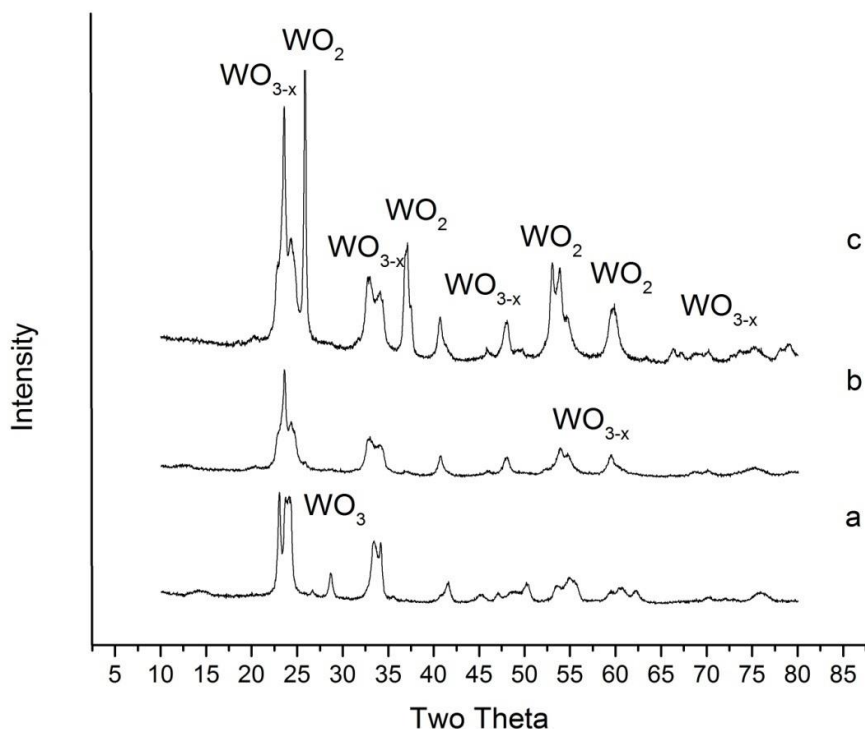


Figure 4.14 XRD patterns of (a) WO_3 raw materials after 30-min firing at (a) 600°C in Ar, (b) 600°C in a H_2 /Ar atmosphere, and (c) 800°C in H_2 /Ar.

The effect of H_2 on the reduction of WO_3 was investigated by heating WO_3 raw materials at various temperatures in Ar or a H_2 /Ar atmosphere. WO_3 was stable after firing at 600°C in Ar (Figure 4.14a). When H_2 was introduced, WO_{3-x} was formed instead, indicating that WO_3 was partially reduced by H_2 (Figure 4.14b). WO_{3-x} is an intermediate product from the reduction of WO_3 , and its formation was due to either low temperature or insufficient reaction time. When the temperature was increased to 800°C, some WO_{3-x} was further reduced to WO_2 (Figure. 4.15c). Based on the above results, the reduction procedure of WO_3 by H_2 could be summarised as



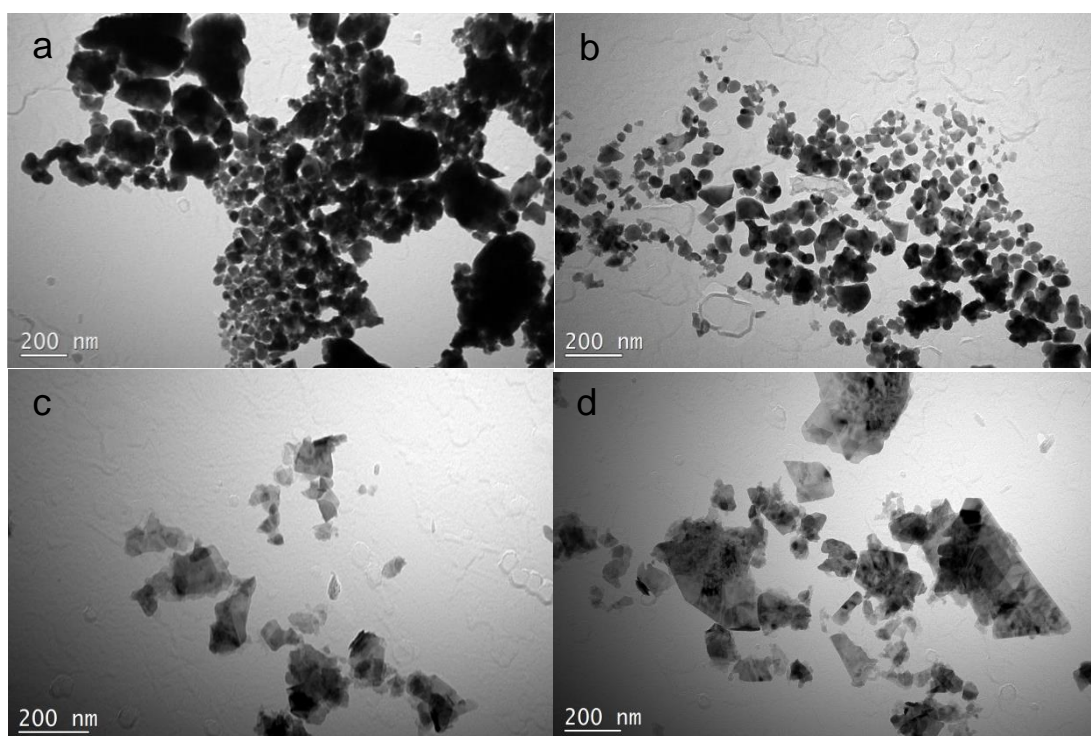


Figure 4.15 TEM images of WO_3 fired at 600°C for 30 min in (a) Ar and (b) H_2/Ar , and the products resulting from 1-h firing of WO_{3-x} with S at (c) 750°C and (d) 850°C in Ar.

According to Figure 4.15a, most of the WO_3 nanoparticles were agglomerated, and some large particles (up to approximately 200 nm) were also observed in the sample after firing at 600°C in Ar. Although 600°C did not reach the normal sintering temperature of bulk WO_3 , some of the WO_3 nanoparticles could still be sintered due to their nanosize effects. Therefore, large WS_2 nanoflakes were generated when H_2 was absent. Numerous WO_3 nanoparticles were sintered before reacting with S and preferred to form large WS_2 flakes after reaction [29]. The morphology of the sample was changed when H_2 was introduced into the reaction system. Most of the resulted WO_{3-x} retained the original nano size with little sintering (Figure 4.15b). This finding occurred because WO_{3-x} had a higher melting point (as high as 1700°C) [30] than WO_3 (1473°C), and thus, WO_{3-x} was more difficult to be sintered.

As analysed above (section 4.1.4), when H_2 was absent, WS_2 nanoflakes were formed due to the lack of oxygen vacancies, which would cause sintering of WO_3 before sulphidation. When WO_{3-x} was used as the raw material, this compound not only had a high sintering temperature but also contained

numerous oxygen vacancies. According to Tenne et al., these oxygen vacancies on WO_{3-x} were vital to the formation of IF nanoparticles [4]. Therefore, it was reasonable to expect the production of WS_2 IF nanoparticles from the reaction of WO_{3-x} with S. However, after the reaction of produced WO_{3-x} with S in Ar, WS_2 nanoflakes were produced rather than the expected IF nanoparticles. Unlike the product obtained from the reaction between WO_3 and S, which was approximately 300 nm in size (Figure 4.3c), the produced nanoflakes were much smaller (an average size of approximately 100 nm). This smaller size was attributed to the high sintering temperature of WO_{3-x} (Figure. 4.15c), and WS_2 was formed before the sintering of WO_{3-x} . In this case, although O vacancies were generated before sulphidation, which would promote the diffusion of S atoms as described in the literature [4], the absence of H_2 led to the change of products from H_2O to SO_2 . This change might cause the crushing of continuous WS_2 layers because S atoms not only diffused into oxides but also diffused out, which broke the diffusion synergy between O and S atoms. The sizes of the produced nanoflakes were increased to 200-400 nm when the reaction temperature was increased to 850°C (Figure 4.15d) due to the sintering of raw materials and crystal growth of the formed WS_2 nanoflakes.

4.2.4 Comparison with H₂S involved reaction

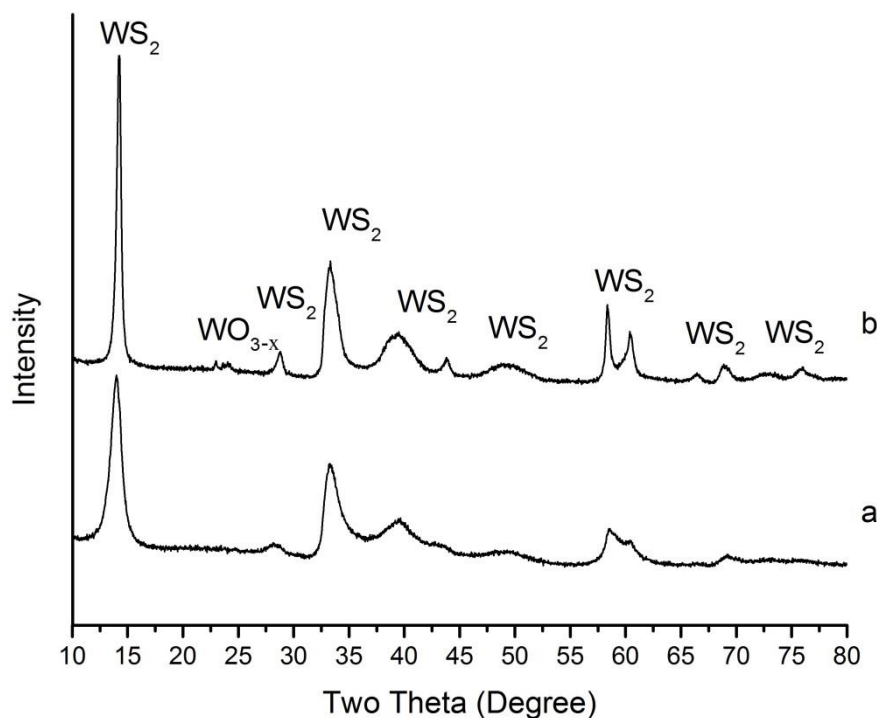
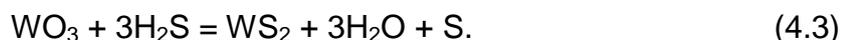


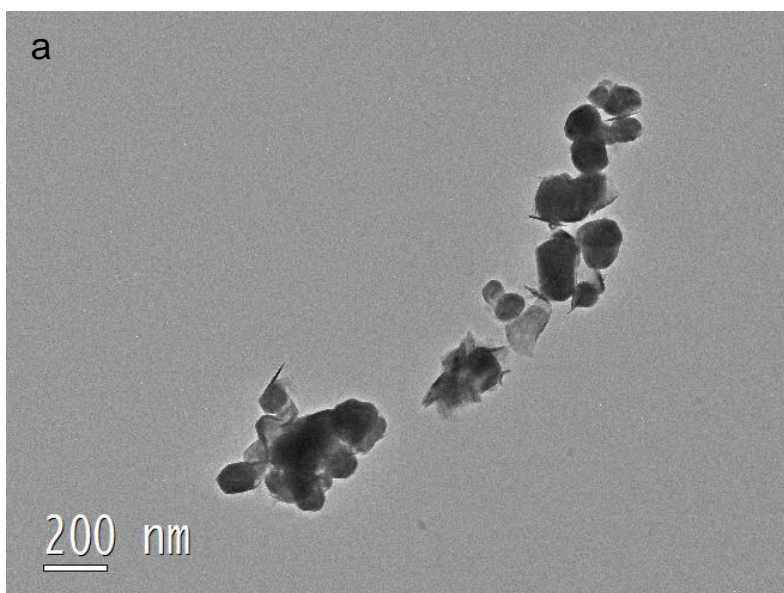
Figure 4.16 XRD patterns of samples resulting from 1-h firing at 850°C *via* the reaction (a) between WO₃ and S in a H₂/Ar atmosphere and (b) between WO₃ and H₂S in an Ar atmosphere.

As mentioned in the literature review (Chapter two), WS₂ IF nanoparticles and nanotubes have already been prepared on a large scale *via* the reaction between WO₃ nanoparticles and H₂S [8]:



In addition, because there is a reaction balance among H₂, S and H₂S at high temperature, the reaction mechanisms of this reaction and Tenne et al.'s technique [8] are quite similar. Therefore, it is necessary to compare the product in the present case with that synthesised in the H₂S atmosphere. To obtain accurate results, the same amount of WO₃ nanopowder was heated at 850°C for 1 h in the Ar/H₂S atmosphere. In Figure 4.16, the XRD patterns of the samples resulting from the sulphidation process by S and H₂S are presented. According to Figure 4.16, WS₂ was formed as the primary phase in the samples resulting from both routes. However, small amounts WO_{3-x} were also observed

in the sample prepared *via* H₂S sulphidation. Therefore, it could be concluded that the reaction extent of reaction (4.2) was higher than that of reaction (4.3).



Figures overleaf

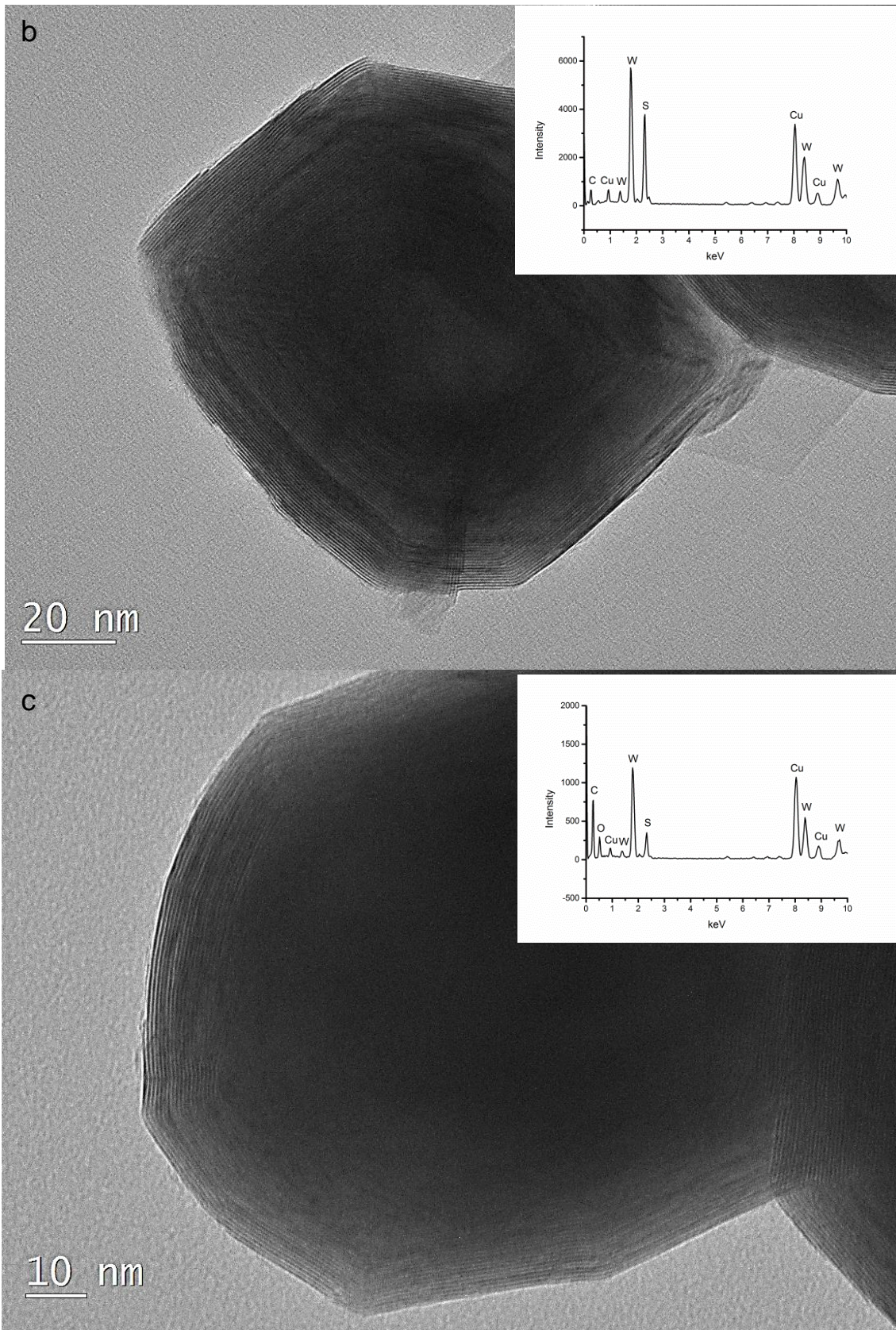


Figure 4.17 (a-c) TEM images of samples resulting from 1-h firing at 850°C in a H₂S/Ar atmosphere. The insets in (b, c) are EDS spectra of the nanoparticles.

Figure 4.17 presents HRTEM images of the sample whose XRD pattern is shown in Figure 4.16. Most of the prepared WS₂ nanoparticles were sintered together with larger diameters (approximately 100 nm on average) than the sample prepared *via* reaction (2) (Figure 4.17a). In addition, unlike the previously synthesised sample, which exhibited a bright interior in almost every particle, nanoparticles with homogenous contrast distribution were observed in the HRTEM image, indicating that the nanoparticles might not have hollow structures. At higher magnification, nanoparticles with two types of morphologies can be observed. In Figure 4.17b, a nanoparticle (~100 nm in diameter) with a typical nest-like structure is observed. Compared with the nanoparticles prepared *via* reaction (2), this nanoparticle has a much thicker wall (approximately 45 nm thicker). In addition, a small bright core with a diameter of approximately 25 nm could be observed, indicating that this nanoparticle had a hollow structure. Because of the large wall thickness and small core diameter, it was difficult for the TEM beam to penetrate through this nanoparticle, and thus, the bright core was hardly observed under low magnification. Further measurement on these WS₂ shells revealed that the lattice fringe was approximately 0.63 nm, which was the same as that for the previously synthesised nanoparticles. The EDS spectrum (inset in Figure 4.17b) also confirms the presence of WS₂. The presence of Cu peaks in the EDS pattern is due to the usage of a Cu grid on the carbon film. Some layer disconnections were also observed on corners of this nanoparticle, which are most likely due to the release of the stored bending energy, which was quite high in a large WS₂ IF nanoparticle. In addition to these hollow nanoparticles, some other nanoparticles that have a different core-shell structure were observed in the same sample. As observed in Figure 4.17c, this type of nanoparticle has a large diameter of approximately 100 nm and a relatively thin shell of approximately 10 nm. The lattice fringe of the shell measured (approximately 0.63 nm), along with the XRD pattern (Figure 4.16b), confirmed that the shell was composed of WS₂. Compared with the EDS pattern in Figure 4.18b, a relatively strong oxygen signal was detected in the present case. The combination of this EDS pattern with the corresponding XRD pattern confirmed that the core was composed of tungsten oxide.

At 850°C, WO_3 nanoparticles were easily sintered in a short time. When S was used as the reducing agent, a large amount of S vapour rapidly diffused to and then reacted with the WO_3 nanoparticles. Therefore, the formation of the WS_2 shell was very fast on the surface of WO_3 nanoparticles, which isolated the particles and prevented their subsequent sintering. When the combination of S and H_2 was replaced by H_2S , the flow rate of S was restricted to 20 ml/min, leading to the relatively slow conversion rate from WO_3 to WS_2 . Therefore, slight sintering of WO_3 nanoparticles occurred during the formation of the closed WS_2 shell, resulting in the generation of larger nanoparticles. Because of the large unreacted tungsten oxide cores and slow H_2S flow rate, the sulphidation process was much slower than the process in reaction (2), leading to the incomplete reaction after firing under the same conditions.

4.2.5 Growth mechanism of WS_2 IF nanoparticles

Because the firing temperature was much higher than the boiling point (445°C) of S, the reaction between WO_3 and S was a typical solid-gas reaction process. According to the TEM observations (Figure 4.10), the sizes of the formed WS_2 IF nanoparticles were similar to those of the WO_3 raw material. Therefore, WO_3 acted as a template during the conversion to WS_2 . To verify this behaviour, some partially reacted WO_3 nanoparticles were produced and investigated.

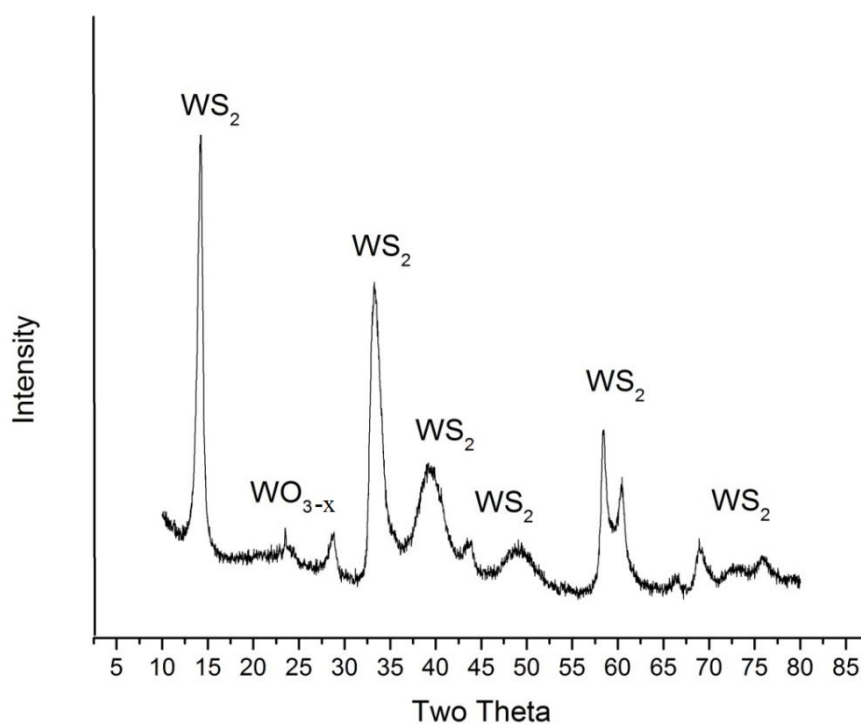


Figure 4.18 XRD pattern of sample resulting from 5-min firing at 850°C in H_2/Ar .

In Figure 4.18, the XRD pattern of sample resulting from firing at 850°C for 5 min under a H₂/Ar atmosphere is presented. When the holding time was decreased to 5 min, WS₂ became the predominant phase in this sample, while minor WO_{3-x} could also be detected, indicating that reaction (2) was very fast at this temperature. This WS₂-WO_{3-x} composite was clearly the reaction intermediate of this reaction.

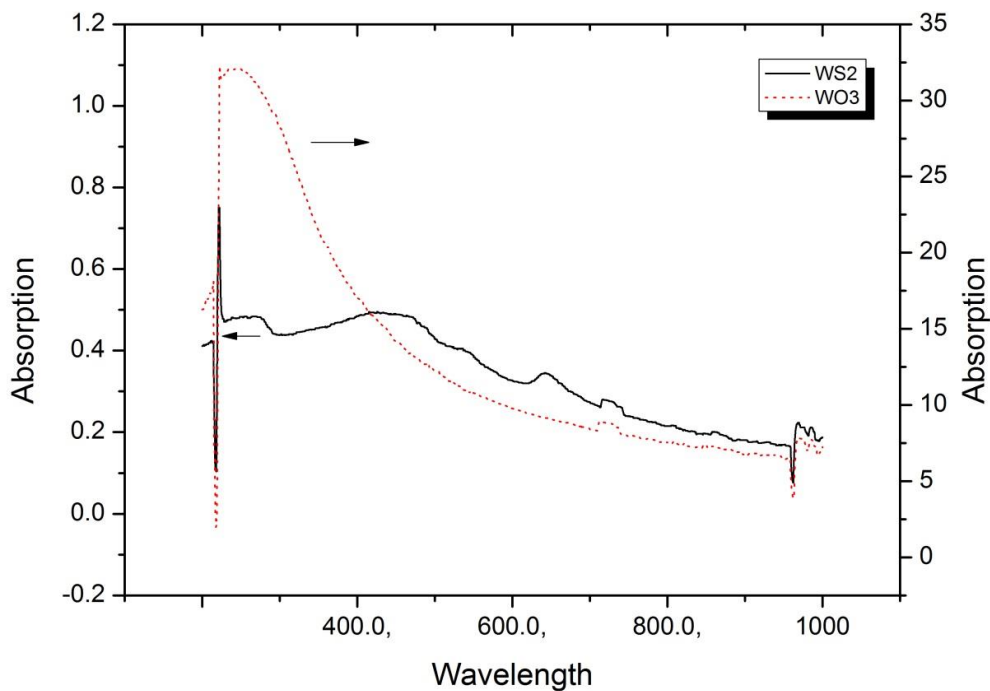


Figure 4.19 UV spectra of WO_{3-x} nanoparticles (dotted line) and WS₂ resulting from 5-min firing at 850°C in H₂/Ar.

Figure 4.19 presents the UV spectra of raw WO_{3-x} nanoparticles and the WS₂ sample. Because of the small sizes, the UV spectrum of WO_{3-x} nanoparticles exhibits a typical shoulder shape with a gradual decrease of absorption from short wavelengths to long wavelengths as well as a characteristic peak centred at 720 nm. In the UV spectrum of the WS₂ sample resulting from 5-min firing at 850°C in H₂/Ar, the characteristic peak of WO_{3-x} is detected, indicating the presence of WO_{3-x} in this sample. In addition, four additional peaks are also observed, centred at 270, 450, 540 and 650 nm, respectively, which is consistent with the UV spectrum of the WS₂ IF nanoparticles presented in

Figure 4.11. Therefore, it could be concluded that this sample was composed of WS₂ IF nanoparticles and WO₃.

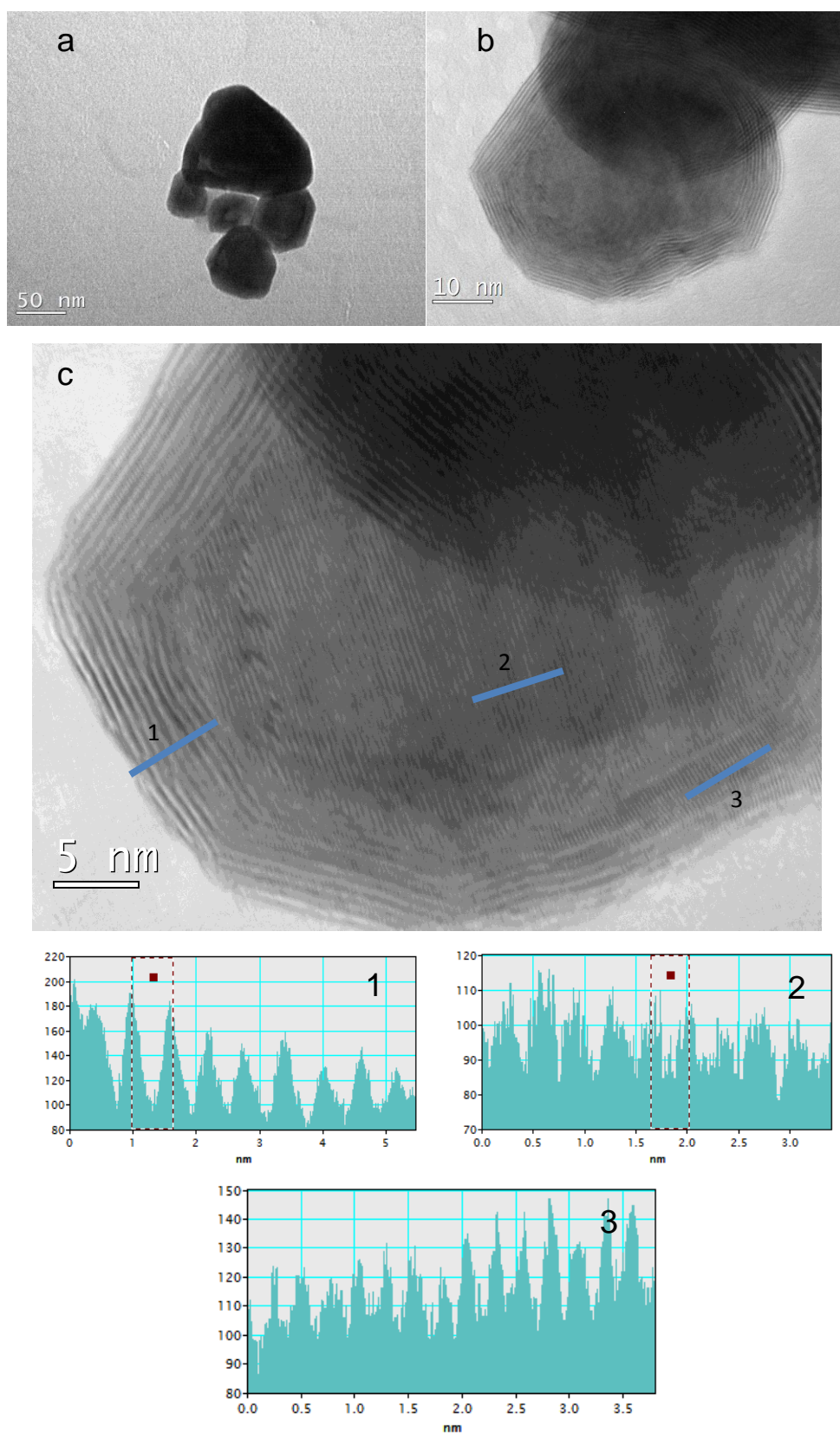


Figure 4.20 (a) TEM and (b, c) HRTEM images of sample after 5-min firing at 850°C under H₂/Ar. The line profiles show different interlayer spacings on lines 1, 2 and 3.

Figure 4.20 presents a series of TEM images revealing the morphology of the reaction intermediate. According to Figure 4.21a, some dense nanoparticles with average diameters of approximately 60 nm were produced rather than hollow IF nanoparticles. A typical nanoparticle with a core-shell structure was observed from the corresponding HRTEM image (Figure 4.20b). Three different interlayer spacings could be observed on the nanoparticle, indicating that this nanoparticle might be composed of different materials (Figure 4.20c). The interlayer spacing of the 5-nm-thick outer shell (approximately 10 layers) was measured to be 0.63 nm, which was the typical lattice spacing of the WS_2 IF nanoparticles. The interlayer spacing of the core was measured to be approximately 0.38 nm, which is consistent with the lattice spacing of the (001) plane of WO_{3-x} . This finding, combined with the previous XRD and UV results, confirmed that the reaction intermediates were WS_2 - WO_{3-x} nanoparticles with a core-shell structure. In addition to these two lattice fringes, some lattice fringes were also observed on the WS_2 shell. The interlayer spacing was approximately 0.28 nm, which matched well with the distance between the WS_2 (100) planes, indicating that this nanoparticle was covered by a curved WS_2 coating.

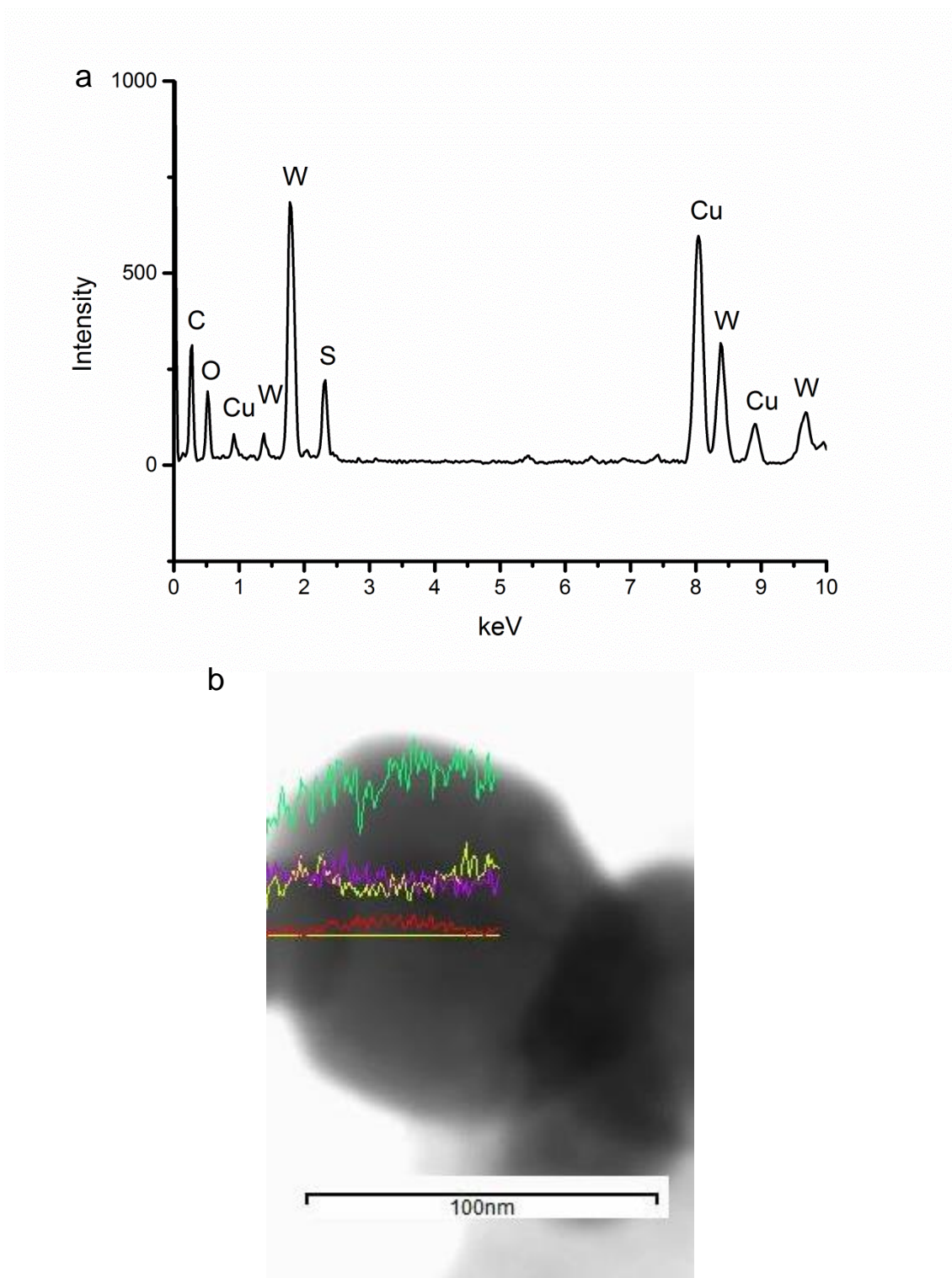


Figure 4.21 (a) EDS spectrum of nanoparticle shown in Figure 4.20. (b) EDS linear analysis along the nanoparticle. The green, yellow, purple and red lines represent C, S, W and O, respectively.

The EDS spectrum on a nanoparticle confirms that the nanoparticle contained three main elements: W, S and O (the signals of C and Cu were from the

carbon films and Cu grids) (Figure 4.21a). According to the EDS linear scan (Figure 4.21b), W, S and O elements were detected on the entire particle. On the shell of this nanoparticle, only signals of W and S were detected. With further detection on the particle interior, O was detected as well as W and S, indicating the presence of tungsten oxide. Combined with the XRD (Figure 4.18) and TEM analysis (Figure 4.20), these results verified that a WO_{3-x} core was enclosed in a WS_2 shell, forming a typical WS_2 - WO_{3-x} core shell nanoparticle structure.

Based on the above analysis, the following reaction mechanism can be suggested. WO_3 acted as a template for the solid-gas reaction between this compound and S. When the temperature is high enough, WO_3 is first reduced by H_2 to form tungsten suboxide (WO_{3-x}) and finally W *via* the radial diffusion of H_2 into the interior of the original WO_3 nanoparticles from all directions. The involvement of H_2 has three important effects on the formation of IF nanoparticles: (1) Suppression of the sintering of WO_3 nanoparticles can occur before their reaction with S (Figure 4.15b), which otherwise will lead to the formation of 2H- WS_2 platelets. (2) Over-reduction of WO_3 nanoparticles to W occurs if the reaction temperature is too high. Because W is appreciably denser than WO_{3-x} , the diffusion of S atoms into the core of W is very difficult. WS_2 tends to be formed only on the surface of W particles, and thus, the reaction cannot reach completion [20]. In addition, because of the high temperature, the formed WS_2 were in more stable flake structures rather than IF structures. (3) The produced WO_{3-x} contained numerous oxygen vacancies, which provide channels for the interdiffusion of O and S. The initially formed WS_2 encapsulates unreacted tungsten oxide cores, leading to the formation of WS_2 - WO_{3-x} composites. Then, the sulphidation rate is dramatically reduced because both O atoms and S atoms need to diffuse through the formed WS_2 shell. Compared with S atoms, O atoms have smaller diameters and thus can easily radially diffuse through the formed WS_2 shell. The diffusion mode for S atoms is completely different from that of O atoms. Because of their large diameter, O atoms can only diffuse along the WS_2 (002) layers until reaching a defect such as a dislocation or disconnection that is large enough for them to diffuse radially through the layer to the next adjacent inner layer. Once this process transports S atoms to the growth front, the S atoms can further react with the WO_{3-x} core.

The diffusion process is slow and is controlled by temperature and the size of the WO_3 raw materials. A high temperature and small starting material size lead to fast diffusion. With the proceeding of the reaction, the WO_{3-x} cores are gradually depleted and converted into WS_2 IF hollow nanoparticles.

Conclusions

WS_2 nanoflakes were synthesised *via* reaction between WO_3 and S in an Ar atmosphere. Upon increasing the reaction temperature, the sizes of the nanoflakes were increased from approximately 200 to 500 nm. Based on the investigation of the reaction mechanism, this size enlargement was attributed to the sintering of raw WO_3 nanoparticles and further crystal growth of the produced WS_2 flakes. When H_2 was involved in the reaction, WS_2 IF nanoparticles with sizes below 100 nm were easily produced. During this reaction, H_2 played an important role in the formation of the IF structure by suppressing sintering of WO_3 and promoting S diffusion. The investigation of the reaction intermediate revealed that the reaction of WO_3 with S and H_2 (Reaction (2)) followed a template reaction mechanism. Compared with other researchers' work, this technique is an environment-friendly technique to produce well-crystallised WS_2 IF nanoparticles on a large scale.

References

- [1] K. S. Coleman, J. Sloan, N. A. Hanson, G. Brown, G. P. Clancy, M. Terrones, H. Terrones, and M. L. H. Green, "The formation of ReS_2 inorganic fullerene-like structures containing Re-4 parallelogram units and metal-metal bonds," *Journal of the American Chemical Society*, vol. 124, pp. 11580-11581, Oct 2 2002.
- [2] P. G. Li, M. Lei, X. F. Wang, H. L. Tang, and W. H. Tang, "Thermal conversion of tungsten oxide nanorods to tungsten disulfide nanoflakes," *Journal of Alloys and Compounds*, vol. 474, pp. 463-467, Apr 17 2009.
- [3] H. A. Therese, N. Zink, U. Kolb, and W. Tremel, "Synthesis of MoO_3 nanostructures and their facile conversion to MoS_2 fullerenes and nanotubes," *Solid State Sciences*, vol. 8, pp. 1133-1137, Oct 2006.

- [4] Y. Feldman, G. L. Frey, M. Homyonfer, V. Lyakhovitskaya, L. Margulis, H. Cohen, G. Hodes, J. L. Hutchison, and R. Tenne, "Bulk synthesis of inorganic fullerene-like MS(2) (M=Mo, W) from the respective trioxides and the reaction mechanism," *Journal of the American Chemical Society*, vol. 118, pp. 5362-5367, Jun 12 1996.
- [5] S. B. Sadale and P. S. Patil, "Synthesis of type-I textured tungsten disulfide thin films on quartz substrate," *Journal of Crystal Growth*, vol. 286, pp. 481-486, Jan 15 2006.
- [6] R. Tenne, L. Margulis, M. Genut, and G. Hodes, "Polyhedral and Cylindrical Structures of Tungsten Disulfide," *Nature*, vol. 360, pp. 444-446, Dec 3 1992.
- [7] Y. Feldman, E. Wasserman, D. J. Srolovitz, and R. Tenne, "High-Rate, Gas-Phase Growth of Mos₂ Nested Inorganic Fullerenes and Nanotubes," *Science*, vol. 267, pp. 222-225, Jan 13 1995.
- [8] Y. Feldman, A. Zak, R. Popovitz-Biro, and R. Tenne, "New reactor for production of tungsten disulfide hollow onion-like (inorganic fullerene-like) nanoparticles," *Solid State Sciences*, vol. 2, pp. 663-672, Oct 2000.
- [9] R. Rosentsveig, A. Margolin, A. Gorodnev, R. Popovitz-Biro, Y. Feldman, L. Rapoport, Y. Novema, G. Naveh, and R. Tenne, "Synthesis of fullerene-like MoS₂ nanoparticles and their tribological behavior," *Journal of Materials Chemistry*, vol. 19, pp. 4368-4374, 2009.
- [10] S. B. Sun, Z. D. Zou, and G. H. Min, "Synthesis of tungsten disulfide nanotubes from different precursor," *Materials Chemistry and Physics*, vol. 114, pp. 884-888, Apr 15 2009.
- [11] A. Margolin, R. Rosentsveig, A. Albu-Yaron, R. Popovitz-Biro, and R. Tenne, "Study of the growth mechanism of WS₂ nanotubes produced by a fluidized bed reactor," *Journal of Materials Chemistry*, vol. 14, pp. 617-624, Feb 21 2004.
- [12] A. Rothschild, J. Sloan, and R. Tenne, "Growth of WS₂ nanotubes phases," *Journal of the American Chemical Society*, vol. 122, pp. 5169-5179, May 31 2000.
- [13] H. A. Therese, J. X. Li, U. Kolb, and W. Tremel, "Facile large scale synthesis of WS₂ nanotubes from WO₃ nanorods prepared by a hydrothermal route," *Solid State Sciences*, vol. 7, pp. 67-72, Jan 2005.
- [14] H. B. Yang, S. K. Liu, J. X. Lil, M. H. Li, G. Peng, and G. T. Zou, "Synthesis of inorganic fullerene-like WS₂ nanoparticles and their lubricating performance," *Nanotechnology*, vol. 17, pp. 1512-1519, Mar 14 2006.
- [15] A. J. van der Vlies, G. Kishan, J. W. Niemantsverdriet, R. Prins, and T. Weber, "Basic reaction steps in the sulfidation of crystalline tungsten oxides," *Journal of Physical Chemistry B*, vol. 106, pp. 3449-3457, Apr 4 2002.

- [16] W. Tremel, "Inorganic nanotubes," *Angewandte Chemie-International Edition*, vol. 38, pp. 2175-2179, 1999.
- [17] R. Tenne, "Advances in the synthesis of inorganic nanotubes and fullerene-like nanoparticles," *Angewandte Chemie-International Edition*, vol. 42, pp. 5124-5132, 2003.
- [18] V. G. Pol, S. V. Pol, and A. Gedanken, "Micro to nano conversion: A One-Step, environmentally friendly, solid state, bulk fabrication of WS₂ and MoS₂ nanoplates," *Crystal Growth & Design*, vol. 8, pp. 1126-1132, Apr 2008.
- [19] G. Seifert, T. Kohler, and R. Tenne, "Stability of metal chalcogenide nanotubes," *Journal of Physical Chemistry B*, vol. 106, pp. 2497-2501, Mar 14 2002.
- [20] L. X. Chang, H. B. Yang, W. Y. Fu, N. Yang, J. J. Chen, M. H. Li, G. T. Zou, and J. X. Li, "Synthesis and thermal stability of W/WS₂ inorganic fullerene-like nanoparticles with core-shell structure," *Materials Research Bulletin*, vol. 41, pp. 1242-1248, Jul 13 2006.
- [21] O. Tevet, O. Goldbart, S. R. Cohen, R. Rosentsveig, R. Popovitz-Biro, H. D. Wagner, and R. Tenne, "Nanocompression of individual multilayered polyhedral nanoparticles," *Nanotechnology*, vol. 21, Sep 10 2010.
- [22] C. Y. Su, H. C. Lin, T. K. Yang, and C. K. Lin, "Structure and optical properties of tungsten oxide nanomaterials prepared by a modified plasma arc gas condensation technique," *Journal of Nanoparticle Research*, vol. 12, pp. 1755-1763, Jun 2010.
- [23] G. L. Frey, R. Tenne, M. J. Matthews, M. S. Dresselhaus, and G. Dresselhaus, "Optical properties of MS₂ (M = Mo, W) inorganic fullerene-like and nanotube material optical absorption and resonance Raman measurements," *Journal of Materials Research*, vol. 13, pp. 2412-2417, Sep 1998.
- [24] G. L. Frey, S. Elani, M. Homyonfer, Y. Feldman, and R. Tenne, "Optical-absorption spectra of inorganic fullerenelike MS₂ (M = Mo, W)," *Physical Review B*, vol. 57, pp. 6666-6671, Mar 15 1998.
- [25] J. A. Wilson and A. D. Yoffe, "Transition Metal Dichalcogenides Discussion and Interpretation of Observed Optical, Electrical and Structural Properties," *Advances in Physics*, vol. 18, pp. 193-&, 1969.
- [26] T. Sekine, T. Nakashizu, K. Toyoda, K. Uchinokura, and E. Matsuura, "Raman-Scattering in Layered Compound 2h-Ws₂," *Solid State Communications*, vol. 35, pp. 371-373, 1980.
- [27] X. L. Li, J. P. Ge, and Y. D. Li, "Atmospheric pressure chemical vapor deposition: An alternative route to large-scale MoS₂ and WS₂ inorganic fullerene-like nanostructures and nanoflowers," *Chemistry-a European Journal*, vol. 10, pp. 6163-6171, Dec 3 2004.

- [28] H. Wu, R. Yang, B. Song, Q. Han, J. Li, Y. Zhang, Y. Fang, R. Tenne, and C. Wang, "Biocompatible inorganic fullerene-like molybdenum disulfide nanoparticles produced by pulsed laser ablation in water," *Acs Nano*, vol. 5, pp. 1276-81, Feb 22 2011.
- [29] R. Tenne, M. Homyonfer, and Y. Feldman, "Nanoparticles of layered compounds with hollow cage structures (inorganic fullerene-like structures)," *Chemistry of Materials*, vol. 10, pp. 3225-3238, Nov 1998.
- [30] L. L. Y. Chang, M. G. Scroger, and B. Phillips, "Condensed Phase Relations in Systems ZrO₂-WO₂-WO₃ and HfO₂-WO₂-WO₃," *Journal of the American Ceramic Society*, vol. 50, pp. 211-&, 1967.

Chapter Five

Synthesis and characterisation of MoS₂ nanoparticles

via solid-gas reaction between MoO₃ and S

Introduction

MoS₂ is another metal dichalcogenide that highly resembles WS₂. This compound has a very similar layered structure with strong in-layer covalent bonds and weak interlayer van der Waals forces. Therefore, similarly to WS₂, nanoflakes, 1D nanoparticles and nanotubes of MoS₂ can also be synthesised. Among these structures, MoS₂ 1D nanoparticles exhibit good performance in many areas such as lubrication [1, 2] and medicine [3]. Therefore, it is necessary to produce this type of material on a large scale with low cost.

Since the first successful synthesis of MoS₂ 1D nanoparticles in 1993 *via* the reaction of MoO₃ films and H₂S [4], many techniques have been proposed based on the sulphidation of MoO₃. For example, two years later, MoO₃ films were replaced by MoO₃ powder and reacted with H₂S in a conventional tube furnace at 850°C [5]. This technique was further optimised using a special vertical furnace containing three heating zones [1]. MoO₃ powder was placed in small ceramic open cylinders placed on a concentric shelf of the middle tube. H₂S flew upwards from the bottom of the furnace and reacted with the evaporated MoO₃. The produced MoS₂ with sizes below 150 nm deposited on the filter on the top part of the reactor and could be easily collected. Because of the modification, this technique became the most feasible approach for large-scale production and has already been applied for commercial production [1]. In addition to these techniques with micron-sized MoO₃ as the raw material, some MoO₃ nanoparticles [6] and nanobelts [7] were used as starting materials to react with H₂S at above 800°C. Both of these techniques could generate MoS₂ 1D nanoparticles with sizes below 100 nm and small amounts of MoS₂ nanotubes. When H₂S was replaced by S, MoS₂ 1D nanoparticles could also be

synthesised from the reaction of MoO_3 , NaBH_4 and S in a sealed ampoule fired at 900°C . However, the yield of MoS_2 IF nanoparticles was not as high as that using the above techniques.

The sizes and morphologies of the reported MoS_2 IF nanoparticles were not determined by those of the MoO_3 precursors. Because of the relatively low melting point (795°C) and high partial pressures of MoO_3 , rapid evaporation of MoO_3 occurred at high temperatures. Therefore, all the synthesis techniques mentioned above were essentially based on the gas-gas reaction between MoO_3 and S vapours rather than the solid-gas reaction occurring for WS_2 synthesis (see chapter 4). Therefore, the morphologies and sizes of MoS_2 products would be irrelative to those of the raw material MoO_3 , losing the “template-growth” mechanism discussed previously in Chapter 4 and making it difficult to produce products with controlled morphologies and sizes. In addition, the use of toxic H_2S as reactants largely increases the production cost.

In the work presented in this chapter, MoS_2 IF nanoparticles were produced *via* a gas-solid reaction process. Because of the usage of large amounts of excessive S powder, highly concentrated S steam was formed instantly when the raw materials were placed into the preheated furnace. Therefore, MoO_3 was fully surrounded by this steam and was rapidly converted into MoS_2 , leaving no time for the melting process. The produced MoS_2 IF nanoparticles had similar sizes and morphologies as those of the MoO_3 raw materials because of the “template growth mechanism”. Therefore, it is possible to control the sizes of the morphologies of products by selecting different raw MoO_3 materials. In addition to the controllability of the morphologies and sizes of products, the avoidance of using H_2S and capability of using a large batch size could make the newly developed route potentially scalable and more environmentally friendly.

Experimental

0.144g MoO_3 (>99.5%, <500 nm Sigma-Aldrich) powder, ultrasonically dispersed in 100 ml ethanol (>99% Sigma-Aldrich) for 2 h and then dried in an oven for 3 h at 80°C, was mixed with various amounts of S (>99.5% Sigma-Aldrich) (excessive amounts of S were used to compensate for its evaporation loss at high test temperatures, as discussed in Chapter 4) for 2 h in a ball mill at 400 rpm. The powder mix was placed in a ceramic boat and fired in a quartz tube furnace at a given temperature between 350-950°C for 1 h. The gases, furnaces and firing schedules were all the same as those used for the WS_2 synthesis described previously (see chapter 4) and will not be repeated here. After firing and cooling to room temperature, the reacted black-coloured mass was collected from the ceramic boat and subjected to further characterisation.

Results and discussion

In Figure 5.1, the XRD patterns of the samples resulting from 1-h firing in H_2/Ar at 350, 450, 650, 750 and 950°C using 29 times excessive S are presented. At as low as 350°C, MoS_2 was already detected even though MoO_2 remained as the primary phase (Figure 5.1a). MoO_2 rather than MoO_3 was detected, indicating that the original MoO_3 had been reduced by H_2 and/or S. To differentiate the effect of S from H_2 , MoO_3 nanoparticles alone were heated at 350°C for 1 h in H_2/Ar . Only MoO_3 , and no MoO_2 , was detected in the sample by XRD (Figure 5.2), verifying that H_2 could not reduce MoO_3 at 350°C; in other words, the formation of MoO_2 illustrated in Figure 5.1a arose from the reduction by S. Thus, it could be considered that the sulphidation process should be involved with the two sub-reactions.

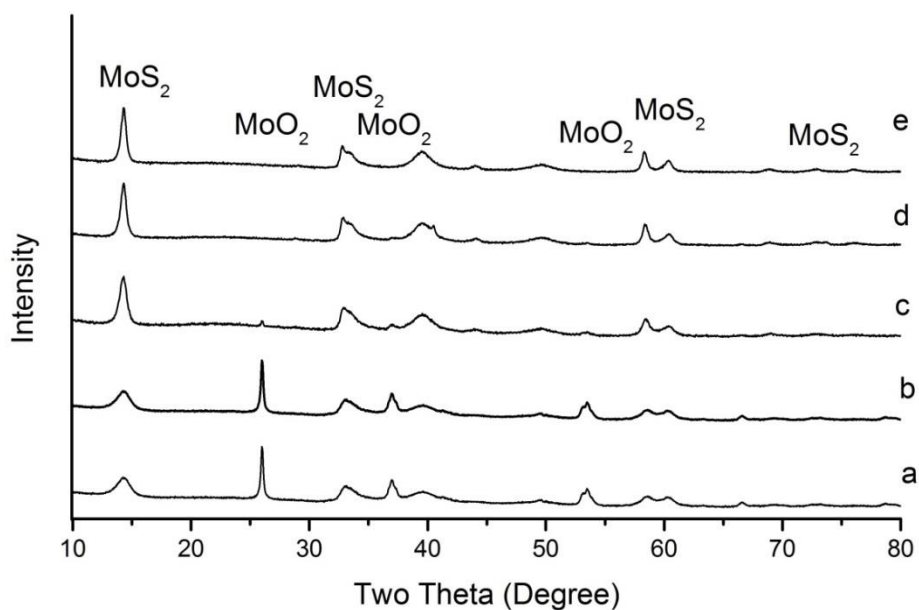


Figure 5.1 XRD patterns of samples resulting from 1-h firing in H_2/Ar at (a) 350°C, (b) 450°C, (c) 650°C, (d) 750°C and (e) 950°C using 29 times excessive S.

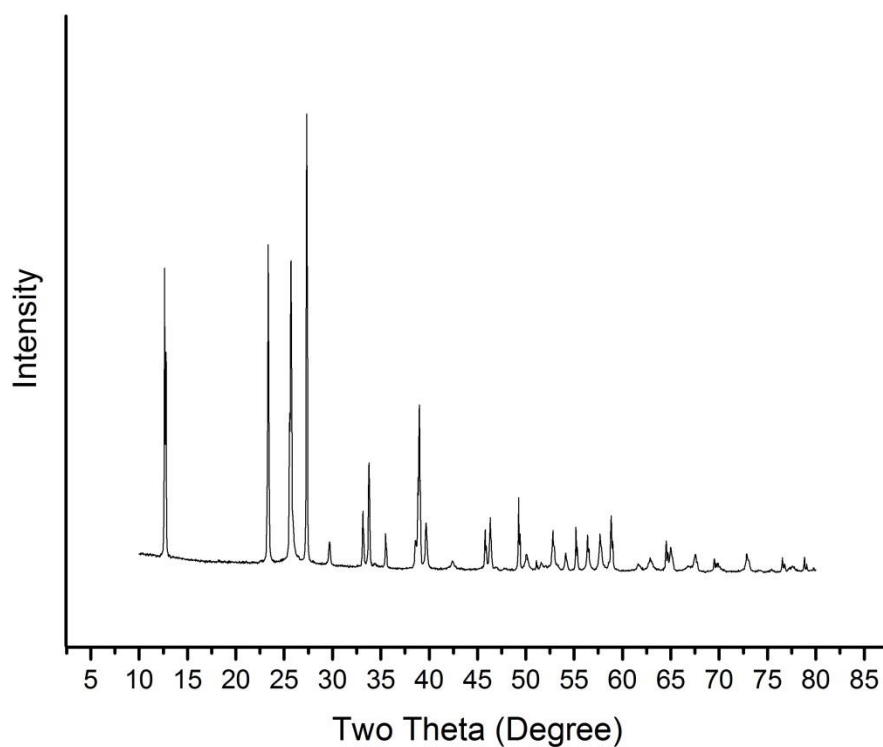
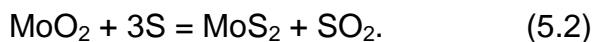


Figure 5.2 XRD pattern of a sample resulting from heating MoO_3 nanoparticles in H_2/Ar at 350°C for 1 h. All the diffraction peaks belong to MoO_3 .

Initially, MoO₃ was reduced by S to form MoO₂ (Reaction (5.1)), which further reacted with S to form MoS₂ (Reaction (5.2)):



No S remained in the fired sample (Figure. 5.1a), indicating that the S had been consumed or carried away after becoming a vapour. The latter conclusion was confirmed by the observation of yellow deposition on the inner surface of the quartz tube. Upon increasing the temperature to 450°C (Figure 5.1b), the heights of the MoS₂ peaks slightly increased, whereas those of the MoO₂ peaks slightly decreased. Upon further increasing the temperature to 650°C (Figure 5.1c), MoS₂ was present as the primary phase along with a small amount of MoO₂, indicating the high reaction extents at this temperature. When the temperature increased to 750°C (Figure 5.1d), phase pure MoS₂ was obtained and remained stable in the sample fired at as high as 950°C (Figure 5.1e). The above results indicate that the reaction temperature had a significant effect on the reaction extent between MoO₃ and S. The calculated ΔG values by the author for both reactions, -29 kJ at 25°C -35 kJ at 25°C, are negative at 298 K, suggesting that these two reactions are thermodynamically favoured even at room temperature. According to this finding and the relatively high reaction extents at 350°C (Figure 5.1a), it could be reasonably suggested that by further optimising the synthesis conditions (e.g., increasing the amount of starting S powder and prolonging the holding time), it should be possible to synthesise phase pure MoS₂ at $\leq 350^\circ\text{C}$.

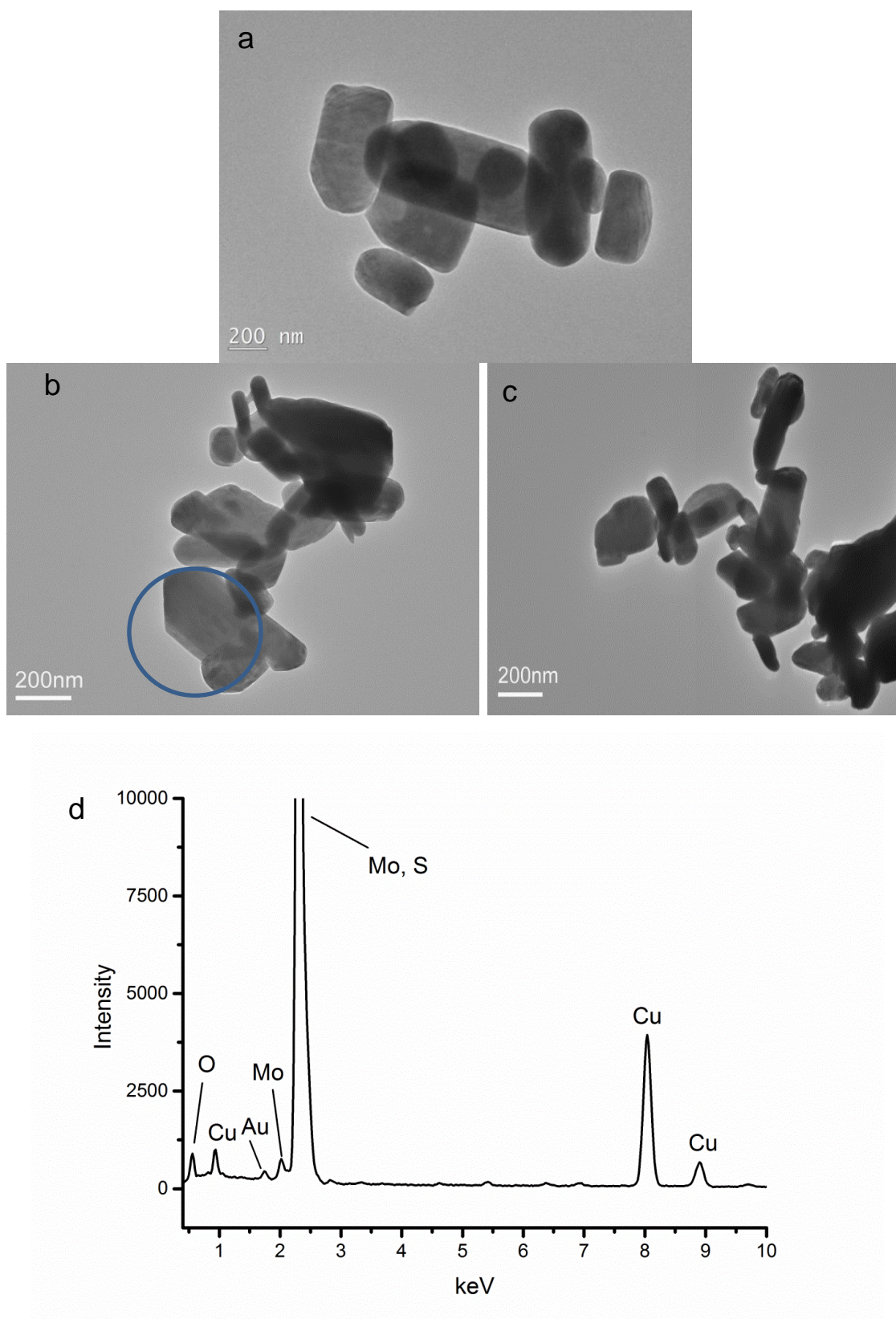
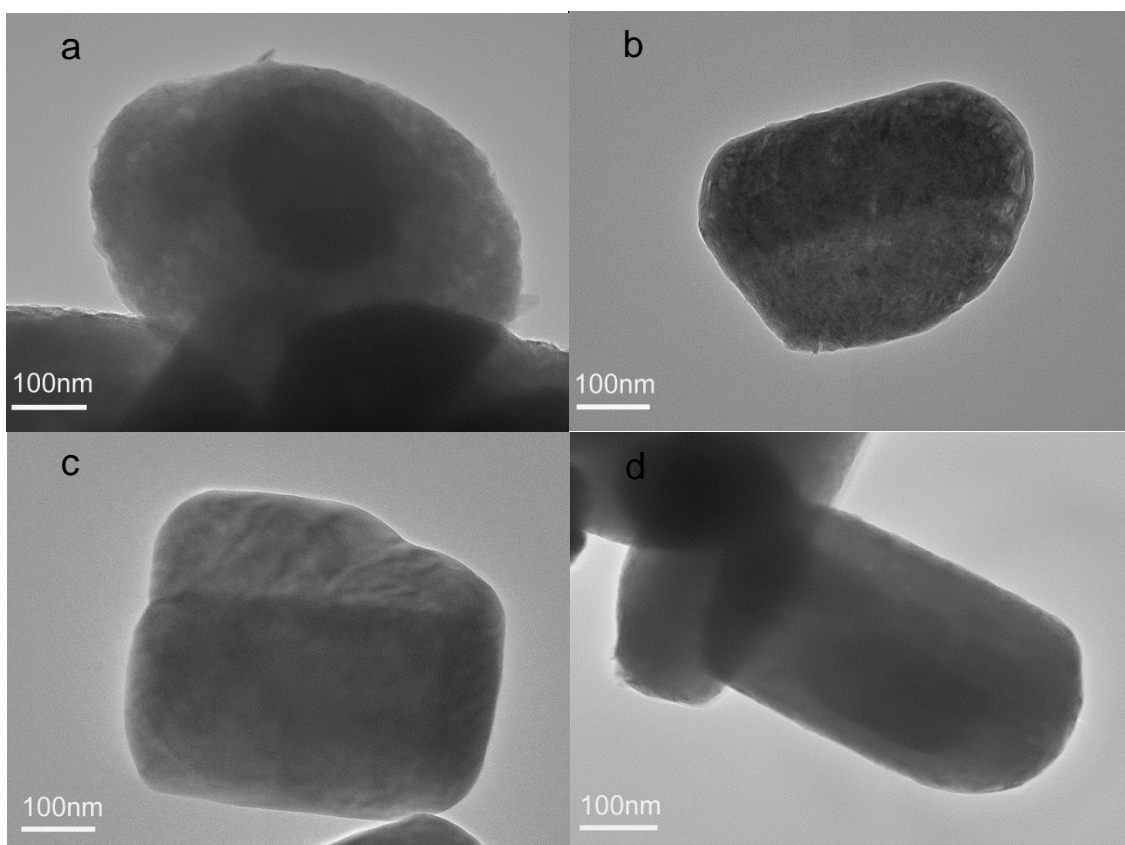
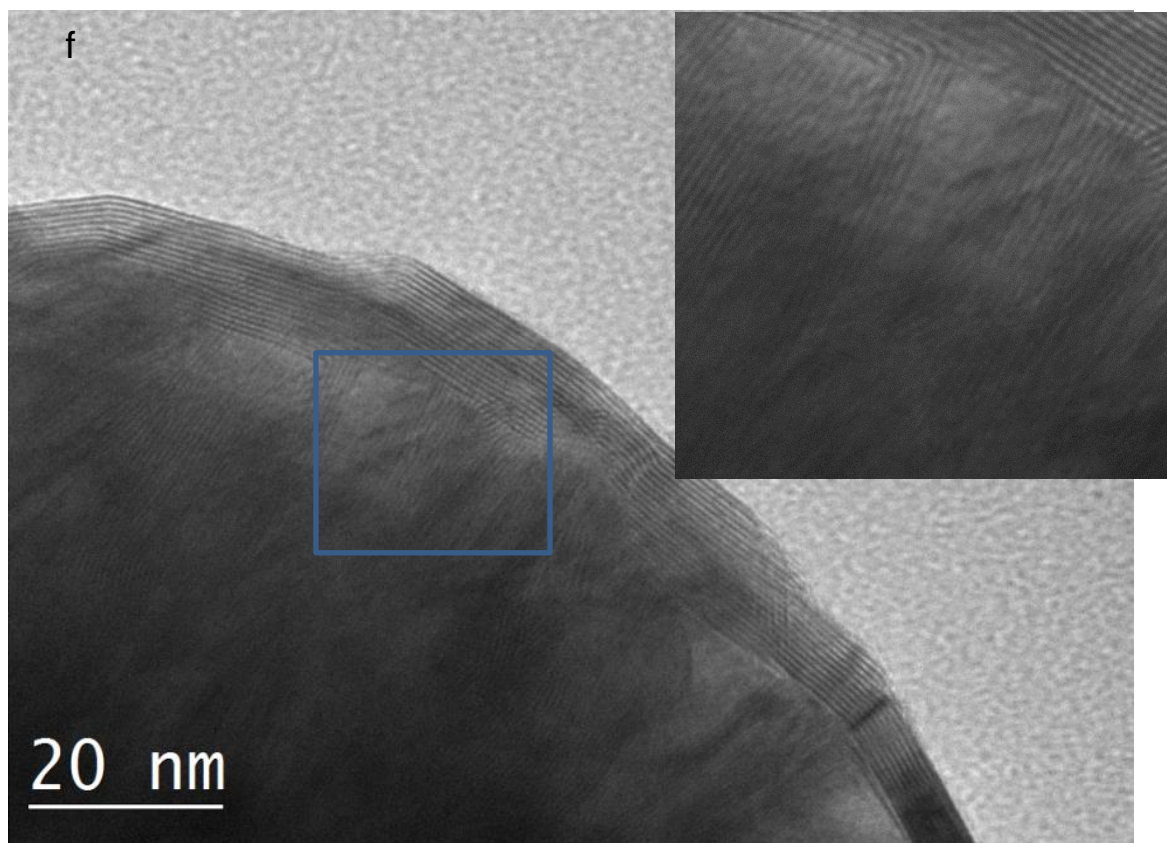
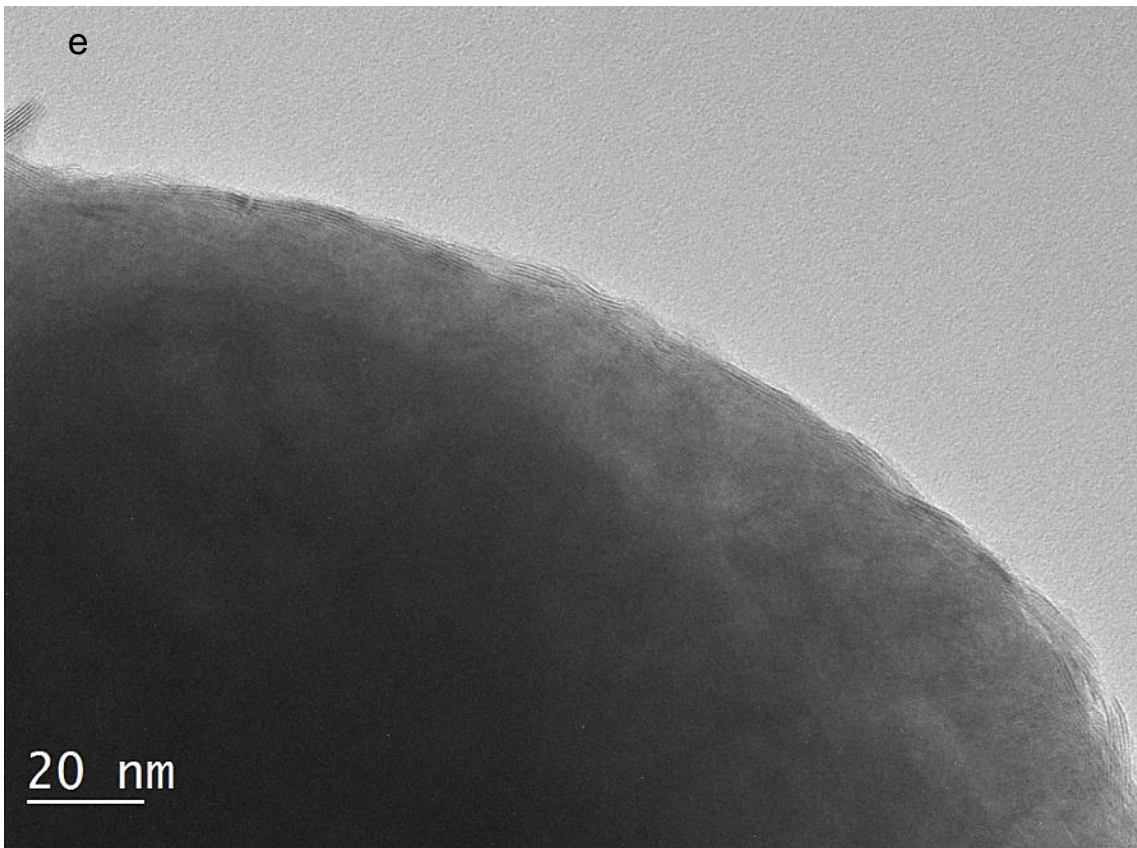


Figure 5.3 TEM images of (a) MoO₃ raw materials and samples synthesised by 1-h firing in H₂/Ar at (b) 450°C and (c) 750°C. (d) EDS spectrum of selected area in (b).

In Figure 5.3, TEM images and selected area EDS spectrum of the raw material MoO_3 and samples whose XRD patterns are shown in Figure 5.1b and d are presented. According to Figure 5.3a, the MoO_3 particles had an irregular shape with an average size of approximately 500 nm. The product phase synthesised at 450°C largely retained the morphologies and sizes of the original MoO_3 particles (Figure 5.3b). The EDS spectrum (Figure 5.3d) reveals that the three constituent elements in the product particle were Mo, S and O. Considering that both MoO_2 and MoS_2 were detected by XRD (Figure 5.1), the particle clearly should be a MoS_2 - MoO_2 composite particle. Upon increasing the reaction temperature to 750°C , although the composition of the sample was transformed into pure MoS_2 , the morphology of the sample was not changed (Figure 5.3c), suggesting that the MoO_3 particles were converted into MoS_2 via the “template-growth” mechanism.





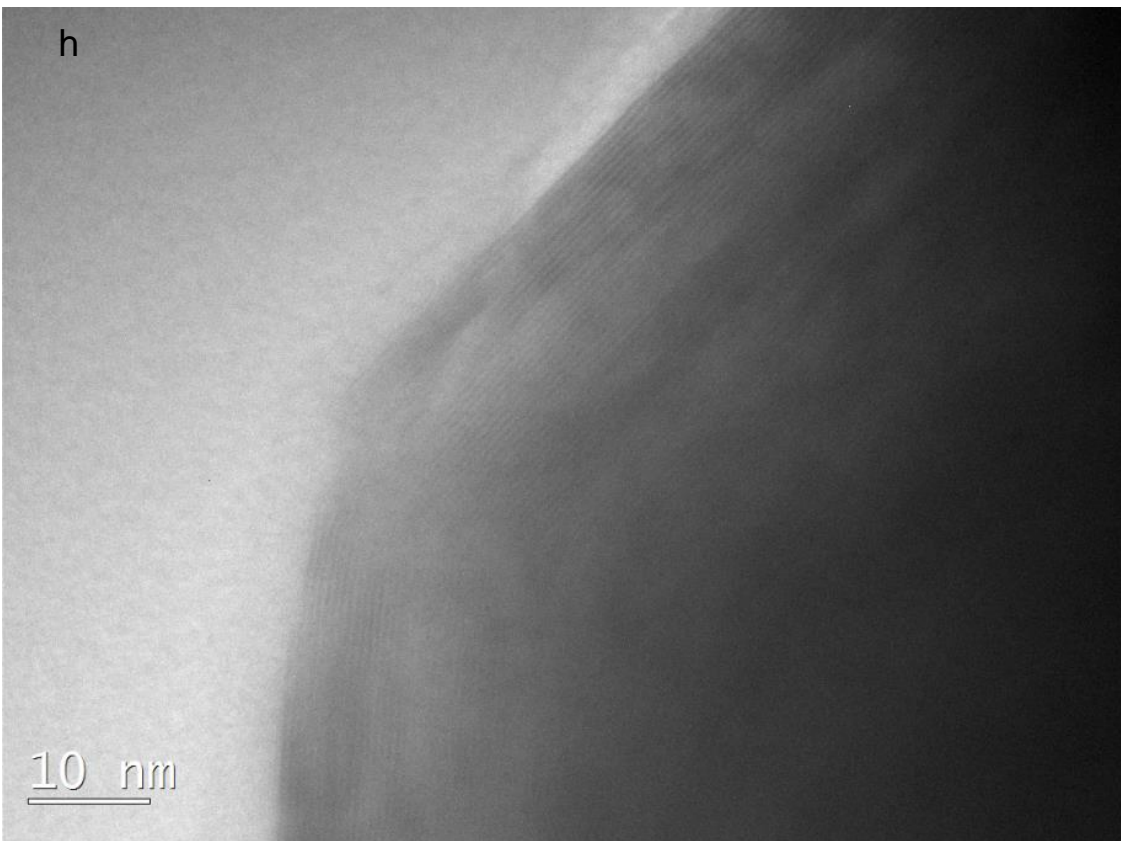
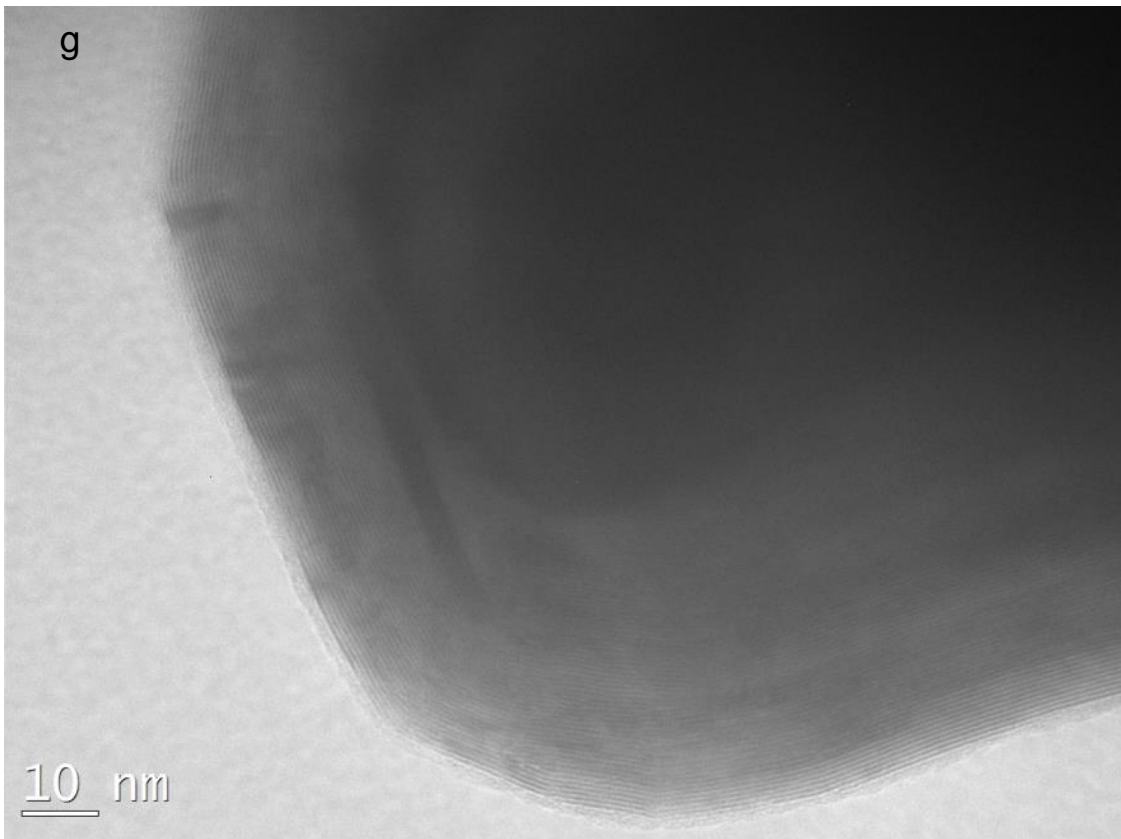


Figure 5.4 HRTEM images of samples resulting from 1-h firing in H_2/Ar at (a, e) 450°C, (b, f) 650°C, (c, g) 750°C and (d, h) 850°C.

In Figure 5.4, HRTEM images of the samples resulting from 1-h firing in H₂/Ar at 450°C, 650°C, 750°C and 850°C under a H₂/Ar atmosphere are presented. As observed in Figure 5.4a, a nanoparticle with a size of approximately 400 nm was produced. The high-magnification image (Figure 5.4e) reveals that this nanoparticle actually had a core-shell structure. The shell part had a layered structure and was mostly continuous with only some discontinuities. The shell was 3-5 nm in thickness, much smaller than the “large” overall sizes, indicating the formation of a “large” inner core. The lattice distance in the shell was measured to be 0.64 nm, which was close to the lattice distance of the (002) plane of 2H MoS₂ bulk material (0.615 nm) [8]. According to Tenne et al., such an expansion is commonly observed with MoS₂ IF nanoparticles due to the strain induced by the curvature of the layers [8]. This finding further verified the formation of MoS₂-MoO₂ core-shell nanoparticles at 450°C. Because of the large particle size and small lattice distance of MoO₂ (approximately 0.34 nm), it was difficult to observe the lattice fringe of the MoO₂ inner core by HRTEM.

Upon increasing the temperature to 650°C, little change was observed in the sizes and morphologies of the products (Figure 5.4b). A particle with a core-shell structure was also observed by HRTEM (Figure 5.4f). The outer shell was generally continuous and contained few discontinuities. However, its thickness increased to approximately 10 nm (Figure 5.4f). In addition, some randomly arranged (002) fragments of MoS₂ were observed on the inner core (insert in Figure 5.4f), indicating higher reaction extents. Because of the large particle size and limited S amount, the sulphidation process could not be completed. Because some of the formed MoS₂ layers were stacked along the radial direction, the layers contained unsaturated bonds at the edge of the layer fragments, which is not energetically favourable [9]. Therefore, a transformation to the thermodynamically more stable arrangement of tangential layers would occur when temperature was high enough.

Figure 5.4c shows the sample obtained after 1-h heat treatment at 750°C. Because of this high temperature, the initially formed (002) fragments had sufficient thermodynamic energy to be rearranged along the tangential direction, leading to the formation of particles with well-crystallised, fullerene-like structures (Figure 5.4c). Because the electron beam could not penetrate such

large particles, the layer structure could only be observed on their edges. The thickness of visible layers was approximately 40 nm with an interlayer spacing of 0.64 nm. For the same reason described above, it was also difficult to observe the hollow inner cores of these particles. Further increasing the temperature to 850°C did not change the morphology of the product (Figure 5.4d), indicating that this product exhibited good stability at a high temperature.

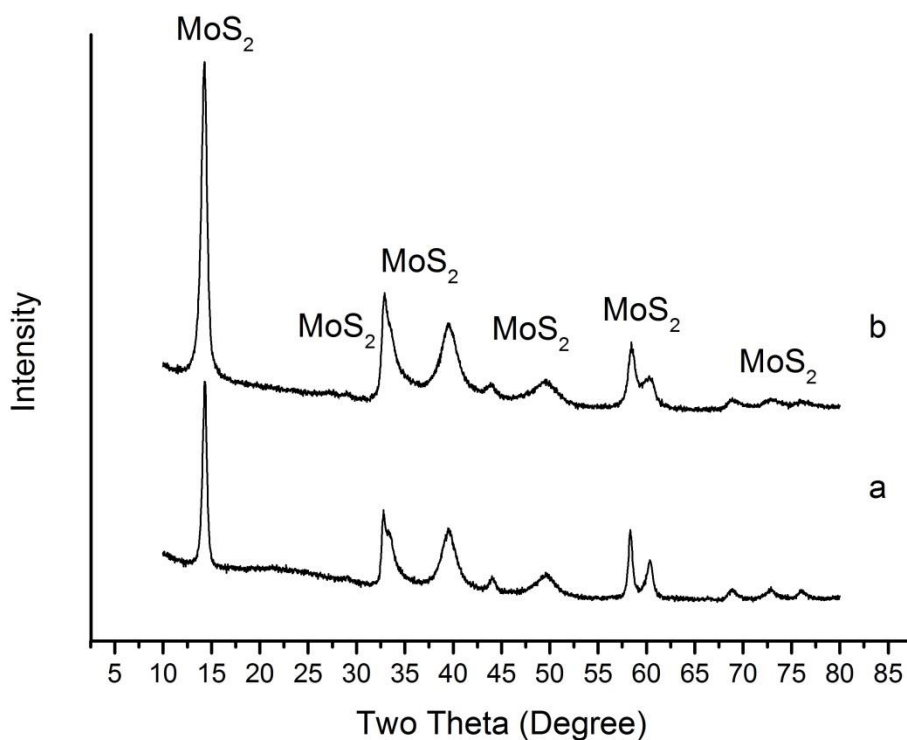
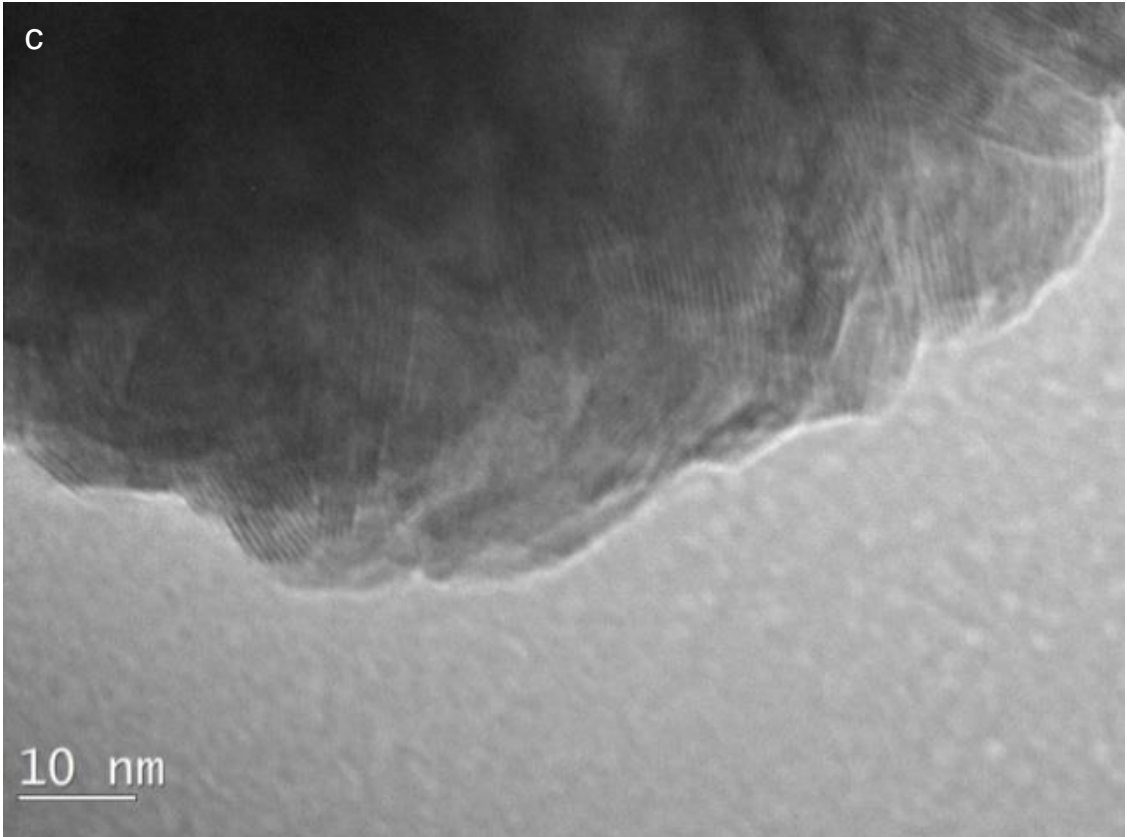
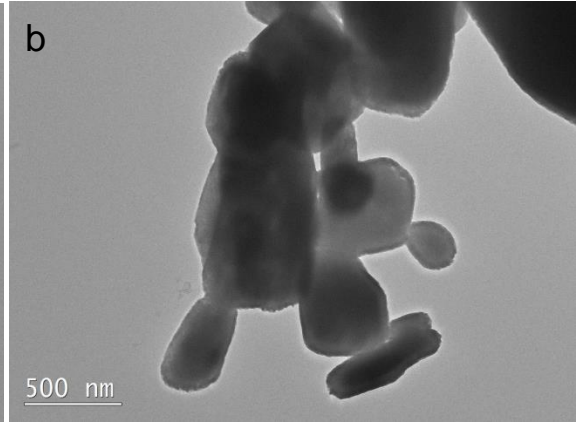
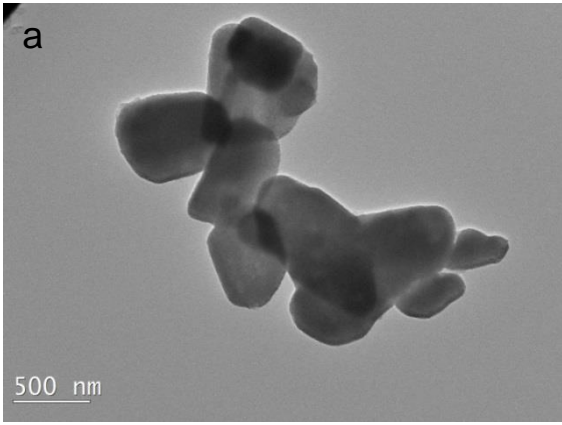


Figure 5.5 XRD patterns of samples resulting from 1-h firing at 750°C in (a) a H₂/Ar atmosphere with S and (b) in a H₂S/Ar atmosphere.



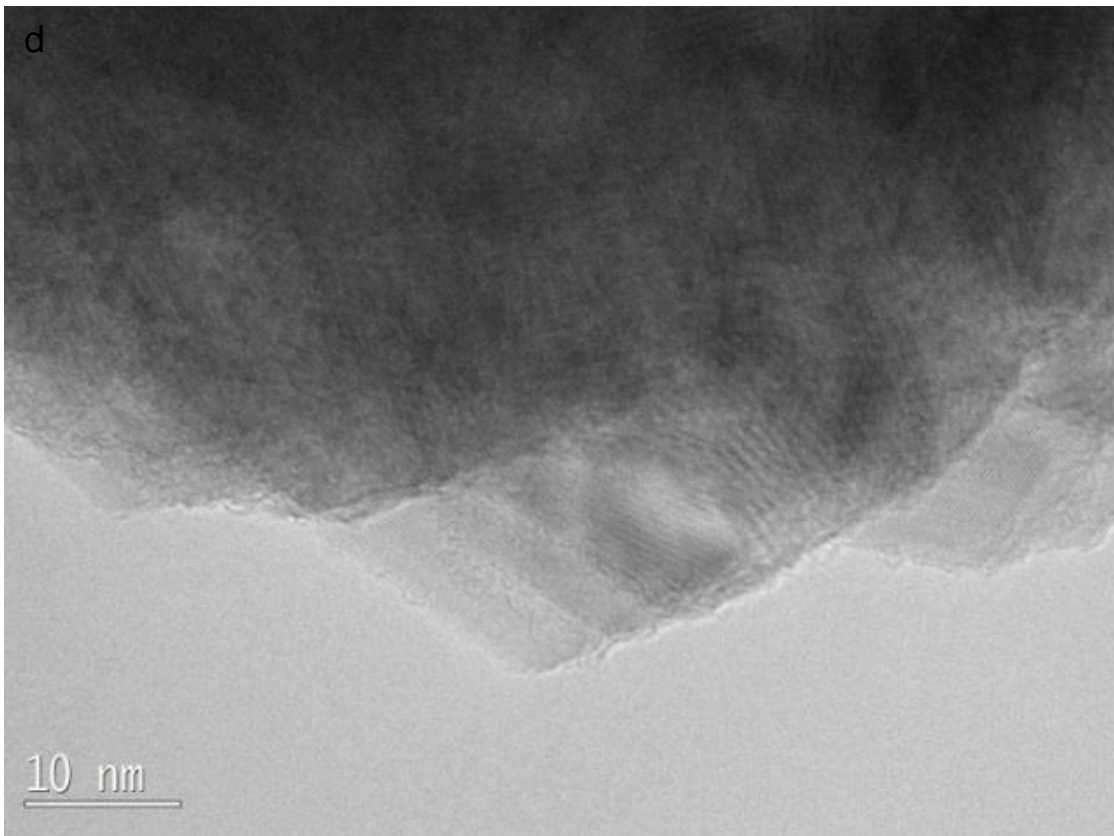


Figure 5.6 TEM and HRTEM images of samples resulting from 1-h firing at (a, c) 750°C and (b, d) 850°C in a H₂S/Ar atmosphere.

As a common sulphidation agent, H₂S is often used for the preparation of MoS₂ IF nanoparticles (Reaction (5.3)) [10]:



In this case, MoO₃ vapour, instead of its solid counterpart, participated in the reaction, resulting in tiny MoS₂ IF nanoparticles. It is clearly difficult to control the morphologies/sizes of MoS₂ products by tailoring those of the MoO₃ particles *via* this route. In addition, because there is a reaction balance among H₂, S and H₂S when the temperature is above 550°C [11], the reaction mechanisms of both H₂/S and H₂S involved reactions that are quite similar. Therefore, it is necessary to compare the product in the present case with that synthesised in a H₂S atmosphere. To compare these two routes (Reactions 5.1 and 5.2 and Reaction 5.3), the same amount of MoO₃ powder was heated at 750°C for 1 h in Ar/H₂S. In Figure 5.5, the XRD patterns and HRTEM images of the products resulting from the sulphidation process using S or H₂S are

presented. At 750°C, the reactions in both cases reached completion, resulting in phase pure MoS₂. Although the sizes and shapes of the products generated from Reaction (3) (Figures 5.6a&b) were similar to those of previous products (Figures 5.3b&c), the corresponding HRTEM images (Figures 5.6c&d) reveal that these two samples did not have an IF structure, as demonstrated in Figure 5.4c. Randomly oriented MoS₂ fragments with a lattice fringe of 0.64 nm rather than continuous layers were observed in the edge areas of the particle synthesised at 750°C (Figure 5.6c). Upon increasing temperature to 850°C, the resulting particles were composed of large amounts of flakes with a narrow lattice distance of 0.27 nm, which perfectly matched the lattice distance of the (100) plane of MoS₂ (0.27 nm) [12] (Figure 5.6d). This finding, combined with the XRD analysis, verified that these flakes were MoS₂. Because of the low flow rate of H₂S (20 ml/min), the MoO₃ was surrounded by low concentrated S atoms, leading to the slow conversion rate from MoO₃ to MoS₂. In addition, because of the small specific surface area and large MoO₃ particle sizes, the conversion rate was further reduced. As noted by Zinc et al. [6], the initially formed MoS₂ nanoparticles contained randomly oriented layer fragments. When sufficient S was used, the nanoparticles gradually rearranged along the tangential direction to decrease the thermodynamic energy, leading to the formation of continuous layers [9]. In this H₂S-involved reaction (Reaction (5.3)), the slow sulphidation rate led to an insufficient S source and thus restricted the rearrangement of MoS₂; therefore, the randomly orientated fragments remained unchanged. Because of the presence of unsaturated dangling bonds on the edges of these fragments, which were unstable at high temperatures, the fragments tended to connect with each other, forming the most stable flake structure. Consequently, MoS₂ nanoflakes were generated from the further crystallisation and growth of these tiny fragments (Figure 5.6d).

Conclusions

Large MoS₂ IF nanoparticles with an average size of approximately 500 nm were produced *via* the reaction of MoO₃ with S and H₂. Compared with the MoO₃ raw materials, the as-synthesised MoS₂ had similar submicron sizes and

shapes, indicating that this reaction followed a “template-growth” mechanism. Therefore, it is possible to control the sizes and shapes of MoS₂ products by selecting different MoO₃ raw materials, which is quite difficult using other techniques. In addition, the use of S rather than toxic H₂S makes this technique environmentally friendly. These benefits, along with the possible large batch size, suggest that this technique could produce MoS₂ IF nanoparticles on a large scale.

References

- [1] R. Rosentsveig, A. Margolin, A. Gorodnev, R. Popovitz-Biro, Y. Feldman, L. Rapoport, Y. Novema, G. Naveh, and R. Tenne, "Synthesis of fullerene-like MoS₂ nanoparticles and their tribological behavior," *Journal of Materials Chemistry*, vol. 19, pp. 4368-4374, 2009.
- [2] H. B. Yang, S. K. Liu, J. X. Li, M. H. Li, G. Peng, and G. T. Zou, "Synthesis of inorganic fullerene-like WS₂ nanoparticles and their lubricating performance," *Nanotechnology*, vol. 17, pp. 1512-1519, Mar 14 2006.
- [3] H. Wu, R. Yang, B. Song, Q. Han, J. Li, Y. Zhang, Y. Fang, R. Tenne, and C. Wang, "Biocompatible inorganic fullerene-like molybdenum disulfide nanoparticles produced by pulsed laser ablation in water," *Acs Nano*, vol. 5, pp. 1276-81, Feb 22 2011.
- [4] L. Margulis, G. Salitra, R. Tenne, and M. Talianker, "Nested Fullerene-Like Structures," *Nature*, vol. 365, pp. 113-114, Sep 9 1993.
- [5] Y. Feldman, E. Wasserman, D. J. Srolovitz, and R. Tenne, "High-Rate, Gas-Phase Growth of MoS₂ Nested Inorganic Fullerenes and Nanotubes," *Science*, vol. 267, pp. 222-225, Jan 13 1995.
- [6] H. A. Therese, N. Zink, U. Kolb, and W. Tremel, "Synthesis of MoO₃ nanostructures and their facile conversion to MoS₂ fullerenes and nanotubes," *Solid State Sciences*, vol. 8, pp. 1133-1137, Oct 2006.
- [7] X. L. Li and Y. D. Li, "Formation MoS₂ inorganic fullerenes (IFs) by the reaction of MoO₃ nanobelts and S," *Chemistry-a European Journal*, vol. 9, pp. 2726-2731, Jun 16 2003.
- [8] Y. Feldman, G. L. Frey, M. Homyonfer, V. Lyakhovitskaya, L. Margulis, H. Cohen, G. Hodes, J. L. Hutchison, and R. Tenne, "Bulk synthesis of inorganic fullerene-like MS₂ (M=Mo, W) from the respective trioxides and the reaction mechanism," *Journal of the American Chemical Society*, vol. 118, pp. 5362-5367, Jun 12 1996.

- [9] N. Zink, H. A. Therese, J. Pansiot, A. Yella, F. Banhart, and W. Tremel, "In situ heating TEM study of onion-like WS₂ and MoS₂ nanostructures obtained via MOCVD," *Chemistry of Materials*, vol. 20, pp. 65-71, Jan 8 2008.
- [10] A. Zak, Y. Feldman, V. Alperovich, R. Rosentsveig, and R. Tenne, "Growth mechanism of MoS₂ fullerene-like nanoparticles by gas-phase synthesis," *Journal of the American Chemical Society*, vol. 122, pp. 11108-11116, Nov 15 2000.
- [11] K. Fukuda, M. Dokiya, T. Kameyama, and Y. Kotera, "Catalytic Decomposition of Hydrogen-Sulfide," *Industrial & Engineering Chemistry Fundamentals*, vol. 17, pp. 243-248, 1978.
- [12] G. M. Cai, J. K. Jian, X. L. Chen, M. Lei, and W. Y. Wang, "Regular hexagonal MoS₂ microflakes grown from MoO₃ precursor," *Applied Physics a-Materials Science & Processing*, vol. 89, pp. 783-788, Nov 2007.

Chapter Six

Synthesis of metal dichalcogenide nanoflakes and IF nanoparticles *via* CVD technique

Introduction

As reviewed in Chapter 2, over the past two decades, transition metal chalcogenides have received significant attention due to their excellent optical, electrical, mechanical and catalytic properties [1-5]. Because of these excellent properties, transition metal chalcogenides can be used or potentially used in many areas such as batteries, lubricants, drug carriers, and dye-sensitised solar cells (DSCs) [6-9].

Among many synthesis techniques, CVD is an efficient technique used to synthesise metal dichalcogenide nanoflakes, IF nanoparticles and nanotubes. Using this technique, a gaseous metal-containing precursor (e.g., WCl_6 , $W(CO)_6$ and $ZrCl_4$) reacts with a chalcogenide vapour (e.g., H_2S , S and Se), followed by nucleation, crystallisation and deposition of the final products. Due to the gaseous reaction process, the morphologies and sizes of the final products can be controlled by tailoring the processing parameters, such as the temperature, time and gas flow rate. For the CVD synthesis, metal halides are usually used as raw materials due to their low boiling points [10, 11].

A CVD technique was first applied to the synthesis of WS_2 IF nanoparticles by Li et al. [10]. WS_2 IF nanoparticles and nanotubes were generated from the reaction of WCl_6 with S at $850^\circ C$ and $750^\circ C$, respectively. However, most of the produced WS_2 IF nanoparticles had poor crystallisation extents and partially filled cores, leading to poor properties [10]. To overcome these issues, a modified route was proposed by Tenne et al. [11]. Instead of S vapour, H_2S was used. In addition, a specially designed facility composed of two connected

furnaces (an auxiliary furnace and a vertical furnace) was used to facilitate the IF nanoparticle formation. WCl_6 powder was initially heated above its boiling point (347°C) in the auxiliary furnace. Then, the evaporated WCl_6 was carried by N_2/H_2 to the top of the vertical furnace, which was preheated to a given temperature and through which H_2S flew constantly. After the reaction, WS_2 was deposited on a filter in the middle of the vertical furnace and could be easily collected [11]. Although the IF nanoparticles and nanotubes obtained after 1-h firing at 850°C were well crystallised, the involvement of toxic H_2S and complexity of the operation made the technique difficult to be used for large-scale production.

To synthesise these nanomaterials, a few techniques have been proposed, of which the most straightforward technique is to heat Zr and S powders directly at 850°C in an inert atmosphere. S vapour was generated and then reacted with solid Zr, forming ZrS_2 nanobelts exhibiting good electrical properties with a turn-on field of $\sim 0.95\text{ V}\mu\text{m}^{-1}$ and a threshold field of $3.6\text{ V}\mu\text{m}^{-1}$ [12]. Upon the replacement of Zr with ZrO_2 , the reaction between ZrO_2 and S did not occur even at a temperature as high as 1300°C [13]. Nevertheless, by replacing S with CS_2 , the reaction temperature could be reduced successfully to 800°C [13]. Another synthesis technique involves the decomposition of ZrS_3 at 900°C in H_2 [14]. In this case, ZrS_2 nanotubes with diameters of approximately 140 nm were produced. Recently, some transition metal chalcogenides were scaled down to their most basic structural components of either a single layer or a few layers and exhibited quite different electrical and mechanical properties [15]. ZrS_2 thin nanodiscs that were approximately 1.6-nm thick with controllable diameters were first produced *via* a liquid reaction of $ZrCl_4$, oleylamine and CS_2 [16]. These nanodiscs exhibited good performance in fast charging/discharging cycles with an 88% average recovery of the reversible capacity [16]. Nevertheless, this technique still suffers from several drawbacks, including the usage of dangerous raw materials and the operational complexity.

In the work presented in this chapter, an additional annealing process was applied on WS_2 samples obtained using conventional CVD synthesis from the reaction of WCl_6 with S to improve their crystallinity. The effects of the processing parameters and annealing conditions on the morphologies and

crystallisation extents of as-prepared WS₂ nanoparticles were studied, and a relevant mechanism is suggested. For the synthesis of ZrS₂, a gas reaction between ZrCl₄ and S at a relatively low temperature (800°C) was introduced. It was observed that that as-prepared ZrS₂ nanoflakes exhibited good photocatalytic performance in the decomposition of 4-nitrophenol (4-NP). As nitrophenols are some of the-most-difficult-to-be-removed pollutants and are inevitably present in pesticides, herbicides, insecticides, synthetic dyes, etc., as-prepared ZrS₂ nanoflakes could be a promising candidate catalyst for potential use in the pollutant purification area[17].

Experimental

First, 0.397 g WCl₆ (>99.9%, Sigma-Aldrich) or 0.23g ZrCl₄ (>99.5% Sigma-Aldrich) and 1g S powder were placed on two separate ceramic boats. A horizontal furnace inserted with a quartz tube was preheated to a target temperature and flushed with Ar at 80 ml/min for 30 min to remove any residual air. Then, the two ceramic boats were pushed into the heating zone of the tube furnace, and H₂ (20 ml/min) was introduced simultaneously with the flowing Ar. S powder was placed in the upstream gas flow, while WCl₆ was placed in the downstream gas flow. Various temperatures and holding times were used to investigate their effects on the reaction. Finally, the reacted mass was collected from the inner wall of the quartz tube, followed by annealing at various temperatures for different periods. To measure the thicknesses of samples, an Agilent 5500 AFM was used to test all the samples using tapping mode. Samples were dispersed in ethanol for 10min by sonication and dropped on a silicon wafer.

Catalytic reduction of 4-NP: As-prepared ZrS₂ nanoflakes were ultrasonically dispersed in 10 mL of distilled water for 30 min to form a homogenous solution/suspension of $0.5 \times 10^{-3} \text{ mol/L}$. This solution was further combined with 10 mL of a $3.2 \times 10^{-3} \text{ mol/L}$ 4-NP aqueous solution and 1 mL of a H₂O₂ solution (30% in weight) under stirring; the mixture was then exposed to the beam of a Xenon lamp (150W) at room temperature. The reaction progress was monitored by characterising (using the techniques described in Section 2.3) a

small portion of the solution that was removed every 30 min from the reacting solution.

Results and discussion

Synthesis and characterisation of WS₂ nanoflakes and IF nanoparticles

6.1 Effect of reaction temperature

Figure 6.1 presents XRD patterns of samples resulting from 1-h firing at 450°C, 550°C, 650°C, 750°C and 850°C. All the reflections in Figure 6.1 could be indexed to the 2H phase of WS₂. Compared with the case of standard hexagonal 2H WS₂, the (002) peak position shown in each pattern was shifted slightly towards the lower 2Theta angle, indicating that crystal lattices of the WS₂ phase had been slightly expanded. This expansion could be attributed to the strain arising from the curvature of the WS₂ layers [18].

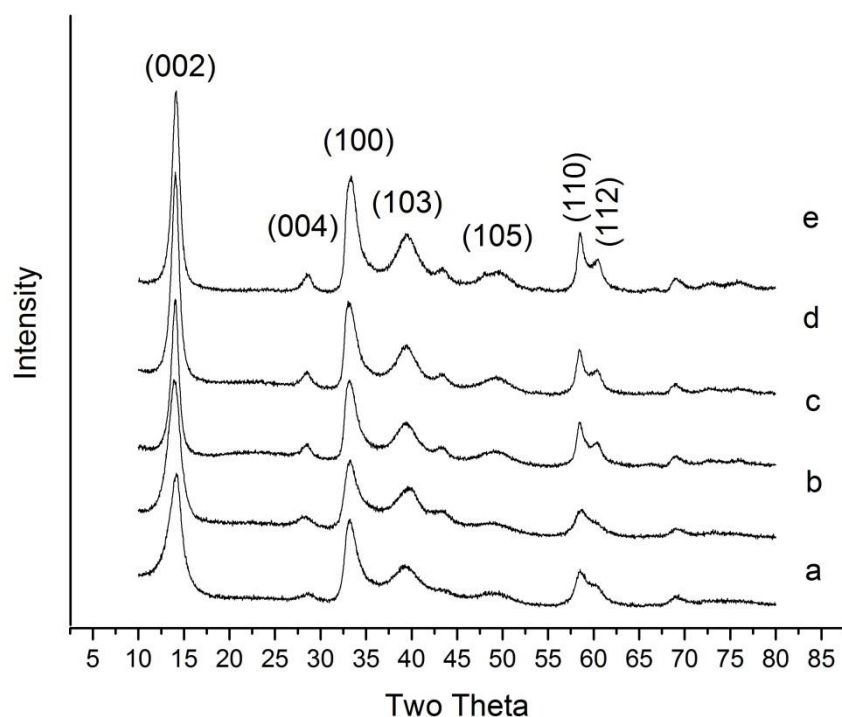
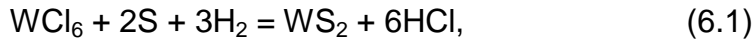


Figure 6.1 XRD patterns of samples resulting from 1-h firing in Ar/H₂ at (a) 450°C (b) 550°C (c) 650°C (d) 750°C, and (e) 850°C.

At 450°C, only WS₂ peaks were detected, indicating that Reaction (6.1),



was already complete (Figure 6.1a). This finding could be attributed to the rapid gas phase reaction between the evaporated WCl₆ and S. As observed from Figures 6.1b-e, WS₂ was the only phase in all the samples obtained at 550°C to 850°C. In addition, its XRD peaks were broad in all the cases, suggesting that the formed WS₂ products might have small grain sizes or poor crystallisation extents. With increasing temperature, the most evident changes in the XRD patterns were the sharpening of the (002) peaks and the separation of (110) and (112) peaks, suggesting the presence of crystallised WS₂ [18]. This finding indicates that increasing the temperature could promote the crystallisation of WS₂. Upon increasing the temperature to 850°C, the (002) peak of the corresponding XRD pattern was not as sharp as that of commercial 2H WS₂, while the other peaks, such as the (004), (110) and (112) peaks, were prominent, suggesting that the stacking of the (002) plane from crystallised WS₂ was not as ordered as that for commercial 2H WS₂.

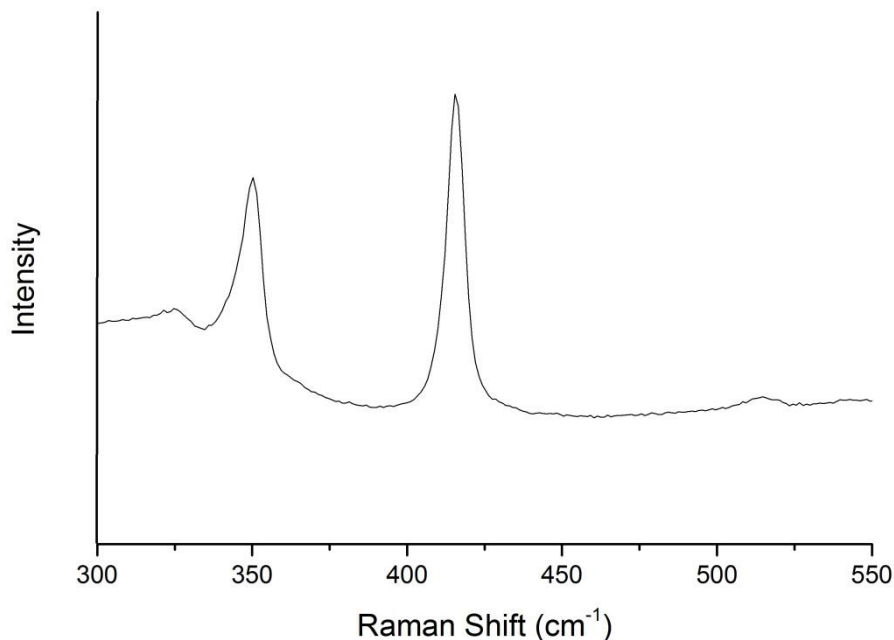


Figure 6.2 Raman spectrum of the sample resulting from 1-h firing in Ar/H₂ at 850°C.

In Figure 6.2, the room-temperature Raman spectrum of the sample resulting from 1-h firing at 850°C is presented; two strong peaks are centred at 350 cm^{-1} and 420 cm^{-1} . The positions of these peaks are slightly red-shifted with respect to those (357 and 423 cm^{-1} , respectively) of the characteristic peaks of the E_{2g} and A_{1g} modes of WS_2 [19]. Such a redshift was also observed for MoS_2 IF nanoparticles and was attributed to the curved MoS_2 layers [8, 10]. Because of the high structural similarity between MoS_2 and WS_2 , the redshift observed in this sample could also be attributed to the presence of WS_2 IF nanoparticles.

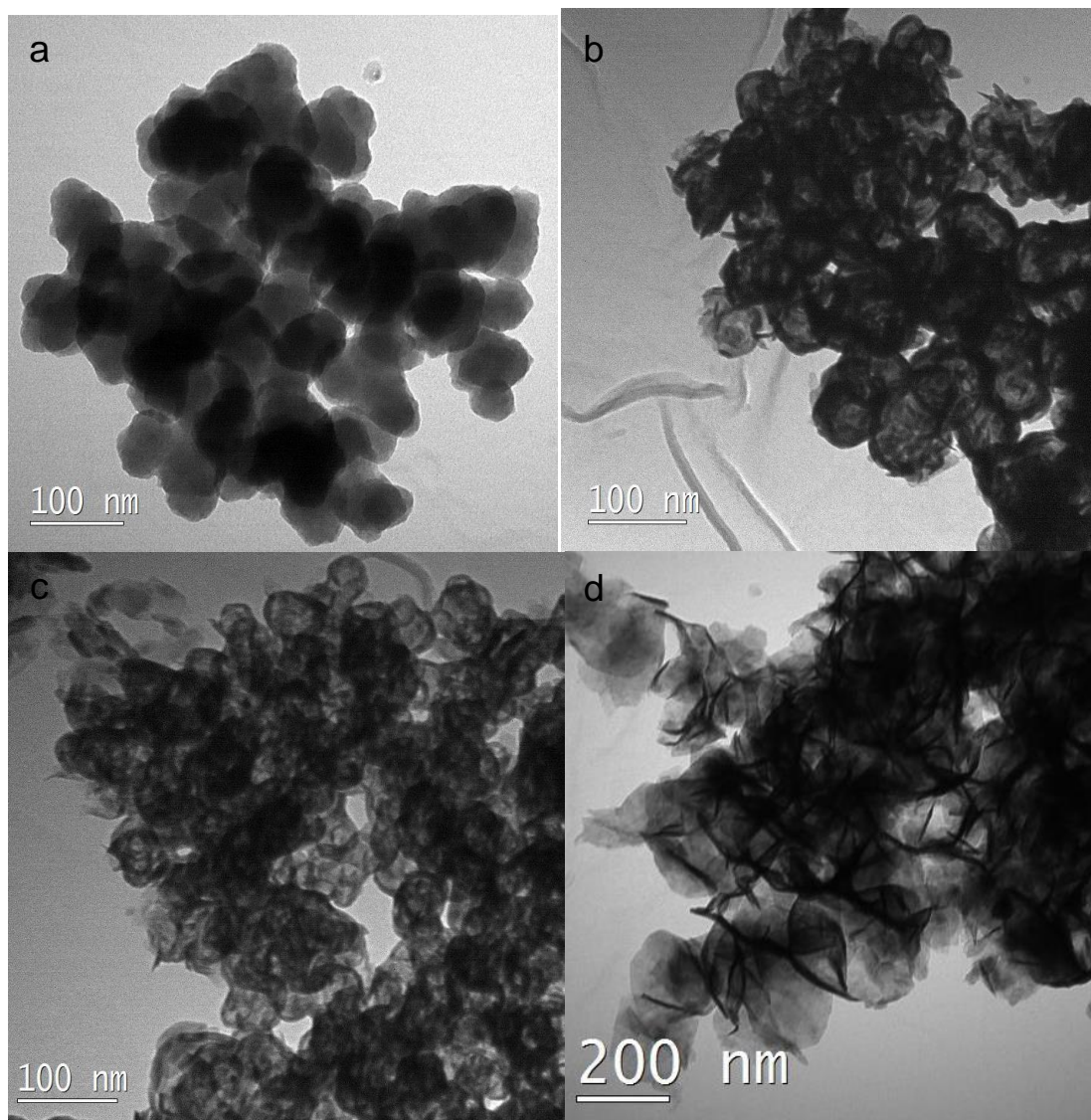
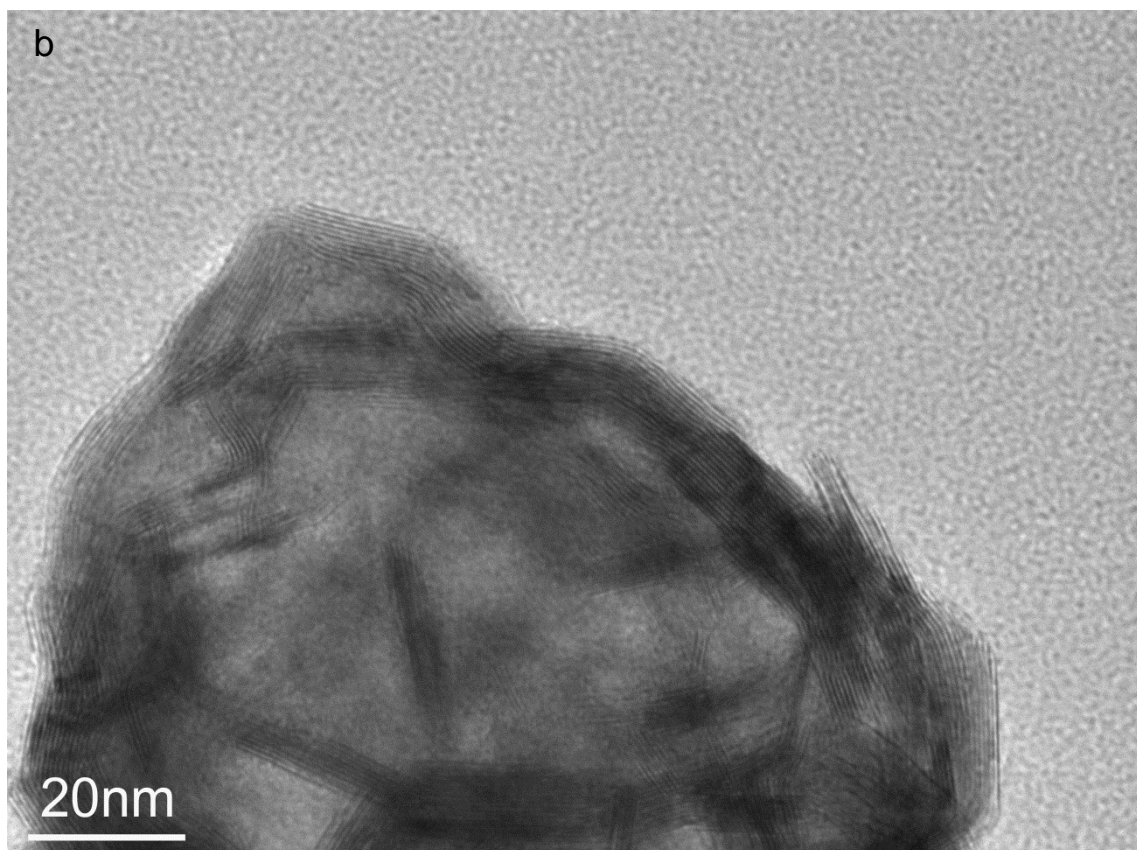
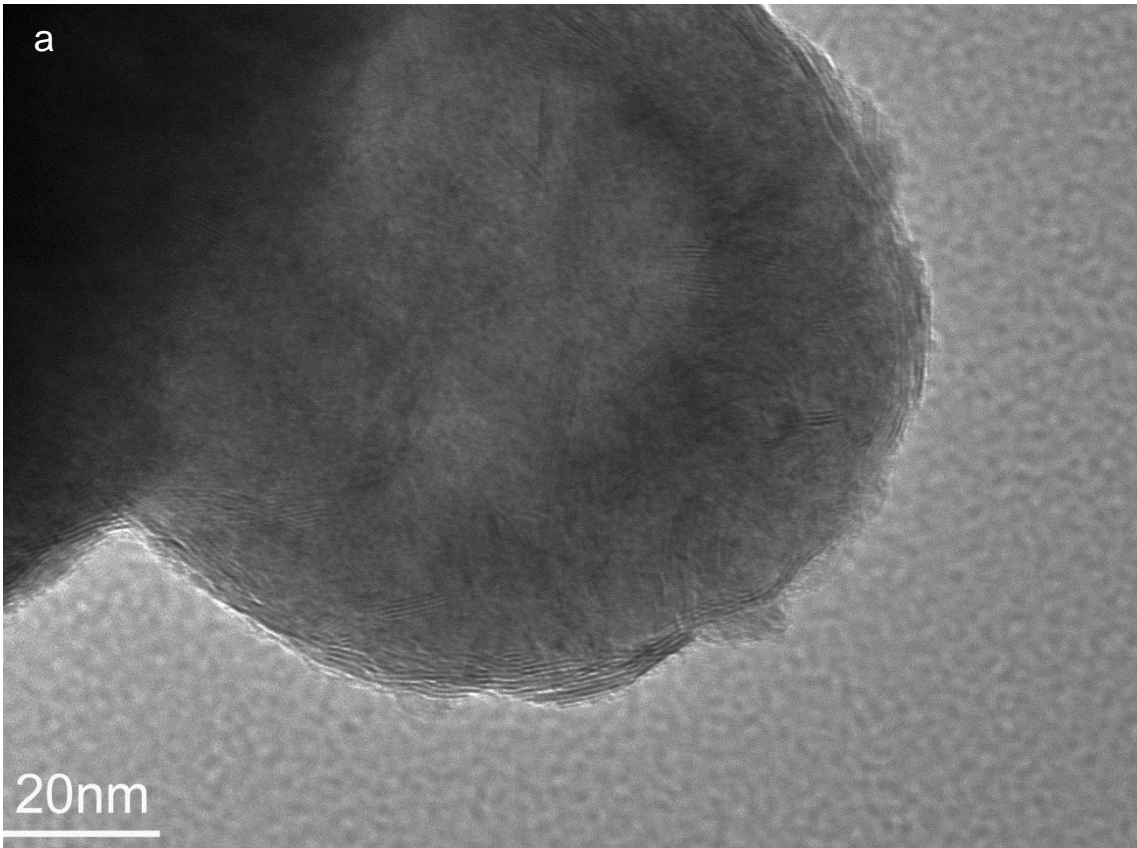


Figure 6.3 TEM images of WS_2 resulting from 1-h firing in Ar/H_2 at (a) 450°C, (b) 650°C, (c) 850°C and (d) 950°C.



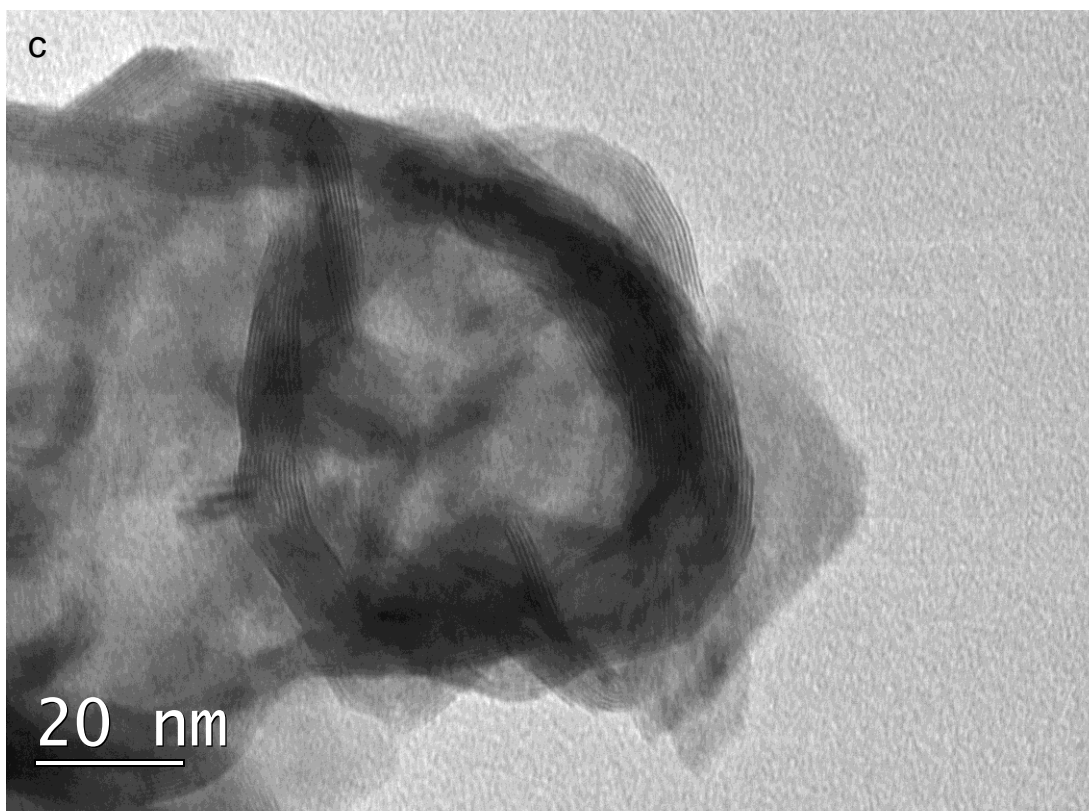


Figure 6.4 HRTEM images of WS₂ produced at various temperatures for 1 h in Ar/H₂: (a) 450°C, (b) 650°C and (c) 850°C.

Figures 6.3 and 6.4 present HRTEM images of the WS₂ samples fired for 1 h at various temperatures in a H₂/Ar atmosphere. At 450°C, WS₂ nanoparticles were the main phase. These nanoparticles were approximately 70 nm on average and with homogenous contrast distribution. A higher magnification image (Figure 6.4a) of an individual nanoparticle reveals that some layered fragments (2-4 layers) with a d-spacing of approximately 0.64 nm were formed on the edge of the particle. The lattice distance was slightly larger than the standard interlayer distance of the (002) plane of hexagonal WS₂ (0.62 nm), which is consistent with the peak shift in the XRD pattern (Figure 6.1). As no lattice fringe was observed from the core area, it could be considered that the nanoparticles were composed of partially crystallised WS₂ shells and amorphous cores. In addition, it was observed that the crystallisation started from the outer surface of the nanoparticle and arranged tangentially to the outer boundary due to the decrease of dangling bonds, which were not a thermodynamically favourable arrangement of WS₂ layers.

Upon increasing the temperature to 650°C, little change was observed in the sizes and shapes of the produced nanoparticles. However, some bright contrast areas were observed in almost every particle, indicating its hollow structure (Figure 6.3b). From Figure 6.4b, the lattice distance of the as-synthesised nanoparticle was measured to be 0.63 nm. Therefore, it was confirmed that these nanoparticles were WS₂ with several (002) layers and a partially filled large hollow core (Figure 6.4b). The thicknesses and sizes of these nanoparticles were measured to be approximately 10 and 80 nm, respectively, leaving large inner voids. Compared with the sample shown in Figure 6.4a, the crystallised shell became thicker (approximately 20 layers). Some defects and disconnections were observed on the outer WS₂ (002) layers, indicating that the crystallisation of these nanoparticles was improved but not completed.

Upon further increasing the temperature to 850°C, the as-prepared WS₂ nanoparticles retained their sizes and shapes, whereas their core areas became brighter than for nanoparticles generated at 650°C (Figure 6.3c). Some disconnections and defects were eliminated, and the IF structure became more apparent (Figure 6.4c). Unlike those synthesised from the sulphidation of WO₃ having thick walls and small hollow cores [20], the WS₂ IF nanoparticles synthesised *via* the present route had thinner walls (approximately 7-20 layers) and larger interior voids (approximately 40 nm).

To further improve the crystallinity of WS₂ IF nanoparticles, the reaction temperature was increased to 950°C. However, rather than expected IF nanoparticles, nanoflakes with curved edges were produced (Figure 6.3d). Their average size was measured to be approximately 200 nm, which was much larger than the as-synthesised IF nanoparticles (Figure 6.4). At this high temperature, the formed WS₂ IF nanoparticles became unstable due to the presence of defects. The nanoparticles tended to disintegrate to relieve the strain energy generated by the curvature of layers. Consequently, WS₂ nanoflakes that were more stable at this large size scale were produced instead.

6.2 Effect of gas flow rate

The flow rate of H_2 is another essential factor for the morphology control of WS_2 . Figure 6.5 presents XRD patterns of the samples resulting from 1-h firing at $850^\circ C$ with H_2 flow rates of 20 ml/min and 50 ml/min. As mentioned above, pure WS_2 was produced at $850^\circ C$ in a H_2 atmosphere at 20 ml/min (Figure 6.5a). The increase of the H_2 flow rate did not change the phase composition of the product, which was still WS_2 (Figure 6.5b). However, TEM analysis reveals that the higher flow rate resulted in a different morphology (Figure 6.6).

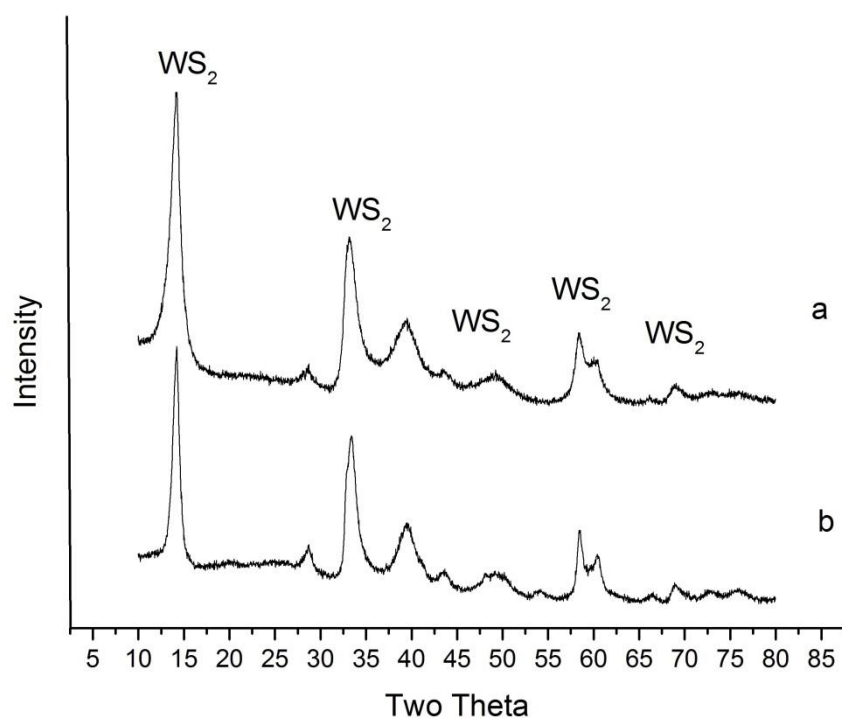


Figure 6.5 XRD patterns of samples resulting from firing at $850^\circ C$ for 1 h in H_2 with flow rates of (a) 20 ml/min and (b) 50 ml/min.

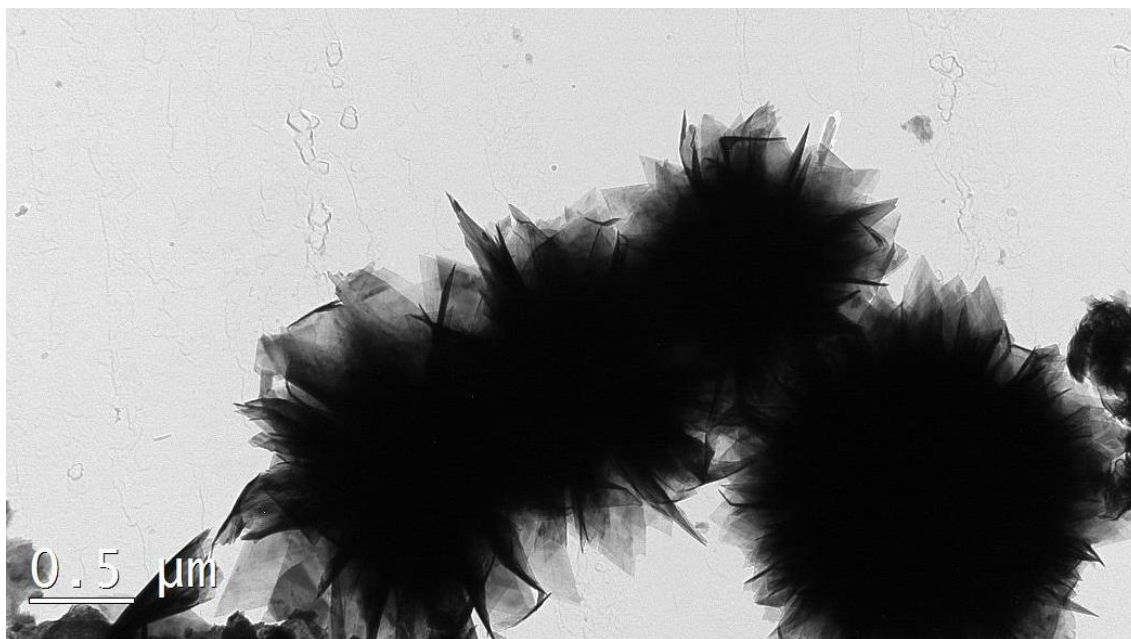


Figure 6.6 A TEM image of WS₂ products fired at 850°C for 1 h with a flow rate of 50 ml/min H₂.

Upon increasing the H₂ flow rate to 50 ml/min, WS₂ nanoflowers were produced rather than IF nanoparticles. These nanoflowers were composed of hundreds of petals with an average size of approximately 500 nm. This structure was also observed by Li et al. [10], and its formation was attributed to the change of particle retention times in the hot zone. When the reaction between WCl₆ and S was performed under a high flow gas rate, the initially formed WS₂ amorphous particles were rapidly blown through the hot zone and did not have sufficient time to generate crystallised layers on their outer surface, which could prevent them from sintering. Therefore, during the deposition process, the amorphous particles tended to stay together as agglomerates, followed by further crystallisation. Each amorphous nanoparticle could cause the formation of a large WS₂ nanoflake and then assembled to form the nanoflower structure.

6.3 Effect of holding time

In Figure 6.8, XRD patterns of samples resulting from firing at 850°C for 2 h and 3 h are presented. Upon extending the holding time to 2 h and 3 h, the compositions of these samples were not changed and remained pure WS₂, indicating that WS₂ was stable at this temperature even in a reducing atmosphere (Figure 6.7). However, as observed from the TEM images (Figure

6.8), a long soaking time led to an obvious change in the morphologies of samples. Unlike the WS_2 products synthesised by a 1-h heat treatment, which exhibited an IF structure (Figure 6.3c), relatively large nanoflakes with sizes of approximately 100-200 nm were formed (Figure 6.8a). Some of these nanoflakes had curved edges with widths of approximately 10-20 nm, which were similar to the thicknesses of IF nanoparticle walls. Upon further increasing the holding time to 3 h, the average size of these WS_2 nanoflakes was increased to 300 nm with more curved edges and severe agglomeration (Figure 6.8b).

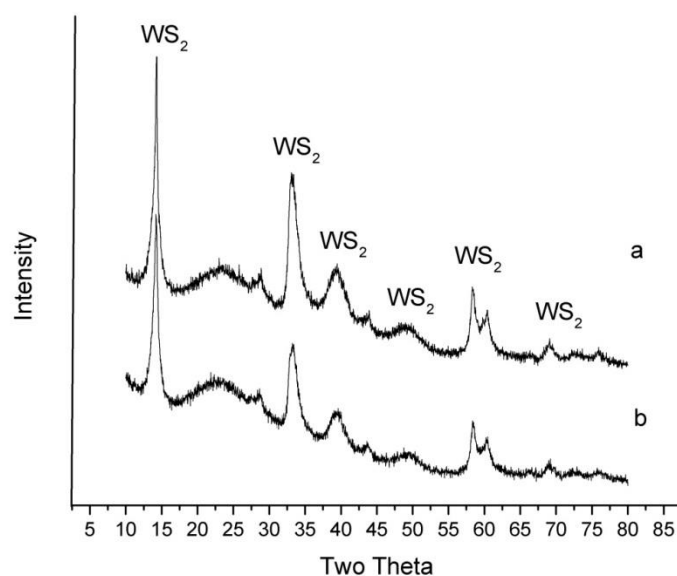


Figure 6.7 XRD patterns of samples resulting from firing at 850°C for (a) 2 h and (b) 3 h.

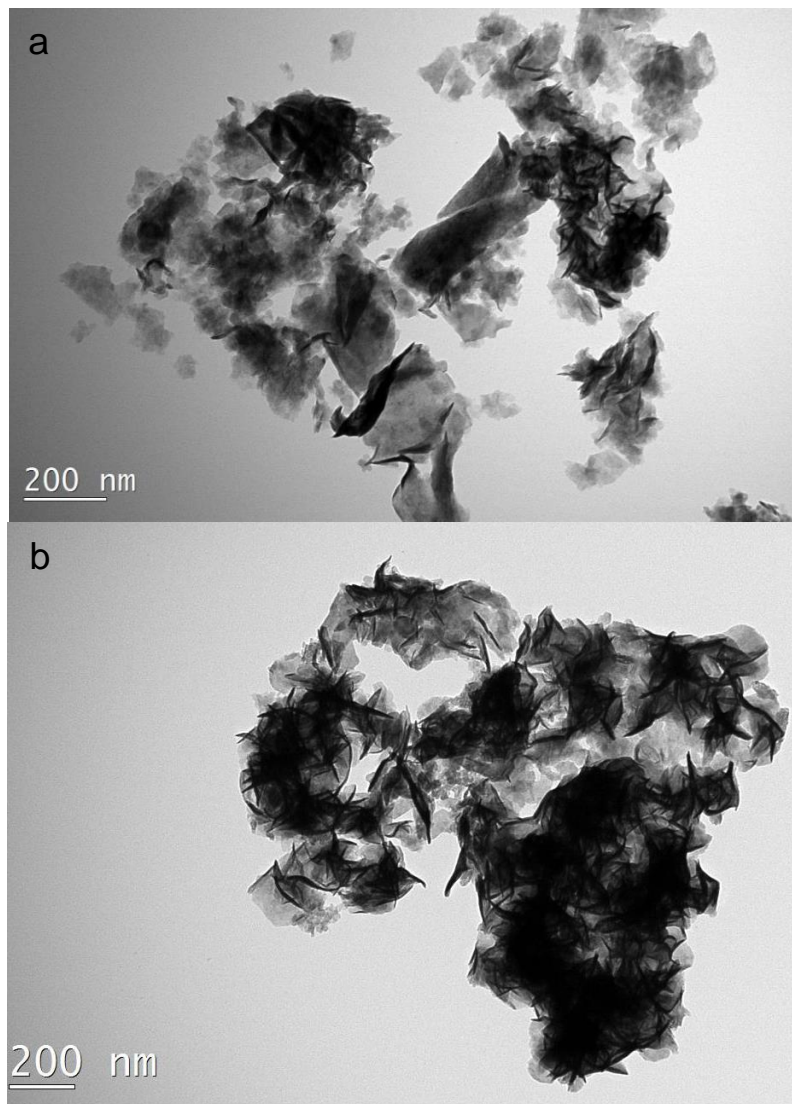


Figure 6.8 TEM images of samples resulting from firing at 850°C in H₂/Ar for (a) 2 h and (b) 3 h.

In this case, WS₂ IF nanoparticles with large inner voids were initially formed (Figure 6.4c). Although the mechanical properties of the synthesised WS₂ IF nanoparticles were not measured, the stiffness of MoS₂ IF nanoparticles with similar thin walls (5-6 layers) was measured to be approximately 1.3 N/m [21]. This stiffness is much lower than the stiffness of MoS₂ IF nanoparticles with thick walls (20-30 layers), which is approximately 424 N/m [5]. Considering the structural similarity between WS₂ and MoS₂, it could be assumed that the as-synthesised WS₂ IF nanoparticles also had much poorer mechanical properties than WS₂ IF nanoparticles with thick walls [11]. This assumption, combined with the presence of numerous defects in the nanoparticles, suggested that the nanoparticles could not maintain the IF structure due to the release of storage strain energy at high temperature [22]. Consequently, the nanoparticles tended

to eventually crush into the most stable flake phase. Because the atoms on the edges of these nanoflakes were not fully bonded, these nanoflakes were unstable and needed to decrease the thermodynamic energy. Therefore, the nanoflakes curved and attracted each other to form clusters. This process was promoted by increasing the holding time. Increasingly more curved nanoflakes were generated and finally led to the formation of larger clusters.

6.4 Annealing of WS₂ products

Although WS₂ IF nanoparticles could be readily formed *via* the CVD route, the produced nanoparticles were not well crystallised and contained some defects and disconnections (Figure 6.4c). To improve the crystallinity of WS₂ IF nanoparticles and reduce the disconnections and defects, the nanoparticles were annealed for 1 h at various temperatures in an Ar atmosphere.

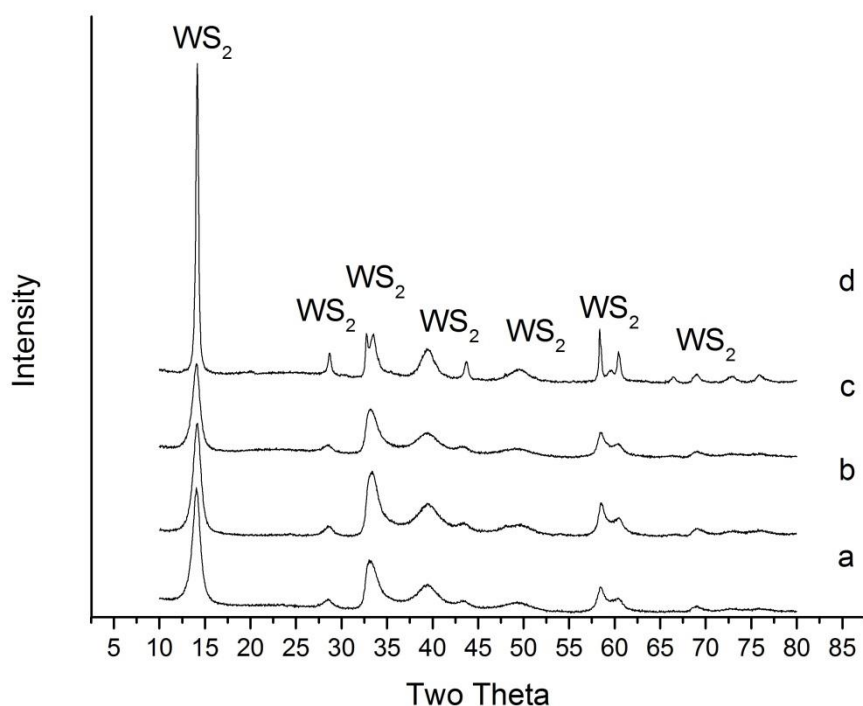
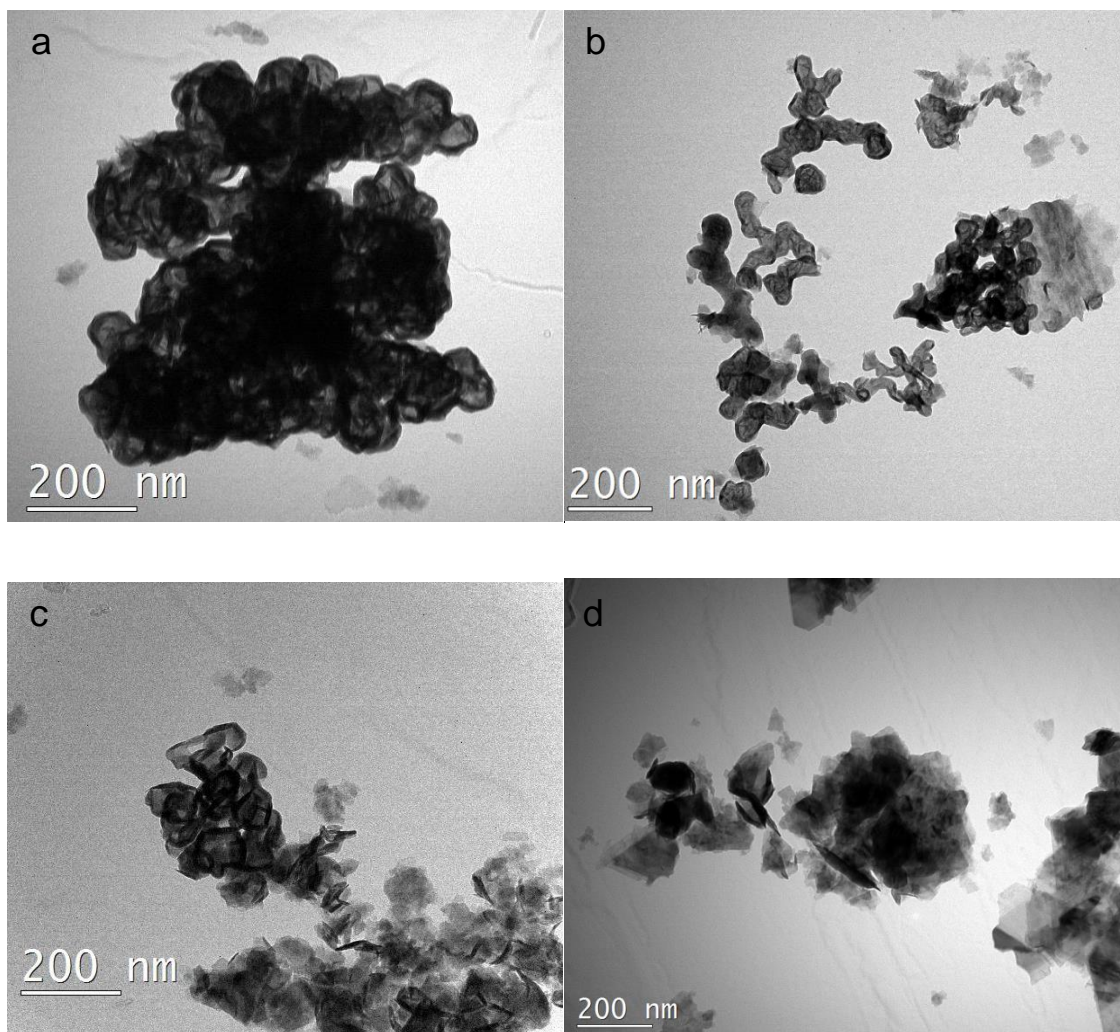
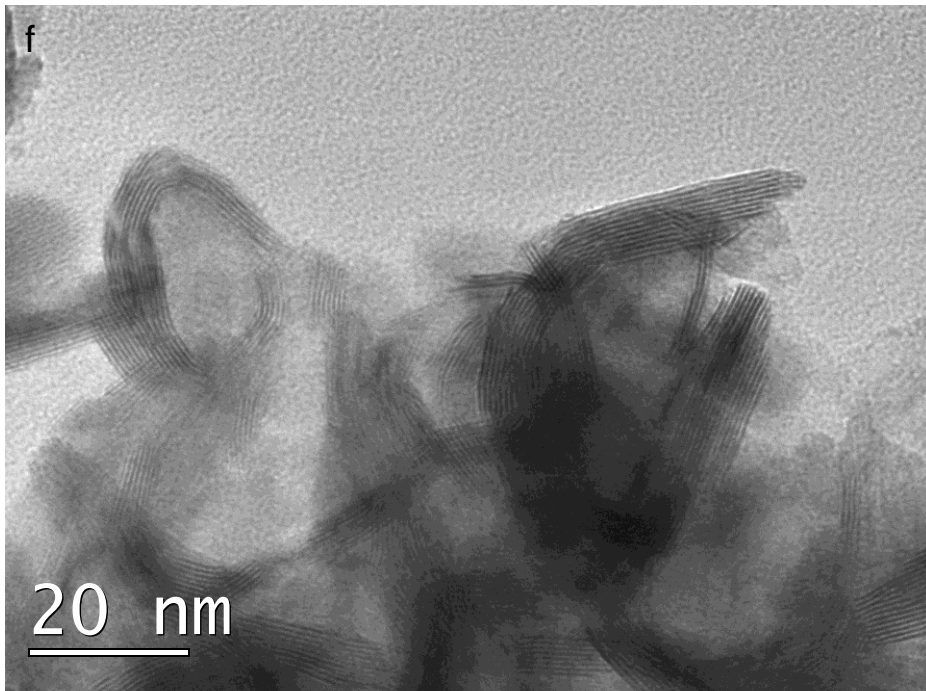
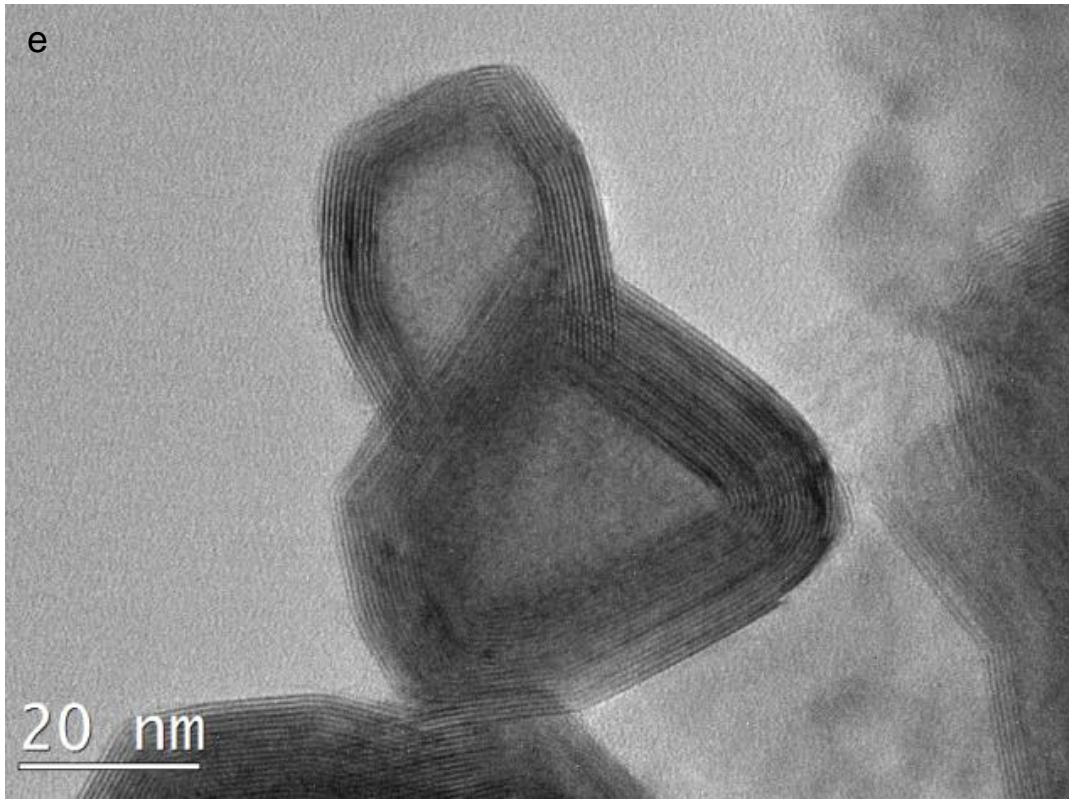


Figure 6.9 XRD patterns of WS₂ products resulting from annealing the pre-synthesised WS₂ at 850°C at (a) 700°C, (b) 800°C, (c) 900°C, and (d) 1000°C for 1 h in an Ar atmosphere.

Figure 6.9 presents XRD patterns of the WS₂ samples after annealing at various temperatures. The annealing process did not change the composition of

the products even at temperatures as high as 1000°C. All the XRD patterns of samples obtained by annealing at 700°C, 800°C and 900°C were essentially same (Figures 6.9a-c). However, the XRD pattern of the sample annealed at 1000°C was quite different, with little overlap and very high intensities (Figure 6.9d). In addition, the (002) peak in Figure 6.9d was characterised by a high-angle shift compared with those of the other samples annealed below 1000°C, indicating that the IF structure might be destroyed.





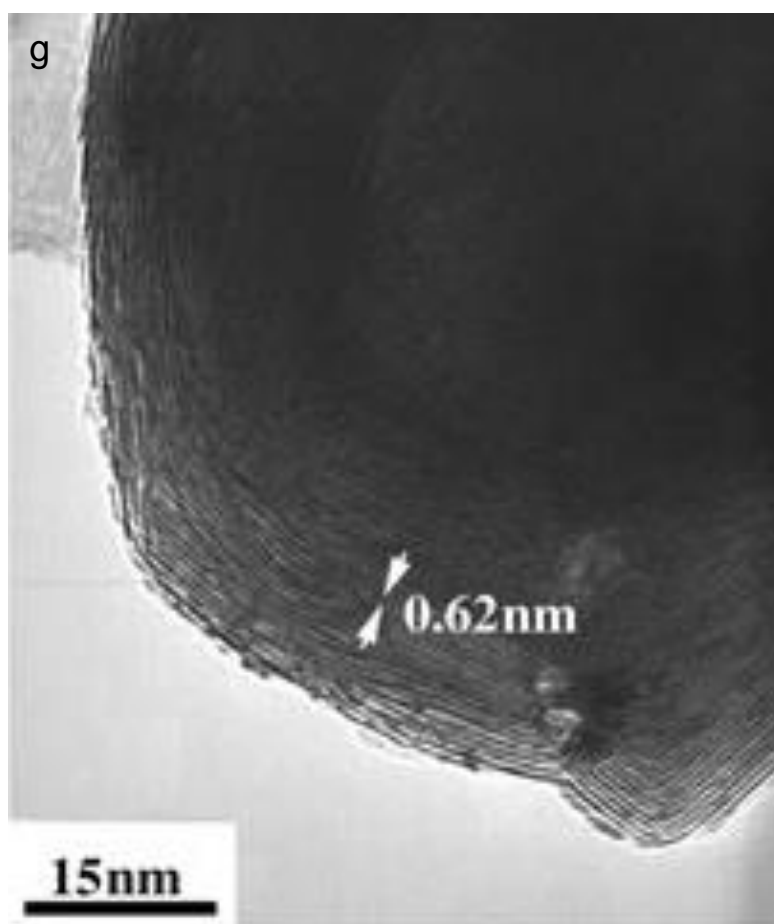


Figure 6.10 TEM images of WS₂ products resulting from 1-h annealing in Ar at (a) 700°C, (b) 800°C, (c) 900°C and (d) 1000°C. HRTEM image of sample resulting from 1-h annealing in Ar at (e) 800°C and (f) 900°C. (g) Typical morphology of synthesised WS₂ IF nanoparticles by Li et al.[10]

Although little difference could be observed from the XRD patterns between the annealed and unannealed samples, the TEM images demonstrate that the morphologies of the annealed samples were quite different. As mentioned previously, WS₂ IF nanoparticles with numerous defects and disconnections were produced at 850°C (Figure 6.4c). After annealing at 700°C for 1 h, these nanoparticles retained similar morphologies to those of the original samples (Figure 6.10a). Upon increasing the annealing temperature to 800°C, hollow IF nanoparticles with an average diameter of 50 nm and large interior voids were obtained (Figure 6.10b). Based on the corresponding HRTEM image (Figure 6.10e), the synthesised WS₂ IF nanoparticles had relatively thin walls (5-15 layers) that were approximately 40 nm in diameter. The lattice distance of the shell was measured to be 0.63 nm. Almost no dislocations or disconnections were observed in the nanoparticles, indicating that the annealing process

promoted WS_2 crystallisation. During the annealing process, additional energy was supplied to promote the crystallisation. Because the initial dangling edges were thermodynamically unstable, they would gradually arrange and connect along the tangential direction to reduce this energy [23].

The IF nanoparticles became unstable upon increasing the temperature to 900°C (Figure. 6.10c). Only a few partially unfolded IF nanoparticles were observed among many agglomerated nanoflakes. In Figure 6.10f, some IF nanoparticles began to crack and unfold from the closed cage structure. Then, nanoflakes with small sizes (below 100 nm) were produced from crushing of IF nanoparticles followed by further crystal growth. This process was promoted when the temperature was increased to 1000°C . No IF nanoparticles were observed by TEM. Numerous nanoflakes that were approximately 300 nm in size were generated instead. This result was consistent with the XRD analysis, which shows the changes in the positions and intensities of the peaks.

As mentioned previously, WS_2 IF nanoparticles were synthesised *via* a similar CVD route from the reaction between WCl_6 and S [10]. According to Figure 6.10g, the produced WS_2 IF nanoparticle contained numerous defects that were also observed in the unannealed sample (Figure 6.4c). Moreover, little lattice fringes could be observed on the nanoparticle interior, indicating poor crystallisation. Compared with this product, the annealed WS_2 IF nanoparticles exhibited much better crystallinity and thus might exhibit better properties such as mechanical properties and thermal stability.

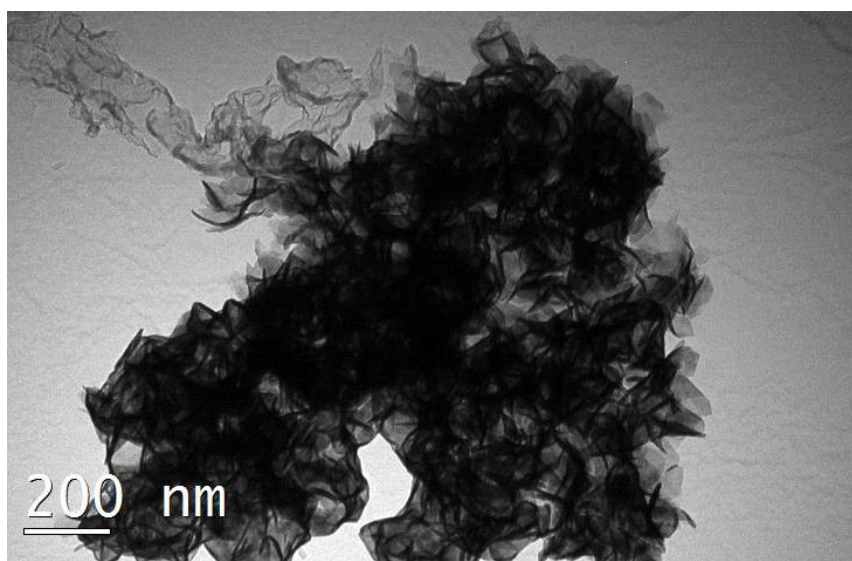


Figure 6.11 TEM image of WS₂ product annealed at 800°C for 4 h in Ar.

In addition to the temperature, the annealing time had a clear effect on the morphology of the WS₂ products. When the WS₂ sample was annealed at 800°C for 4 h in Ar, WS₂ nanoflakes with an average size of approximately 200 nm were generated rather than IF nanoparticles (Figure 6.11). Similar to Figure 6.8b, these nanoflakes had curved edges with similar small thicknesses and were highly agglomerated. Therefore, the generation of these nanoflakes was also attributed to the crushing of the initially formed WS₂ IF nanoparticles.

6.5 Comprehensive analysis on the synthesis of WS₂ IF nanoparticles

The synthesis of WS₂ IF nanoparticles followed a typical CVD mechanism. Because both WCl₆ and S have low boiling points (347°C and 445°C, respectively), they became gaseous phases immediately after being pushed into the hot zone of the preheated furnace. The initially formed species could most likely be WCl_xS_y which is unstable at high temperature [24, 25]. Subsequent heating led to the nucleation of WS₂ amorphous particles from the gas phase, which were deposited on the inner surface of the quartz tube, followed by crystallisation of the nanoparticles. Because the reactivity was the highest at the particle surface, the crystallisation speed on the surface was higher than that on the interior, leading to the formation of a crystalline-WS₂-coated amorphous core (Figure 6.4a). Because the density of the crystallised WS₂ was larger than that of the amorphous phase, a concentration gradient was present from the shell to the core. The further crystallisation process bears a resemblance to the so-called “coffee stain effect” [26, 27]. To balance the density difference without mass change, the formed WS₂ core-shell nanoparticles tended to shrink to reduce their volumes. However, the initially formed, crystallised WS₂ shell could not shrink as amorphous cores. Therefore, the further crystallisation process resulted in a mass transfer from the interior of the particle to the particle boundary. This process lasted until the core was depleted and, thus, a hollow IF nanoparticle was formed (Figure 6.4c). When the annealing process was absent, hollow IF nanoparticles could be

synthesised but with numerous defects and disconnections, suggesting poor crystallisation extents (Figure 6.4). The additional annealing process provided sufficient energy to facilitate crystallisation by rearranging (002) fragments into continuous shells (Figure 6.10) because dangling bonds on the edges of (002) fragments were eliminated by reconnection with each other. The formed IF nanoparticles exhibited the lowest energy and thus the best stability.

Conclusions

Well-crystallised WS₂ IF nanoparticles with sizes below 100 nm were produced *via* a simple CVD route from the reaction of WCl₆, H₂ and S. For this technique, annealing was a vital process to improve the crystallisation extents of the produced IF nanoparticles. Although WS₂ IF hollow nanoparticles with similar sizes could also be formed *via* CVD without annealing, the resulting nanoparticles contained numerous defects and disconnections, leading to poor stability and mechanical properties. A reaction mechanism was proposed based on the experimental results. The generation of the hollow structure was based on mass transfer from the interior to the surface. Because of the production of well-crystallised WS₂ IF nanoparticles, this technique might provide an alternative method for the synthesis of WS₂ IF nanostructures.

Synthesis and characterisation of ZrS₂ nanoflakes

6.6 Composition and morphology of products

In Figure 6.12a, the XRD pattern of the sample resulting from 1-h firing at 800°C is presented. All the diffraction peaks match with those of standard ZrS₂ (JCPDS card No. 11-619), indicating that the product phase was phase pure ZrS₂. A TEM image (Figure 6.12b) reveals that the ZrS₂ particles had angular shapes and a narrow size distribution (10-30 nm), implying their high surface energy. Consequently, some nanoflakes were overlapped with one another to reduce the surface energy. A HRTEM image (Figure 6.12c) further reveals that the ZrS₂ nanoflakes were well crystallised. The surfaces of the nanoflakes were orthogonal to the direction of the electron beam, giving a lattice distance of 0.31

nm, which matches with that between the (100) planes of ZrS₂ (Figure 6.12c). According to AFM analysis (Figure 6.12d), the sizes of the ZrS₂ nanoflakes were in the range of 10-30 nm, which was consistent with the TEM observations. The thicknesses of some representative particles (the marked ones) were measured to be approximately 1.6 nm, indicating that the particles were composed of only 3 atomic layers [15].

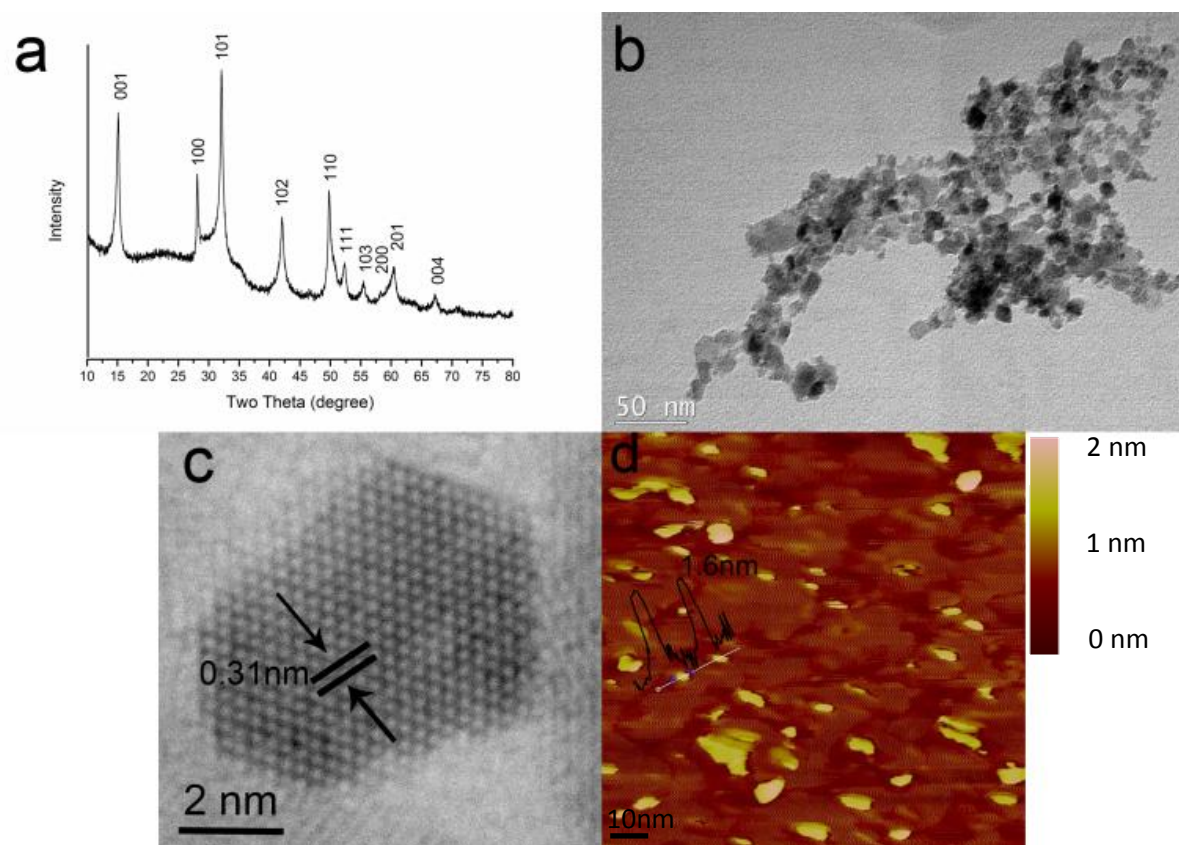


Figure 6.12 (a) XRD, (b and c) TEM and (d) AFM images ($1 \times 1 \mu\text{m}$) of the sample resulting from 1-h firing at 800°C in H₂/Ar.



Figure 6.13 presents the XRD patterns of the samples resulting from 1-h firing at 650°C, 700°C, 750°C and 900°C. At 650°C, the primary phase in the sample was ZrS₃ rather than the expected ZrS₂, indicating that ZrCl₄ and S reacted to form ZrS₃ according to Reaction (6.2). Because excess S was added to compensate for the S loss at high temperature, this reaction was essentially performed in an S-rich atmosphere. It has been demonstrated that ZrS₃ is the

thermodynamically stable phase at low temperatures and in the excess sulphur regime [11]. Upon increasing temperature to 700°C, small amounts of ZrS_2 were detected in addition to the primary phase ZrS_3 , indicating that ZrS_3 was not stable at this temperature and started to decompose to ZrS_2 (Figure 6.13b) according to Reaction (6.3). Upon further increasing the temperature to 750°C, ZrS_2 became the primary phase, and only minor amounts of ZrS_3 remained (Figure 6.13c). When the temperature reached 900°C, the ZrS_2 peaks became increasingly higher, whereas the ZrS_3 peaks almost disappeared (Figure 6.13d). Based on the above analysis, the overall reaction process could be described as follows: ZrS_3 was initially generated from the reaction between $ZrCl_4$ and S and remained stable until 650°C. Upon increasing the temperature to above 650°C, ZrS_3 started to gradually decompose into ZrS_2 . High temperature would accelerate this decomposition process until the reaction was completed and phase pure ZrS_2 was obtained.

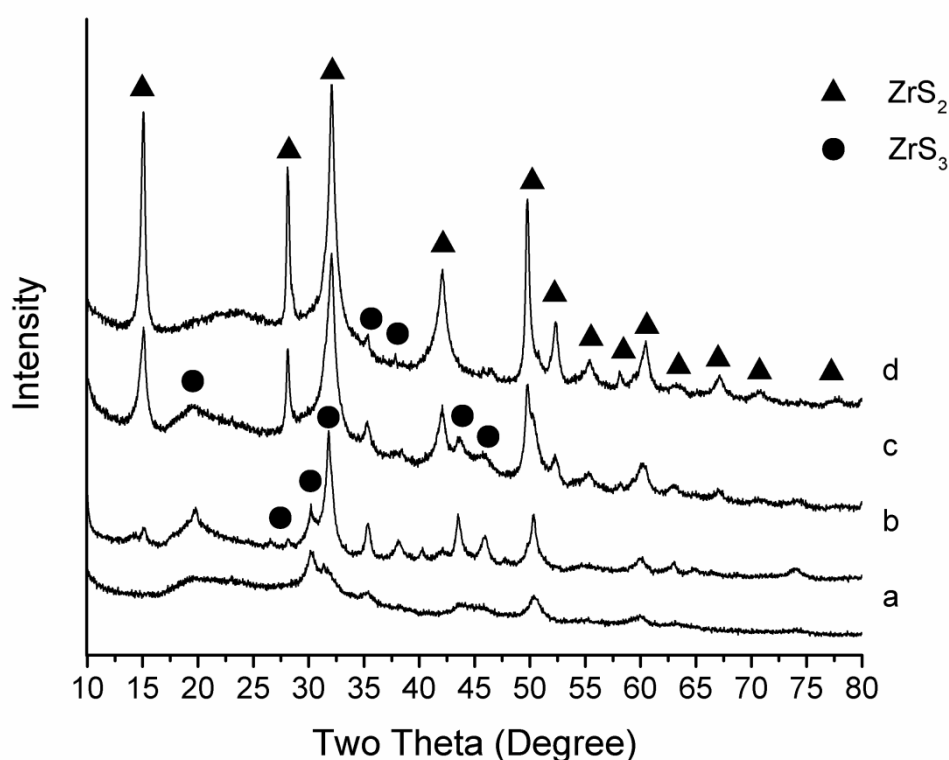


Figure 6.13. XRD patterns of samples resulting from 1-h firing in H_2/Ar at (a) 650°C, (b) 700°C, (c) 750°C and (d) 900°C.

6.7 Effect of temperature

Figure 6.14 presents TEM images of some of the samples whose XRD patterns are shown in Figure 6.13. The ZrS_3 nanosheets resulting from 1-h firing at 650°C (Figure 6.14a) were nearly transparent, implying their very small thicknesses. The average size and thickness of the curved nanosheets were measured to be approximately 150 nm and 7 nm, respectively. Due to their small thicknesses and relatively high surface energies, the ZrS_3 nanoflakes tended to curve and connect with each other to maintain the minimum thermodynamic energy [17], which explained their agglomeration. Upon increasing temperature to 750°C , these ZrS_3 nanoflakes became unstable and were reduced by H_2 (Reaction (6.3)). The loss of S atoms during the reduction caused crushing of the initial nanoflakes into tiny fragments [11], which finally crystallised to ZrS_2 (Figure 6.14b). At 900°C , the crystal growth rate of ZrS_2 increased, leading to the formation of larger flakes with an average size of approximately 100 nm (Figure 6.14c).

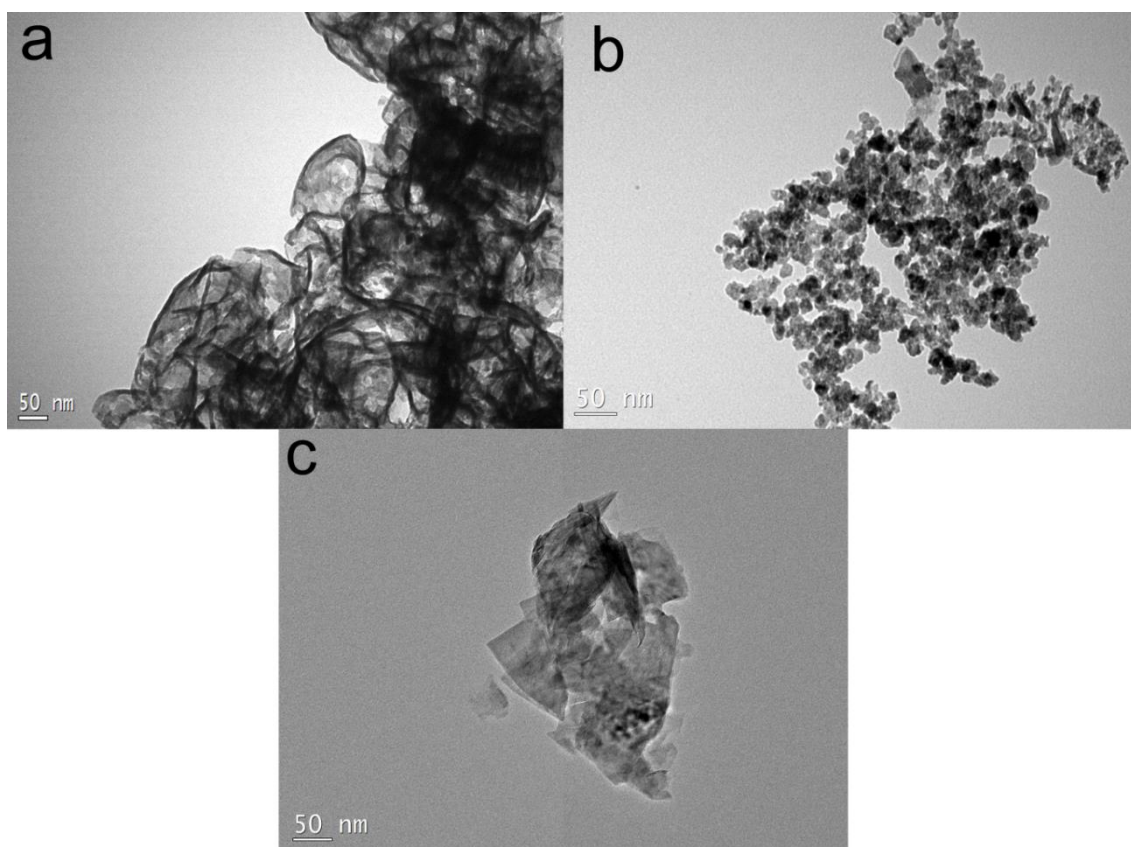


Figure 6.14. TEM images of samples resulting from 1-h firing at (a) 650°C , (b) 750°C and (c) 900°C in Ar/H_2 atmosphere.

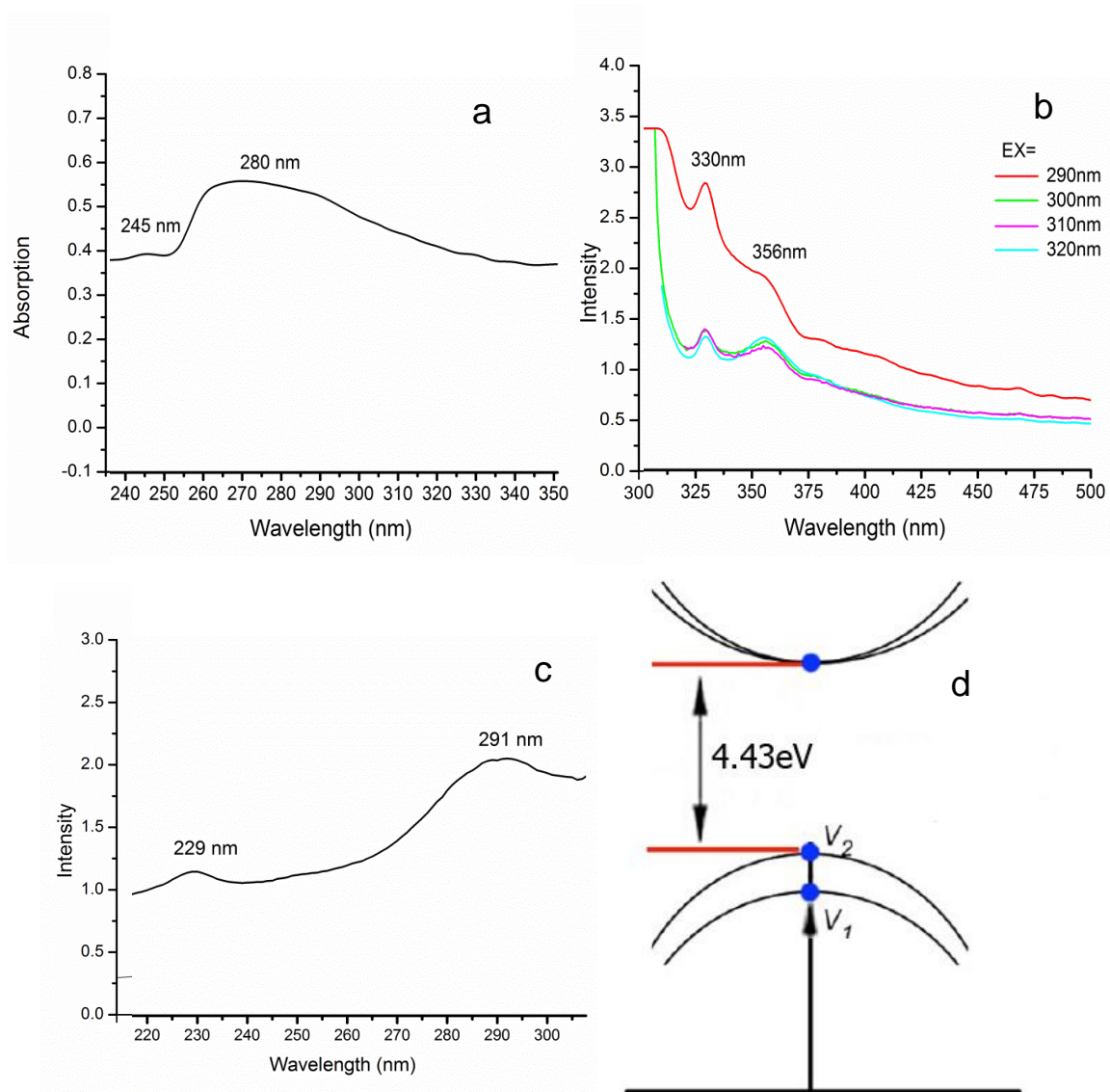


Figure 6.15 (a) UV-vis spectrum of as-synthesised ZrS_2 nanoflakes. (b) PL spectrum of as-synthesised ZrS_2 nanoflakes with various excitation wavelengths. (c) Corresponding PLE spectrum with 330-nm detection wavelength. (d) Diagram of the band structure of the as-synthesised ZrS_2 nanoflakes close to the K point (V_1 and V_2 are the two valence band maxima).

In Figure 6.15, the UV-vis, PL and PLE spectra of the ZrS_2 nanoflakes resulting from 1-h firing at 800°C in H_2/Ar are presented. In Figure 6.15a, two peaks centred at 245 nm and 280 nm are observed. Compared with the characteristic UV-vis absorption peak of a ZrS_2 thin film, which is centred at approximately 400 nm [18], the absorption peak in Figure 6.15a exhibits an obvious blue-shift, arising from the strong quantum confinement effect. According to Figure 6.15b, several fluorescence spectra were measured with various excitation

wavelengths between 290 and 320 nm. The strongest emissions of the ZrS₂ nanoflakes occurred at 330 and 356 nm (UV area) when a 290-nm excitation wavelength was used. Upon changing the excitation wavelengths, the fluorescence band position remained unchanged, indicating that the fluorescence was generated under the same initial and final states even when the excitation wavelength was varied between 290 and 320 nm. This effect was attributed to the fast energy relaxation from the excitation state, which was excited by the photo-excitation to the ground state. In Figure 6.15c, the PL-excitation (PLE) spectrum of the ZrS₂ nanoflakes with a detection wavelength of 330 nm is presented. A strong peak (~291 nm) and a weak peak (~229 nm) are observed. Although ZrS₂ is an indirect gap semiconductor, it could be transferred to a direct gap semiconductor upon decreasing the atomic layers [19]. The obvious luminescence of as-synthesised ZrS₂ nanoflakes (Figure 6.15b) indicated such an indirect-to-direct band structure change, which was consistent with the thin-layered structure observed by HRTEM (Figure 6.12c) and AFM (Figure 6.12d). The two excitation peaks in the PLE spectrum could be assigned to two excitation processes: (1) excitation from the V2 point to the conduction band minimum (band gap ~4.43 eV) and (2) excitation from the V1 point to the conduction band minimum (band gap ~5.06 eV). These band gaps were much larger than those reported for monolayer ZrS₂ (~2 eV) [19] because of the strong quantum confinement of the as-synthesised ZrS₂ nanoflakes.

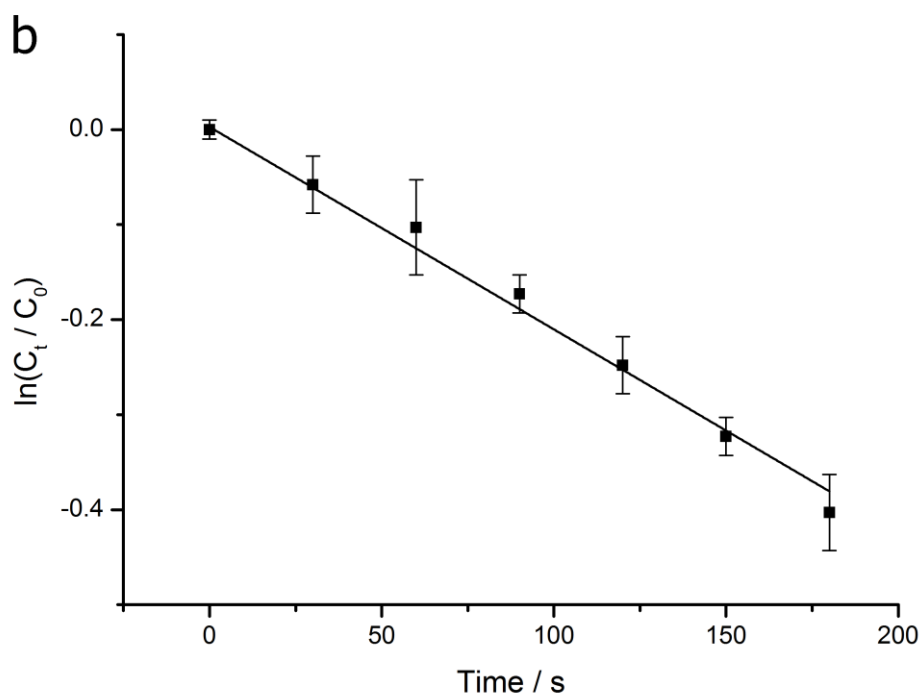
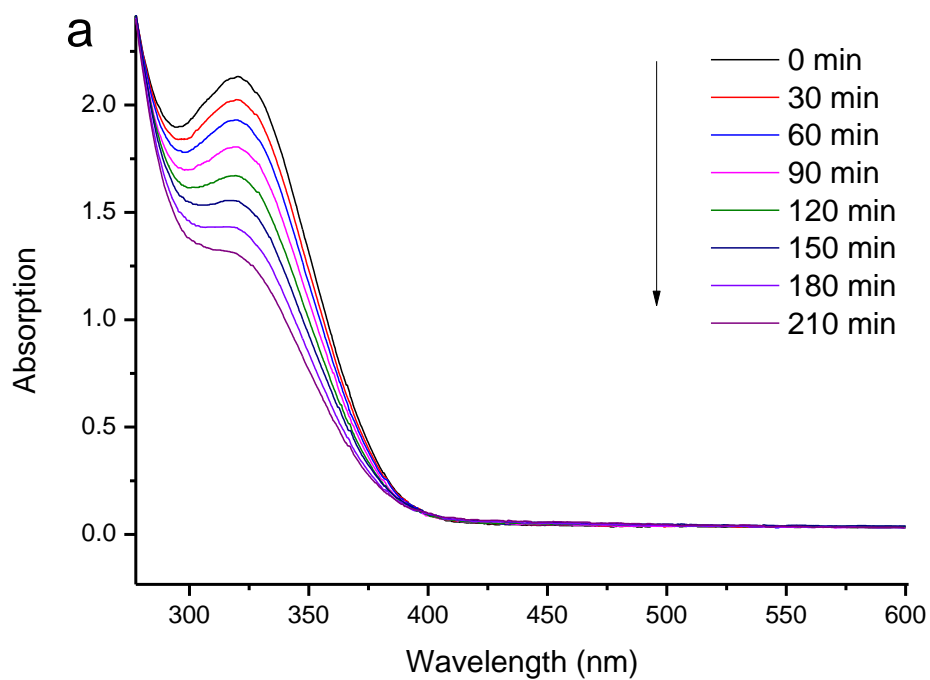


Figure 6.16 (a) Time-dependent UV-vis absorption spectrum during degradation of 4-NP on ZrS₂ catalyst. (b) Plot of $\ln(C_t/C_0)$ versus time using ZrS₂ as catalysts.

Some semiconductor materials such as TiO₂ and ZnO have been reported to exhibit strong photocatalytic activities [20, 21]. When these materials are irradiated with light of a suitable wavelength, electrons will jump from the

valence band (VB) to the conduction band (CB), leaving holes behind. In aqueous suspension systems, the generated electron holes can react with OH⁻ groups to form ·OH radicals, which are the strongest oxidising species [22, 23] and thus can easily oxidise some organic compounds. Because the synthesised ZrS₂ nanoflakes have a large band gap (4.15 eV), excited electrons need a relatively long time to refill the electron holes, which extend the lifetime of ·OH radicals, leading to strong oxidation. In this work, H₂O₂ was used as an electron acceptor to enhance the oxidation process for two reasons. One was that H₂O₂ could accept excited electrons, generating more radical ·OH radicals, and the other was that the acceptance of excited electrons by H₂O₂ inhibited the recombination of electrons and holes and thereby further improved the oxidation performance. In Figure 6.16, the UV-vis spectrum evolution of the 4-NP degradation with time is shown. The 4-NP-H₂O₂ solution had a UV absorption peak centred at approximately 320 nm, which was the characteristic peak of 4-NP [21]. Upon the addition of ZrS₂ nanoflakes, the peak height at 320 nm clearly decreased with time. The ratio of the 4-NP concentrations at times t (C_t) and 0 (C₀) was measured from the relative intensity ratio of the respective absorbance, A_t/A₀, at 320 nm. A linear relationship between ln(C_t/C₀) and time was obtained (Figure 6.16b), indicating a first-order reaction. Standard deviation from the mean was determined to estimate the error in ln(C_t/C₀). From the slope of the straight line in Figure 6.16b, the reaction rate constant when using ZrS₂ nanoflakes as a catalyst was $2.22 \times 10^{-3} \text{ min}^{-1}$.

Conclusions

ZrS₂ nanoflakes were produced *via* a conventional CVD technique by heating ZrCl₄ and S. The generated ZrS₂ nanoflakes had a narrow size distribution (10-30 nm) and thin thickness (~1.6 nm). Because of the small size, these nanoflakes exhibit strong quantum confinement and luminescence effects. In addition, these nanoflakes also exhibit good photocatalytic activity for the decomposition of 4-NP.

References

- [1] X. F. Duan, Y. Huang, R. Agarwal, and C. M. Lieber, "Single-nanowire electrically driven lasers," *Nature*, vol. 421, pp. 241-245, Jan 16 2003.
- [2] M. R. Gao, Y. F. Xu, J. Jiang, and S. H. Yu, "Nanostructured metal chalcogenides: synthesis, modification, and applications in energy conversion and storage devices," *Chemical Society Reviews*, vol. 42, pp. 2986-3017, 2013.
- [3] J. Chen and F. Wu, "Review of hydrogen storage in inorganic fullerene-like nanotubes," *Applied Physics a-Materials Science & Processing*, vol. 78, pp. 989-994, Apr 2004.
- [4] G. L. Frey, S. Elani, M. Homyonfer, Y. Feldman, and R. Tenne, "Optical-absorption spectra of inorganic fullerenelike MS₂ (M = Mo, W)," *Physical Review B*, vol. 57, pp. 6666-6671, Mar 15 1998.
- [5] O. Tevet, O. Goldbart, S. R. Cohen, R. Rosentsveig, R. Popovitz-Biro, H. D. Wagner, and R. Tenne, "Nanocompression of individual multilayered polyhedral nanoparticles," *Nanotechnology*, vol. 21, Sep 10 2010.
- [6] Y. L. Liang, R. J. Feng, S. Q. Yang, H. Ma, J. Liang, and J. Chen, "Rechargeable Mg Batteries with Graphene-like MoS₂ Cathode and Ultrasmall Mg Nanoparticle Anode," *Advanced Materials*, vol. 23, pp. 640+, Feb 1 2011.
- [7] H. B. Yang, S. K. Liu, J. X. Lil, M. H. Li, G. Peng, and G. T. Zou, "Synthesis of inorganic fullerene-like WS₂ nanoparticles and their lubricating performance," *Nanotechnology*, vol. 17, pp. 1512-1519, Mar 14 2006.
- [8] H. Wu, R. Yang, B. Song, Q. Han, J. Li, Y. Zhang, Y. Fang, R. Tenne, and C. Wang, "Biocompatible inorganic fullerene-like molybdenum disulfide nanoparticles produced by pulsed laser ablation in water," *Acs Nano*, vol. 5, pp. 1276-81, Feb 22 2011.
- [9] H. C. Sun, D. Qin, S. Q. Huang, X. Z. Guo, D. M. Li, Y. H. Luo, and Q. B. Meng, "Dye-sensitized solar cells with NiS counter electrodes electrodeposited by a potential reversal technique," *Energy & Environmental Science*, vol. 4, pp. 2630-2637, Aug 2011.
- [10] X. L. Li, J. P. Ge, and Y. D. Li, "Atmospheric pressure chemical vapor deposition: An alternative route to large-scale MoS₂ and WS₂ inorganic fullerene-like nanostructures and nanoflowers," *Chemistry-a European Journal*, vol. 10, pp. 6163-6171, Dec 3 2004.
- [11] A. Margolin, F. L. Deepak, R. Popovitz-Biro, M. Bar-Sadan, Y. Feldman, and R. Tenne, "Fullerene-like WS₂ nanoparticles and nanotubes by the vapor-phase synthesis of WCl_(n) and H₂S," *Nanotechnology*, vol. 19, Mar 5 2008.
- [12] Y. L. Zhang, X. C. Wu, Y. R. Tao, C. J. Mao, and J. J. Zhu, "Fabrication and field-emission performance of zirconium disulfide nanobelt arrays," *Chemical Communications*, pp. 2683-2685, 2008.

- [13] B. T. Kaminskii, G. N. Prokof'eva, A. S. Plygunov, and P. A. Galitskii, "Manufacture of zirconium and hafnium sulfide powders," *Soviet Powder Metallurgy and Metal Ceramics*, vol. 12, pp. 521-524, 1973/07/01 1973.
- [14] M. Nath and C. N. R. Rao, "Nanotubes of group 4 metal disulfides," *Angewandte Chemie-International Edition*, vol. 41, pp. 3451-3454, 2002.
- [15] J. N. Coleman, M. Lotya, A. O'Neill, S. D. Bergin, P. J. King, U. Khan, K. Young, A. Gaucher, S. De, R. J. Smith, I. V. Shvets, S. K. Arora, G. Stanton, H. Y. Kim, K. Lee, G. T. Kim, G. S. Duesberg, T. Hallam, J. J. Boland, J. J. Wang, J. F. Donegan, J. C. Grunlan, G. Moriarty, A. Shmeliov, R. J. Nicholls, J. M. Perkins, E. M. Grievson, K. Theuwissen, D. W. McComb, P. D. Nellist, and V. Nicolosi, "Two-Dimensional Nanosheets Produced by Liquid Exfoliation of Layered Materials," *Science*, vol. 331, pp. 568-571, Feb 4 2011.
- [16] J. T. Jang, S. Jeong, J. W. Seo, M. C. Kim, E. Sim, Y. Oh, S. Nam, B. Park, and J. Cheon, "Ultrathin Zirconium Disulfide Nanodiscs," *Journal of the American Chemical Society*, vol. 133, pp. 7636-7639, May 25 2011.
- [17] T. Vincent and E. Guibal, "Chitosan-supported palladium catalyst. 3. Influence of experimental parameters on nitrophenol degradation," *Langmuir*, vol. 19, pp. 8475-8483, Sep 30 2003.
- [18] Y. Feldman, G. L. Frey, M. Homyonfer, V. Lyakhovitskaya, L. Margulis, H. Cohen, G. Hodes, J. L. Hutchison, and R. Tenne, "Bulk synthesis of inorganic fullerene-like MS(2) (M=Mo, W) from the respective trioxides and the reaction mechanism," *Journal of the American Chemical Society*, vol. 118, pp. 5362-5367, Jun 12 1996.
- [19] T. Sekine, T. Nakashizu, K. Toyoda, K. Uchinokura, and E. Matsuura, "Raman-Scattering in Layered Compound 2h-Ws₂," *Solid State Communications*, vol. 35, pp. 371-373, 1980.
- [20] Y. Feldman, A. Zak, R. Popovitz-Biro, and R. Tenne, "New reactor for production of tungsten disulfide hollow onion-like (inorganic fullerene-like) nanoparticles," *Solid State Sciences*, vol. 2, pp. 663-672, Oct 2000.
- [21] A. Yella, M. Panthofer, M. Kappl, and W. Tremel, "Snapshots of the Formation of Inorganic MoS₂ Onion-Type Fullerenes: A "Shrinking Giant Bubble" Pathway," *Angewandte Chemie-International Edition*, vol. 49, pp. 2575-2580, 2010.
- [22] G. Seifert, T. Kohler, and R. Tenne, "Stability of metal chalcogenide nanotubes," *Journal of Physical Chemistry B*, vol. 106, pp. 2497-2501, Mar 14 2002.
- [23] N. Zink, H. A. Therese, J. Pansiot, A. Yella, F. Banhart, and W. Tremel, "In situ heating TEM study of onion-like WS₂ and MoS₂ nanostructures obtained via MOCVD," *Chemistry of Materials*, vol. 20, pp. 65-71, Jan 8 2008.

- [24] D. Britnell, G. W. A. Fowles, and D. A. Rice, "Preparation of Halide Sulfides and Halide Selenides of Molybdenum and Tungsten," *Journal of the Chemical Society-Dalton Transactions*, pp. 2191-2194, 1974.
- [25] E. Milke, R. Koppe, and M. Binnewies, "Formation and Stability of Gaseous WS₂Cl₂, WS₂Br₂ and WS₂I₂ - A Combined Experimental and Theoretical Study," *Zeitschrift Fur Anorganische Und Allgemeine Chemie*, vol. 636, pp. 1313-1317, 2010.
- [26] R. D. Deegan, O. Bakajin, T. F. Dupont, G. Huber, S. R. Nagel, and T. A. Witten, "Capillary flow as the cause of ring stains from dried liquid drops," *Nature*, vol. 389, pp. 827-829, Oct 23 1997.
- [27] N. Loges, K. Graf, L. Nasdala, and W. Tremel, "Probing cooperative interactions of tailor-made nucleation surfaces and macromolecules: A bioinspired route to hollow micrometer-sized calcium carbonate particles," *Langmuir*, vol. 22, pp. 3073-3080, Mar 28 2006.

Chapter Seven

One-Step Synthesis and Characterisation of WS₂ based Nanorattles via Gas-Solid Reaction

7.1 Synthesis of W@WS₂ nanorattles and their catalytic performance

7.1.1 Introduction

Nanorattles, nanoparticles with a core-in-hollow-shell structure, have received a great deal of attention because of their unique properties and great application potentials. For example, metal-cored nanorattles could exhibit excellent catalytic activities, arising from their unique structure in which the nanoparticle cores are effectively isolated, avoiding their agglomeration and exposing more active surface. Consequently, they could perform much better than their naked or conventionally coated nanoparticle counterparts [1].

To synthesise nanorattle materials, several techniques and methodologies have been suggested, among which the template synthesis is the most commonly used because of its good reliability and controllability. With this technique, a core-shell structured precursor was initially coated with another material, forming a three-layered egg-like composite particle (analogous to 'yolk, egg white, and eggshell').which was further subject to chemical etching or calcination to remove the 'egg white' part, creating a nanorattle with a core inherited from the precursor and a shell from the coating. With this technique, several types of nanorattles with different core/shell sizes and thicknesses were prepared, e.g., Au@ZrO₂ nanorattles from an Au-SiO₂-ZrO₂ composite precursor,[2] hybrid Au-Pt @ α -Fe₂O₃ from an Au-Pt- polyelectrolyte multilayers (PEMs)- α -FeOOH precursor,[3] Pt@hollow porous carbon (hmC) from a Pt-SiO₂- phenol-formaldehyde resin (PF) precursor,[4] or Pt-TiO₂-phenol precursor,[5] and SiO₂@TiO₂ from a SiO₂-polystyrene-sulfonated polystyrene-TiO₂ composite.[6] In spite of these, this technique still suffered from several drawbacks including the requirement of a core-shell structured precursor

produced by a complex multi-step process using hazardous etching agents, thus was not applicable to a large scale production.

Another modified template synthesis technique was the so-called preshell-postcore technique.[7] Hollow nanospheres were used as nanoreactors into which reactant precursors diffuse and then react.[8-11] By using this method, Cu@SiO₂[8] and Ag@polypyrrole-chitosan (PPy-CS) nanorattles[11] were prepared. Although this modified route could partially overcome the drawbacks of the conventional template synthesis route stated above and improve the product purity, the complex reaction processes used and the involvement of ultraviolet irradiation made it also difficult to be used for a large scale production.

Apart from the template-based synthesis routes, interdiffusion processes based on the Kirkendall effect and the Ostwald ripening mechanism were used. However, they were only applicable to some special cases such as Co@CoSe[12] and ZnS nanorattles.[13]

To overcome the drawbacks of the techniques reported so far, a scalable one-step synthesis technique by simply heating oxide precursors and S at a low temperature in H₂/Ar was developed by the author, and used to produce several types of nanorattles. In this chapter, the work on the synthesis of W@WS₂ nanorattles will be presented. The thicknesses of WS₂ shells and sizes of W cores were tailored by altering the gas flow rate. Based on the results, a reaction mechanism was proposed. In addition, to explore potential applications of as-prepared nanorattles, their catalytic performance was investigated as an example by using the conversion reaction from 2-Nitroaniline (2-NA) to o-Phenylenediamine (OPD) as a working tool. This conversion reaction was usually catalysed by highly costive catalysts such as gold nanoparticles[14]. The present work demonstrated that as-prepared nanorattles showed much better catalytic activity and thus could be potentially used to replace those costive catalysts.

7.1.2 Experimental

Preparation of W@WS₂ nanorattles

For the synthesis of W@WS₂ nanorattles, very similar procedure as described in Chapter 4 was used while the only difference is the usage of high flow rate Ar and H₂. 0.232g WO₃ nanoparticle (<100nm, 99.5%, Sigma-Aldrich) and S powder (99%, Sigma-Aldrich) were used as the starting raw materials. The former was initially ultrasonically dispersed in 100ml ethanol for 2h before oven-drying at 80°C. The dry WO₃ powder and S in the molar ratio of 1:10 (excessive amounts of S were used to compensate its evaporation loss during the heating/reaction processes), were mixed in a ball mill at 400rpm for 2h. A quartz tube in an electronic furnace was flowed with Ar at 80ml/min for 30min to remove any residual air and then heated to a given temperature between 750 and 950°C. After introducing H₂ at 40ml/min along with Ar at 80ml/min, into the tube, the S and WO₃ mixture contained in a ceramic boat was pushed to the hot zone of the tube. After 1h at the given temperature, the reacted sample was furnace-cooled to room temperature, and subjected to further characterisation.

Characterisation

Phases in reacted powder samples were identified using an X-ray diffractometer (D500 Siemens) with CuK α radiation ($\lambda=0.154$ nm) at 2° (2 θ)/min. ICDD cards used for phase identifications included WS₂ (No. 84-1398), WO₃ (No. 32-1395), W₁₈O₄₉ (No. 36-101) and α -W (No. 47-1319). A JEOL 2100 TEM at an accelerating voltage of 200 kV was used to observe microstructures of the reacted samples.

Catalytic reduction of 2-nitroaniline

2.94 mg W@WS₂ nanorattles were ultrasonically dispersed in 10 mL distilled water for 30min to produce a homogenous suspension with 1.6×10^{-3} M (with respect to the tungsten precursor concentration). 10 mL of 3.2×10^{-3} M 2-NP aqueous solution was mixed with 10 mL of 0.12M NaBH₄ aqueous solution *via*

stirring for 30 min at room temperature. Then, 10 mL W@WS₂ nanorattle suspension was added, and the resulting mixture was continuously stirred until the yellow solution became colourless. The reaction progress was monitored by UV-vis measurements (performed on a Jenway 6715 UV/visible spectrophotometer at room temperature) on 1 mL of the solution taken out every 3 min from the reacting solution.

7.1.3 Results and Discussion

1. Effect of heating temperature on synthesis and phase morphology

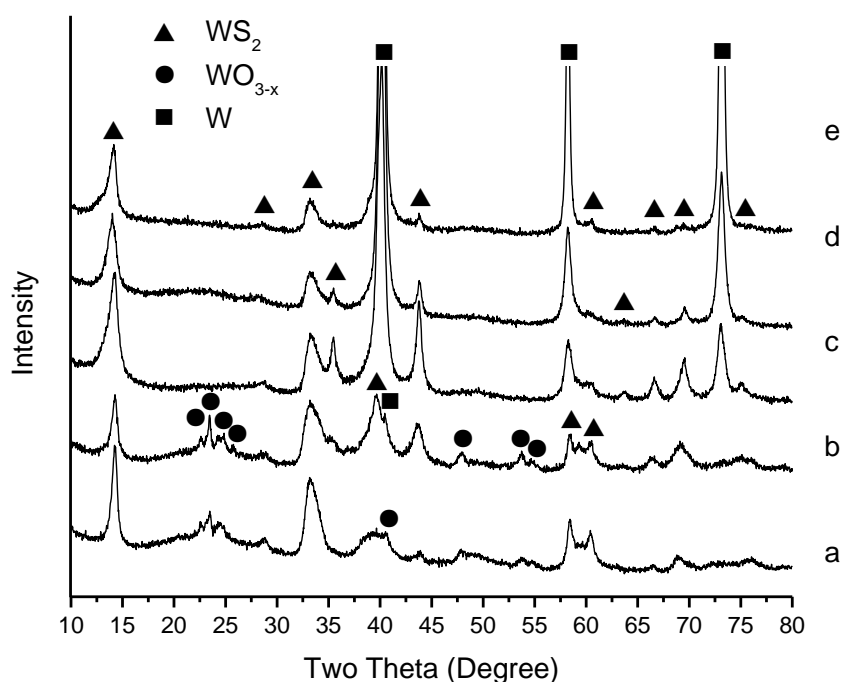
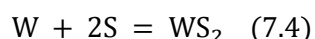
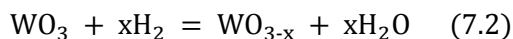
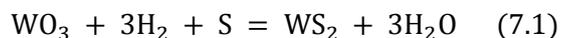


Figure 7.1 XRD patterns of samples resultant from 1h firing at (a) 650°C (b) 700°C (c) 750°C (d) 850°C and (e) 950°C.

Figure 7.1 shows XRD patterns of samples resultant from 1h firing at 650, 700, 750, 850 and 950°C respectively. At 650°C (Figure 7.1a), WS₂ was already formed as the primary phase, while only minor amounts of WO_{3-x} was detected, indicating a high extent of conversion from WO₃ to WS₂ (Eq.(7.1)). Due to the high flow rate of H₂, most of the S vapour sublimed from the original S powder was blown out and thus the concentration of S in the local atmosphere

surrounding the WO_3 was low. Consequently, some WO_3 was left without taking part in the sulphidation. Then, these unreacted WO_3 would be further reduced by H_2 to form WO_{3-x} (Eq. (7.2)). At $650^\circ C$, no W was detected, indicating that WO_3 was only partially reduced by H_2 to WO_{3-x} rather than W.



On increasing the temperature to $700^\circ C$ (Figure 7.1b), in addition to WS_2 and WO_{3-x} , small amounts of α -W were detected, indicating that the residual WO_{3-x} was further reduced to W at this temperature (Eq. (7.3)). Due to this relatively low reaction temperature and depletion of S, further sulphidation of WO_{3-x} and W was ceased, leaving both of them in the sample. On further increasing the temperature to $750^\circ C$, WO_{3-x} completely disappeared (Figure 7.1c). Instead, W peaks became higher, whereas WS_2 peaks changed little. These results were attributed to the enhanced reduction rate of tungsten oxides (Eqs. (7.2) and (7.3)) at this higher temperature. Although no phase changes were seen at higher reaction temperatures, the relative ratio between W and WS_2 increased, indicating the formation of more W (Figure 7.1d and e). With increasing the reaction temperature, the H_2 reduction rates corresponding to Eqs. (7.2) and (7.3) became higher. As a result, WO_3 was reduced to W directly (Eq. (7.5)) before the sulphidation (Eq. (7.1)). Although the formed W also could further react with S to form WS_2 (Eq. (7.4)), the reaction rate was much lower than that between WO_3 and S [15]. Consequently, less WS_2 was generated.

Compared with Figure 4.9, many differences could be observed because of the lack of S. For example, all samples obtained in the case were composed of WS_2 and WO_{3-x}/W while pure WS_2 was produced at 800 and $850^\circ C$ when sufficient S was supplied. Moreover, similar sample compositions which are

WS₂ and W could be found in Figure 4.9f and Figure 7.1e but with different reasons (high temperature reduction of oxides and insufficient S respectively).

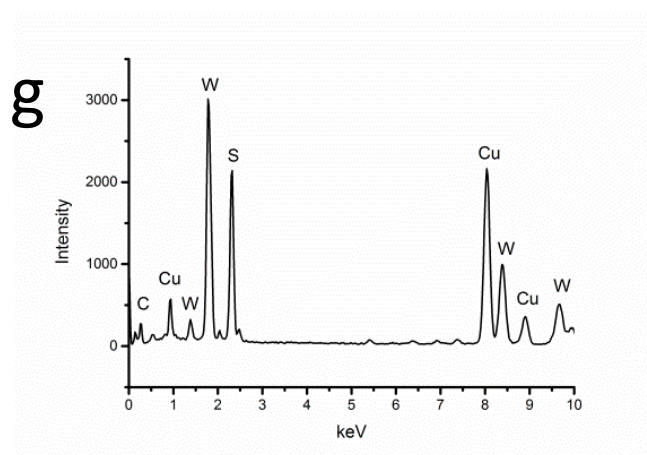
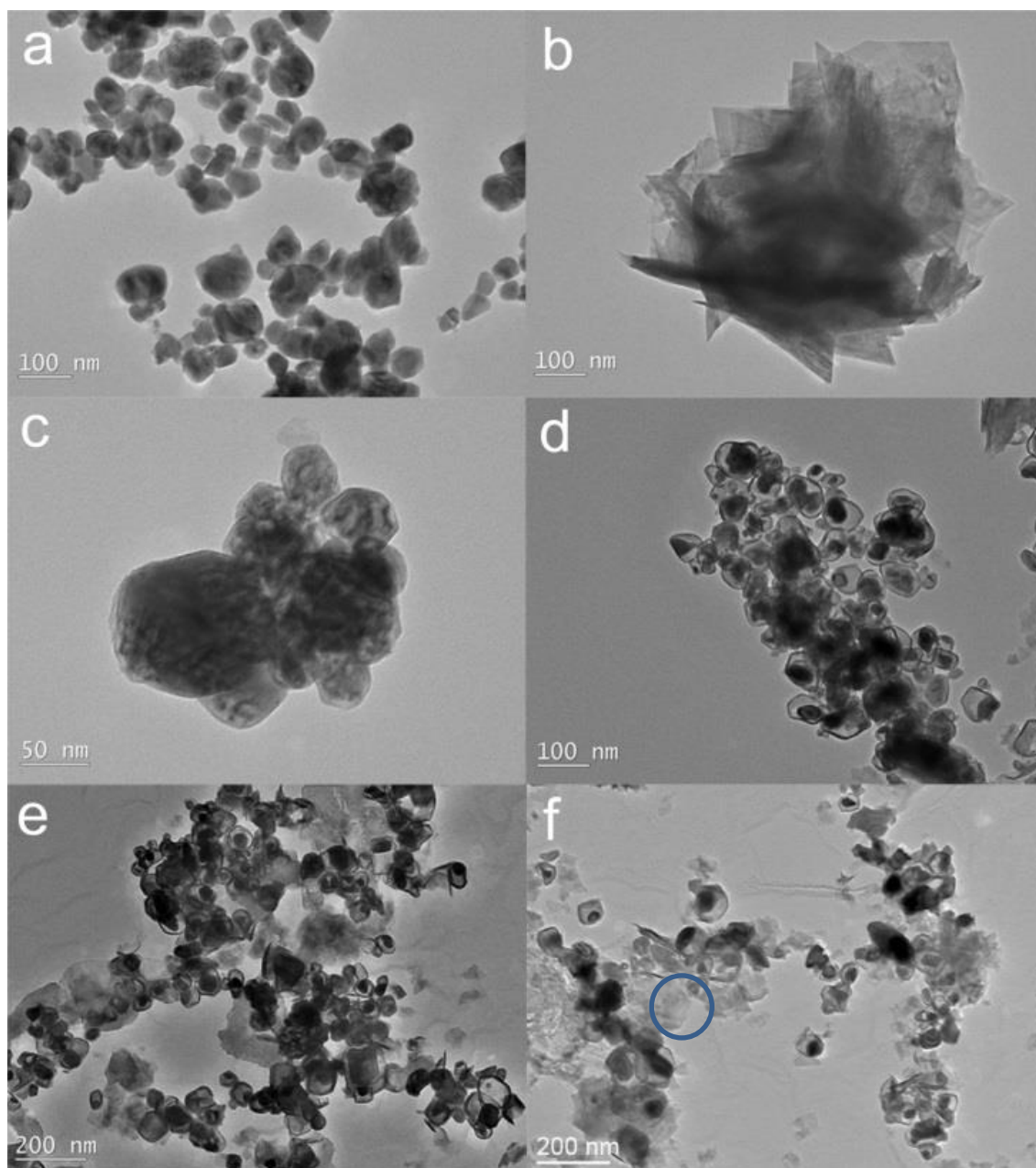


Figure 7.2 TEM images of (a) WO_3 raw materials and WS_2 -W composites synthesised at (b) 650°C , (c) 700°C , (d) 750°C , (e) 850°C and (f) 950°C . (g) EDS spectrum of selected area from (f)

Figure 7.2 illustrates TEM images of the samples whose XRD patterns are shown in Figure 7.1. At 650°C , nanoflakes with the average size of about 400nm were formed as the main product (Figure 7.2b). On increasing the temperature to 700°C , solid nanoparticles with diameters from about 40 to 100nm were formed (Figure 7.2c). On further increasing the temperature to 750°C (Figure 7.2d) and 850°C (Figure 7.2e), nanorattles with shell diameters of 30-90nm were formed as the primary phase. Their sizes and shapes were essentially similar to those of the original WO_3 precursor (Figure 7.2a), indicating that they were formed *via* the so-called template growth mechanism [16]. The thicknesses of the outer shells (5-10nm) were much smaller compared to the overall diameters, leaving “large” inner voids. A solid core was also found in almost every nanosphere. The average size of the cores was estimated to be about 30nm which was smaller than the void sizes (50-100nm) of the hollow nanospheres. Thus, the encapsulated solid nanoparticles should be able to move freely within the nanospheres, which explained the different positions of the solid cores seen in different nanorattles. Although the same product phases (WS_2 and W) were identified in the sample fired at 950°C (Figure 7.1e), their morphologies were different from those in the samples fired at 750 and 850°C (Figure 7.2d & e). Much less nanorattles but more agglomerated WS_2 nanoflakes (confirmed by EDS (Figure 7.2g)) were formed many (Figure 7.2f). Based on the results shown in Figures 7.1&7.2, it could be concluded that the optimal temperature for the nanorattles generation was within a narrow range from 750 to 850°C .

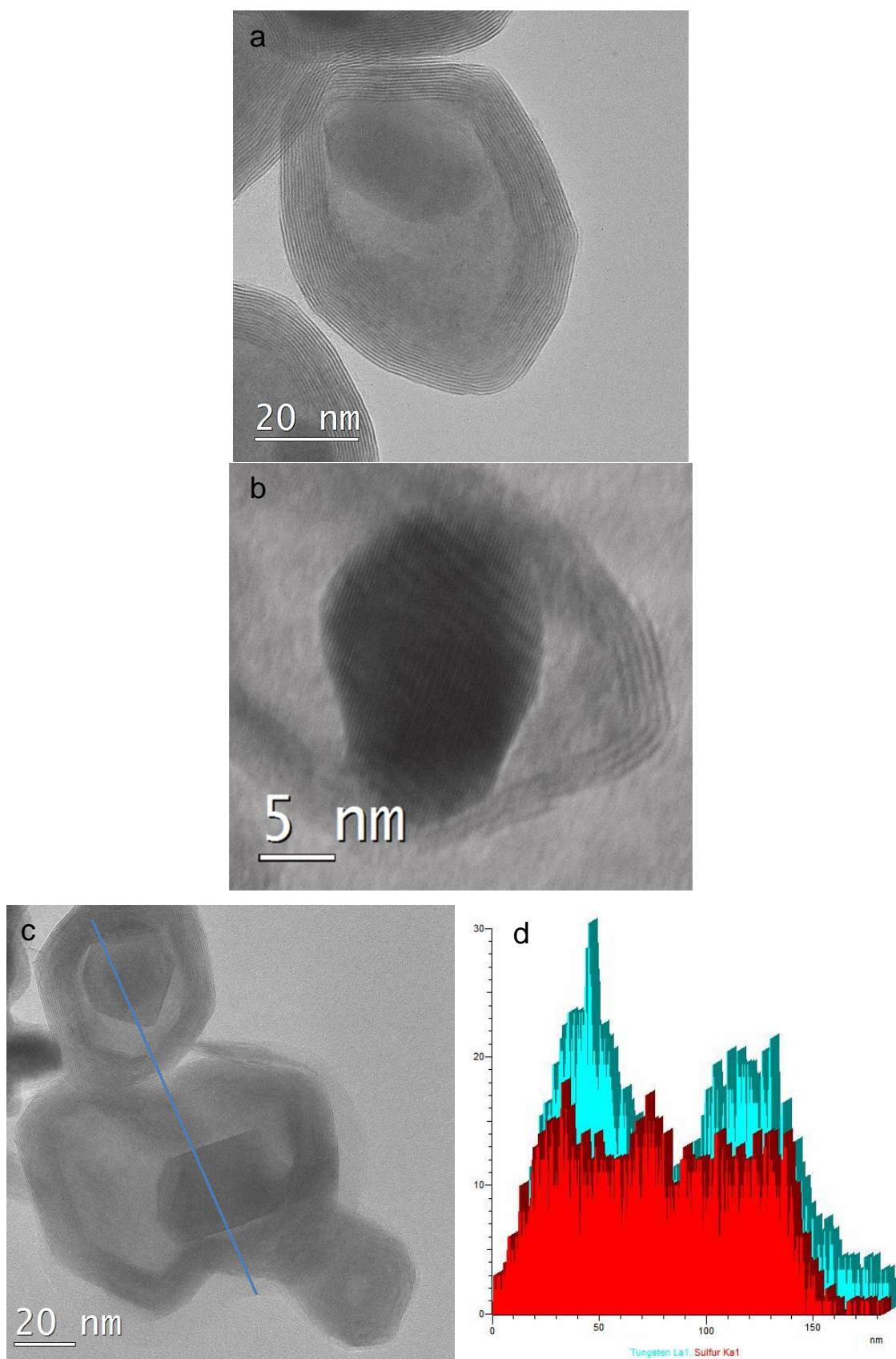


Figure 7.3 (a, b and c) HRTEM images of W@WS₂ nanorattles synthesised at 850°C; (d) EDS line scan of nanorattles shown in 3b. Red indicates sulphur and blue indicates tungsten.

Shown in Figure 7.3 are HRTEM images and selected area EDS line scan spectra of as-prepared W@WS₂ nanorattles. According to Figure 7.3a, the size, shell thickness and core size of this nanorattle were estimated to be 60, 10 and 25nm respectively. TEM image and corresponding EDS line scan spectrum (Figure 7.3c and d) show that only S and W were detected along the scanning line. The signal of S almost maintained stable during the whole scan process, indicating that the amount of S was consistent on the selected line of nanorattles. However, unlike the S pattern, the EDS spectrum of W in the same area was different. Two obvious peaks could be clearly observed, indicating the appearance of W-rich area. The positions of these two W peaks quite matched the positions of cores while no obvious S peak was shown at the same positions. This, along with the XRD analysis (Figure 7.1d), verified that the composition of these two cores was W. Moreover, both W and S signals could still be collected from the bright areas of nanorattles suggested that W cores were enclosed in continuous WS₂ shells.

Unlike most of the nanorattles synthesised previously which had polymer or amorphous ceramic shells, the nanorattles produced with this work had well crystallised fingerprint-like shells. The lattice fringe was measured as around 0.63nm which is slightly bigger than the lattice distance (0.618nm) of the (002) plane of 2H WS₂ [16] which were also found in Chapter 4. Such a slight expansion was commonly observed in WS₂ IF nanoparticles, and was attributed to the strain arising from the curvature of the layers, [16]. Figure 7.3b further shows a high magnification HRTEM image of the core part in a nanorattle. The lattice fringes with $d=0.224\text{nm}$ corresponding to the (111) planes of W were identified. No tungsten oxide coating was found on the encapsulated W nanoparticle. It is well known that the non-passivated metal nanoparticles, including tungsten nanoparticles, self-ignite immediately upon exposure to air [17]. However, this was not observed in the present case because W nanoparticles had been enclosed by the WS₂ shells, avoiding their direct contact with air. Therefore, the W cores should have a better stability than uncoated W nanoparticles.

2. Effect of H₂ flow rate on synthesis and phase morphology

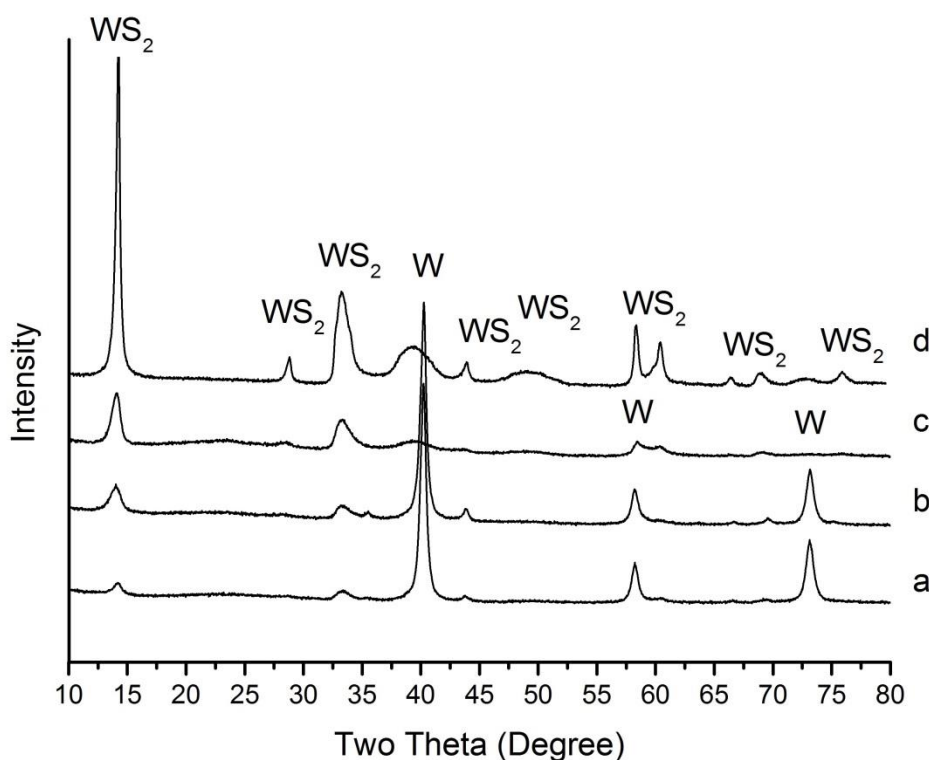


Figure 7.4 XRD patterns of samples resultant from 1h firing at 850°C under different H₂ flow rates: (a) 60ml/min, (b) 40ml/min, (c) 20ml/min and (d) 0ml/min.

It was well documented that WO₃ nanoparticles and nanofibres could react with S in H₂ to form WS₂ IF nanoparticles and nanotubes respectively *via* tailoring the synthesis parameters [18]. However, in this study, despite the use of the same raw materials and similar firing schedules, W@WS₂ nanorattles were formed instead, which is considered to be related to the flow rate of H₂. To verify this, Figure 7.4 shows XRD patterns of samples resultant from 1h firing at 850°C in H₂ flowing at 0 (i.e., Ar), 20, 40 and 60ml/min respectively. The effect of the H₂ flow rate on the product phases in the fired samples is evident. At a high flow rate (40 or 60ml/min), WS₂ and W were formed as the product phases (Figure 7.4a and b). On the other hand, at a low flow rate (0 or 20ml/min), WS₂ became the only product phase (Figure 7.4c and d). Clearly, use of a high flow rate of H₂ favoured the formation of W but inhibited the formation of WS₂. As mentioned above, with increasing the flow rate of H₂, the concentration of S in the local atmosphere surrounding WO₃ was reduced. So less WO₃ was converted in to WS₂ (Eq. (1)) whereas more was reduced to W (Eq. (5)).

Although the product phases in the reacted sample in the absence of H_2 were the same as in the sample in the presence of H_2 , peak intensities of the product phases in the former were much higher than in the latter, indicating the better crystallinity in the former (Figure 7.4c and d).

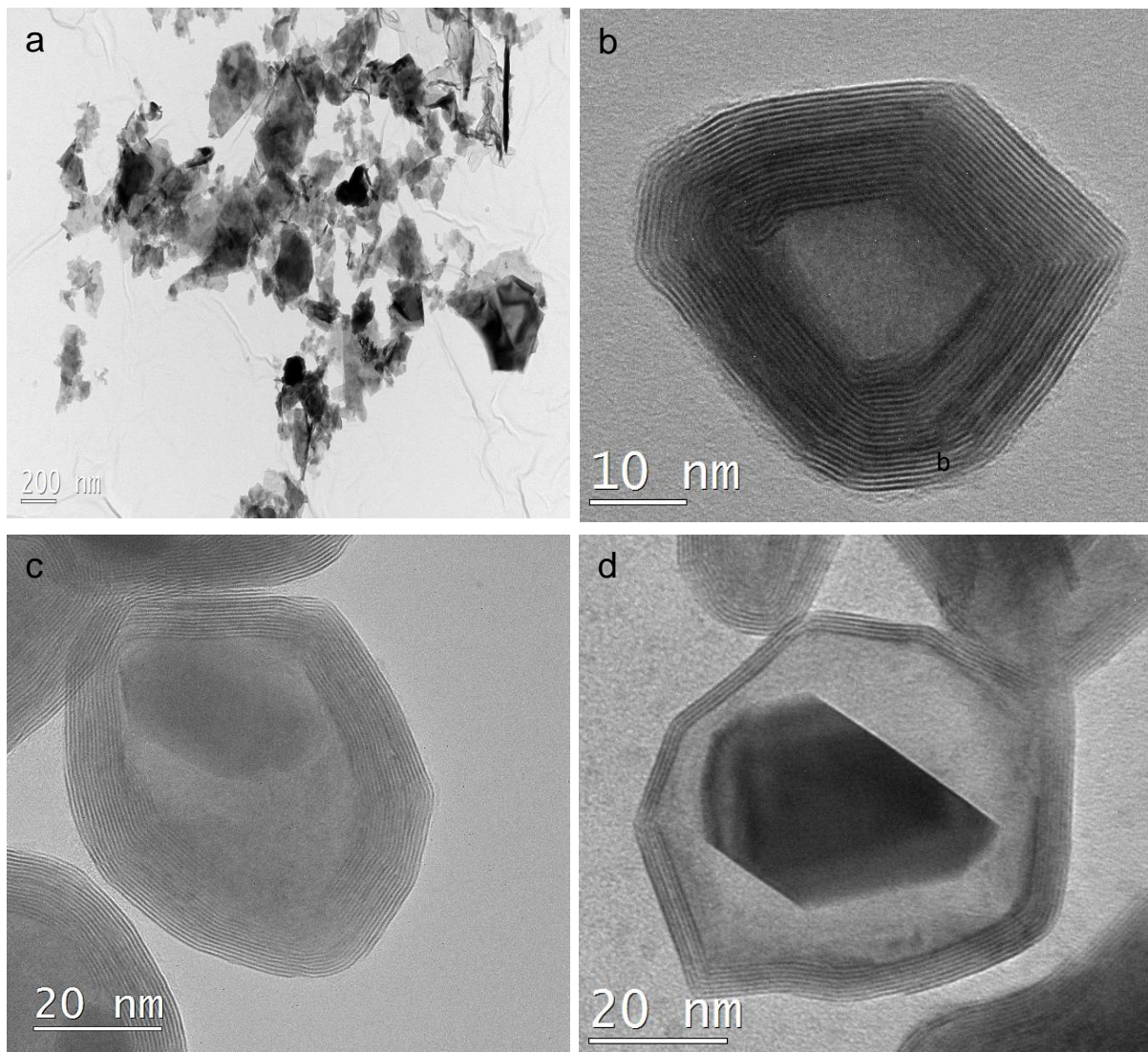


Figure 7.5 HRTEM images of sample synthesised at 850°C for 1h under different H_2 flow rates: (a) $0\text{ml}/\text{min}$, (b) $20\text{ml}/\text{min}$ (identical with the flow rate used for WS_2 IF nanoparticle production), (c) $40\text{ml}/\text{min}$ and (d) $60\text{ml}/\text{min}$. (e) high magnification HRTEM image of W core in a nanorattle.

Shown in Figure 7.5 are HRTEM images of W@WS_2 nanorattles synthesised at 850°C corresponding to different H_2 flow rates (the Ar flow rate was fixed at $80\text{ml}/\text{min}$). Typically, four different morphologies were obtained with different H_2 flow rates. When H_2 was not used, WS_2 nanoflakes (confirmed by XRD shown in Figure 7.4) with the average size of about 300nm were generated (Figure

7.5a). However, upon introducing H_2 at 20ml/min, the product morphology changed from nanoflakes to hollow IF nanoparticles of about 40nm in diameter and 10nm in shell thickness (Figure 7.5b). Therefore, it could be concluded that H_2 was indispensable in the formation of IF nanoparticles.

The role of H_2 in the formation WS_2 IF nanoparticles from WO_3 was investigated before [16]. When H_2 was absent, the inward diffusion of H_2S and outward diffusion of H_2O had to pass through the nanoparticle lattice planes along the radial direction, so the diffusion rates of both S and O atoms were very slow. Consequently, WO_3 nanoparticles tended to sinter with each other before sulphidation, resulting in the formation of large WS_2 flakes (Figure 7.5a). When H_2 was used, it initially reduced WO_3 to WO_{3-x} containing more vacancies. Then relevant species could diffuse through the vacancies much more rapidly, which facilitated the formation of WS_2 IF shells on the surface of WO_{3-x} nanoparticles. These initially formed WS_2 shells were vital for the formation of WS_2 IF nanoparticles as they prevented the sintering of tungsten oxides (Figure 7.5b). When a high H_2 flow rate was used (e.g.40ml/min or 60ml/min), $W@WS_2$ nanorattles, instead of WS_2 IF nanoparticles, were generated (Figure 7.5c and d). According to Figure 7.5c and d, nanorattles resultant from firing under 40ml/min and 60ml/min H_2 had similar overall size (about 60nm). However, in the case of the latter, thinner shells (~3nm) and larger core (~40nm) were obtained compared to in the case of the former (~10nm in thickness and 30nm in core size).

3. Formation mechanism of W@WS₂ nanorattles

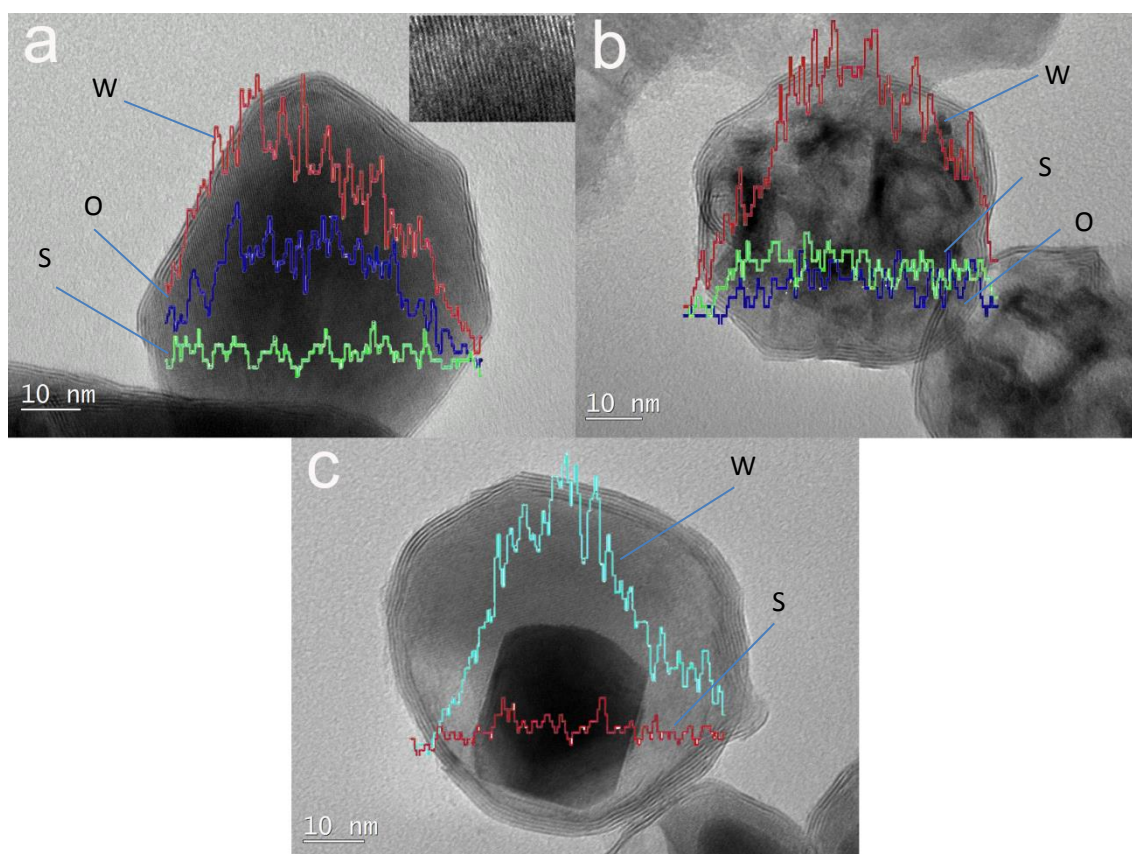


Figure 7.6 HRTEM images of WS₂-W nanorattles synthesised at 750°C for (a) 10min (c) 30min and (e) 1h and shown in (b), (d) and (f) are corresponding EDS line scan of nanorattles respectively.

To further assist understanding the formation mechanism of W@WS₂ nanorattles, WO₃ and S mixtures were heated at 750°C for 10min, 30min and 1h respectively under a given H₂/Ar flow rate (H₂=60ml/min, Ar=80ml/min). After 10min at 750°C, the formation of nanoparticles with a core-shell structure started to become evident (Figure 7.6a). Their shells were found to be about 3nm thick, which is much thinner compared to the “large” overall diameters (about 70nm), leaving a “large” solid core inside. The lattice distances of outer shell and inner core were 0.63nm and 0.38nm respectively. The former was close to that (0.618nm) between the (002) planes of WS₂ and the latter to that (0.378nm) between the (100) planes of W₁₈O₄₉, indicating that this nanoparticle was composed of a WS₂ shell and a W₁₈O₄₉ core. According to the EDS line scan, W, S and O elements were detected on the whole particle. The peak height of S changed very little along the scanning line, indicating that it was purely from the WS₂ shell. In other words, the solid core did not contain S. On

the other hand, O was only detected at the area corresponding to the solid core, and W peaks became strong at the same area, indicating that the solid core was composed of W and O. The above results additionally confirmed the coexistence of WS_2 and $W_{18}O_{49}$. On increasing the holding time to 30min, WS_2 shells remained unchanged while bright contrast inner cores were seen. EDS revealed that oxygen content corresponding to the inner core decreased evidently (Figure. 7.6b). The contrast change and the reduction in O indicated that the $W_{18}O_{49}$ core formed initially was further reduced to an intermediate W suboxide core or a mixed $W_{18}O_{49}$ -W core. On further increasing holding time to 1h, $W@WS_2$ nanorattles with diameter of about 60nm and shell thickness of 3nm were formed (Figure 7.6c). The corresponding EDS line scan showed that this nanoparticle had a W-rich area and homogeneous S distribution. This, along with the XRD shown in Figure 7.1c, verified that a W core was enclosed in a WS_2 shell, forming a typical structure of $W@WS_2$ nanorattle.

Based on the results show in Figure 7.6 and the discussion above, and the growth mechanism of WS_2 IF nanoparticles from WO_3 nanoparticles[16, 19], the growth mechanism of $W@WS_2$ nanorattles could be proposed as follows. At $>650^\circ C$, WO_3 nanoparticles were initially reduced by H_2 to WO_{3-x} containing many O vacancies (Eq. (2)) before the sulphidation by S (Eq. (1)). The O vacancies in WO_{3-x} facilitated the diffusion of S during the further reaction[16]. The synergy (competition) between the H_2 reduction and S sulphidation processes determined the morphologies of the final products. When the concentrations of S and H_2 were appropriate, a continuous WS_2 shell would be firstly formed on the surface of WO_{3-x} (Eq.(1)), preventing effectively the merging/sintering between WO_{3-x} nanoparticles, which otherwise would lead to the formation of relatively large tungsten oxide precursors. As reported before, if the sintered WO_{3-x} precursors were larger than 200nm, WS_2 IF nanoparticles, even if formed, would not be stable and thus tend to convert quickly into 2H flakes[20]. Therefore, the initially formed WS_2 shell played vital role in restricting the precursor's size to below the critical value. When the H_2 flow rate was appropriately low, the relative concentration of S in the atmosphere surrounding WO_{3-x} was high, so there would be sufficient amounts of S which diffused to the interface of WS_2 and WO_{3-x} and reacted with the latter to form WS_2 IF nanoparticles (Eq (1)). On the other hand, if H_2 flow rate was high, the

concentration of S would be low. In this case, it would become much more difficult for the sulphidation reaction (Eq. (7.1)) to complete. Consequently, intermediate WS_2 - WO_{3-x} core-shell nanoparticles would be formed. Because WS_2 is stable under H_2 atmosphere at $750^\circ C$, H_2 diffused through the initially formed WS_2 shell to reduce the WO_{3-x} core to W. Since W has a higher density ($19.25g/cm^3$) than WO_3 ($7.16g/cm^3$), the volume shrinkage occurred with the reduction process, as a result, $W@WS_2$ nanorattles would be formed. Depending on the flow rates of H_2 , the thicknesses of WS_2 shells and corresponding sizes of cores varied. A high H_2 flow rate resulted in a thin shell and a large cores, and vice-versa (Figure 7.5b-d). This was because with increasing the flow rate of H_2 , the concentration of S in the local atmosphere surrounding the precursor particles decreased. Consequently, less WO_3 was converted to WS_2 , leaving WS_2 - WO_3 nanoparticles with thinner shells. Upon the depletion of S, the thicknesses of WS_2 shells were fixed and would not change in the following H_2 reduction process. Finally, $W@WS_2$ nanorattles with thin shells were formed.

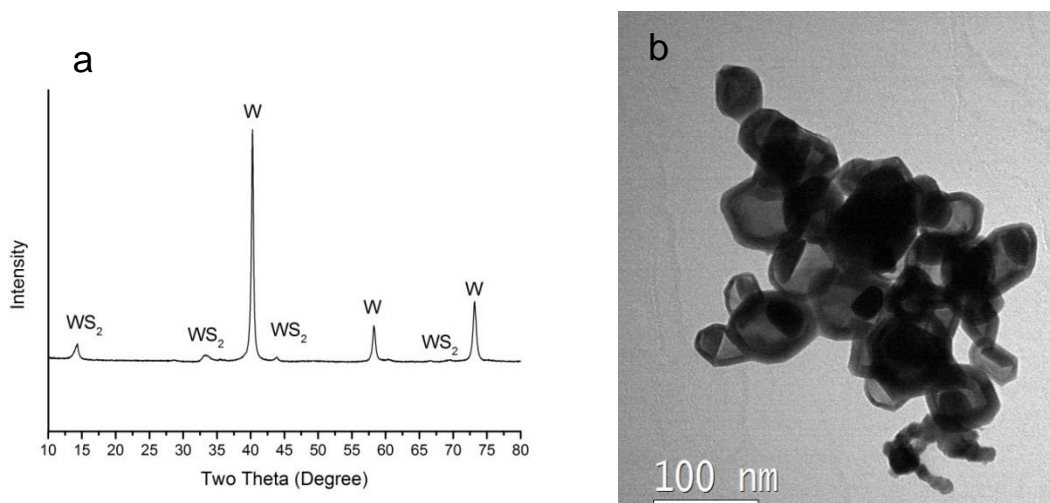
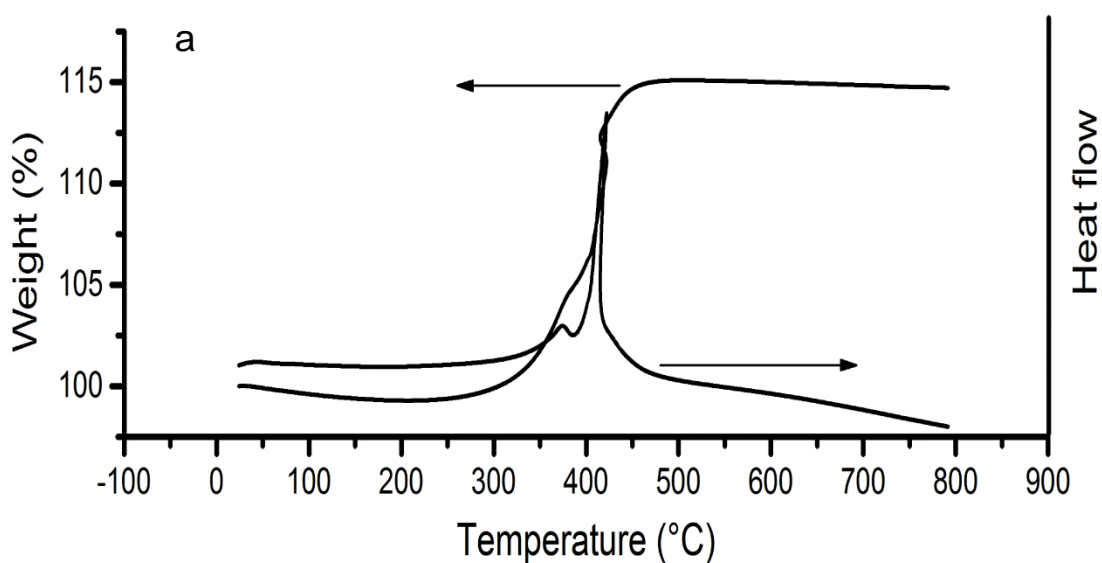


Figure 7.7 (a)XRD and (b)TEM images of sample resultant from 1h firing of as-synthesised nanorattles at $1000^\circ C$ under Ar atmosphere.

4. Thermal stability of as-prepared $W@WS_2$ nanorattles

It is expected that as-prepared $W@WS_2$ nanorattles fabricated at $850^\circ C$ for 1h under different H_2 flow rate at 40ml/L would have very high thermal stability in

an inert atmosphere, considering that WS_2 IF nanoparticles have a high decomposition temperature around $1300^\circ C$ [21]. XRD results shown in Figure 7.7a indicated that after 1h annealing at $1000^\circ C$, no phase change occurred in the sample which was still composed of W and WS_2 . The corresponding TEM image (Figure 7.7b) further revealed that $W@WS_2$ nanorattles survived after the heat treatment. Compared with untreated sample no obvious changes found. W nanoparticles were still enclosed in the WS_2 shells and isolated from each other. These results indicated that as-synthesised $W@WS_2$ nanorattles had good compositional and structural stabilities at appropriately high temperatures.



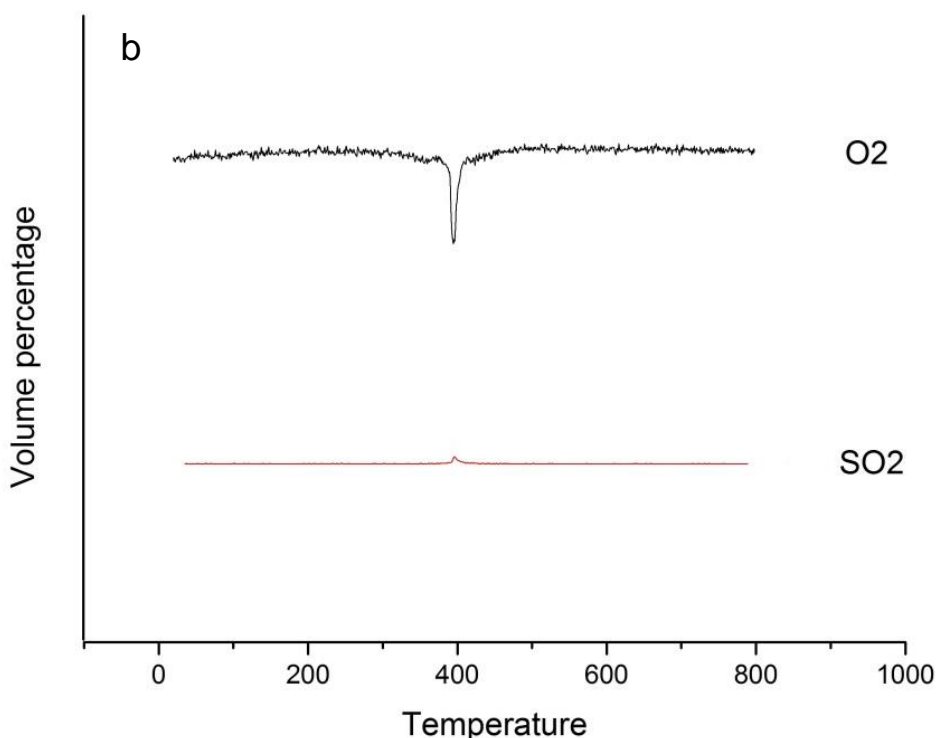


Figure 7.8 (a) TGA, DTA and (b) MS spectrum of synthesised W@WS₂ nanorattles, examined under air atmosphere with heating rate of 10°C/min.

To further investigate the thermal stability of W@WS₂ nanorattles in an oxidising atmosphere, thermal gravity analysis(TGA), differential thermal analysis (DTA) and mass spectrum (MS) tests were performed in air and the results are shown in Figure 7.8. According to Figure 7.8, the mass of sample did not change at below about 290°C, indicating that no reaction occurred below this temperature. When temperature was increased to above 290°C, the mass of the sample was gradually increased to around 3.7% with increasing the temperature to about 380°C. On the corresponding DTA curve, there is a small exothermic peak in the temperature range of 290°C-380°C, peaked at about 360°C. In addition, the mass spectrum also shows a very small absorption peak of O₂ centred at around 360°C while no change in the amount of SO₂ was observed. As the oxidation of naked W nanoparticles starts at 280°C [17], based on above analysis, it can be considered that the mass increase and exothermic reaction should be attributable to the oxidation of small amounts of naked W nanoparticles coexisting with the nanorattles which calculated to be around 13% in weight. The reason for the remaining small amounts of W was

not clear, although it could be because of that some finest WO_3 nanoparticles reacted rapidly with H_2 to form W in a short time, which remained in the final products due to the slow reaction between W and S.. The mass gain lasted with increasing temperature, but reached a plateau when the temperature was increased to around 450°C . The total mass gain after the TG test was 15%, which was a balance between the 26% mass gain from the W oxidation (weight increase) and the 8.5% mass loss from the WS_2 oxidation.

In addition, another strong and sharp exothermal peak was found in the temperature range of 380°C - 450°C , centred at about 410°C . Compared with the oxidation of passivated W nanoparticles [17], the exothermal peak is much sharper, indicating that a violent reaction occurred. The corresponding mass spectrum shows that two gases were associated with the reaction: O_2 and SO_2 (Figure 7.8b). Furthermore, their different peak intensities indicated that the O_2 consumption was much more than the SO_2 release. These results confirmed the almost simultaneous oxidation of WS_2 and W in the temperature range of 380°C - 450°C . Since the oxidation temperature of WS_2 IF nanoparticles is around 360°C [21], the WS_2 shell was firstly oxidised and collapsed when temperature was above this value. Then, the enclosed W would start to be oxidised. Because the W cores were not covered by tungsten oxides, they were ignited in air, generating a large amount of heat. The above results indicated that the oxidation temperature of W nanoparticles in as-prepared nanorattles was increased to 290°C to 380°C in air, indicating their enhanced thermal stability compared with W nanoparticles in an oxidising atmosphere.

7.5 Catalytic activity of as-prepared nanorattles

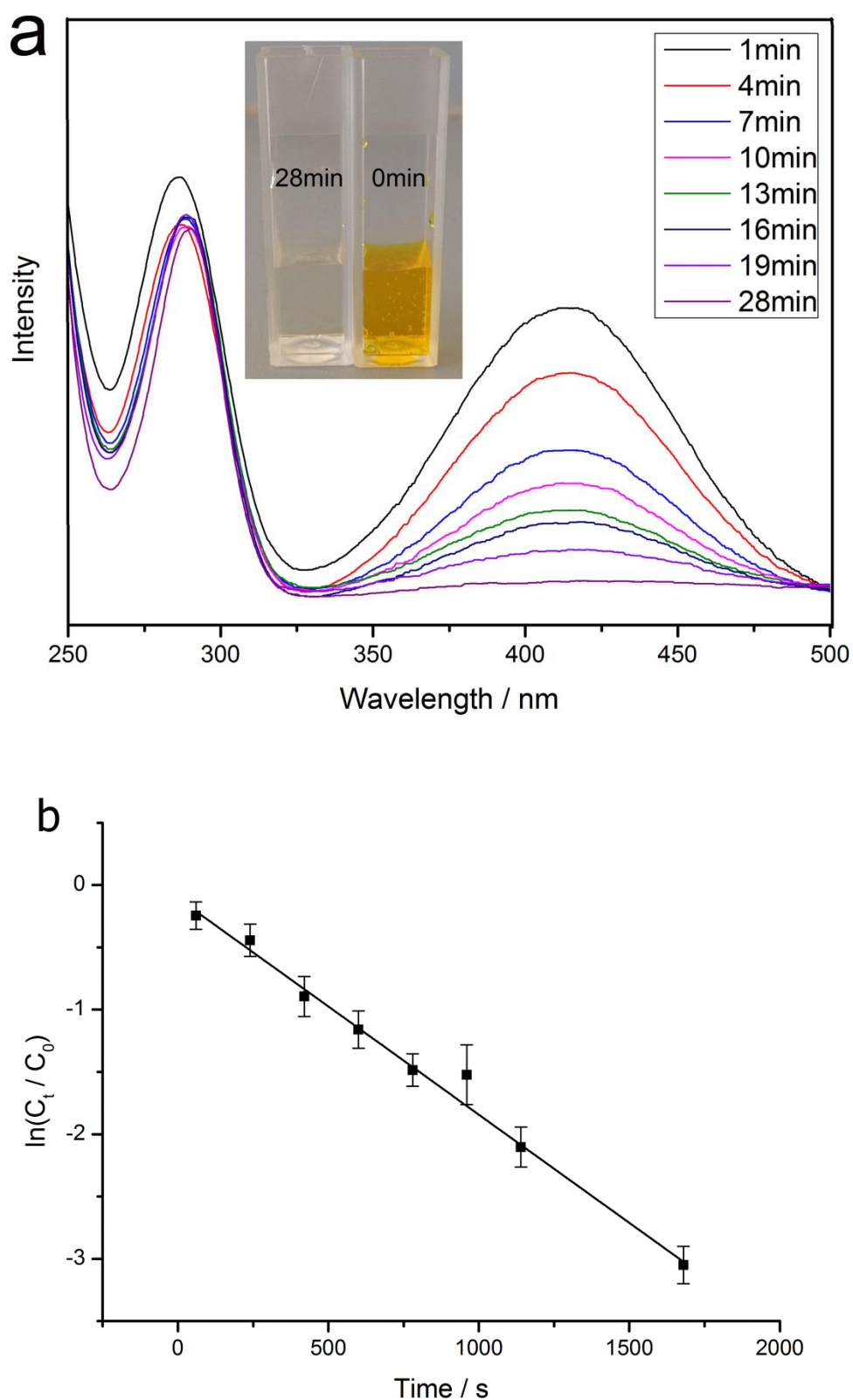
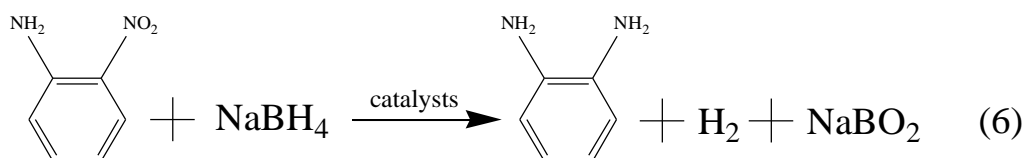


Figure 7.9 (a) Time-dependent UV-vis spectral changes of the reaction mixture (2-NA and NaBH_4 solution) catalysed by W@WS_2 nanorattles. The Insert

picture shows together the solutions before and after 28min reaction. (b) Plot of $\ln(C_t/C_0)$ versus time.



The as-prepared nanorattles were used as a catalyst to catalyse several important reactions including 2-NA conversion and H₂ production from NaBH₄. Here, as an example, the catalytic performance of as-prepared nanorattles in the case of 2-NA to OPD conversion will be presented. To convert the toxic 2-NA to OPD *via* hydrogenation, NaBH₄ water solution was used as H₂ source (Eq. (6)). 2-NA almost did not react with NaBH₄ if no catalyst was used, even after a long time period, e.g., two days [22]. Therefore, an appropriate type and amount of catalyst needs to be used to accelerate the reaction. In this work, as-prepared nanorattles were tentatively used as the catalyst to accelerate this reaction.

Shown in Figure 7.9 is the UV-vis spectrum evolution of 2-NA and NaBH₄ reaction mixture with reaction time when as-prepared nanorattles were used as the catalyst. 2-NA solution had two UV absorption peaks centred at around 280nm and 410nm respectively [23]. Upon addition of W@WS₂ nanorattles, the peak height at 410nm reduced evidently with the time. In addition, the peak centred at 280nm was also found to be shifted to 290nm gradually. After 30min reaction, only the 290nm peak which was the characteristic peak of OPD [24] could be found in the UV-vis spectrum, indicating that 2-NA was completely converted to OPD. The ratio of 2-NA concentrations at times t (C_t) and 0 (C_0), was measured from the relative intensity ratio of the respective absorbance, A_t/A_0 , at 410 nm. A linear relationship between $\ln(C_t/C_0)$ and time was obtained (Figure 7.9b), indicating a first-order reaction. Standard deviation from the mean was determined to estimate the error in $\ln(C_t/C_0)$. From the slope of the straight line in Figure 7.10b, the reaction rate constant when using W@WS₂ nanorattle as an catalyst was determined as $1.74 \times 10^{-3} \text{ s}^{-1}$.

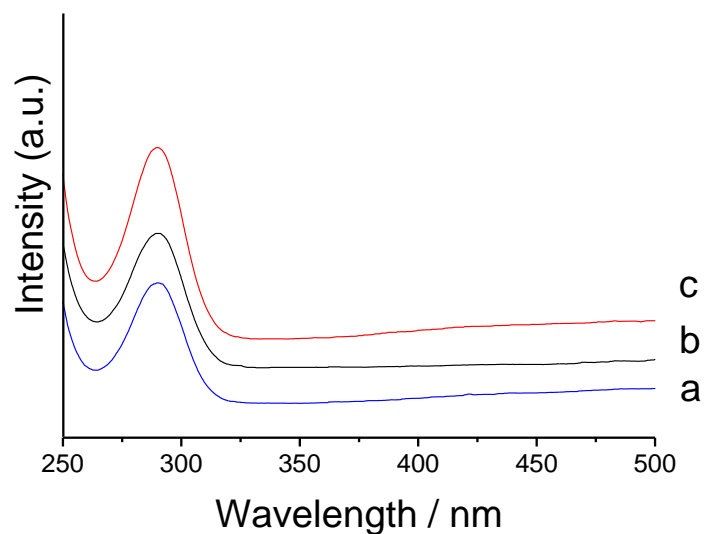


Figure 7.10 UV-vis absorption spectrum of the reaction solutions catalysed by W@WS₂ nanorattles, after (a) 1 cycle, (b) 2 cycles and (c) 3 cycles. Plots were offset for better observation.

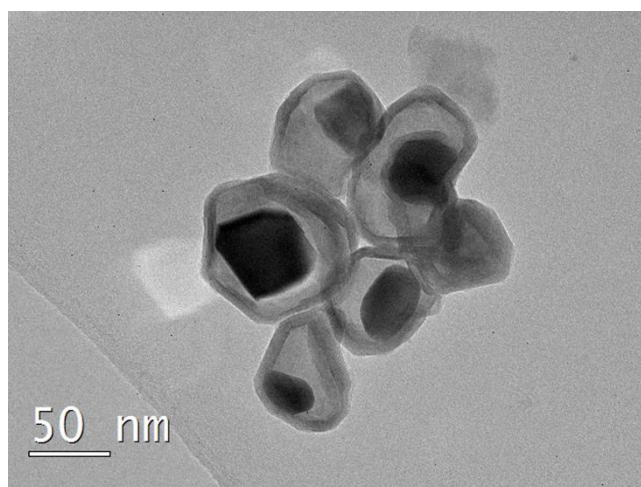


Figure 7.11 TEM image of sample after 3 cycles catalytic reaction.

The nanorattles could be recycled by simple centrifugation. To test their stability as a catalyst, they were repeatedly used to catalyse the reaction for 3 cycles. The UV-vis spectrum from each cycle is shown in Figure 7.10. Only the characteristic peak of OPD at 290nm appeared in each cycle, indicating that 2-NA had been completely converted into OPD, which further indicated that even after 3 cycles the nanorattles still exhibited catalytic activity. Nevertheless, the time to the complete reaction was increased with the cycle, 37, 52 and 70min for cycles 1, 2 and 3 respectively, indicating the gradually decreased catalytic

activity with the cycle. Interestingly, after 3 cycles, the nanorattles still retained their morphologies (Figure 7.11). These results suggested that as-synthesised nanorattles not only had excellent structural stability but also good catalytic stability.

The catalytic performance of as-prepared nanorattles was close or slightly better than that of the popular Au@SiO₂ nanorattle catalysts (the rate constant was $1.69 \times 10^{-3} \text{ s}^{-1}$ [25]) for the conversion reaction, but much better than immobilized Au nanoparticles (the rate constant was $1.27 \times 10^{-3} \text{ s}^{-1}$). [14] These, along with the much lower cost of as-prepared nanorattles, suggested that they could be potentially used to replace the expensive gold-based catalysts currently used. Furthermore, it is believed that they also could be potentially used to catalyse other important reactions, e.g. H₂ generation reactions (the work is ongoing and will be reported in another future publication). Nevertheless, future work is still needed to clarify the catalytic mechanism and further optimise the sizes of the catalysts to further improve their catalytic performance.

7.1.4 Conclusions

W@WS₂ nanorattles were prepared *via* a novel one-step sulphidation process, i.e., by heating WO₃ nanopowder and S at a temperature between 750-950°C in a H₂/Ar atmosphere. By varying the H₂ flow rate, WS₂ nanoflakes, IF nanoparticles and W@WS₂ nanorattles with different shell thicknesses could be readily produced. Based on the results, the reaction mechanism was proposed. When H₂ was used, WO_{3-x}-WS₂ core-shell nanoparticles were initially formed. After the depletion of S, the WO_{3-x} core could not be converted into WS₂ but reduced by H₂ to W gradually, leading to the formation of W@WS₂ nanorattles. The catalytic activity of as-prepared W@WS₂ nanorattles were tested using the conversion reaction from 2-NA to OPD as a working tool. They showed better catalytic performance than Au-based nano catalysts currently used or proposed. It is believed that the synthesis strategy used in this work could be readily extended to fabricate other transitional metal nanorattles such as Mo@MoS₂ and Ti@TiS₂. Furthermore, the as-prepared nanorattles could be similarly used

to catalyse other important reactions.

7.2 Synthesis of WS₂@WS₂ nanorattles and their catalytic activity in the hydrogen evolution reaction

7.2.1 Introduction

Because of their rapid depletion and growing environmental concerns, fossil fuels will be replaced by renewable resources in the future. Compared with traditional fossil fuels, hydrogen is frequently advocated as the alternative “clean and renewable” energy carrier because of its high energy density and environmentally friendly combustion product [26, 27]. Among various techniques of hydrogen production, steam reforming is the most commonly used by industry. In this technique, hydrogen and carbon dioxide are readily generated by the reaction of methane with water. However, this technique suffers from several drawbacks, including the involvement of non-renewable methane and the generation of carbon dioxide as a by-product. An appealing approach to overcome the drawbacks of this technique and other conventional techniques is through the splitting of water by either light or electricity [27, 28]. When sufficient energy is supplied, water can be readily decomposed into H₂ and O₂. Because water is abundant on earth and oxygen is a safe side product, this technique can be used to produce H₂ on a large scale. However, in this technique, the existence of a high overpotential of the hydrogen evolution reaction (HER, $2\text{H}^+ + 2\text{e}^- = \text{H}_2$) largely limits its efficiency because most of the electric energy is wasted without being used for generating H₂. To solve this problem, it is necessary to find suitable electrocatalysts that can decrease the overpotential of the HER. Platinum metal has already been demonstrated to be an excellent catalyst in HER, resulting in nearly a zero overpotential [29]. However, its low abundance and extremely high price greatly limit its application in this aspect.

Recently, transition metal sulphides MS₂ (M = Mo and W) have attracted tremendous attention because of their outstanding electrocatalytic properties for the HER [30-36]. It has been proposed and experimentally verified that their

electrocatalytically active sites are on their metallic edges [30, 37]. To improve the electrocatalytic performance of MS_2 , it is necessary to increase the concentration of their metallic edges. Several technical routes have been proposed, including decreasing the sizes of the particles, improving their dispersion and introducing large amounts of sulphur defects [35, 38-45]. Moreover, considering that metal sulphides exhibit relatively poor electrical conductivity, which hinders the H_2 evolution, several alternative techniques have been developed, by which conductive materials were added to improve the electrical conductivity [33, 46, 47]. For example, because of its high conductivity and large thin layer structure, reduced graphene oxide (rGO) was used as one of the most effective additives to increase the conductivity of MS_2 . After the in-situ synthesis of MS_2 -rGO composites, MS_2 nanoflakes were dispersed homogeneously on large basal planes of rGO. These nanoflakes were connected by more conductive rGO, resulting in a dramatic increase in the overall conductivity [33, 46].

Some transition metal sulphides are known to have a graphite-like layered structure, in which adjacent layers are weakly bonded by van der Waals forces. Similarly to graphite, which can be exfoliated to monolayer graphene, monolayer MS_2 also can be produced and used as an excellent electrocatalyst for the HER [36, 48-50]. This behaviour is attributed to the dramatic increase in the electrical conductivity associated with the conversion from 2H MS_2 (semiconductor) to 1T MS_2 (conductor). Further investigation on these monolayer compounds has revealed that the active sites not only concentrate on the edges of layers but also on the basal planes, leading to the great improvement [36].

In terms of the literature review performed by the author, WS_2 monolayers fabricated by Cheng et al. exhibited the best electrocatalytic performance among all the WS_2 -based catalysts (the overpotential was approximately 100 mV and the Tafel slope was 48 mV/dec) [48]. Initially, WCl_6 and S were dissolved in the mixture of oleylamine and 1-octadecene. Then, this solution was heated to 360°C under a N_2 atmosphere. After the reaction, the as-synthesised product was washed and finally annealed in Ar at 500°C to remove any organic residues, leading to the formation of agglomerated WS_2 monolayers. Nevertheless, this technique suffered from several drawbacks,

including complicated operation and a low yield and thus was not applicable to a large-scale production.

In this chapter, novel WS₂@WS₂ nanorattles were fabricated by simply heating nanorattle precursors and S at a low temperature. Because of the nanorattle structure, enclosed thin WS₂ nanoflakes can completely expose their edges in solution without agglomerating with each other. Therefore, this material exhibited similar catalytic performance as that reported for WS₂ monolayers. This finding, along with the simple operation process and possible large batch sizes, makes this technique suitable for future large-scale production.

7.2.2 Experimental

0.1g W@WS₂ nanorattles prepared using the technique described in Chapter eight (synthesised after 1-h heat treatment at 850°C in Ar) were used as the key precursor. These nanorattles were ultrasonically dispersed in 100ml ethanol for 1 h before 2-h oven-drying at 80°C. The dry nanorattles were mixed with excessive S powder (the molar ratio of nanorattle to S was 1:20) and were then heated at 350°C in an Ar atmosphere for 1 h to completely sulphurise the W cores. UV spectra were obtained by a Jenway 6715 UV/visible spectrophotometer.

Electrochemical measurements were performed with a 3-electrode cell using a CHI 602D potentiostat from CHI instruments, Inc. In this process, 40 mg of the catalyst, 20 mg conductive carbon black and 0.8 ml of 5 wt% Nafion solution were dispersed in 10 ml of 4:1 v/v water/ethanol by 1-h sonication to form a homogeneous ink. Then, 5 µl of the catalyst ink (containing 19 µg of the catalyst) was loaded onto a gold electrode with a 2-mm diameter (loading ~ 0.6 mg/cm²). Linear sweep voltammetry (using the potentiostat from CH Instruments) with a scan rate of 2 mVs⁻¹ was conducted in 0.5 M H₂SO₄ using a Ag/AgCl electrode (in 1 mol/L KCl) as the reference electrode and a Pt wire as the counter electrode. In 0.5 M H₂SO₄, the potential of the reversible hydrogen electrode (RHE) is equal to the potential of the Ag/AgCl electrode plus 0.22 V: $E(\text{RHE}) = E(\text{Ag/AgCl}) + 0.22 \text{ V}$.

7.2.3 Results and discussion

1. Composition and morphology analysis of $WS_2@WS_2$ nanorattles

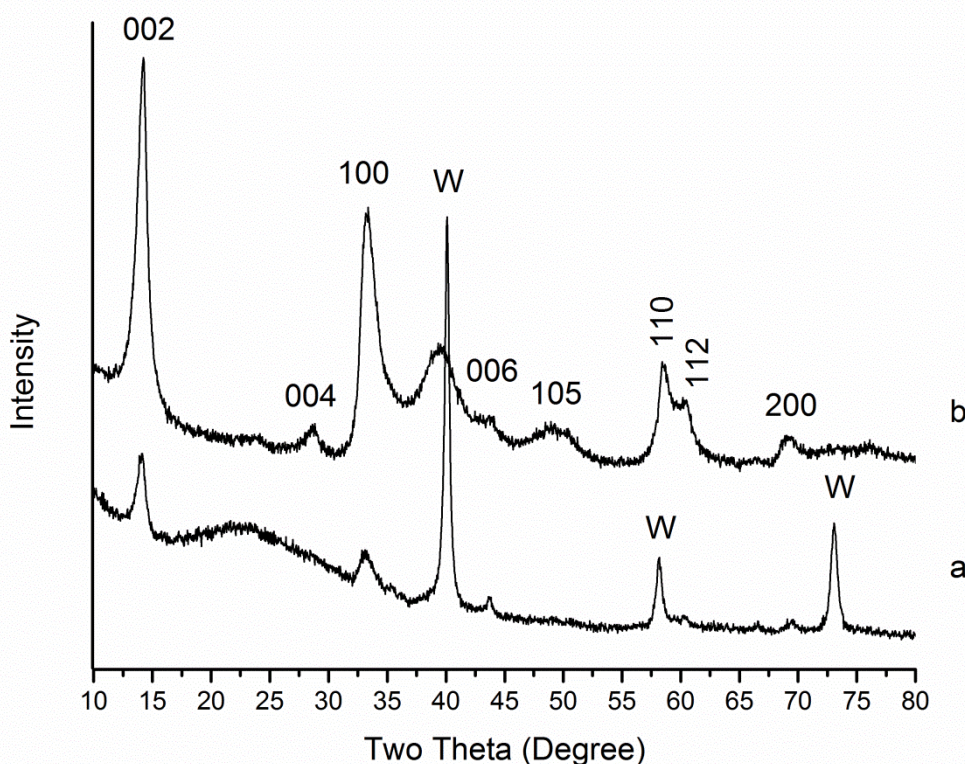


Figure 7.12 XRD patterns of (a) $W@WS_2$ nanorattles and (b) product after 1-h sulphidation of $W@WS_2$ nanorattles at 350°C. All indexed planes belong to WS_2

As discussed before (Chapter eight), as-synthesised $W@WS_2$ nanorattles were composed of WS_2 inorganic fullerene-like (IF) hollow nanospheres and an encapsulated mobile W core. The typical XRD pattern of $W@WS_2$ nanorattles given in Figure 7.12a shows the characteristic peaks of WS_2 and W. The low-angle shift ($\sim 0.2^\circ$) of the (002) peak of WS_2 was attributed to the formation of the WS_2 IF structure. After 1-h sulphidation at 350°C, W was completely converted into WS_2 with no discernible impurities (Figure 7.12b). The broadening of the characteristic peaks indicated that the product still maintained nanoscale dimensions. Moreover, compared with the precursor, the (002) peak of WS_2 shifted to higher 2θ angle ($\sim 0.1^\circ$), suggesting that the generated WS_2 did not have an IF structure. The (100) peak exhibited an apparent asymmetry,

which usually occurred in the XRD pattern of synthetic carbons due to the presence of turbostratic stacking of the layers [51]. Therefore, the generated WS_2 might also exhibit a similar structure with random orientated layers.

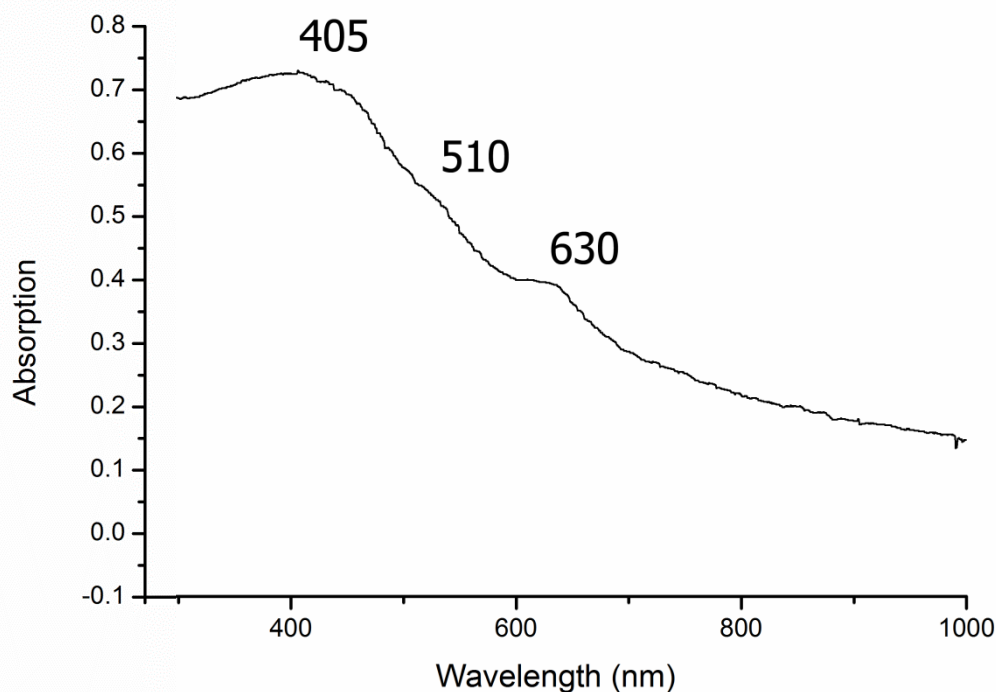


Figure 7.13 UV-vis spectrum of a sample fired at 350°C for 1 h under an Ar atmosphere.

The optical absorption spectrum was measured for the sample composed of pure WS_2 phase obtained after 1-h heat treatment at 350°C. According to Figure 7.13, the absorption of the UV beam gradually increased with decreasing wavelength. Such a shoulder-form spectrum is usually due to tiny particle sizes. According to Tenne et al. [52], a bulk WS_2 material has two characteristic peaks assigned, respectively to A and B excitons at 636 and 525 nm. These two excitons were also observed on Figure 7.13, i.e., a weak absorption edge at 510 nm and an obvious absorption peak at 630 nm, indicating that the sample was composed of the WS_2 phase, which was consistent with the XRD identification. The blue-shift of the two peaks suggested that this sample contained WS_2 IF nanoparticles with thin layers [52]. In addition to these two

peaks, a much stronger broad peak centred at 405 nm was observed from the UV spectrum. As the energy shift associated with the lateral size reduction in layered metal dichalcogenides is significant [53]., the obvious blue-shift arising from the strong quantum confinement effect suggested that the sizes of the product were very small.

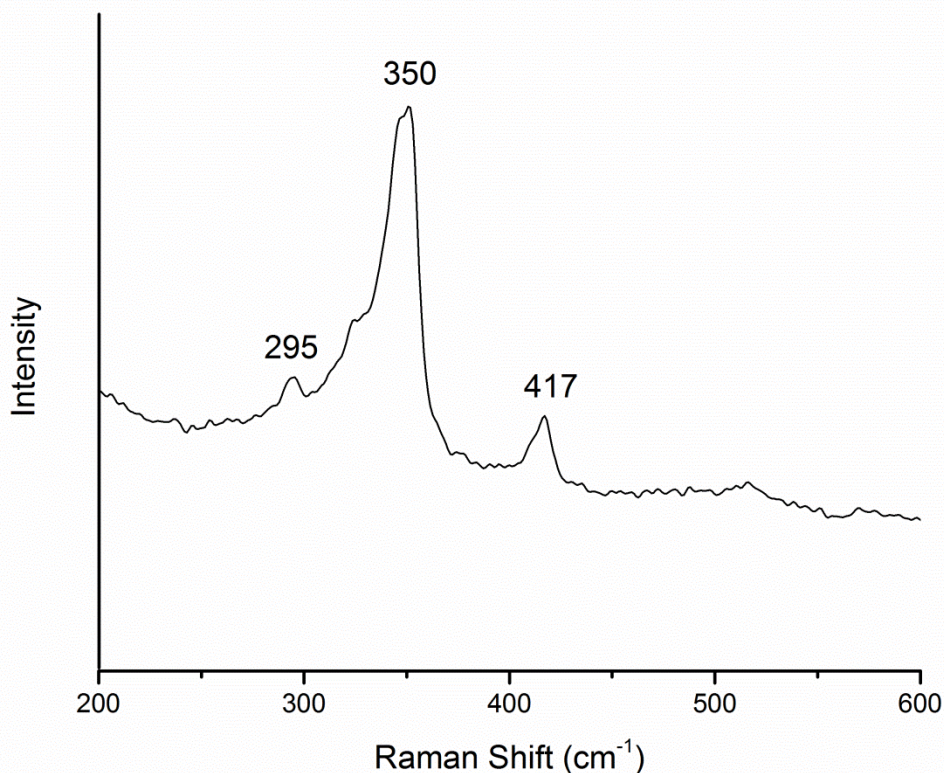


Figure 7.14. Room-temperature Raman spectrum of the sample fired at 350°C for 1 h under an Ar atmosphere.

Figure 7.14 presents the Raman spectrum of the product after 1-h sulphidation at 350°C. Apart from some weaker peaks, three pronounced peaks centred at 295 ($2LA-2E_{2g}$) cm^{-1} , 350 (overlapped peak of 2LA mode and E_{2g} mode) cm^{-1} and 417 (A_{1g}) cm^{-1} were clearly observed. The peaks matched with the characteristic peaks of WS_2 [54]. Moreover, the A_{1g} mode redshifted by 5 cm^{-1} compared with the WS_2 bulk material, arising from the increased restoring force caused by the van der Waals interactions established among layers [54]. Because the redshift is always observed for ultrathin WS_2 flakes, it could be expected that this sample might be composed of ultrathin WS_2 flakes.

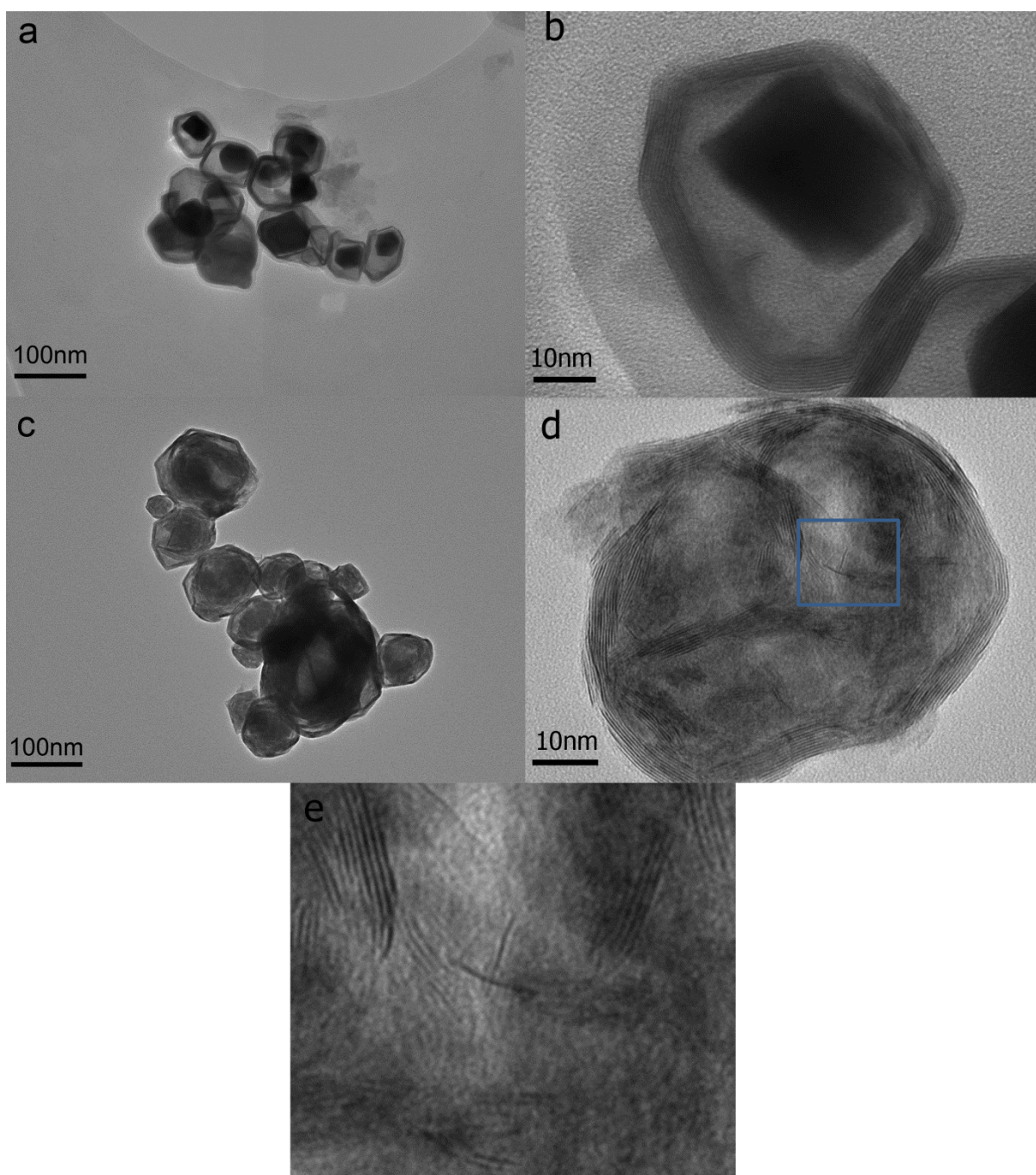


Figure 7.15. TEM images of (a, b) $W@WS_2$ nanorattles and (c, d) product after 1-h sulphidation of $W@WS_2$ nanorattles at $350^\circ C$. (e) High-magnification image of select area of (d).

Figure 7.15 presents TEM images of the samples whose XRD patterns are shown in Figure 7.12. As observed in Figure 7.15a, the original $W@WS_2$ nanorattles had a small size distribution from 30 nm to 90 nm (Figure 7.15a). The thicknesses of the outer shells (5-10 nm) were much smaller compared with the overall sizes, leaving “large” inner voids (Figure 7.15b). W cores were also observed in almost every nanoparticle. The average size of the W cores

was estimated to be approximately 30 nm, which was smaller than the void sizes (50-100 nm) of the hollow nanospheres. After sulphidation, the product nanoparticles retained the shell shapes and sizes of the nanorattle precursors (Figure 7.15c). The high-resolution image shows a continuous, layered shell with a lattice distance of approximately 0.63 nm, indicating that the original WS₂ IF shell was not damaged during sulphidation (Figure 7.15d). However, solid W cores were replaced by many loosely assembled WS₂ nanoflakes (Figure 7.15e). Because of the limitation of outer WS₂ shells, the lateral dimension of each WS₂ nanoflake was not larger than the sizes of the WS₂ IF shells. In addition, the thicknesses of each nanoflake were no larger than 5 nm because of the low reaction temperature. Because the HER catalytic performance of WS₂ is related to its edge concentration [30, 37], these loosely assembled WS₂ nanoflakes are expected to exhibit good catalytic performance.

2. Properties of WS₂@WS₂ nanorattles

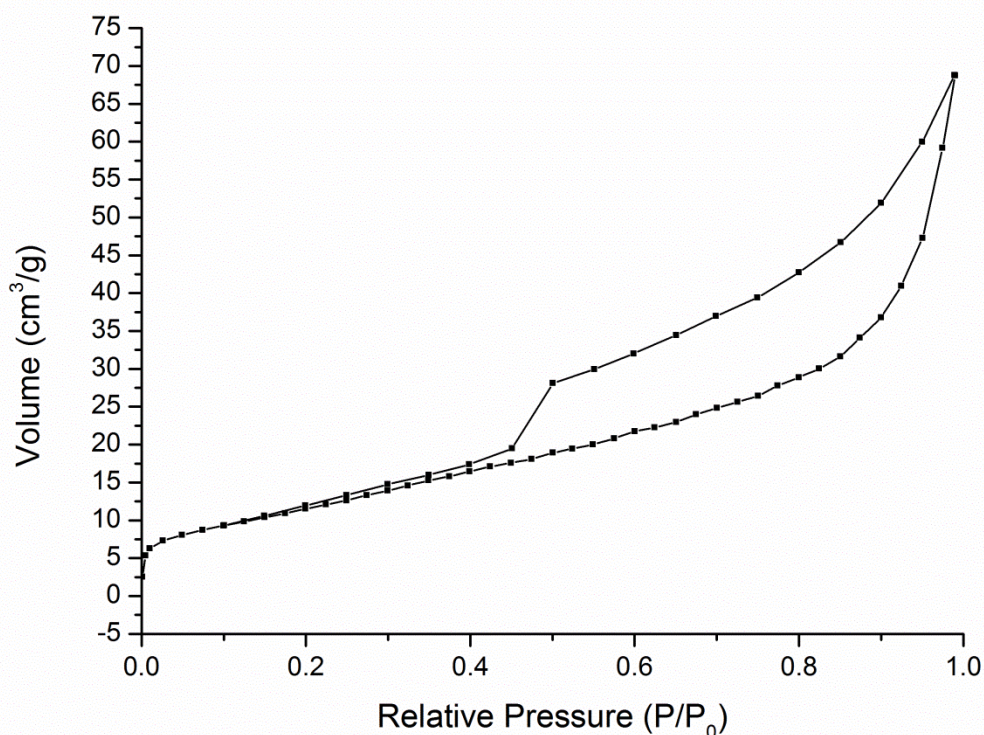
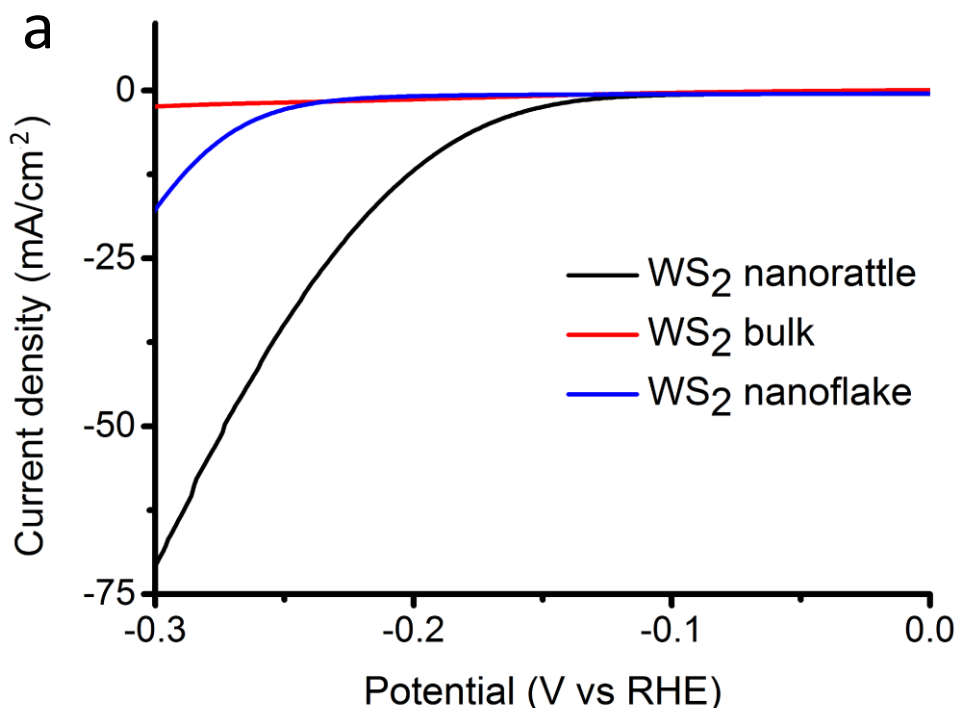


Figure 7.16. Nitrogen adsorption–desorption isotherms of as-synthesised WS₂@WS₂ nanorattles

The N_2 adsorption-desorption isotherms measured for the as-prepared $WS_2@WS_2$ (Figure 7.16) can be classified as type-IV with the jump beginning at a relative pressure in the range $P/P_0 = 0.4-0.5$, indicating that the uniform mesoporosity was produced by the ion exchange process [55]. Barrett–Joyner–Halenda (BJH) analyses based on this result revealed that the average specific surface area (SSA) and the average pore size of the nanorattles were $\sim 48 \text{ m}^2/\text{g}$ and 4.2 nm, respectively. Compared with the $W@WS_2$ nanorattle precursor (SSA is approximately $20 \text{ m}^2/\text{g}$), the sulphidation process resulted in a great increase of the SSA. This result is due to the conversion from a single solid W core (low SSA) to several WS_2 tiny nanoflakes (high SSA). In addition, the mesoporous structure made these nanorattles permeable to many molecules such as 4-NP, 4-NA and methyl blue. Therefore, reactant species could easily diffuse through the WS_2 shell and react each other on the surfaces of the WS_2 nanoflakes enclosed.



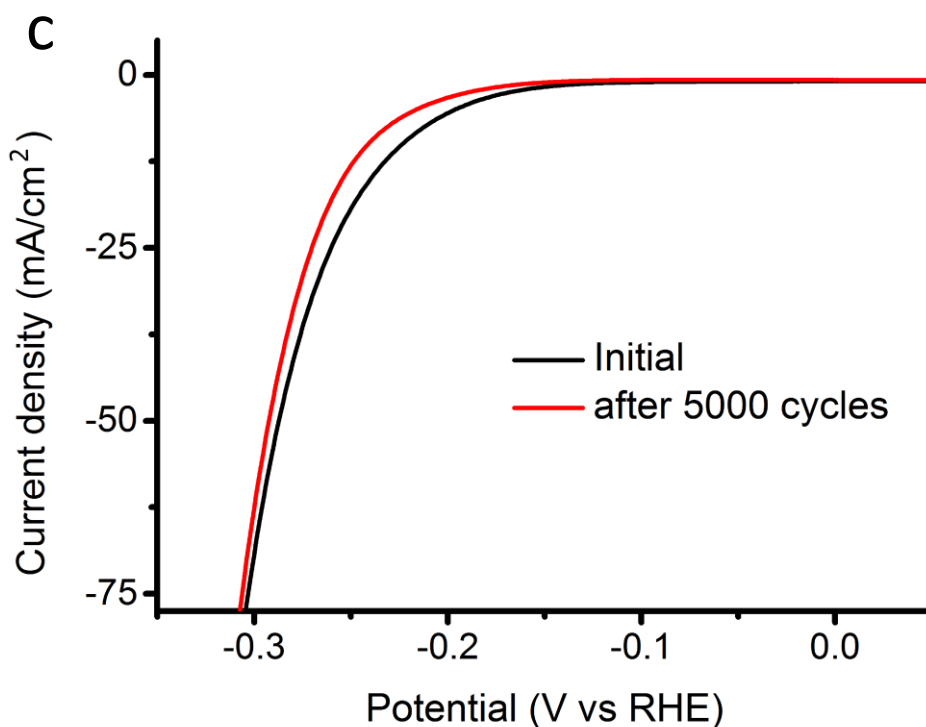
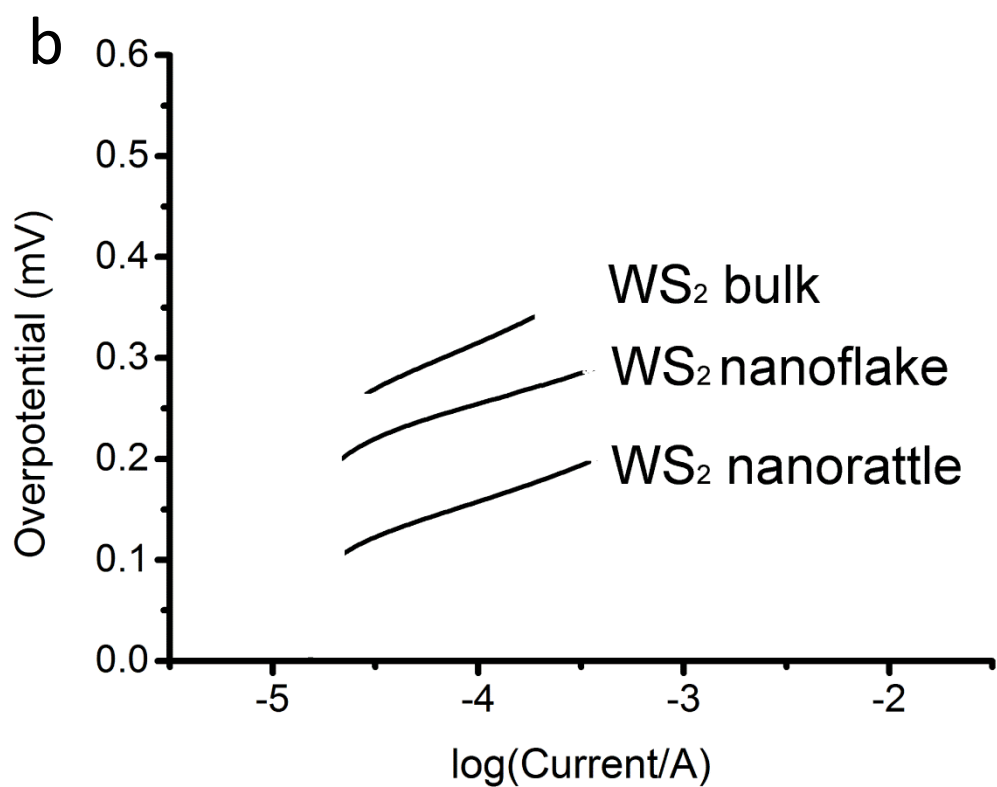


Figure 7.17. (a) Polarisation curves of bulk WS₂, WS₂ nanoflakes and WS₂ nanorattles. (b) Corresponding Tafel plots and (c) durability test showing negligible current loss even after 5000 CV cycles.

The HER electrocatalytic performance of WS₂@WS₂ nanorattles on a gold electrode was measured using the standard three-electrode electrochemical configuration in 0.5 M H₂SO₄ electrolyte, as described in the “Experimental” section. According to Figure 7.17a, the WS₂@WS₂ nanorattles exhibited a small onset overpotential of 100 mV versus the reversible hydrogen electrode (RHE). Compared with bulk WS₂ (250 mV vs. RHE) and WS₂ nanoflakes (200 mV vs. RHE), this value is much smaller, which suggests the much better catalytic activity of the WS₂@WS₂ nanorattles. Moreover, the cathode current density was 71 mA/cm² at an overpotential of -300 mV, which is much higher than that of bulk WS₂ (2.7 mA/cm²) and WS₂ nanoflakes (18 mA/cm²). Because the current density is proportional to the quantity of evolved H₂, this large value indicated that a large amount of H₂ was released at this low potential. The corresponding Tafel plots in Figure 7.17b reveal three slopes: 68 mV/dec, 71 mV/dec and 92 mV/dec for the WS₂ nanorattle, WS₂ nanoflake and bulk WS₂, respectively. It is apparent that the Tafel slope value for the WS₂ nanorattle is much lower than that of the other two materials, indicating better HER catalytic performance.

Table 7.1. HER parameters of various WS₂ samples

Materials	Tafel slope (mV/dec)	Overpotential (mV)	J ^a (mA/cm ²)	C _{dl} ^b (μF)
WS ₂ nanorattle	68	100	71	3.6
WS ₂ nanoflake	71	200	18	1.1
WS ₂ bulk	92	250	2.7	0.8

(a) Current densities (j) were recorded at overpotential (η) = 300mV. (b) C_{dl} were estimated by plotting the ΔJ (J_a-J_c) at 0.15 V vs. RHE against the scan rate, where the slope is twice C_{dl}.

Table 7.2. Comparison of the HER performances of various types of WS₂ materials

Synthesis Methods	Overpotential (mV)	Tafel Slope (mV/dec)
Hydrothermal synthesis in the presence of graphene nanosheets, and then vacuum annealing at 300°C[46]	~200	58
Sulfidation of a tungsten precursor in H ₂ S at 450°C[32]	200-250	135
Lithium intercalation and exfoliation of bulk WS ₂ materials[47]	280	110
Lithium intercalation and exfoliation of bulk WS ₂ materials[49]	80-100 (1T) ~200 (2H)	60 (1T) 110 (2H)
Sonochemical exfoliation from WS ₂ nanotubes[56]	~150	~200
Direct reaction of W and S[57]	477	N/A
Reaction of WO ₃ with sulfur at 600°C[45]	~100	72
High temperature solution synthesis[48]	~100	48
Reaction of W@WS ₂ nanorattle with sulfur at 450°C (this work).	~100	68

Because the active sites of WS₂ were on their metallic edges, WS₂ IF nanoparticles, due to their closed cage structures, exhibited poor HER performance. However, WS₂ nanoflake cores in the produced WS₂ nanorattles exhibited much better catalytic effects in the HER process. Although pristine WS₂ nanoflakes should have similar numbers of active sites as those of WS₂ nanorattles, their severe agglomeration results in poor contact between their catalytic sites and the reactants, leading to inferior HER performance. This problem

was solved by introducing this nanorattle structure, which not only prevented the agglomeration of nanoflakes but also supplied sufficient space for the catalytic reaction. As a result, as-prepared WS₂ nanorattles exhibited a considerably improved HER performance. The double layer capacitance is a parameter used to estimate the active sites of catalysts [36] because the double layer capacitances of catalysts are linearly proportional to their effective active surface areas [36]. Therefore, the largest C_{dl} of the WS₂ nanorattles (Table 7.1) suggested that these nanorattles had more active sites than the other two materials. Compared with work performed by other researchers, the as-synthesised nanorattles exhibited one of the lowest overpotential values, the highest current density at 0.3 V and a good Tafel slope (Table 7.2), indicating that they had the great potential of being used as an alternative HER catalyst. In addition to good catalytic activity, the stability of a catalyst is very important. To test the stability of the nanorattle catalyst, the HER process was continuously performed for 5000 cycles in H₂SO₄ solution. Figure 7.17c presents the polarisation curves measured before and after the 5000 CV cycles ranging from 0.05 to 0.35 V at a scan rate of 100 mV/s. The almost coinciding two curves indicated that the WS₂ nanorattles exhibited excellent, long-time electrochemical stability.

7.2.4 Conclusions

WS₂@WS₂ nanorattles were prepared *via* a simple solid-gas reaction. In this technique, as-synthesised W@WS₂ and S were used as the raw materials and were fired at 350°C for 1 h in Ar. Well-dispersed WS₂ nanoflakes (the sizes and thicknesses were below 100 nm and 5 nm, respectively) with abundant edges were generated in-situ in the WS₂ shells. These nanoflakes exhibited good HER activity with a small onset overpotential of 100 mV and a small Tafel slope of 68 mV/dec. It is believed that the synthesis strategy used in this work can be readily extended to fabricate other transitional metal nanorattles such as WC@WS₂, MoS₂@MoS₂ and WSe₂@WSe₂.

- Advanced Materials*, vol. 21, pp. 3621-3638, Sep 25 2009.
- [2] P. M. Arnal, M. Comotti, and F. Schuth, "High-temperature-stable catalysts by hollow sphere encapsulation," *Angewandte Chemie-International Edition*, vol. 45, pp. 8224-8227, 2006.
- [3] W. S. Choi, H. Y. Koo, and D. Y. Kim, "Scalable synthesis of chestnut-bur-like magnetic capsules loaded with size-controlled mono- or bimetallic cores," *Advanced Materials*, vol. 19, pp. 451-+, Feb 5 2007.
- [4] S. Ikeda, S. Ishino, T. Harada, N. Okamoto, T. Sakata, H. Mori, S. Kuwabata, T. Torimoto, and M. Matsumura, "Ligand-free platinum nanoparticles encapsulated in a hollow porous carbon shell as a highly active heterogeneous hydrogenation catalyst," *Angewandte Chemie-International Edition*, vol. 45, pp. 7063-7066, 2006.
- [5] Y. H. Ng, S. Ikeda, T. Harada, S. Higashida, T. Sakata, H. Mori, and M. Matsumura, "Fabrication of hollow carbon nanospheres encapsulating platinum nanoparticles using a photocatalytic reaction," *Advanced Materials*, vol. 19, pp. 597-+, Feb 19 2007.
- [6] Z. Kai, X. H. Zhang, H. T. Chen, C. Xin, L. L. Zheng, J. H. Zhang, and Y. Bai, "Hollow titania spheres with movable silica spheres inside," *Langmuir*, vol. 20, pp. 11312-11314, Dec 21 2004.
- [7] X. W. Lou, L. A. Archer, and Z. C. Yang, "Hollow Micro-/Nanostructures: Synthesis and Applications," *Advanced Materials*, vol. 20, pp. 3987-4019, Nov 3 2008.
- [8] H. J. Hah, J. I. Um, S. H. Han, and S. M. Koo, "New synthetic route for preparing rattle-type silica particles with metal cores," *Chemical Communications*, pp. 1012-1013, Apr 21 2004.
- [9] S. Cavaliere-Jaricot, M. Darbandi, and T. Nann, "Au-silica nanoparticles by "reverse" synthesis of cores in hollow silica shells," *Chemical Communications*, pp. 2031-2033, 2007.
- [10] A. B. Fuertes, M. Sevilla, T. Valdes-Solis, and P. Tartaj, "Synthetic route to nanocomposites made up of inorganic nanoparticles confined within a hollow mesoporous carbon shell," *Chemistry of Materials*, vol. 19, pp. 5418-5423, Oct 30 2007.
- [11] D. M. Cheng, X. D. Zhou, H. B. Xia, and H. S. O. Chan, "Novel method for the preparation of polymeric hollow nanospheres containing silver cores with different sizes," *Chemistry of Materials*, vol. 17, pp. 3578-3581, Jul 12 2005.
- [12] Y. D. Yin, R. M. Rioux, C. K. Erdonmez, S. Hughes, G. A. Somorjai, and A. P. Alivisatos, "Formation of hollow nanocrystals through the nanoscale Kirkendall Effect," *Science*, vol. 304, pp. 711-714, Apr 30 2004.
- [13] B. Liu and H. C. Zeng, "Symmetric and asymmetric Ostwald ripening in the fabrication

- of homogeneous core-shell semiconductors," *Small*, vol. 1, pp. 566-571, May 2005.
- [14] L. J. Wang, J. L. Shi, Y. Zhu, Q. J. He, H. Y. Xing, J. Zhou, F. Chen, and Y. Chen, "Synthesis of a Multinanoparticle-Embedded Core/Mesoporous Silica Shell Structure As a Durable Heterogeneous Catalyst," *Langmuir*, vol. 28, pp. 4920-4925, Mar 20 2012.
- [15] L. X. Chang, H. B. Yang, W. Y. Fu, N. Yang, J. J. Chen, M. H. Li, G. T. Zou, and J. X. Li, "Synthesis and thermal stability of W/WS₂ inorganic fullerene-like nanoparticles with core-shell structure," *Materials Research Bulletin*, vol. 41, pp. 1242-1248, Jul 13 2006.
- [16] Y. Feldman, G. L. Frey, M. Homyonfer, V. Lyakhovitskaya, L. Margulis, H. Cohen, G. Hodes, J. L. Hutchison, and R. Tenne, "Bulk synthesis of inorganic fullerene-like MS₂ (M=Mo, W) from the respective trioxides and the reaction mechanism," *Journal of the American Chemical Society*, vol. 118, pp. 5362-5367, Jun 12 1996.
- [17] Y. S. Kwon, A. A. Gromov, A. P. Ilyin, A. A. Ditts, J. S. Kim, S. H. Park, and M. H. Hong, "Features of passivation, oxidation and combustion of tungsten nanopowders by air," *International Journal of Refractory Metals & Hard Materials*, vol. 22, pp. 235-241, 2004.
- [18] H. B. Yang, S. K. Liu, J. X. Li, M. H. Li, G. Peng, and G. T. Zou, "Synthesis of inorganic fullerene-like WS₂ nanoparticles and their lubricating performance," *Nanotechnology*, vol. 17, pp. 1512-1519, Mar 14 2006.
- [19] A. J. van der Vlies, G. Kishan, J. W. Niemantsverdriet, R. Prins, and T. Weber, "Basic reaction steps in the sulfidation of crystalline tungsten oxides," *Journal of Physical Chemistry B*, vol. 106, pp. 3449-3457, Apr 4 2002.
- [20] R. Tenne, M. Homyonfer, and Y. Feldman, "Nanoparticles of layered compounds with hollow cage structures (inorganic fullerene-like structures)," *Chemistry of Materials*, vol. 10, pp. 3225-3238, Nov 1998.
- [21] C. Schuffenhauer, G. Wildermuth, J. Felsche, and R. Tenne, "How stable are inorganic fullerene-like particles? Thermal analysis (STA) of inorganic fullerene-like NbS₂, MoS₂, and WS₂ in oxidizing and inert atmospheres in comparison with the bulk material," *Physical Chemistry Chemical Physics*, vol. 6, pp. 3991-4002, 2004.
- [22] J. Lee, J. C. Park, and H. Song, "A nanoreactor framework of a Au@SiO₂ yolk/shell structure for catalytic reduction of p-nitrophenol," *Advanced Materials*, vol. 20, pp. 1523-+, Apr 21 2008.
- [23] T. Zych, T. Misiaszek, and M. M. Szostak, "Polymorphism of 2-nitroaniline studied by calorimetric (DSC), structural (X-ray diffraction) and spectroscopic (FT-IR, Raman, UV-Vis) methods," *Chemical Physics*, vol. 340, pp. 260-272, Nov 9 2007.
- [24] X. Du and J. H. He, "Carrier effect in the synthesis of rattle-type Au@hollow silica nanospheres by impregnation and thermal decomposition method," *Microporous and*

- Mesoporous Materials*, vol. 163, pp. 201-210, Nov 15 2012.
- [25] L. F. Tan, D. Chen, H. Y. Liu, and F. Q. Tang, "A Silica Nanorattle with a Mesoporous Shell: An Ideal Nanoreactor for the Preparation of Tunable Gold Cores," *Advanced Materials*, vol. 22, pp. 4885-+, Nov 16 2010.
- [26] M. S. Dresselhaus and I. L. Thomas, "Alternative energy technologies," *Nature*, vol. 414, pp. 332-337, Nov 15 2001.
- [27] J. A. Turner, "Sustainable hydrogen production," *Science*, vol. 305, pp. 972-974, Aug 13 2004.
- [28] M. G. Walter, E. L. Warren, J. R. McKone, S. W. Boettcher, Q. X. Mi, E. A. Santori, and N. S. Lewis, "Solar Water Splitting Cells," *Chemical Reviews*, vol. 110, pp. 6446-6473, Nov 2010.
- [29] J. K. Norskov, T. Bligaard, A. Logadottir, J. R. Kitchin, J. G. Chen, S. Pandelov, and J. K. Norskov, "Trends in the exchange current for hydrogen evolution," *Journal of the Electrochemical Society*, vol. 152, pp. J23-J26, 2005.
- [30] B. Hinnemann, P. G. Moses, J. Bonde, K. P. Jorgensen, J. H. Nielsen, S. Horch, I. Chorkendorff, and J. K. Norskov, "Biornimetic hydrogen evolution: MoS₂ nanoparticles as catalyst for hydrogen evolution," *Journal of the American Chemical Society*, vol. 127, pp. 5308-5309, Apr 20 2005.
- [31] T. F. Jaramillo, K. P. Jorgensen, J. Bonde, J. H. Nielsen, S. Horch, and I. Chorkendorff, "Identification of active edge sites for electrochemical H₂ evolution from MoS₂ nanocatalysts," *Science*, vol. 317, pp. 100-102, Jul 6 2007.
- [32] J. Bonde, P. G. Moses, T. F. Jaramillo, J. K. Norskov, and I. Chorkendorff, "Hydrogen evolution on nano-particulate transition metal sulfides," *Faraday Discussions*, vol. 140, pp. 219-231, 2009.
- [33] Y. G. Li, H. L. Wang, L. M. Xie, Y. Y. Liang, G. S. Hong, and H. J. Dai, "MoS₂ Nanoparticles Grown on Graphene: An Advanced Catalyst for the Hydrogen Evolution Reaction," *Journal of the American Chemical Society*, vol. 133, pp. 7296-7299, May 18 2011.
- [34] D. Merki and X. L. Hu, "Recent developments of molybdenum and tungsten sulfides as hydrogen evolution catalysts," *Energy & Environmental Science*, vol. 4, pp. 3878-3888, Oct 2011.
- [35] J. Kibsgaard, Z. B. Chen, B. N. Reinecke, and T. F. Jaramillo, "Engineering the surface structure of MoS₂ to preferentially expose active edge sites for electrocatalysis," *Nature materials*, vol. 11, pp. 963-969, Nov 2012.
- [36] M. A. Lukowski, A. S. Daniel, F. Meng, A. Forticaux, L. S. Li, and S. Jin, "Enhanced Hydrogen Evolution Catalysis from Chemically Exfoliated Metallic MoS₂ Nanosheets," *Journal of the American Chemical Society*, vol. 135, pp. 10274-10277, Jul 17 2013.

- [37] M. V. Bollinger, J. V. Lauritsen, K. W. Jacobsen, J. K. Nørskov, S. Helveg, and F. Besenbacher, "One-dimensional metallic edge states in MoS₂," *Physical review letters*, vol. 87, p. 196803, Nov 5 2001.
- [38] Z. Z. Wu, B. Z. Fang, Z. P. Wang, C. L. Wang, Z. H. Liu, F. Y. Liu, W. Wang, A. Alfantazi, D. Z. Wang, and D. P. Wilkinson, "MoS₂ Nanosheets: A Designed Structure with High Active Site Density for the Hydrogen Evolution Reaction," *Acs Catalysis*, vol. 3, pp. 2101-2107, Sep 2013.
- [39] J. F. Xie, H. Zhang, S. Li, R. X. Wang, X. Sun, M. Zhou, J. F. Zhou, X. W. Lou, and Y. Xie, "Defect-Rich MoS₂ Ultrathin Nanosheets with Additional Active Edge Sites for Enhanced Electrocatalytic Hydrogen Evolution," *Advanced Materials*, vol. 25, pp. 5807-+, Oct 2013.
- [40] T. F. Jaramillo, J. Bonde, J. D. Zhang, B. L. Ooi, K. Andersson, J. Ulstrup, and I. Chorkendorff, "Hydrogen Evolution on Supported Incomplete Cubane-type [Mo₃S₄](4+) Electrocatalysts," *Journal of Physical Chemistry C*, vol. 112, pp. 17492-17498, Nov 13 2008.
- [41] H. I. Karunadasa, E. Montalvo, Y. J. Sun, M. Majda, J. R. Long, and C. J. Chang, "A Molecular MoS₂ Edge Site Mimic for Catalytic Hydrogen Generation," *Science*, vol. 335, pp. 698-702, Feb 10 2012.
- [42] D. Merki, S. Fierro, H. Vrubel, and X. L. Hu, "Amorphous molybdenum sulfide films as catalysts for electrochemical hydrogen production in water," *Chemical Science*, vol. 2, pp. 1262-1267, 2011.
- [43] H. Vrubel, D. Merki, and X. L. Hu, "Hydrogen evolution catalyzed by MoS₃ and MoS₂ particles," *Energy & Environmental Science*, vol. 5, pp. 6136-6144, Mar 2012.
- [44] Z. B. Chen, D. Cummins, B. N. Reinecke, E. Clark, M. K. Sunkara, and T. F. Jaramillo, "Core-shell MoO₃-MoS₂ Nanowires for Hydrogen Evolution: A Functional Design for Electrocatalytic Materials," *Nano Letters*, vol. 11, pp. 4168-4175, Oct 2011.
- [45] Z. Z. Wu, B. Z. Fang, A. Bonakdarpour, A. K. Sun, D. P. Wilkinson, and D. Z. Wang, "WS₂ nanosheets as a highly efficient electrocatalyst for hydrogen evolution reaction," *Applied Catalysis B-Environmental*, vol. 125, pp. 59-66, Aug 21 2012.
- [46] J. Yang, D. Voiry, S. J. Ahn, D. Kang, A. Y. Kim, M. Chhowalla, and H. S. Shin, "Two-dimensional hybrid nanosheets of tungsten disulfide and reduced graphene oxide as catalysts for enhanced hydrogen evolution," *Angewandte Chemie*, vol. 52, pp. 13751-4, Dec 16 2013.
- [47] J. Kim, S. Byun, A. J. Smith, J. Yu, and J. X. Huang, "Enhanced Electrocatalytic Properties of Transition-Metal Dichalcogenides Sheets by Spontaneous Gold Nanoparticle Decoration," *Journal of Physical Chemistry Letters*, vol. 4, pp. 1227-1232, Apr 18 2013.

- [48] L. Cheng, W. Huang, Q. Gong, C. Liu, Z. Liu, Y. Li, and H. Dai, "Ultrathin WS₂ Nanoflakes as a High-Performance Electrocatalyst for the Hydrogen Evolution Reaction," *Angewandte Chemie International Edition*, pp. n/a-n/a, 2014.
- [49] D. Voiry, H. Yamaguchi, J. W. Li, R. Silva, D. C. B. Alves, T. Fujita, M. W. Chen, T. Asefa, V. B. Shenoy, G. Eda, and M. Chhowalla, "Enhanced catalytic activity in strained chemically exfoliated WS₂ nanosheets for hydrogen evolution," *Nature materials*, vol. 12, pp. 850-855, Sep 2013.
- [50] D. Voiry, M. Salehi, R. Silva, T. Fujita, M. W. Chen, T. Asefa, V. B. Shenoy, G. Eda, and M. Chhowalla, "Conducting MoS₂ Nanosheets as Catalysts for Hydrogen Evolution Reaction," *Nano Letters*, vol. 13, pp. 6222-6227, Dec 2013.
- [51] Z. Q. Li, C. J. Lu, Z. P. Xia, Y. Zhou, and Z. Luo, "X-ray diffraction patterns of graphite and turbostratic carbon," *Carbon*, vol. 45, pp. 1686-1695, Jul 2007.
- [52] G. L. Frey, R. Tenne, M. J. Matthews, M. S. Dresselhaus, and G. Dresselhaus, "Optical properties of MS₂ (M = Mo, W) inorganic fullerene-like and nanotube material optical absorption and resonance Raman measurements," *Journal of Materials Research*, vol. 13, pp. 2412-2417, Sep 1998.
- [53] J. P. Wilcoxon, P. P. Newcomer, and G. A. Samara, "Synthesis and optical properties of MoS₂ and isomorphous nanoclusters in the quantum confinement regime," *Journal of Applied Physics*, vol. 81, pp. 7934-7944, Jun 15 1997.
- [54] A. Berkdemir, H. R. Gutierrez, A. R. Botello-Mendez, N. Perea-Lopez, A. L. Elias, C. I. Chia, B. Wang, V. H. Crespi, F. Lopez-Urias, J. C. Charlier, H. Terrones, and M. Terrones, "Identification of individual and few layers of WS₂ using Raman Spectroscopy," *Scientific Reports*, vol. 3, Apr 30 2013.
- [55] F. Zhang, Y. F. Shi, X. H. Sun, D. Y. Zhao, and G. D. Stucky, "Formation of Hollow Upconversion Rare-Earth Fluoride Nanospheres: Nanoscale Kirkendall Effect During Ion Exchange," *Chemistry of Materials*, vol. 21, pp. 5237-5243, Nov 10 2009.
- [56] C. Choi, J. Feng, Y. G. Li, J. Wu, A. Zak, R. Tenne, and H. J. Dai, "WS₂ nanoflakes from nanotubes for electrocatalysis," *Nano Research*, vol. 6, pp. 921-928, Dec 2013.
- [57] S. Wirth, F. Harnisch, M. Weinmann, and U. Schroder, "Comparative study of IVB-VIB transition metal compound electrocatalysts for the hydrogen evolution reaction," *Applied Catalysis B-Environmental*, vol. 126, pp. 225-230, Sep 25 2012.

Chapter Eight

Conclusions and Suggestions for Future Work

Conclusions

In summary, WS_2 , MoS_2 and ZrS_2 nanoparticles with controllable morphologies have been successfully produced on large scale *via* two techniques and the optimized heat production parameters have been identified.

For the synthesis of WS_2 *via* solid-gas reaction of WO_3 , H_2 and S, H_2 played a very important role on the formation of WS_2 nanoflakes and IF nanoparticles. When H_2 was absent, although WS_2 could be readily generated, it was impossible to obtain IF nanoparticles. Instead, WS_2 nanoflakes were fabricated. By analysing the products obtained by different heat treatment using various techniques, the main effects of H_2 were clarified: (1) initially forming continuous WS_2 coating on the surface of Tungsten oxide cores to maintain the nanosizes and isolate them from agglomeration; (2) building a proper synergy between S and O interdiffusion during sulfurization by generating O vacancies.

Beside the involvement of H_2 , the production of WS_2 was also found to be closely related to many other parameters such as temperature, holding time, raw material size and amount. By varying these parameters, lots of WS_2 nanoparticles with various morphologies were produced. Among these products, a unique $W@WS_2$ nanorattle structure drew the author's attention because it had good potential to be used as nanoreactor. After further investigation on this kind of nanorattles, they showed decent catalytic performance on the conversion from 2-Nitroaniline (2-NA) to o-Phenylenediamine (OPD), arising from the presence of WS_2 shells which could efficiently isolate each W core

from agglomeration while leaving sufficient room for the catalytic reaction. When the W cores were further converted to WS_2 from the reaction with S, $WS_2@WS_2$ nanorattles were firstly fabricated. Because the synthesised WS_2 cores were tiny and well-dispersed, these $WS_2@WS_2$ nanorattles exhibited excellent catalytic HER performance.

Because MoS_2 highly resembles WS_2 , the solid-gas reaction was also applied to produce MoS_2 nanomaterials. MoS_2 particles with typical IF structure were synthesised under similar heat treatment conditions as the production WS_2 IF nanoparticles. By analysing the sizes of produced WS_2 and MoS_2 and the morphologies of reaction intermediates, both of these two reactions follow a “template growth” mechanism. Based on the comparison with the products obtained from conventional H_2S involved technique, the yield and morphology of produced WS_2 and MoS_2 from this new route are quite similar. Moreover, the usage of relatively simple equipment and replacement of toxic H_2S with H_2 and S make the technique have good potential to be used on large scale production.

Apart from solid-gas reaction, CVD is another efficient technique used to synthesise metal dichalcogenides. However, WS_2 IF nanoparticles produced *via* CVD usually have a large amount of defects or even disconnection, leading to poor mechanical properties. To address this problem, an additional annealing process was introduced in our experiments to heal these defects. During the investigation, many parameters such as temperature, reaction time and gas flow rate were thoroughly analysed to obtain an optimized condition. Based on this optimized condition, well-crystallized WS_2 IF nanoparticles were produced after annealing. Then, CVD was also applied on the synthesis of ZrS_2 nanoflakes with very tiny sizes (<30nm). Because of the small size, these nanoflakes exhibit strong quantum confinement and luminescence effects. In addition, these nanoflakes also exhibit good photocatalytic activity for the decomposition of 4-NP which is a major pollutant on many areas.

Further Work

In the future, as-synthesised IF nanoparticles have good potential to be used as reinforcement in various composites arising from their good mechanical properties and spherical structure. For example, because of their excellent shock wave resistance, they can be mixed with metal or ceramic matrix to form a kind of new composite armour. Because of the small sizes of as-synthesised ZrS_2 , these nanoflake might also exhibit good performance in fast charging/discharging cycles recovery of the reversible capacity. Based on similar principle with the good catalytic HER performance, the $WS_2@WS_2$ nanorattles might also be good candidate in the battery area (e.g. Li and Na battery). Moreover, by adding some visible absorber such as CdS, these nanorattles could also show decent photocatalytic performance. Here are some plans in detail:

As mentioned in the literature review (Chapter two), WS_2 nanotubes were readily produced from the template reaction of WO_3 nanowhiskers and H_2S . As a result, it is possible to produce WS_2 nanotubes on large scale by replacing WO_3 nanoparticles with nanowhiskers via the same H_2S -free route. Similarly, MoS_2 nanotubes might also be produced by the same route when MoO_3 whiskers are used as precursor. Because all current techniques on the synthesis of MoO_3 nanotubes are essentially based on the gas-gas reaction mechanism, it will be the first report on “template growth” of MoS_2 nanotubes. Therefore, it will be much easier to control the sizes of products than common techniques.

Although ZrS_2 nanoflakes have already been produced, the detailed mechanism is still unclear. To understand the mechanism, it is important to investigate the decomposition process of ZrS_3 . Therefore, ZrS_3 nanosheets should be produced at first and then heated under different temperatures and holding times. By analysing the compositions and morphologies of products, it is possible to summarise a reasonable synthesis mechanism.

Because of the high similarity between WS_2 and MoS_2 , $Mo@MoS_2$ nanorattles can also be produce via the same technique which might also have good catalytic performance. Besides, since both WS_2 and MoS_2 are biocompatible

materials, the corresponding nanorattles are safe to be used as drug delivery vehicle.

As discussed in Chapter seven, S atoms can diffuse through WS_2 shells of $W@WS_2$ nanorattles to react with W cores, leading to the formation of $WS_2@WS_2$ nanorattles. Therefore, some other materials such as carbon can also react with W cores by the same route. Consequently, $WC@WS_2$ nanorattles are able to be prepared. Because WC also has decent HER catalytic performance, this new $WC@WS_2$ nanorattle material might also exhibit excellent HER catalytic performance.